Plasma boundary phenomena in tokamaks

1990 Nucl. Fusion 30 1225

(http://iopscience.iop.org/0029-5515/30/7/005)

REVIEW PAPER

PLASMA BOUNDARY PHENOMENA IN TOKAMAKS

P.C. STANGEBY
Institute for Aerospace Studies,
The University of Toronto,
Toronto, Ontario, Canada
and
JET Joint Undertaking,
Abingdon, Oxfordshire, United Kingdom

G.M. McCRACKEN
Culham Laboratory,
Euratom-UKAEA Fusion Association,
Abingdon, Oxfordshire, United Kingdom

ABSTRACT. Effects of the plasma boundary can have a substantial influence on the behaviour of the entire plasma in tokamaks. Progress in the field, particularly that over the last decade, is reviewed, with emphasis on experimental observation. Simple modelling for interpretation is also included.

1. INTRODUCTION

For physical systems in which the transport and other properties of the medium are fixed, central conditions are entirely controlled by edge conditions. It is not yet clear to what degree this situation characterizes tokamak plasmas. Since the fusion plasma must produce net energy in the core, the range of permissible conditions in the centre is closely defined by the Lawson criterion. The edge conditions, on the other hand, appear to permit a wide latitude: the solid surface contacting the plasma can, in principle, be made of any material and can be shaped arbitrarily; the magnetic geometry at the edge can be manipulated substantially without causing significant perturbation to the centre. Constraints on tolerable heat loads and erosion rates must, however, be satisfied. Such constraints turn out to be quite limiting.

The principal task is to optimize the choice of edge conditions in order to achieve the required conditions in the central plasma, consistent with engineering constraints on the edge structures. The principal obstacle to progress in this task is our limited understanding concerning the relation between the edge plasma and the central plasma.

It is already evident that some aspects of tokamak operation are largely controlled, or even dominated, by edge processes. With regard to particle confinement, the plasma and impurity densities are often largely set by edge conditions, with the particle transport in the main plasma being more or less fixed. (In some operating modes, however, changes can occur in the main plasma transport, leading to strong impurity accumulation). Energy confinement of tokamaks may be a function of central (local) plasma properties. However, in some important operating conditions, such as the H-mode, pellet fuelling, improved Ohmic confinement (IOC, ASDEX), the supershot mode (TFTR), etc., the edge conditions play key roles in the improvement of the energy confinement. In addition, 'profile-consistency' models would have the temperature throughout the plasma directly dependent on the edge temperature.

The weakness of our understanding of tokamak edge conditions, and of their relation to central conditions, is due in part to the weakness of the experimental database. Historically, in fusion research, diagnosis of the edge has been much less extensive than that of the centre. Fortunately, this situation is improving as greater efforts regarding edge diagnostics are being undertaken. The 1980s have seen increasing emphasis on edge studies in virtually all devices, and a number of new tokamaks officially committed to the study of plasma-surface interactions (TEXTOR, Tokamak de Varennes, JET) have come into operation. The bulk of edge measurements and the main advance in understanding of edge phenomena have undoubtedly occurred in the past decade or so. The last Nuclear Fusion review on edge processes [1] was published in 1979, and it is therefore timely that the field be reviewed again. This earlier review focused largely on the candidate edge materials and their properties when subject to plasma exposure, e.g. ion sputtering yields, with less emphasis on the edge plasma behaviour itself. Although materials questions have not all been answered by any means, this field has nevertheless reached a relatively mature state, and will therefore not be dealt with here, except peripherally. The interested reader is directed to the excellent and comprehensive Data Compendium for Plasma-Surface Interactions [2] issued by Nuclear Fusion as a Special Supplement in 1984.

The focus in the present review will be on the processes occurring at the edge, and on the connection between edge plasma and central plasma processes.

The following terminology will be employed: the 'edge' is taken to be synonymous with the *boundary plasma* (BP), which can be divided into two zones radially — the *radiating layer* (RL) and the *scrape-off layer* (SOL). The SOL is the region outside of the *last closed magnetic flux surface* (LCFS) or separatrix. The RL is the region where atomic physics processes (for both the main fuel and the impurities) strongly influence local energy and particle balance. When light impurities such as carbon and oxygen dominate — currently the typical situation, with metals generally playing a minor role — the RL extends a distance of order 0.1 m inside the LCFS.

Measurements of the most basic properties of the BP, the electron density n_e and the electron temperature T_e, are still not made routinely and systematically on any tokamak, even in the relatively accessible SOL. Measurements of n_e and T_e in the RL are still more scarce and measurements of other key quantities such as ion temperature T_i are rarely made anywhere in the BP. Such paucity of basic experimental information restricts our understanding of edge phenomena. Generalizations are difficult at this early stage. Accordingly, in much of the review, and by way of illustration of principles, extensive use will be made of data and analyses from two specific tokamaks — DITE and JET — with which the authors are most familiar and whose edge regions have been comparatively well diagnosed. The work will also emphasize concepts, and will attempt a critical — rather than a comprehensive — review. Much edge literature is largely

phenomenological in nature and is therefore difficult to incorporate in a logical framework. Such work, of course, constitutes the basic building material for the logical edifice and would be given full coverage in any review written solely for the tokamak edge community. For a review directed at the general fusion community, however, it seemed to the authors more appropriate to emphasize the key ideas and to reference the literature which directly bears on these ideas.

The field of tokamak edge studies has been comprehensively reviewed elsewhere. The Proceedings of a NATO Advanced Study Institute summer school on the Physics of Plasma-Wall Interactions in Controlled Fusion have been published in 1986 [3]. In addition, the work of the tokamak edge community is reviewed regularly, every two years, in a number of invited papers at the series of International Conferences on Plasma-Surface Interactions in Controlled Fusion Devices, and published as special volumes by the Journal of Nuclear Materials [4].

The review is organized into the following sections: Section 2 reviews the techniques used for edge diagnosis and summarizes the basic experimental information (n_e and T_e); Section 3 reviews simple models of the SOL in order to provide a logical framework for the review; Sections 4, 5 and 6 deal with the most important effects of the BP on tokamak operation, namely, the influence on the fuel particles (Section 4), on impurities (Section 5) and on energy (Section 6); Section 7 reviews the methods of manipulating and controlling edge conditions in tokamaks; Section 8 reviews the experimental database for the edge during auxiliary heating of tokamaks; Sections 9 and 10 deal with two special topics, fluctuations and asymmetries at the edge.

Predictive numerical codes have been used extensively for the design of future tokamaks such as ITER. Such work is beyond the scope of the present review. Emphasis is placed here on physical models which can be used to interpret experimental results.

The cut-off date for inclusion of material in the review was generally early 1989. A few recent developments such as the 'carbon bloom' (Section 5.3.2) and the use of beryllium limiters (Section 5.7) were added during final preparation of the manuscript.*

* For List of Symbols, see page 1374.

2. MEASUREMENTS OF PLASMA DENSITY AND TEMPERATURE IN THE EDGE PLASMA OF TOKAMAKS

As for the main plasma, understanding of the plasma edge and control of edge conditions is critically dependent on measurements of the local plasma parameters. The edge measurement problem is perhaps a more challenging one, however, since more quantities need to be known, higher spatial resolution is required, and two- or three-dimensional variation exists. As with the main plasma, measurements are required of n_e, T_e, T_i, impurity density n_{imp}, neutral hydrogen density n_{H^0}, radiated power P_R and fluctuation levels; in addition, knowledge is required of neutral impurity and hydrogen influx rates, flow speeds of hydrogenic and impurity ions along the magnetic field $\vec{B}$ to surfaces, heat and particle outflux rates to surfaces, etc. The edge plasma exhibits very strong radial variations, with scale lengths of order 10 mm. Larger scale variation exists along $\vec{B}$. In many cases the edge structure is fully three-dimensional and various asymmetries can occur, for example, between electron-drift-side and ion-drift side fluxes.

The values of electron temperature and plasma density constitute the most important experimental information about the tokamak edge; these data are reviewed in Section 2.1. The non-specialist may then prefer to skip Section 2.2, which describes the edge diagnostic techniques in some detail.

2.1. Radial profiles of $n_e(r)$, $T_e(r)$ in the edge

The most basic experimental information about edge conditions are the values of $n_e(r)$, $T_e(r)$ in the RL and the SOL (r is the minor radial co-ordinate). For purposes of understanding edge effects it is important to have systematic and comprehensive information on these quantities. Unfortunately, the edge measurements that do exist are typically for limited operating conditions.

In Table I, a collection of edge n_e and T_e values are given for a wide range of limiter tokamaks with Ohmic heating. Divertor tokamaks have n_e and T_e gradients along $\vec{B}$ and are treated separately (Section 7.3). Auxiliary heating and the SOL are treated in Section 8. The values shown are ones either measured at the LCFS or extrapolated to it. Each of the tokamaks can be operated at a range of average plasma density $\bar{n}_e$ and plasma current I_p values, and these reported edge values are only representative of achievable conditions. For the most part, however, there is not the information available in the published literature to indicate the range of achievable edge conditions or their dependence on

TABLE I. EDGE PARAMETERS FOR LIMITER TOKAMAKS

Tokamak	R_m (m)	a (m)	I_p (kA)	B_T (T)	$\bar{n}_e$ (10^{19} m^{-3})	Limiters	L_c (m)	Edge $\bar{n}_e$ (10^{18} m^{-3})	Edge T_e (eV)	λ_n (mm)	λ_{T_e} (mm)	Data[a]	Refs
TOSCA	0.3	0.08	8	0.5	1	1 pol.	0.94	0.6	10	11	30	M	[24]
TM3	0.4	0.08	10–40	1–2.5		1 pol.	1.3	4	30			M	[25]
TCA	0.61	0.18	75	1.5		1 pol.	1.92	12	10	20	>140	E	[26]
JFT-2	0.90	0.195	110	1.7	2.8	1 rail	8.5	3–5	30–50	14		M	[27]
JFT-2M	1.31	0.42 × 0.6	160	1.25	2–3			1	12			M	[28]
ISXB	0.92	0.26	170	1.2	2–4	1 rail	9–14	2.5	30–40	20	50	M	[29]
	0.92	0.24	116	1.3	4	1 rail			20			M	[30]
TFR 600	0.98	0.19		4		1 pol.	3.1	20	18	7	5–10	E	[31]
	0.98	0.17	220	4.2		1 rail		2	6	11	>100	-30	[32]
TEXT	1.0	0.27	100	1.0	0.8	1 pol.	3.1	1.3	17	20	30	M	[33]
	1.0	0.255	200	2	2	1 rail		9	45	20	23	M	[34]
DITE	1.17	0.26	180	2.1		2 pol.		7	50	20	15	E	[22]
	1.17	0.21	100	2.0	3	1/2 pol.		9	20	20	40	M	[15]
PLT	1.34	0.40		~3	2.2	1 rail	32	0.6	25	25	14	-60	[35]
T-10	1.5	0.325			2.5	1 pol.		2.4	5	13	>100	M	[21]
	1.5	0.325	200	2.8	3	1 rail		3	7	30–50		-20	[10, 36]
ASDEX	1.65	0.38		2.8	2	1 tor.		1.5	20	15	10–15	M	[37]
TEXTOR	1.75	0.44	350	2.0	2.5	4 rail	11	1	20	10		M	[38]
	1.75	0.44	340	2.0	3.7	1 tor.		3.5	25	9–13.5	26	M	[39, 40]
TFTR	2.55	0.83	1400		3	2 rail	30–50	3	8	25	58	-60	[41]
	2.55	0.83	1400			1 tor.		1.4	55	46	50	E	[42]
JET	2.98	1.14	3400	3.4	3	4 rail	40	4	50	40	60	E	[12]
	2.98	1.14	3000	3.4	3	1 tor.		1.3	40	25	45	M	[43]
ALCATOR A	0.60	0.10	250	6.0	35	1 pol.	1.98	80	12	12	7	M	[44]
ALCATOR C	0.64	0.16	300	6.0	20	2 pol.	1.0	400	15–20	3		E	[45]
								40	12			M	[45]
FT	0.83	0.20	300	8.0	3.5	1 pol.	2.6	40	18	5	90	E	[14]
			500	8.0	17			150	15	4	>100	E	[14]

[a] M: data measured at the limiter edge; E: data extrapolated to the limiter edge. When the data were not measured and cannot be extrapolated, the distance behind the limiter where the measurements were made is noted in mm.

$\bar{n}_e$, I_p, etc. Where a range of conditions has been reported, a mid-range value is given in Table I.

It is clear that progress in the field of edge physics will require a more concerted effort to acquire such fundamental information. Fortunately, a number of new diagnostic techniques — both for solid probes and for non-disturbing techniques (see Section 2.2) — have been developed recently which can explore the entire edge region. What is probably more important, however, is a programmatic commitment on each tokamak to deploy the resources needed and to make available operational time for systematic studies.

Edge diagnosis — at least within the SOL — is complicated by the poloidal and toroidal asymmetries, i.e. 2-D and 3-D effects. In this situation it is not sufficient to measure $n_e(r)$ and $T_e(r)$ at one poloidal and one toroidal location only. The degree of SOL non-symmetry appears to be largely governed by the type of limiter configuration — rail (or mushroom), poloidal, toroidal (see Section 3.1) — and in this regard it is fortunate that the trend in recent years is towards toroidal limiter tokamaks. These appear to create the most symmetric SOLs (Section 10) since each SOL flux tube makes a complete toroidal and

poloidal transit; because parallel field transport is generally fast, this means that any poloidal/toroidal variation in cross-field fluxes into the SOL flux tube will be averaged out — and the SOL as a whole will tend to be uniform at a given minor radius. It appears that cross-field transport into the SOL is generally poloidally non-uniform, with a ballooning transport favouring the outside (large major radius side) [5-8]; other poloidal/toroidal variations can exist, e.g., associated with the location of gas injection.

Poloidal limiter tokamaks appear to be particularly susceptible to formation of asymmetrical SOLs. The most systematic poloidal survey of SOL n_e and T_e values was carried out on ALCATOR C (poloidal limiter) using the 80 probe DENSEPAK array [8, 9]. This study, discussed in more detail in Section 10, revealed very strong poloidal variations of n_e and T_e in the SOL, with differences of a factor of ten or more for a given minor radius. The explanation for the strong asymmetry is probably that communication between SOL flux tubes is interrupted by the poloidal limiter and, therefore, any poloidal variation in cross-field transport directly manifests itself as a poloidal variation in n_e and T_e, i.e., there is not the same averaging effect as with toroidal limiters.

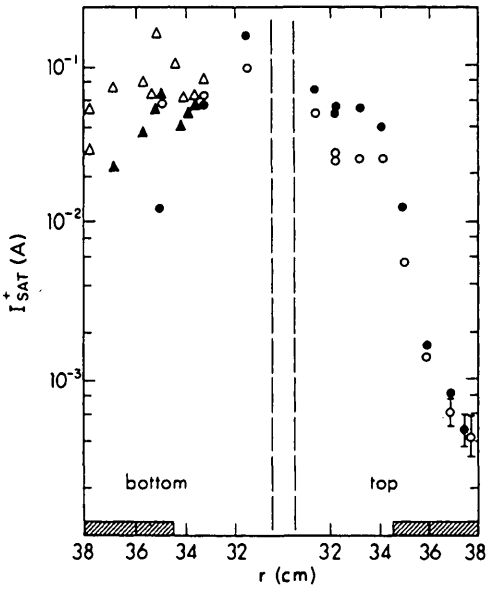

FIG. 1. T-10: Radial dependence of ion saturation currents for Mach probes at the top and bottom of the plasma column [10]. Solid symbols are for the ion side, open symbols for the electron side.
●, ○ — r_L = 28 cm, $\bar{n}_e = 2.8 \times 10^{19}$ m^{-3};
▲, △ — r_L = 32 cm, $\bar{n}_e = 3.2 \times 10^{19}$ m^{-3};
r_L is the radius of the rail limiter.
The poloidal ring limiter is at r = 34.5 cm.

Rail limiters, which are superficially the least symmetrical configuration, appear, in fact, to be intermediate in their symmetry between poloidal and toroidal limiters. Figure 1 shows an example of SOL probe measurements made in T-10 [10], at the top and bottom of the torus, by probes which distinguished between the electron and ion drift directions of the ion saturation current to the probe I_s^+. The values of I_s^+ indicate the magnitude of the plasma density on each side (Section 2.2.1). A single rail limiter was either at r = 28 cm or at 32 cm, with a full poloidal limiter tip at r = 34.5 cm. As can be seen, in the rail limiter SOL there is only a small top/bottom asymmetry, less than a factor of two, while in the poloidal limiter SOL the differences are extremely large. The explanation would again appear to be that SOL flux tubes for a rail limiter tokamak make at least one (and typically more) poloidal/toroidal transits, achieving some averaging effect. Nevertheless, rail limiters have been found in other, more detailed, studies on T-10 [11] to produce significant 2-D and 3-D edge structure related to the multiple connection lengths for different parts of the limiter surface (see Section 10).

Because of the complexity of rail and poloidal limiter SOLs, the focus in this review will be on data from toroidal limiter tokamaks, primarily JET, for which a systematic survey of SOL $n_e(r)$ and $T_e(r)$ values has been carried out over a wide range of operating conditions [12]. Results for SOL $n_e(r)$, $T_e(r)$, λ_n, λ_T are shown in Figs 2–5 (λ_n and λ_T are the radial decay lengths of electron density and temperature).

The current generation of large, long-pulse tokamaks may approach more closely true steady-state edge conditions, with attendant simplifications in interpretation. Presumably, achievement of steady state, particularly at the edge, requires discharge times which are long compared not only with the times τ_p and τ_E (the particle and energy confinement times) characteristic of the plasma but also with the times characteristic of changes in surface conditions.

A further possible simplification may be simply related to size: for very large tokamaks, the 'edge' and 'core' may be logically separable zones, while for smaller devices distinctions between 'edge' and 'core' may be harder to discern. Although edge databases are not really sufficient to establish clear-cut patterns of behaviour, the impression given by these data is contradictory and often non-intuitive. On a small tokamak, for example, the relationship between n_{LCFS}, the density at the LCFS (Section 3.1), and $\bar{n}_e$ is rather baffling; sometimes, n_{LCFS} scarcely increases with $\bar{n}_e$ at all [13, 14]; sometimes it increases linearly

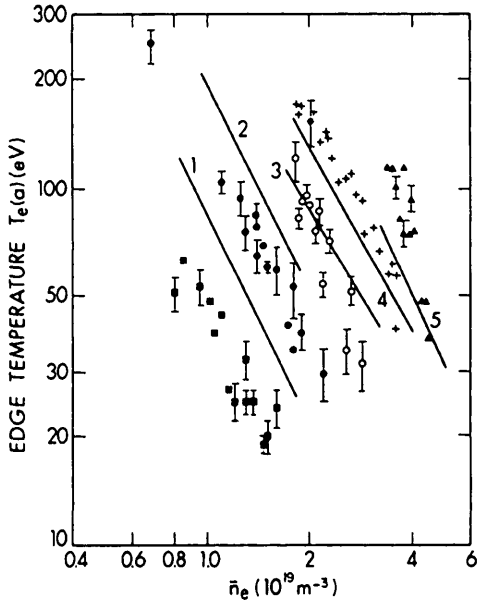

FIG. 2. JET probe results [12]. Effect of line average density $\bar{n}_e$ on temperature T_e at the LCFS (■ = 1 MA, 2.1 T; ● = 2 MA, 2.1 T; ○ = 3 MA, 3.4 T; + = 4 MA, 3.5 T; ▲ = 5 MA, 3.5 T). The solid lines are from a simple model given in Section 3, Eq. (3.55).

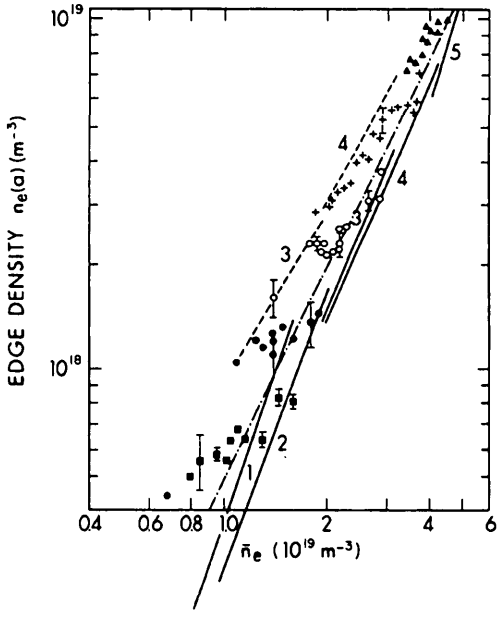

FIG. 3. JET probe results [12]. Effect of $\bar{n}_e$ on the electron density at the LCFS (■ = 1 MA, 2.1 T; ● = 2 MA, 2.1 T; ○ = 3 MA, 3.4 T; + = 4 MA, 3.5 T; ▲ = 5 MA, 3.5 T). The lines are from models in Sections 3 and 4. Solid lines: model of Eq. (3.57) based on the empirical value of the particle confinement time τ_p for JET, Eq. (3.49). Dash-dotted line: model of Eq. (4.15a) with an estimated value of the effective penetration velocity for hydrogen, $v_0 = 3 \times 10^4$ m·s^{-1} [198]. Dashed line: model of Eq. (4.17) based on values of v_0 calculated using the NIMBUS neutral Monte Carlo code [23].

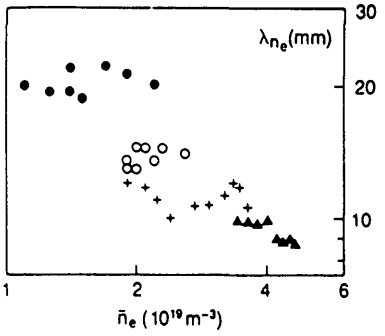

FIG. 4. JET probe results [46]. Effects of $\bar{n}_e$ and I_p on the density scrape-off length in the SOL, λ_n (● = 2 MA, 2.1 T; ○ = 3 MA, 3.4 T; + = 4 MA, 3.4 T; ▲ = 5 MA, 3.4 T).

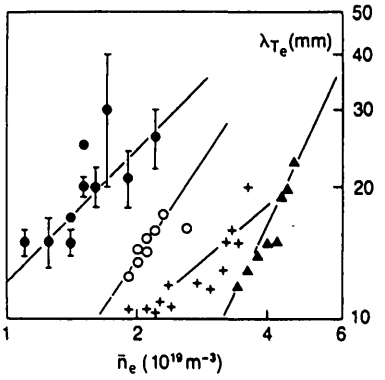

FIG. 5. JET probe results [46]. Effects of $\bar{n}_e$ and I_p on the temperature scrape-off length in the SOL, λ_T (● = 2 MA, 2.1 T; ○ = 3 MA, 3.4 T; + = 4 MA, 3.4 T; ▲ = 5 MA, 3.4 T).

[15–17] and sometimes non-linearly [18–20]. Edge temperatures in small devices typically show little variation despite changes in I_p, etc. T_{LCFS} generally decreases with increasing $\bar{n}_e$, but sometimes only weakly [13, 14, 21], sometimes as approximately $\bar{n}_e^{-1}$ [15, 17] and sometimes as approximately $\bar{n}_e^{-2}$ [10, 20]; often, T_e appears to be 'stuck' in the 10–20 eV range, and can even be uninfluenced by significant increases in auxiliary heating [19, 22]. The machine size required to achieve effective separation of 'core' and 'edge' may be quite large. The effective depth of hydrogen recycle refuelling, for example, is substantial; using a Monte Carlo neutral study on JET [23] it was calculated that this depth is $\simeq 0.5\ \bar{n}_e^{-1}$ [m] for $\bar{n}_e$ in [10^{19} m^{-3}], which is large compared to the minor radius typical for operation of most medium and small tokamaks. This matter is discussed further in Section 4.

As is evident from the JET Ohmic results in Figs 2 and 3, these edge conditions appear to be intuitively understandable. T_{LCFS} drops rapidly as $\bar{n}_e$ increases, evidently due to dilution (i.e., more particles for the same power), and increases with I_p, evidently due to greater heat input.

To a first approximation, $\bar{n}_{LCFS} \propto n_e^2$, which is expected on the basis of the simplest edge fuelling model (see Section 4). As will be discussed later, the JET Ohmic SOL data appear also to be explicable when subjected to more detailed analysis, regarding both trend and absolute magnitude. The properties of the SOL, however, are complicated by the application of auxiliary heating (Section 8).

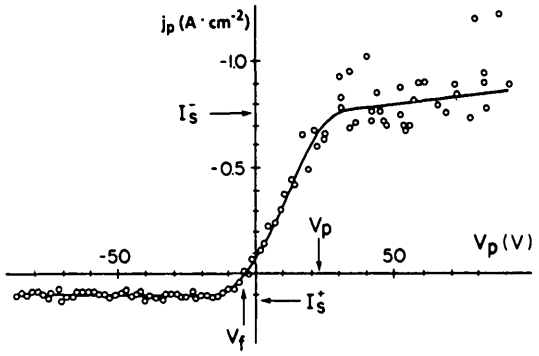

FIG. 6. Langmuir probe characteristic taken in the DITE tokamak, with a plasma current of 120 kA, a toroidal field of 2 T, and the probe 35 mm behind the limiter [58].

2.2. Diagnostic methods

2.2.1. *Langmuir probes*

The Langmuir probe (LP) has been the principal edge diagnostic in the field, providing most of the data on n_e and T_e. In its simplest form the LP consists of an electrically biased, electron/ion collecting element inserted into the edge plasma. From the current-voltage (I-V) characteristic of such a probe, the local values of n_e and T_e can be deduced; information is also provided on the local plasma potential (further details are given in Sections 3.2 and 3.3). In at least two critical aspects the LP is ideally suited to edge diagnosis: (a) spatial resolution is possible down to millimetre scales, and (b) the LP is robust enough to withstand the heat fluxes in the edge. In addition, the inherent simplicity and low cost permit deployment of LP arrays, making it possible, in principle, to measure the multi-dimensional and asymmetrical properties of the edge. On the other hand, interpretation of the I-V characteristic to extract n_e, etc., is non-trivial. It is clear that insertion of an object into the plasma is perturbing, and the task of probe interpretation is to account for this disturbance. Probes which are flush-mounted into existing edge structures, such as limiters, are non-disturbing; however, their interpretation poses other difficulties.

A typical LP I-V characteristic, as measured in the DITE tokomak, is shown in Fig. 6. This is an example of a single probe characteristic, where only one small collector (i.e. the probe) is inserted and the probe potential, V, is measured relative to the potential of a large structure in contact with the edge plasma, typically the limiter.

Provided the area ratio between the reference surface and the probe is large, the I-V characteristic reflects plasma conditions near the probe. Double and triple probe arrangements are also used where a separate reference surface is not required (or available). The principal features of the single probe I-V characteristic (Fig. 6) are:

- Saturation currents I_s^+/I_s^- registered at large negative/positive probe potential V;
- The probe floating potential V_f at which the net probe current is zero;
- The local plasma potential V_p, which is not clearly defined from the characteristic, but which is close to the 'knee' where I_s^- is first attained;
- An approximately exponential variation of I with regard to V between the two saturation levels.

We now give a brief outline of probe interpretation, without derivations (these are given in Sections 3.2 and 3.3).

The most basic interpretation of the I-V characteristic is that regarding I_s^-: when the probe is at or above the local plasma potential, the random thermal electron flux to the probe is unimpeded. One would thus anticipate that:

$$I_s^- = (1/4) n_e \bar{c}_e A_{pr} e \qquad (2.1a)$$

where A_{pr} is the probe collecting area, e is the unit charge, and

$$\bar{c}_e = (8kT_e/\pi m_e)^{1/2} \qquad (2.1b)$$

is the electron thermal velocity. For a non-magnetized plasma, this expectation appears to be generally valid; this is, however, not the case for strongly magnetized plasmas, as will be discussed.

In the exponential portion of the characteristic for $V < V_p$, electrons are repelled and, assuming a Maxwellian energy distribution for electrons (giving a Boltzmann factor — see Section 3.2), one would anticipate an electron current

$$I^- = I_s^- \exp[e(V - V_p)/kT_e] \quad (2.2)$$

Since $m_i \gg m_e$, this would then also approximate to the total current I, at least until $V \ll V_p$. Again it should be noted that simple exponential behaviour does not generally occur for strongly magnetized plasmas (see below).

In analogy to I_s^-, one might expect that a relation similar to Eq. (2.1a) would apply for I_s^+. For 1-D plasma flow to a surface, however, one has

$$I_s^+ \approx 0.5\, n_e\, c_s\, A_{pr} e \quad (2.3)$$

where $c_s = [k(T_e + T_i)/m_i]^{1/2}$, the (isothermal) ion acoustic velocity (see Section 3.2), and A_{pr} is the probe area. Z = 1 ions are assumed. Briefly, the explanation of this unexpected behaviour is that insertion of the probe is more disturbing for the ions than for the electrons. For $V < V_p$, most of the applied potential V appears as a voltage drop across the thin electrostatic sheath between the collector and the plasma (sheath thickness: of order the Debye length). This 'shielding' of the plasma from the applied electric field by the sheath is, however, imperfect. A 'pre-sheath' penetrates deep into the plasma, attracting ions and repelling electrons. The total potential drop in the pre-sheath is $\approx 0.5\ kT_e/e$ which, from the Boltzmann factor, implies that n_e (= n_i) at the sheath edge is about $0.5\ n_{e\infty}$. Thus the ions in the pre-sheath are subject to a pressure gradient force, dp_i/dx, as well as to the electrostatic force, which forces are additive (and are, indeed, of virtually equal magnitude for Z = 1 ions). For the electrons, by contrast, the two forces almost exactly cancel and thus the assumption of an undisturbed Maxwellian electron distribution, as implicit in the use of the Boltzmann factor, is valid. The ion distribution, however, is strongly perturbed and the assumption of a Maxwellian ion distribution at the sheath edge is not valid [47–51]. The ions are indeed accelerated to the acoustic velocity c_s (i.e. supersonic in terms of the ion thermal velocity $\bar{c}_i \equiv (8kT_i/\pi m_i)^{1/2}$) — a result which was first derived by Bohm [48] by considering the conditions required for a monotonic potential variation within the sheath; the same result, however, can be obtained by considering the limiting conditions for the pre-sheath [50–52]. This example of probe interpretation thus demonstrates the need to take into account the disturbing effect of the probe on the plasma.

Returning to the case of I_s^-: evidently, the validity of Eq. (2.1a) for $V > V_p$ should also be questioned since the electron distribution is disturbed. Indeed, since $|I_s^-| > |I_s^+|$, the drawing by the probe of the current I_s^- can be powerfully disturbing to the plasma and the interpretation of this part of the characteristic is difficult even for non-magnetic plasmas. In general, $I = I_s^+ + I^-$, while, at $V = V_f$, $|I^-| = I^+ = I_s^+$. Since V_f is well defined from the characteristic, it is convenient to fit the measured I–V characteristic by

$$I = I_s^+(1 - \exp[e(V - V_f)/kT_e]) \quad (2.4)$$

By combining Eqs (2.2) and (2.3), one obtains a relation for the potential drop across the sheath for floating conditions, $V_{sf} \equiv V_f - V_p$, and thus the value of the local plasma potential V_p. Probe measurements at different spatial locations can thus provide the important quantity $\vec{E}$. Allowing for the secondary electron emission coefficient δ for the surface, one can show [52] that (see Eq. (3.25))

$$V_{sf} = \frac{kT_e}{2e} \ln\left[2\pi \frac{m_e}{m_i}\left(1 + \frac{T_i}{T_e}\right)(1 - \delta)^{-2}\right] \quad (2.5)$$

The derivation is given in Section 3.3. For example, for H^+ ions, $T_i = T_e$ and $\delta = 0$, one obtains $V_{sf} = -2.49\ kT_e/e$, which is the basis for the commonly stated approximation that "the plasma potential is $\approx 3T_e$ above V_f".

Turning then to the practicalities of probe interpretation: I_s^+ and V_f can be simply read from the I–V characteristic. The value of T_e can then be obtained from a log-plot of $(I/I_s^+ - 1)$, Eq. (2.4). A better method, in common use, employs a numerical, non-linear least-squares fit to the measured I–V characteristic using the function in Eq. (2.4). Thus, one obtains T_e, I_s^+ and V_f as the three primary measured quantities. With knowledge about T_i, both n_e and V_p can then be inferred from Eqs (2.3) and (2.5), respectively. T_i is rarely measured in the edge and it is usually assumed that $T_e = T_i$ in extracting n_e values from I_s^+. The error involved in this assumption is probably not greater than a factor of two in most cases: edge measurements of T_i have generally shown $T_i \gtrsim T_e$ [53–55] but not $T_i \gg T_e$ and, in any case, the error is only of the form $(1 + T_i/T_e)^{1/2}$.

The foregoing outline of probe interpretation is much abbreviated. This topic, however, has been extensively reviewed in the following publications, to

which the interested reader is referred. The classical probe reviews by Chen [56] and by Swift and Schwar [57], although now two decades old, remain relevant and highly useful for non-magnetic plasmas as well as for many aspects of magnetic plasmas. With regard to the use of probes in fusion plasmas specifically, the reader is referred to the recent review by Manos and McCracken [58] and to the review by Stangeby [59] focused on the interpretation of plasma probes for fusion experiments. A number of other recent probe reviews [60–66] are also available.

Three specific points will now be reviewed in more detail, namely: (i) probe size effects, (ii) the practically usable portion of the I-V characteristic, and (iii) comparison of n_e measured by probes and other (non-disturbing) techniques.

In order to examine these questions, one should consider first the basic picture of plasma flow to solid surfaces in the presence of strong magnetic fields [48, 67]. Because particle motion along $\vec{B}$ is much faster than cross-field motion, the sink action of the solid surface reduces the plasma density all along the magnetic flux tube subtended by the solid. The resulting cross-field density gradient then provides, by diffusion, the particle influx required for particle balance; in the simplest picture — and the one most typical of tokamak edge conditions — particle creation within the flux tube, for example by ionization, can be neglected compared with the cross-field source from the rest of the plasma. Two different, but closely related, configurations may be considered — the probe and the SOL. In the simplest probe configuration, no other solid surface is present, (Fig. 7). Because of the large difference in the $\|\vec{B}$ versus the $\perp\vec{B}$ flux densities, the probe reduces the plasma density over a great length L_p along $\vec{B}$ [48, 67]. The probe *disturbance* or *collection*

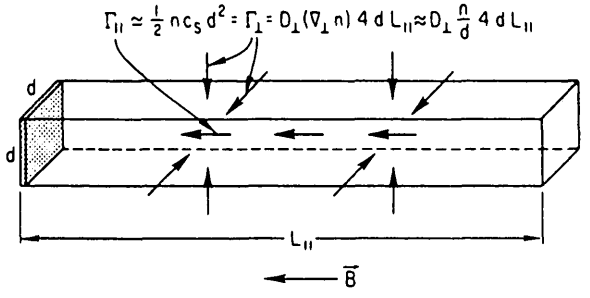

FIG. 7. Schematic of particle flows induced by insertion of a solid surface into a plasma with a magnetic field. Since parallel-field motion is rapid, initially a long flux tube is almost evacuated of plasma, setting up in the steady state a cross-field density gradient of order n/d which supplies plasma to the flux tube. A natural 'collection' or 'disturbance' length, $L_p = L_{\|}$, is thus defined.

length, $L_p \gg d$, where d is the characteristic probe size $\perp \vec{B}$, extends along $\vec{B}$ away from the probe in each direction (Fig. 7). The SOL configuration, examined in detail in Section 3 (see Fig. 26), involves two solid surfaces subtending each end of a magnetic flux tube at the tokamak edge. In this case, the $\|\vec{B}$ distance involved, the *connection* length L_c is, of course, fixed by the magnetic and structural geometry. Although the two configurations differ in this respect, various aspects of them are identical. To minimize duplication, all derivations are deferred to Section 3, but they are quoted in this section, as required.

We now discuss the three specific issues of the probes:

(a) *Probe size effects*

We first compare the ion and electron Larmor radii $\ell_{e,i}$:

$$\ell_{e,i} = \frac{v_{e,i}\, m_{e,i}}{eB} \tag{2.6}$$

with the characteristic size of the probe, d, where $v_{e,i}$ are the specific particle velocities. For a 'strong magnetic field' [60, 68],

$$\ell_e < d < \ell_i \tag{2.7}$$

while for a 'very strong magnetic field',

$$d > \ell_{e,i} \tag{2.8}$$

Typically, B = 1–10 T in fusion devices, while the probe sizes are typically d = 1–30 mm. As plasma pulse lengths have become longer in fusion devices and the plasma energy densities have increased, the probe sizes have tended to increase, for heat dissipation reasons. Typically, probes on JET and TFTR, for example, have $d \simeq 10$ mm [69, 70]. When, for example, $T_i = 100$ eV and B = 4 T, then $v_i \simeq 10^5\ m \cdot s^{-1}$; therefore, $\ell_i \simeq 0.5$ mm (D^+) and thus the 'very strong magnetic field' regime often obtains.

The key aspect of the very strong magnetic field regime is that the magnetic field totally dominates cross-field transport to the probe, even for the ions, and individual particle trajectory effects are unimportant. As shown in Fig. 7, the value of L_p is given [51, 67, 71, 72] approximately by the flux balance expression:

$$\Gamma_{\|} \simeq \tfrac{1}{2} n c_s d^2 = \Gamma_{\perp}(\nabla n_{\perp}) 4 d L_p \simeq D_{\perp} \frac{n}{d} 4 d L_p \tag{2.9}$$

where $\Gamma_\parallel$ and $\Gamma_\perp$ are the parallel and perpendicular particle flux densities and $D_\perp$ is the perpendicular diffusion coefficient. Thus

$$L_p \approx d^2 c_s / 8 D_\perp \qquad (2.10)$$

Example: d = 10 mm, $T_e = T_i = 100$ eV, $c_s = 10^5\ m \cdot s^{-1}$ (D^+), $D_\perp = 1\ m^2 \cdot s^{-1}$; therefore, $L_p \approx 1$ m, i.e. the disturbed zone is extremely long and narrow.

Recently, this relation for L_p has been directly tested on DITE [73] using an object of variable size d and a 'search probe' located at a fixed distance x along $\vec{B}$ away from the object. It was found that the disturbance caused by the object, as registered by the search probe signal, only became significant for $x \approx d^2 c_s / 8 D_\perp$, with $D_\perp$ equal to the Bohm diffusion value, $D_\perp^{Bohm} \equiv 0.06\ T_e[eV]/B[T]$ [48].

The great length of L_p has a number of important implications [51]:

(i) The probe does not, as is sometimes assumed, provide measurements of local n_e or T_e values, but rather ones which are averaged over a length L_p along $\vec{B}$. If the (parallel) gradient scale lengths of n_e and T_e are shorter than L_p, they cannot be measured by the probe.

(ii) If L_p exceeds L_{cp}, the connection length of the probe, i.e. the distance along $\vec{B}$ from the probe to the next solid surface such as a limiter, then the natural collection process of the probe is interfered with, and this must be taken into account in the probe interpretation [72, 74, 75]. Because of the large probe sizes often employed in tokamaks this situation is not infrequently encountered [8, 76, 77].

A second aspect related to probe size is the effective collection area, A_{eff}. In the very strong magnetic field regime, one expects that, irrespective of the actual area of the probe, $A_{eff} = A_\perp$, where $A_\perp$ is the area of the collector projected in the direction of $\vec{B}$; the reason for this is that the ion drift speed *along* $\vec{B}$ approaches c_s, almost independent of the angle between $\vec{B}$ and the surface [78–81]. Particularly in smaller tokamaks, probes are often operated (only) in the strong magnetic field regime, and uncertainties arise in the value of A_{eff} because of finite Larmor radius effects. This was demonstrated on DITE [82] using a special probe consisting of a 1 × 5 mm post in front of a 10 × 5 mm plate (Fig. 8). Although $A_\perp^{plate} = 9A_\perp^{post}$, the plate I_s^+ was found to be only about three times the post I_s^+,

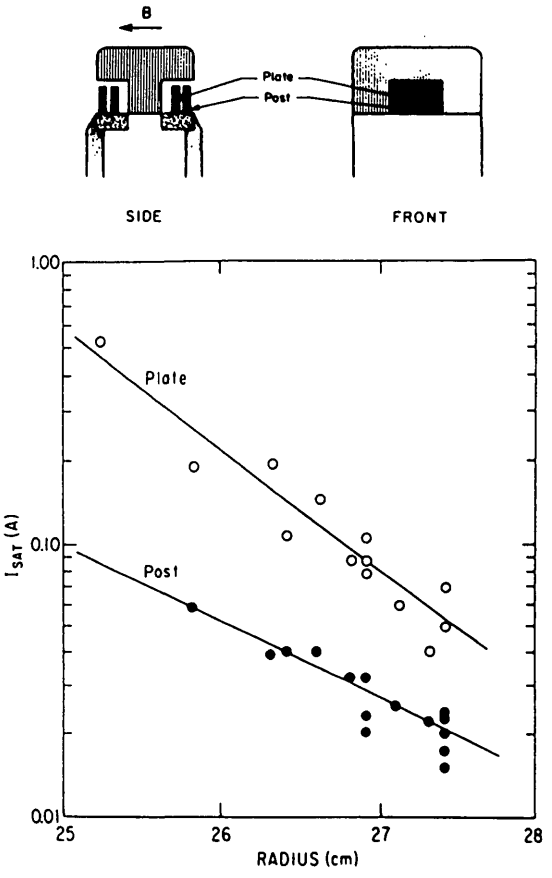

FIG. 8. Effects of probe size, illustrated by a probe including a 1 mm × 5 mm post collector in front of a 10 mm × 5 mm plate collector. The values of $I^+_{s\,plate}/I^+_{s\,post}$ are clearly less than the ratio of the projected areas, i.e. 9, indicating finite ion Larmor radius collection by the post [82].

indicating that the post could collect ions over much of its entire circumferential area because of finite ℓ_i. By contrast, when the post and the plate were both biased for electron collection, it was found that $I^-_{plate} \approx 9I^-_{post}$. From the viewpoint of having a well-defined value of A_{eff}, and thus a reliable measurement of n_e, it would therefore appear to be advisable to employ probes that are large enough to be in the very strong magnetic field regime, although this can make for rather large values of L_p, raising separate problems.

A particularly attractive probe configuration involves mounting the probe within an existing edge structure, such as a limiter, with the probe face flush to the main surface. This arrangement, which has been used successfully on a number of tokamaks (D-III [19, 83–85], DITE [86], JET [87], T-10 [36], DIII-D [88]), enjoys a number of advantages:

— Measurements are made where they are generally of greatest interest, i.e., at the edge structure location;
— The heat load on the probe will not be a problem if the structure itself has been properly designed for thermal loads;
— The probe is non-disturbing;
— Most of the problems in connection with finite L_p are avoided;
— Small probes can be used, which makes it practical to collect I_s^-;
— The arrangement is relatively inexpensive and large arrays are practical.

A number of problems are encountered, however. At least on large tokamaks, limiter surfaces, etc. are aligned to be almost tangential to $\vec{B}$. Any variations or uncertainties in θ, the angle of $\vec{B}$ to the surface, have a large effect on A_{eff}. In addition, as $\theta \to 0$, the probe sheath changes in its fundamental nature [78, 89, 90] and finite ℓ_i effects become important. Unless the probe diameter is very large compared with the annular insulating gap between the probe and the main surface, further finite ℓ_i effects occur, because of ion collection on the probe sides.

At sufficiently small values of θ, the secondary electrons cannot escape from the surface because they are recaptured on their first gyro-cycle. Since the value of δ can approach unity for materials of interest [54, 91, 92], and since V_{sf} (Eq. (2.5)) and the heat flux to surfaces (Section 3) are strongly dependent on values of δ near unity, uncertainties are introduced regarding the precise (effective) value of δ. Fortunately, these uncertainties do not generally affect the measurement of the principal quantities of interest for Langmuir probes, namely n_e and T_e.

(b) *Practically usable portion of the I–V characteristic*

In a non-magnetic plasma, the exponential portion of the characteristic from which T_e is found can span orders of magnitude in variation of I, and the observed ratio of I_s^-/I_s^+ is close to the simple result $\bar{c}_e/(4c_s)$, which is ~60 for a hydrogen plasma. The most obvious difference in the probe characteristics for tokamak plasmas is the greatly reduced ratio I_s^-/I_s^+, which is typically 5–10 [58, 93] (see, e.g., Fig. 6). Although less obvious, the transitional portion of the characteristic is not exponential for the most part.

When I_s^- is being collected, the probe's electron collection length is presumably even longer than the ambipolar value given by Eq. (2.10), namely

$$L_p^e \simeq \bar{c}_e d^2/D_\perp^e \tag{2.11}$$

where $D_\perp^e$ is not necessarily equal to the ambipolar value $D_\perp^{amb}$. Bohm [48] first provided an explanation for the reduced ratio of I_s^-/I_s^+: the electrons suffer collision with the ions in being drawn to the probe down the long flux tube of length L_p^e. The friction results in an enhanced density drop along the tube [67], thus reducing the electron flux density at the probe below $1/4\, n_{e\infty}\, \bar{c}_e$, where $n_{e\infty}$ is the electron density far from the surface of the probe. It has been calculated [71] that

$$I_s^- = \left(\frac{r'}{1 + r'}\right) \frac{1}{4}\, n_{e\infty}\, \bar{c}_e e A_{pr} \tag{2.12}$$

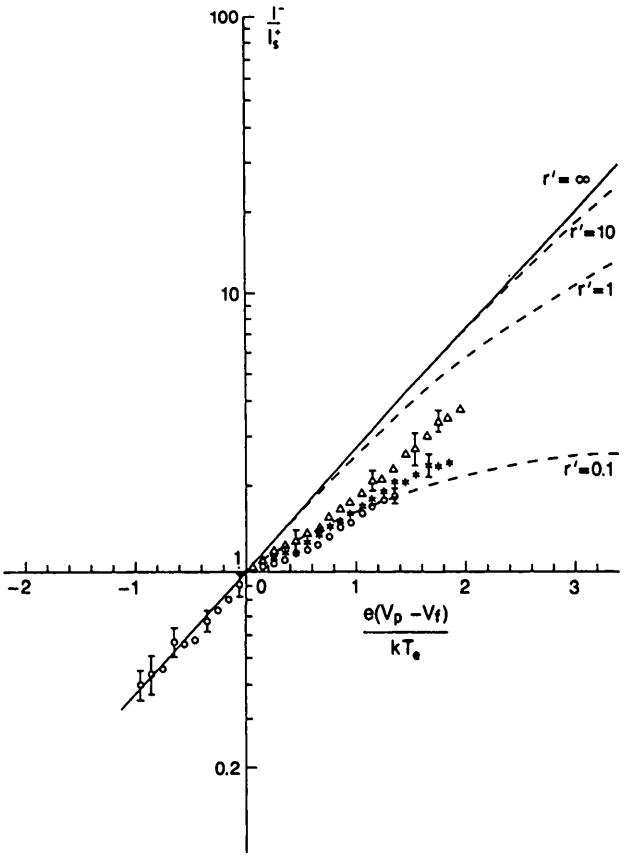

FIG. 9. Example of net electron collection by a single Langmuir probe on JET [94]. The current is normalized to the measured value of I_s^+. The probe voltage V relative to the measured floating potential, normalized by T_e, is measured using only data for $V < V_F$. The latter data follow an exponential, in contrast to data for $V > V_F$. For comparison, the dotted lines show theoretical characteristics for different values of the reduction parameter r', Eq. (2.12). The value of r' is calculated using Eq. (2.13). JET edge data indicate $r' \simeq 1$. Different symbols indicate different discharge conditions.

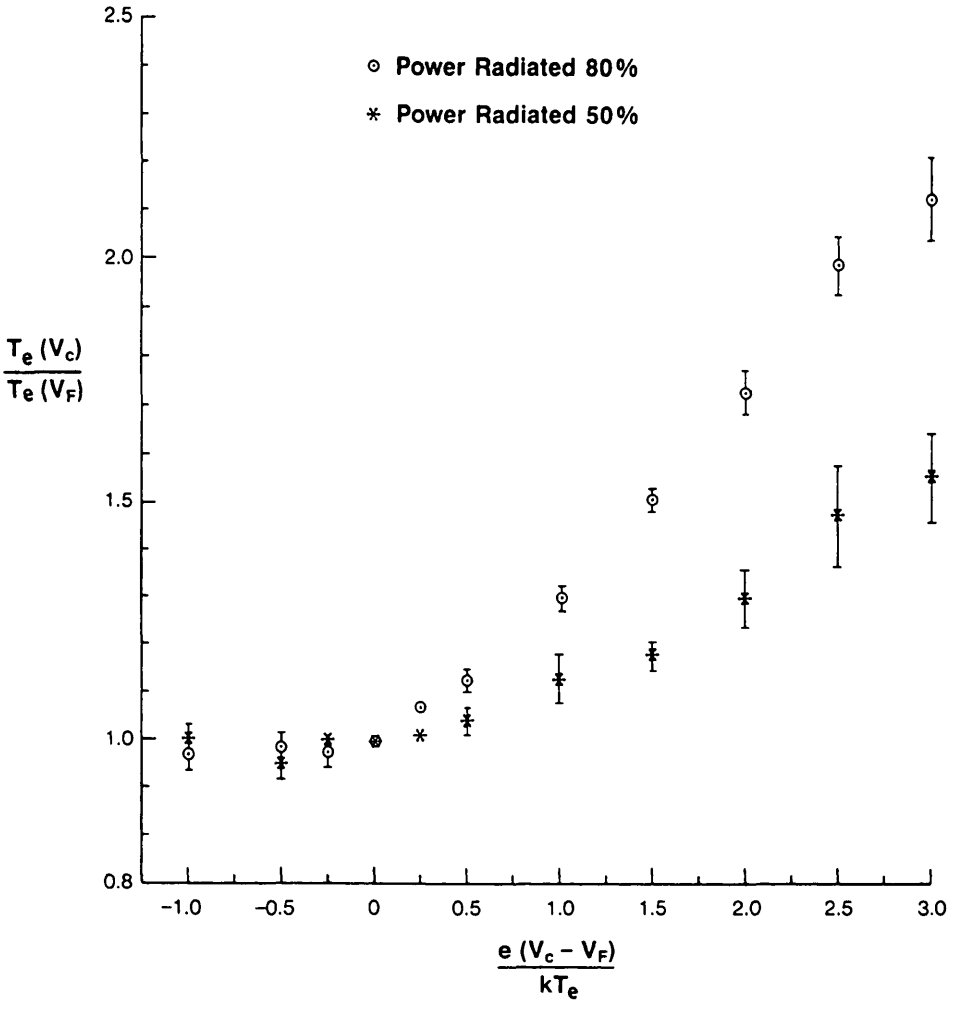

FIG. 10. Use of JET data to infer T_e by employing different voltage (upper) cut-offs V_C to the data [94]. For $V_c \lesssim V_F$, the electron current is exponential and gives a value of T_e independent of V_c. For $V_c \gtrsim V_F$, the best exponential fit to the data gives spuriously high values of T_e. Distortion appears to be worst for highly radiating, i.e. impure, plasmas.

where r′ is a reduction factor given [59, 94] by

$$r' = 2(\lambda_{ei}/d)(1 + T_i/T_e)(D_\perp^e/D_\parallel^e)^{1/2} \qquad (2.13)$$

with λ_{ei} the electron-ion collisional mean free path, $D_\parallel^e$ the classical parallel electron diffusion coefficient and $d^2 = A_{pr}$, the probe area.

It can also be argued [71] that it is not only I_s^- which is reduced by the frictional losses with ions but the electron currents at all probe voltages, at least for $V > V_f$ (for $V = V_f$ the ions and electrons have the same drift speed). The reduction factor r′ is a function of probe voltage [71] and so the transitional portion, $V_f \lesssim V \lesssim V_p$, is non-exponential. Figure 9 gives an example of probe measurements made on JET [94], showing the departure from exponential behaviour starting at $V = V_f$. If one simply fits the basic I-V characteristic (Eq. (2.4)) to the data, employing data up to a maximum probe voltage V_c, then reasonable fits can often be obtained even for $V_c > V_f$, since the departure from exponential variation is not clearly marked and the data are always, to a degree, noisy. Nevertheless, this can lead to erroneously high values of T_e (see Fig. 10) [94]. For $V_c \lesssim V_f$, the inferred value of T_e is approximately independent of the precise value of V_c. It thus appears to be necessary to restrict the use of Langmuir probe data to probe voltage values below V_f.

Another reason to avoid using probe data for $V > V_f$ are plasma fluctuations, since a sheath rectification

effect further distorts the I–V characteristic [57, 59, 95–99]. This distortion is governed by the normalized fluctuation level of the plasma potential, $\tilde{\eta}_{np} \equiv e\tilde{V}_p/kT_e$. For small values of $\tilde{\eta}_{np}$ the distortion only occurs for $V \simeq \bar{V}_p$, but for increasing $\tilde{\eta}_{np}$ the distortion extends further down the I–V characteristic, approaching V_f. In principle, sufficiently high levels of $\tilde{\eta}_{np}$, namely $\approx 10^2$, would distort the characteristic even for $V < V_f$ [59].

Restriction of data to $V < V_f$ means that one is only sampling the high energy tail of the electron distribution, which may not be Maxwellian. No simple way to avoid having to pay this price is evident, although special probe methods have been proposed for dealing with non-Maxwellian distributions [100].

(c) *Comparison of the use of Langmuir probes with other, non-disturbing techniques in tokamaks*

Considering how centrally important Langmuir probe measurements have been for the evolution of tokamak edge physics, it is suprising how little has been done to confirm the reliability of the technique by comparing probe results with other, non-disturbing methods. Part of the problem is that sharp (radial) density gradients exist in the edge and, while Langmuir probes are well suited to making radially localized measurements, other techniques often have poorer spatial resolution. Microwave measurements of n_e, for example, integrate along a line of sight. By use of a Langmuir probe array, however, Proudfoot [101] was able to make comparisons of microwave and Langmuir probe measurements of n_e on DITE. Thus, a large number of spatially distributed points were measured along each of three vertical microwave chords. Results are shown in Fig. 11. The Langmuir probe values of n_e were obtained using Eq. (2.3) together with the assumption that $T_e = T_i$ and that A_{eff} was given by the full circumferential area of the cylindrical probe pin, diameter 0.5 mm (i.e., the strong magnetic field assumption). Uncertainties in the validity of these two assumptions mean that the excellent agreement indicated in Fig. 11 may not be meaningful to a factor of more than about two.

Ditte and Grave [102] have also compared microwave and Langmuir probe measurements of n_e on ASDEX. Assuming $T_e = T_i$ and the very strong magnetic field regime ($A_{eff} = A_\perp$ for a 2 × 2 mm probe pin), they found that the probe values of n_e were lower by a factor of 1.8 compared with the microwave values.

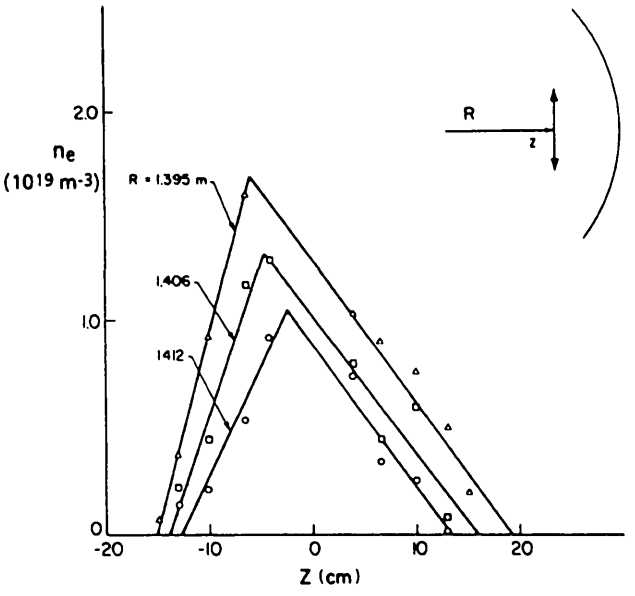

FIG. 11. Langmuir probe and microwave interferometry measurements of n_e made on DITE. The probe configuration is described in Ref. [792], with the interpretation based on Eq. (3.3), and A_{pr} is the total surface area of the probe. The microwave integrates along z. The density is fitted by straight lines.

Vasin et al. [36] have reported a comparison of Langmuir probe and microwave measurements in the edge of T-10. Eight vertical microwave chords were used and $n_e(r)$ was obtained by Abel inversion. The distances of the chords from the centre were: −30, −21, −12, −3, +6, +15, +24 and +33 cm; the Shafranov shift of plasma surfaces was allowed for in the inversion. The probe (1 × 2 mm) was located at r = 34.5 cm. Results of the comparison are given in Fig. 12, showing agreement to within 40% — the error of the Abel inversion. In the probe analysis, Eq. (2.3) was used, together with the assumptions $T_e = T_i$ and the very strong magnetic field regime ($A_{eff} = A_\perp$).

The lithium beam technique can provide measurements of both n_e and T_e in the edge plasma with excellent spatial resolution, ~1 mm (see Section 2.2.2). Comparisons of results using this technique and a movable Langmuir probe on TEXTOR, reported by Pospieszczyk et al. [40] are therefore most valuable (Fig. 13). Although the measurements were made at the top of the torus (lithium beam) and at the outside midplane (probe), the results should be comparable (see Section 10 on asymmetries). The agreement is better than a factor of two, both for n_e and T_e.

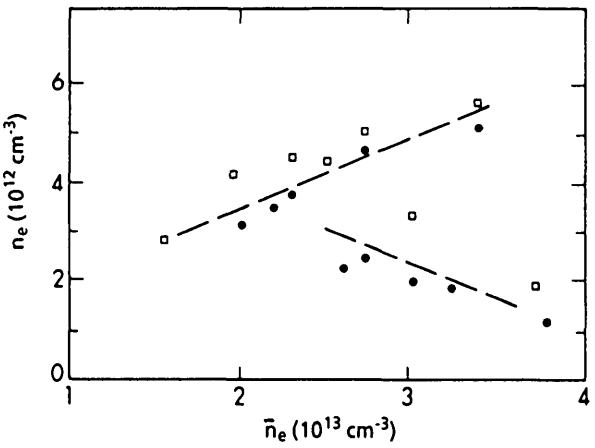

FIG. 12. T-10: Measurements of the electron density in the SOL by a microwave interferometer (□) and a Langmuir probe (●) [36]. Two runs of increasing and decreasing $\bar{n}_e$.

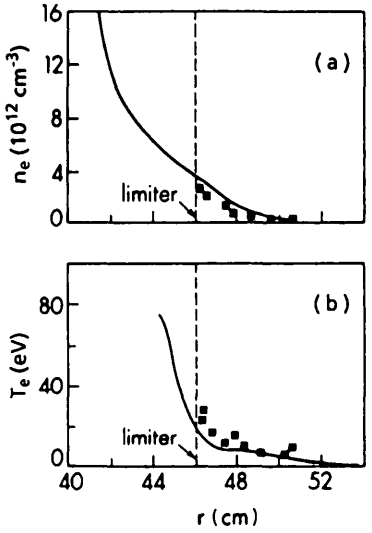

FIG. 13. TEXTOR: Measurements of n_e and T_e using a lithium beam (continuous line) and a Langmuir probe (points) [40].

It thus appears that Langmuir probe measurements in the edge of tokamaks agree with measurements using non-disturbing techniques to within a factor of two or better. More refined testing will require measurements of both T_i and T_e (to establish c_s); confirmation that the probe is in either the strong or the very strong magnetic field regime should be provided by such measurements or by comparison of A_{eff} for different probes in the same plasma (see, e.g., Fig. 8).

2.2.2. *Atomic beam techniques for measuring n_e and T_e*

The method of studying the boundary layer with atomic beams is intrinsically less disturbing than the use of solid probes [103]. Techniques have been developed for measuring both density and temperature profiles. Since a neutral beam moving through a plasma is usually attenuated by electron impact ionization, the electron density can be obtained by measuring this attenuation. The atomic density $n_a(r)$ as a function of position is given by

$$n_a(r) = -\int_0^r n_a(r')\, n_e(r')\, \frac{\overline{\sigma v}_i}{v_a}\, dr' \qquad (2.14)$$

where $\overline{\sigma v}_i$ is the ionization rate coefficient and v_a is the velocity of the injected atoms. The intensity of photon emission from an excited level m is given by

$$I_{ph}(r) = n_a(r)\, n_e(r)\, \overline{\sigma v}_{\ell m}/4\pi \qquad (2.15)$$

where $\overline{\sigma v}_{\ell m}$ is the excitation rate coefficient for excitation from level ℓ to level m. We make the assumption that this is the only excitation process which populates the level m and that depopulation occurs only by spontaneous emission. By eliminating $n_a(r)$ from Eqs (2.14) and (2.15) we obtain an expression for $n_e(r)$ only in terms

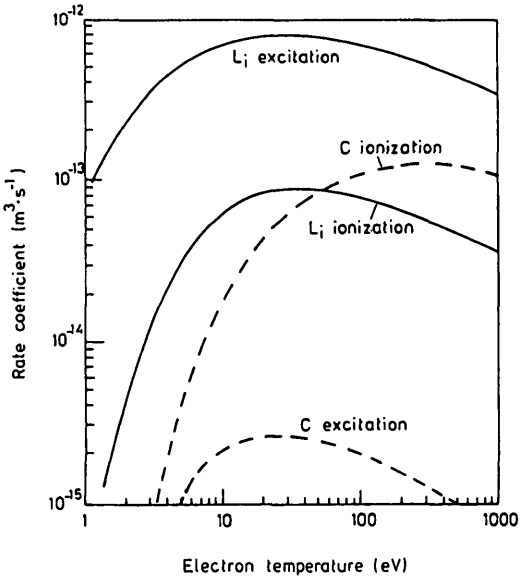

FIG. 14. Rate coefficients for electron impact excitation [786, 787] and ionization [788] of lithium and carbon. A branching ratio of 0.42 is used for excitation of carbon.

of the light intensity $I_{ph}(r)$ and the rate coefficients. If we choose an atom such as sodium or lithium, the ratio of the ionization rate to the excitation rate coefficients is nearly independent of temperature (above 10 eV), see Fig. 14. We can then write the electron density as

$$n_e(r) = \frac{v_a\, I_{ph}(r)}{\overline{\sigma v}_{\ell m} \int_0^r (\overline{\sigma v}_i/\overline{\sigma v}_{\ell m}) I_{ph}(r')\,dr'} \qquad (2.16a)$$

which can be simplified to

$$n_e = \frac{v_a\, I_{ph}(r)}{\overline{\sigma v}_i \int_0^r I_{ph}(r')\,dr'} \qquad (2.16b)$$

if the ratio $\overline{\sigma v}_i/\overline{\sigma v}_{\ell m}$ is only a weakly dependent function of T_e and hence of r. Therefore, an accurate density profile can be obtained with only an approximate estimate of the temperature profile.

The emission from the excited lithium atoms is generally observed in the direction normal to the direction of the beam. The intersection of the beam and the direction of observation defines the volume of the plasma over which the measurement is made. The whole radial profile can be measured using an interference filter and a detector array allowing a complete profile to be measured in a single discharge with good time resolution, ~100 μs. This technique has been used successfully by a number of groups to obtain density profiles [103–107]. Using a lithium oven, a beam with a thermal energy of 500°C has been injected into TEXTOR. The penetration depth was $n_e\ell = 2 \times 10^{16}$ m^{-2}, which is sufficient to make measurements in the SOL of many tokamaks. However, to penetrate into the region inside the limiter radius, it is necessary to have a beam with a higher initial velocity. Beams with keV energies have been developed for diagnostics of the confined plasma [107–110], but these suffer from lack of spatial resolution when applied to the boundary layer. A source with a mean energy of about 6 eV can be obtained by laser ablation of a layer of lithium fluoride, ~100 nm thick, on a glass substrate. In this case the velocity of the neutral beam is measured directly, using a time of flight method, with a filter and a photomultiplier as a detector. The detector array and the photomultiplier observe the same volume. Such a neutral source has a penetration of about 1×10^{17} m^{-2}. Measurements of density profiles in the boundary layer in TEXTOR are shown in Fig. 15.

The atomic beam technique poses difficulties if there are other effects, leading either to enhanced ionization (e.g. due to ionization of excited states) or to enhanced de-excitation (e.g. due to collisions at high density). These problems, and ways of alleviating them, have been discussed by Pospieszczyk and Ross [104]. Because the excitation rate is large for lithium, the ionization rate is enhanced by as much as 50% at a density of 1×10^{19} m^{-3}, and has to be explicitly taken into account [104]. When this correction has been made, the measured density profiles agree well with those obtained by an HCN interferometer. A further factor which has to be considered is the velocity distribution of the atom beam which reduces the spatial resolution obtainable. This has been discussed by Guenther et al. [109]. A disadvantage of the laser blow-off source compared with the thermal beams is that measurements of the profile can only be made once, or at most a few times during the discharge, whereas with the thermal beam the profile can be measured practically continuously. Development of a continuous neutral beam with an energy of 0.1–10 keV and with adequate intensity would considerably enhance the usefulness of these techniques [111].

A similar approach has been taken to measure temperature profiles, using two elements with a significantly different energy dependence of their ionization cross-sections [112]. By differentiating Eq. (2.14) and using Eq. (2.15) we can derive the expression

$$\frac{v_a}{n_e(r)}\left[\frac{1}{I_{ph}(r)}\frac{dI_{ph}(r)}{dr}\frac{1}{n_e(r)}\frac{dn_e(r)}{dr} - \left(\frac{1}{\overline{\sigma v}_{\ell m}}\frac{d\,\overline{\sigma v}_{\ell m}}{dr}\right)\right] = \overline{\sigma v}_i = f(T_e) \qquad (2.17)$$

When using an element for which $\overline{\sigma v}_i$ is temperature dependent in the observed radial volume, a T_e profile can be derived if the intensity ($I_{ph}(r)$) and the density ($n_e(r)$) gradients are known. Using a 50 nm layer of LiF on top of a 500 nm layer of carbon, simultaneous measurements of the density and temperature profiles have been made in the boundary layer of TEXTOR [105]. The lithium beam is used to obtain the density directly, and the temperatures are derived using the carbon intensity distribution and the density profiles. An iterative procedure is used to obtain the best fit to the emission profile with the derived density and temperature profiles. Density and temperature profiles

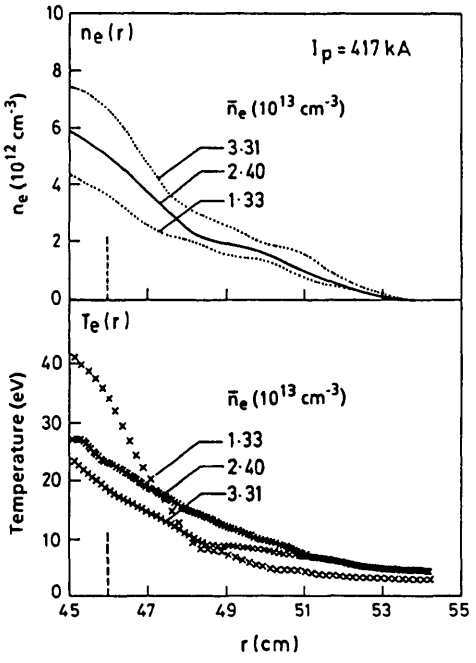

FIG. 15. TEXTOR: Density and temperature profiles as a function of central $\bar{n}_e$, using lithium and carbon atomic beams. The dashed curve is the position of the main limiter.

derived in this way are shown in Fig. 15. The systematic error in these measurements due to inaccuracies in the ionization and excitation functions is estimated to be about 20%. The other major source of error is the background radiation to be subtracted, which is more difficult to estimate.

2.2.3. *Other optical methods for measuring n_e and T_e*

Thomson scattering of electromagnetic waves from electrons is a widely used and essentially non-perturbing method for measuring electron density and temperature [113]. When an electromagnetic wave interacts with an electron, the oscillating electric field excites a secondary wave. The power scattered into the secondary wave from electrons of density n_e, in a direction ψ with respect to the electric field vector of the primary wave, is given by

$$P_s d\Omega = \left(\frac{e^2}{m_e e^2}\right)^2 \sin^2 \psi \; n_e \ell P_0 d\Omega \qquad (2.18)$$

where P_0 is the power in the primary wave and ℓ is the length of the scattering volume. If an absolute calibration can be carried out, the intensity of the scattered light is a direct measure of the local electron density in the scattering volume. This measurement has the advantage that it does not depend on a knowledge of the plasma parameters. Intensity calibration may be carried out by comparison with Rayleigh scattering from a gas at known density. Frequently, the Thomson scattering measurements are simply normalized to microwave measurements of the line integral density (see Section 2.2.4).

The electron temperature is also easily derived from Thomson scattering. Because of the motion of the electrons, both the incident and the scattered waves will be Doppler shifted in frequency. The velocity distribution of the electrons will result in a frequency distribution of the scattered waves. For a Maxwellian distribution of electrons the FWHM of the scattered radiation is given by

$$\Delta\lambda = 4\lambda_0[2 \ln 2(kT_e/m_e c^2)]^{1/2} \sin \psi/2 \qquad (2.19)$$

This Doppler broadening is large and easily measured, even for modest temperatures ($\Delta\lambda$ = 30 nm at T_e = 100 eV). It is usually assumed that the electrons have a Maxwellian distribution and so measurements at two or three wavelengths are sufficient to determine the temperature [114]. This allows measurements at a number of different radial positions to be made simultaneously with relatively straightforward systems. In general, the problem with the Thomson scattering system is to collect sufficient photons and hence to obtain a reasonable signal-to-noise ratio. Standard systems used in tokamaks are usually designed for relatively high temperatures and are therefore unsuitable for edge measurements. However, a system designed for the edge region in ASDEX has shown that good results can be obtained [115]. In order to optimize the number of photons collected, a high intensity laser of 12 J was employed. Low beam divergence (1 mrad) and large aperture collection optics were used. The lower limit to the detectable density was 5×10^{17} m^{-3}, determined by fluctuations in the background level. Results of density and temperature profiles near the separatrix are shown in Fig. 16.

One of the principal limitations of these optical techniques, discussed in this section and in Section 2.2.2, is the access required. Typically two ports are necessary, one port for the primary beam and another port, orthogonal to the first one, for viewing the emitted radiation. While such access is relatively straightforward at the centre of the plasma, it is more difficult at the edge, and special diagnostic ports are often required. Given the usual competition for access, this can be a serious drawback.

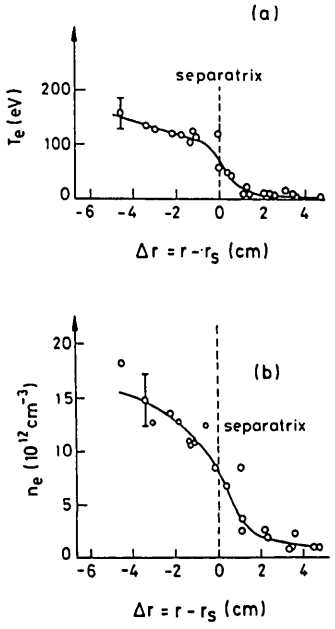

FIG. 16. ASDEX: Profiles of electron temperature (a) and electron density (b) versus distance from the magnetic separatrix in the equatorial plane, for an ohmically heated discharge with $\bar{n}_e = 4 \times 10^{13}$ cm^{-3}, $t = 1.05$ s, $I_p = 320$ kA, $B = 2.17$ T [115].

In comparison, the Langmuir probes discussed in Section 2.2.1 require little access. Frequently, they can be installed in vessel components with only electrical connections. Even a moving probe can be installed through a modest sized single port (~50 mm dia.). A further difficulty with the optical techniques is limited spatial resolution compared to the Langmuir probe, which can readily obtain a radial resolution of ~1 mm. On the other hand, the disturbance of the plasma by the presence of the probe does result in more complicated interpretation, as discussed in Section 2.2.1.

2.2.4. *Microwave methods for measuring n_e and T_e*

(a) Microwave interferometry

The microwave interferometer is one of the basic diagnostics of plasma physics [116]. The refractive index of a plasma is determined by the electron density. By measuring the phase difference between an electromagnetic wave travelling through a plasma and a similar wave travelling through air or vacuum, the electron density can be determined. The maximum density that can be measured, n_c, is determined by a cut-off where the frequency ω of the probing beam equals the plasma frequency:

$$n_c = \omega^2 \frac{\epsilon_0 m_e}{e^2} \tag{2.20}$$

However, since a wide range of microwave sources of varying frequency are available, this is rarely a problem. The main problem with regard to measurements in the boundary is that the technique measures a line integral. In the central plasma, where gradients are not large and where there is often circular symmetry, inversion techniques can be used to unfold the line integrals. In the edge, where gradients are large, this is more difficult. Nevertheless, since it is such a straightforward and reliable absolute technique, it is often valuable to have at least the line integral measurement. More details are given in the review by Soltwisch [116].

(b) Microwave reflectometry

Reflectometry is a microwave technique which can be used to determine density profiles and density fluctuations [117]. An electromagnetic wave with angular frequency ω is launched into the plasma along the density gradient. When the wave reaches the critical value of density, it is reflected. The reflected beam is compared with a reference beam in an interferometer and the phase difference resulting from the path in the plasma is measured. If the source frequency is kept constant, movements in the critical density layer can be measured. Although it is possible in principle to use either the 'ordinary' mode (E∥B) or the extraordinary mode (E⊥B), we consider here only the ordinary mode. This mode propagates as if in an unmagnetized plasma with a dielectric constant given by

$$\epsilon = 1 - \omega_p^2/\omega^2 \tag{2.21}$$

where $\omega_p = (n_e e^2/\epsilon_0 m_e)^{1/2}$ is the plasma frequency. For $\omega > \omega_p$, ϵ is positive and the wave propagates with a refractive index $\mu = \epsilon^{1/2}$. A wave of frequency ω travelling in a plasma of varying density is therefore totally reflected at the point where $\omega = \omega_p$, i.e. it is reflected at the point where the density equals the critical value, given in Eq. (2.20).

The interferometer system used in a practical arrangement measures the phase delay ϕ_{ph}. This can be calculated by solving the wave equation for an inhomogeneous plasma. The result is given by

$$\phi_{ph} = \frac{2\omega}{c} \int_{\ell_c}^{\ell} \mu(\ell)\, d\ell - \pi/2 \qquad (2.22)$$

where ℓ is the path length along the microwave beam.

The wave reflection takes place over a finite distance $\Delta\ell$ given by

$$\Delta\ell = \frac{1}{2} \left\{ \frac{\lambda}{2\pi} \left(\frac{d\epsilon}{d\ell} \right)^{-1/2} \right\}^{2/3} \qquad (2.23)$$

$\Delta\ell$ is < 10 mm for normal tokamak conditions.

One of the principal differences between reflectometry and transmission interferometry is that reflectometry is a local technique, rather than a line integral. Thus, no inversion process is necessary. Reflectometry is well suited to making measurements in the edge region, where only limited information can be obtained by transmission interferometry. It is, however, very important that the line of sight of the reflectometer is along the density gradient, otherwise significant losses will be caused by refraction.

The simplest measurements which can be made using a reflectometer are those of density fluctuations, by observing the radial movement of the critical density at fixed frequency. The measured phase change $\Delta\phi_{ph}$ is given by

$$\Delta\phi_{ph} = \frac{2\omega}{c} \bar{\mu}\, \Delta\ell \qquad (2.24)$$

where $\bar{\mu}$ is the average refractive index along the ray path. It has been shown that $\bar{\mu} = 0.6 \pm 15\%$ for a wide range of profiles [117]. For a probing frequency of 30 GHz, a phase change of one fringe corresponds to 10 mm, and so movements of ~ 1 mm are detectable. To obtain density profiles, it is necessary to sweep the wave frequency and thereby measure $d\phi_{ph}/d\omega$. It is then possible to unfold the density profile between $R_c(\omega_1)$ and $R_c(\omega_2)$. The density profile is obtained from the analytical solution of Abel's integral equation:

$$\ell - \ell_c(\omega_p) = \frac{c}{\pi} \int_0^{\omega_p(\ell_c)} \frac{d\phi_{ph}}{d\omega} (\omega_p^2(\ell_c) - \omega^2)^{-1/2}\, d\omega \qquad (2.25)$$

Since the lowest probing frequency is not zero, data must be obtained for the density profile outside $\ell_c(\omega)$, for example from Langmuir probe measurements.

An elaboration of the broad-band sweep technique is to have a narrow-band sweep of, say, ten independent sources [118]. The frequency of each source is swept by about 1%. The phase change $d\phi_{ph}/d\omega$ at each frequency is thus obtained and an interpolation technique is used to obtain $d\phi_{ph}/d\omega$ at all frequencies within the range used. The same inversion technique is then used to obtain the density profile as in the broad-band sweep. This technique is in the process of development [118].

(c) Electron cyclotron emission

The occurrence of cyclotron emission in plasmas is due to the motion of the electrons in the strong magnetic field. The radiation occurs both at the fundamental and at harmonics of the fundamental. The intensity of the emission is strongly dependent on the electron temperature, and the frequency is determined by the local magnetic field. Because the magnetic field varies inversely with the major radius, the intensity variation with frequency is a measure of the electron temperature profile. Use of this emission has developed into a sophisticated and widely used technique for measuring temperature [119]. Under most conditions in tokamaks the density is sufficiently high that the plasma acts like a black body. The intensity of the emission is given by

$$I_{ph}(\omega) = \frac{\omega^2 T_e(R)}{8\pi^3 c^2} \qquad (2.26)$$

Because of the changing magnetic field and hence the changing emission frequency with radius, the effective spatial resolution is quite good. However, in the boundary plasma, where the density is lower, the plasma is often optically thin [120]. This leads to reduced spatial resolution and, consequently, to large errors in the temperatures. The best experimental technique in the boundary is the use of heterodyne receivers which have good spatial resolution [121]. Results on JET indicate that temperatures down to ~ 100 eV can be measured with a spatial resolution of 20 mm.

2.2.5. *General optical methods*

One of the most obvious ways of diagnosing the plasma edge is to use emission spectroscopy. At the electron temperatures involved, the radiation comes mainly from low ionization states and is in the visible region of the spectrum. Observation is thus simple and non-perturbing. The emission is strong for many states and the states themselves are readily identified. Using 2-D detector arrays and optical filters, the spatial

distribution of a particular ionization state can be quickly determined [122]. An example of the spatial distribution of different carbon charge states is shown in Fig. 17 [123]. Because the emitting atom is unaffected by the electric or magnetic fields, although the lines may be affected by Zeeman splitting, the spatial distribution is determined by the velocity distribution of the atoms entering the plasma and by the profiles of the local plasma density and temperature. Since the density and temperature can be determined independently, conclusions can be drawn about the velocities of the neutral atoms [124].

However, careful analysis is required to obtain more details. By combining Eqs (2.14) and (2.15) we can obtain the photon emission distribution for a given initial velocity v_0 and a given spatial distribution of plasma density and temperature. However, further problems arise in the interpretation of real data. Observation of the plasma is through windows in the vacuum vessel, and any line of sight measurement involves a line integral of the radiating region since the plasma is optically thin in the visible region of the spectrum. In order to unfold the data, numerous lines of sight are required. If the plasma is cylindrically symmetric, then Abel inversion is straightforward, though tedious. However, if the radiation is localized in the plasma boundary, it is possible to directly obtain a useful picture of the distribution. Viewing tangentially along the magnetic field gives a picture of the radial distribution and viewing vertically normal to the field gives a picture of the toroidal distribution (see Fig. 18) [124]. Observation of ions in low charge states, in contrast to neutrals, gives a picture of the particle flow in the presence of electric and magnetic fields. In principle, information about the local fields can sometimes be derived, but in practice this is difficult [125].

In order to reconstruct the local densities from the observed line intensities, it is also necessary to take into account the 'photon efficiency' (PE) of the particular state observed. This is the number of photons

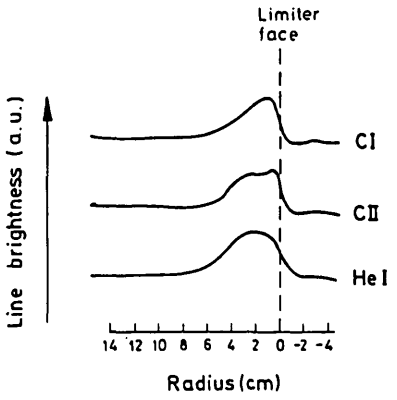

FIG. 17. DITE: Profiles of the radial intensity along the median plane near the limiter in a discharge with $\bar{n}_e = 5 \times 10^{19}$ m^{-3} [123].

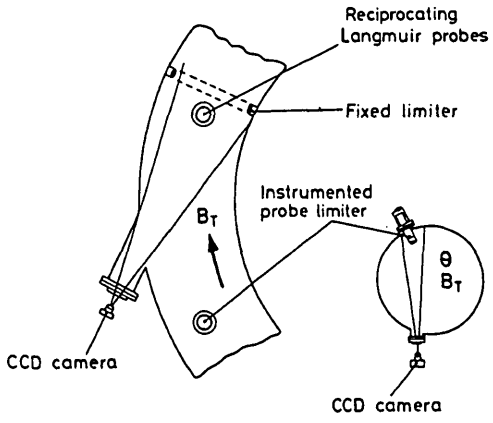

FIG. 18. CCD view of the torus in the tangential and vertical directions, showing the radial and toroidal spatial distributions at a limiter.

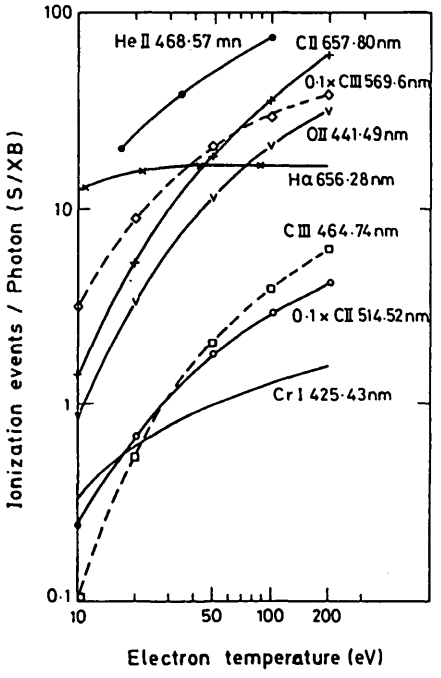

FIG. 19. Ionization events per photon for some impurity lines, used for flux measurements, as a function of T_e [128].

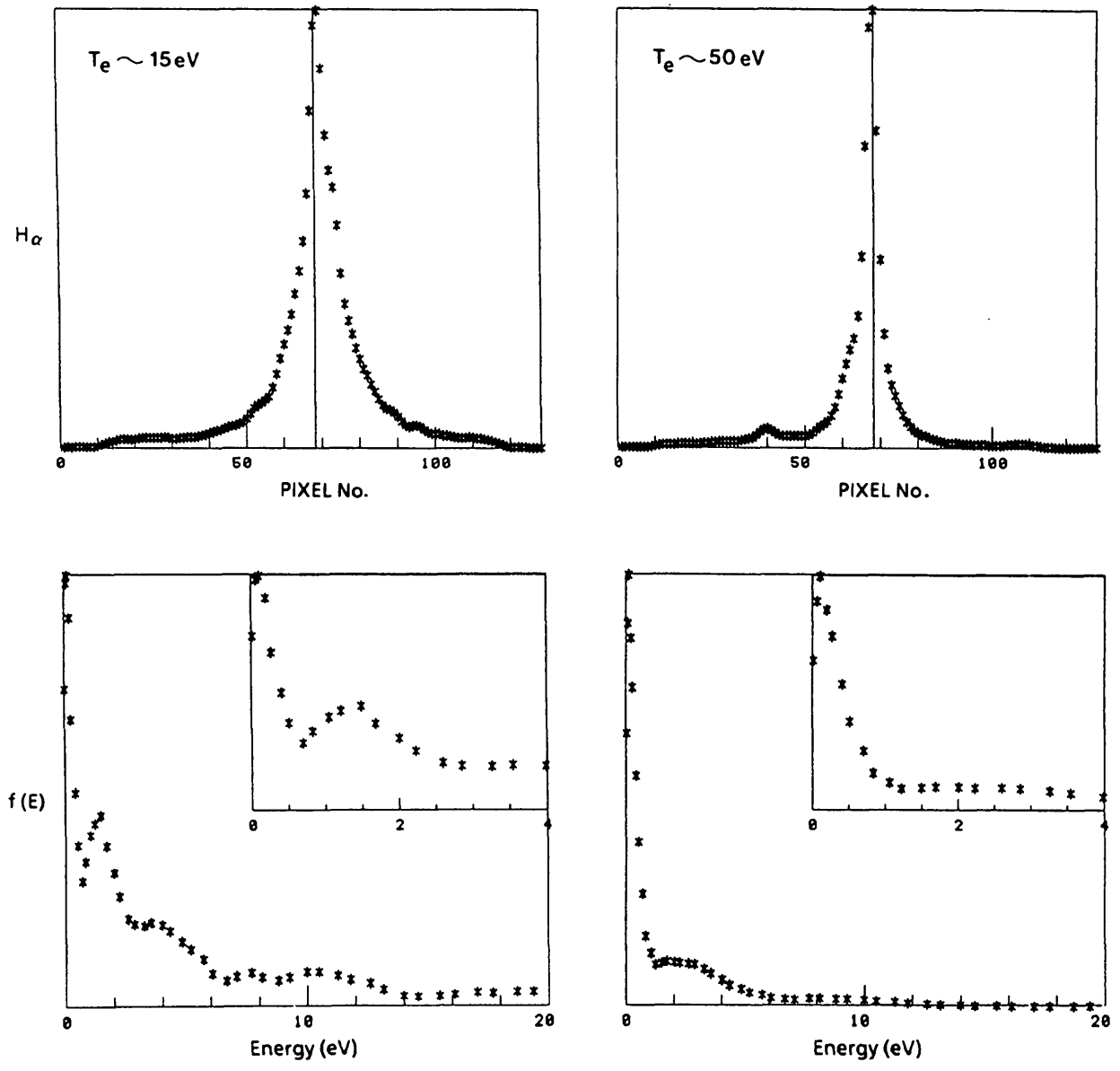

FIG. 20. Helium line shapes and energy spectra derived from recycling of hydrogen plasma at the graphite probe limiter surface in DITE for edge electron temperatures of 15 eV and 50 eV [129].

emitted before ionization to the next highest charge state occurs, i.e.,

$$PE = \frac{b_r \overline{\sigma v}_{\ell m}}{\overline{\sigma v}_i} \qquad (2.27)$$

where b_r is the branching ratio.

The photon efficiency depends on the local electron temperature and, therefore, $T_e(r)$ must be known in order to obtain the ion or atom density concerned. In some special cases, e.g. hydrogen, the photon efficiency is only a very weak function of T_e and, to first order, it can be ignored [126, 127]. Some useful inverse photon efficiencies are presented in Fig. 19 [128].

Although, as noted above, the neutral velocity can be determined from penetration of the neutrals into the plasma, this requires independent knowledge of the local electron density and temperature distribution. For any species observable spectroscopically, it is possible

in principle to determine its velocity distribution by observing the Doppler shift or Doppler broadening of the line with respect to a standard unshifted line [129, 130]. The Doppler shift, $\Delta\lambda$, is given by $\Delta\lambda = (v_a/c)\lambda_0$.

The technique turns out to be fairly straightforward for the light ion species where energies are high, masses are low and therefore velocities are high. An example is shown in Fig. 20. The neutral hydrogen line H_α is broadened and shifted to the shorter wavelengths, indicating an ion energy of ~8 eV, with the atom velocity vector being predominantly towards the observer. This corresponds to atoms leaving the limiter surface. Detailed interpretation again proves difficult because of the angular distribution of the atoms from the limiter and because of Zeeman splitting. In many cases the problem of Zeeman splitting can be overcome by choosing the appropriate viewing direction and using a polarizer to eliminate one component of the Zeeman split lines [129]. It can usually be assumed that the atoms are released from a surface in a cosine distribution, so that the experimental data may be fitted by using trial values of the ion energy. However, such an approach does not necessarily provide a unique solution.

In the case of impurity atoms, for example carbon or oxygen, the Doppler shift is often too small to be readily observable with conventional spectroscopic techniques. ($E = 2$ eV, $m = 16$, $v_a = 5 \times 10^3$ m·s^{-1}, $\Delta\lambda = 0.1$ Å). However, such measurements are possible using laser resonance fluorescence, as discussed in the next section.

2.2.6. *Laser resonance fluorescence*

This is a very sensitive technique for measuring the density of an atomic species. In the present review, we can only give an outline of the possibilities, and the reader is referred to other publications for further details [103, 131]. The technique is basically to use an intense light source to optically pump atoms into an excited state and then to observe the characteristic radiation as they decay to their initial state or to another state. For a two-level system, the number of photons emitted from the excited state is given by

$$\frac{dn_2}{dt} = u(\nu)\,[B_{12}n_1 - B_{21}n_2] - A_{21}n_2 \qquad (2.28)$$

where n_1 and n_2 are the densities of the initial and final states, and B_{12}, B_{21} and A_{21} are the Einstein coefficients for absorbed emission, induced emission and spontaneous emission, respectively. If the intensity of the radiation is very high and the pulse is sufficiently long, the number of atoms in the upper level will saturate. The saturation level is given by

$$\frac{n_1}{n_1 + n_2} = \frac{g_2}{g_1 + g_2}\,\frac{s}{s+1} \qquad (2.29)$$

where the saturation parameter s is given by

$$s = \frac{P_L(\lambda)}{8\pi hc^2}\left(\frac{g_1 + g_2}{g_1}\right)\lambda^5 \qquad (2.30)$$

where $P_L(\lambda)$ is the power of the laser, λ is the wavelength, and g_1 and g_2 are statistical weights.

For large values of s, the population of the excited state is independent of the incident power level and is determined only by the statistical weights of the states. Intensities sufficient for saturation are relatively easily achieved for wavelengths in the visible and the near-UV range, but are difficult to achieve in the vacuum UV range. Not only does the power required increase strongly with decreasing wavelength, but the sources available are in general weaker.

The total emitted flux for a laser pulse length t is given by

$$\int_0^t P_L dt = n_2 A_{21}\tau = \frac{g_2 n_2}{g_1 + g_2}\,\frac{sA_{21}t}{s+1} \qquad (2.31)$$

The measurement of the atomic density is thus very straightforward. Calibration can be carried out using a vapour of the atom species required, for example from an oven. If this is not possible, a comparison can be made with Rayleigh scattering using a gas. This allows some of the geometry and efficiency factors to be eliminated [103]. The technique is very sensitive, particularly in the case of atoms with strong resonance lines, such as sodium. Measurements of the density of iron and of other impurities have been made in tokamaks [131]. Densities of iron atoms as low as 10^{12} m^{-3} have been measured. The light impurities, such as carbon and oxygen, are more difficult to measure because their resonance lines are in the vacuum UV range, between 120 nm and 200 nm. Recently, the rather difficult but very important measurement of the density of neutral hydrogen has been made, using the Lyman L_α resonance line [132]. By using a very narrow-band laser and exciting successively different wavelengths

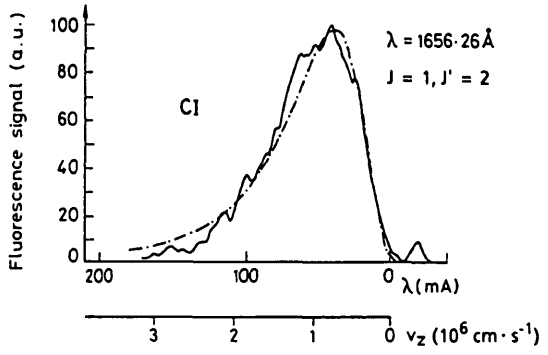

FIG. 21. Fluorescence profile of the 1656.26 Å line ($^3P_1 \rightarrow {}^3P_2^0$), measured during bombardment of a graphite target with 1.5 keV Ar ions; the dash-dotted line is a predicted Thomson velocity distribution (E_0 = 8.3 eV) [133].

close to the fundamental frequency, the Doppler broadening of the line and hence the velocity distribution of the species can be measured. Although this is a more tedious process, requiring many laser pulses to get the full velocity distribution, it has been successfully carried out for sputtered atoms [133] (Fig. 21).

The detection limit is usually determined by the level of the background signal. Errors arising from the presence of magnetic fields, anisotropic and polarized radiation and other effects have been discussed by Bogen and Hintz [103].

2.2.7. *Ion temperature measurements*

One of the standard ways of measuring the ion temperature in a confined plasma is to study the charge exchange neutral energy distribution [134]. The conventional technique for doing this is to use a charge stripping cell and electrostatic analysis of the resulting ions. This is unsuitable for edge measurements as it is difficult to measure energies below ~300 eV. However, time of flight methods for analysing the neutrals themselves have been developed which have adequate detection sensitivities down to <20 eV [135, 136]. The interpretation of these low energy spectra in terms of ion temperature is difficult, because they are again line integrals. They therefore require detailed electron density and temperature profiles and a neutral code such as DEGAS [136] to unfold them. So far, this has not been attempted for the boundary. However, the neutral fluxes and spectra are exceedingly valuable in their own right, since they determine the amount of sputtering which occurs at the walls owing to the charge exchange atoms [135-137].

It is by no means certain that $T_e = T_i$ in the boundary since the densities are low, leading to non-equilibrium situations, and there is the possibility of turbulent heating of the ions. In fact, the limited data available indicate that T_i is in the range (1–3) T_e [138–141]. The ion temperature in the boundary is quite important, since it is a factor influencing the sputter yield of impurities from the wall and limiter. Methods of making measurements are limited. One successful technique uses the retarding field analyser [138–141]. By sweeping the retarding field with the help of grids, an integral distribution of ions above a given energy can be obtained. The differential spectrum can be derived either computationally or by electronic circuitry. While this technique is relatively simple to use for ion beams, problems arise in magnetized plasmas.

It is first necessary to separate the ions and electrons. If slits or grids of a size comparable to the Debye length are used, then a sheath is set up and the electron flow into the analyser is reduced to the value of the ion flow. However, such devices will only withstand relatively low power and hence can only be used in cool, low density plasmas. When a narrow slit or a fine grid is used, a further problem is that the effect of the finite ion Larmor radius must be considered. The thickness of the grid must be kept small in order that the attenuation of ions with transverse energy is not too severe. This problem can be alleviated to some extent by calculating the transmission factor of a given geometry as a function of energy and using this to correct the experimental data.

Integral energy distributions measured in the DITE tokamak are shown in Fig. 22 [140]. The simplest

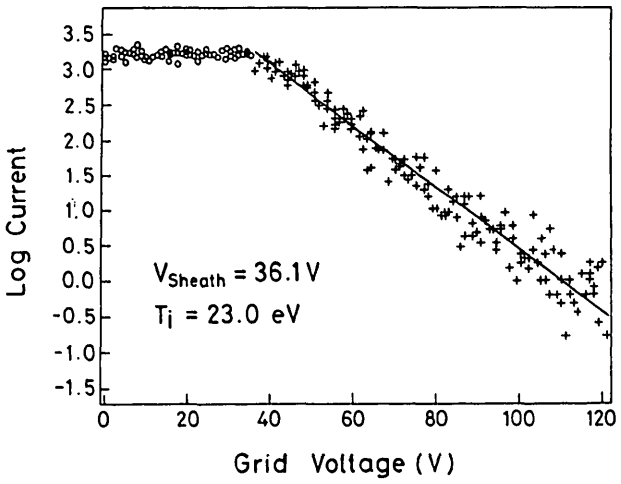

FIG. 22. DITE: Integral energy distribution of ions in the plasma boundary [140].

interpretation of these data is that they are due to a shifted Maxwellian ion energy distribution. When the pre-sheath potential drop is neglected (see Section 3.3), the sheath potential can be derived from the displacement of the distribution with respect to the origin, and the ion temperature can be derived from the logarithmic slope of the high energy tail [140]. However, the interpretation does depend on the form of the energy distribution and on the charge state distribution. As discussed in Section 3.2, the theoretical form for the distribution is still being debated. We assume that the distribution approximates a Maxwellian in the high energy tail. This part of the characteristic can then be used to derive the ion temperature. Results for the ion temperature as a function of density for the DITE tokamak are shown in Fig. 23 [139].

A more sophisticated analyser, which in principle can measure both energy distribution and charge-to-mass ratio, has been described by Matthews [142]. Using an electric field normal to the existing tokamak magnetic field, the ions are constrained in a cycloidal orbit. The distance travelled along the magnetic field is a measure of the parallel velocity. By sweeping the electric field, ions of different mass-to-charge ratio are electrically detected. An example of the distribution of oxygen and carbon charge states observed in the DITE

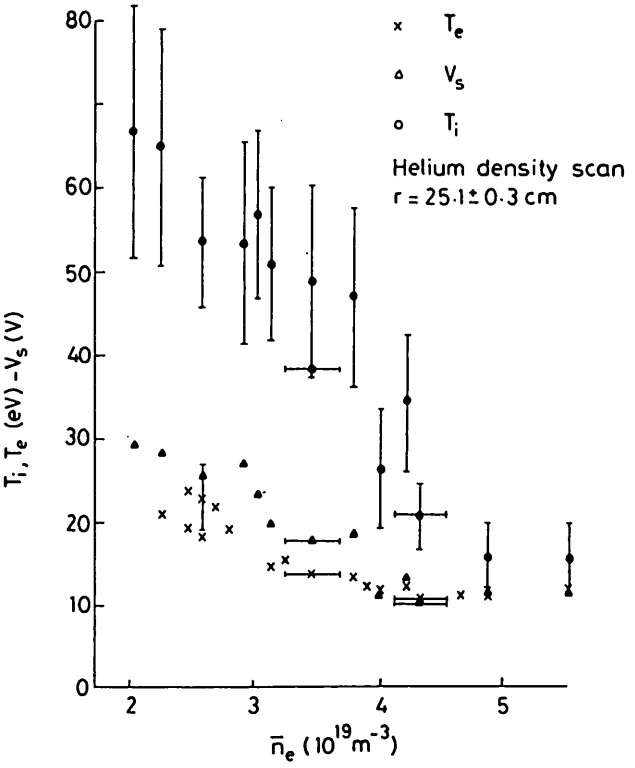

FIG. 23. DITE: Dependence of ion temperature T_i, floating potential V_{sf} and electron temperature T_e in the plasma boundary of a helium discharge. The peaks corresponding to the various charge states of oxygen and carbon are identified. I_p = 100 kA [139].

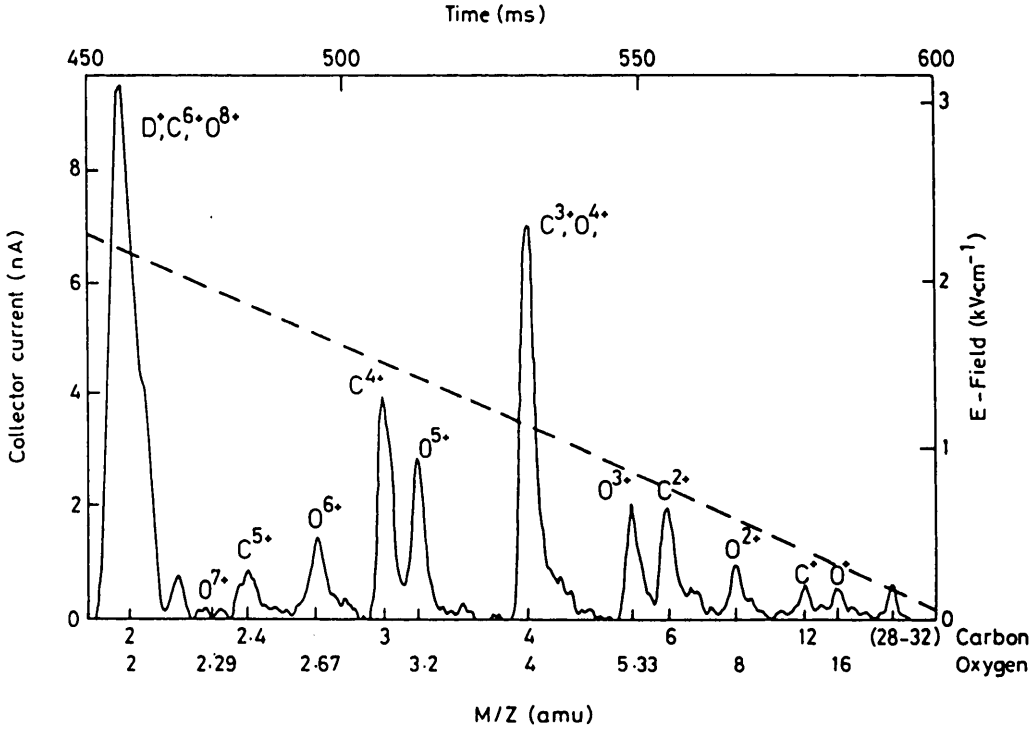

FIG. 24. DITE: Mass spectrum of the ions in the plasma boundary of a deuterium discharge. The peaks corresponding to the various charge states of oxygen and carbon are identified. I_p = 100 kA [142].

tokamak boundary is shown in Fig. 24. This technique is an important advance in obtaining the charge state distribution of impurities in the SOL, which was not known previously; it deserves to be applied more widely. The charge state determines the energy gained by the ion in the sheath and hence the effective sputter yield.

2.2.8. *Surface temperature measurement*

The measurement of surface temperatures of the critical plasma-facing elements is an important part of plasma edge diagnostics. The direct measurement of temperature helps in assessing the relative importance of different impurity production processes. Most obviously, one can detect whether overheating of the surface is causing sublimation of the wall or of the limiter material.

There are two main approaches to the measurement of surface temperature. One approach is to put a sensor, e.g. a thermocouple or thermistor, in the surface itself, leading signals out through the vacuum vessel. However, such sensors are delicate and there is serious risk of damage if they are put close to the surface of the component. Runaway electrons or disruptions, even if infrequent, can lead to catastrophic damage. If the sensors are remote from the surface, then they are more secure, but this leads to a time lag in the measurement of temperature, and extrapolation back to the surface temperature has considerable uncertainties.

The second approach is to use remote sensors, typically infra-red ones. Relying on the Planck radiation law, which gives the intensity of radiation $I_{ph}(\lambda)$ in a wavelength range λ to $\lambda + d\lambda$ as

$$I_{ph}(\lambda)d\lambda = \frac{\epsilon_s hc^3 d\lambda}{\lambda^5 \left[\exp\left(\frac{hc}{k\lambda T}\right) - 1\right]} \qquad (2.32)$$

where h is the Planck constant, k is the Boltzmann constant, T is the absolute temperature and ϵ_s is the surface emissivity, one can calculate the surface temperature from the absolute level of radiation at a particular wavelength. Many infra-red sensors and detector systems are now available commercially. Near room temperature it is necessary to have sensors in the 2 μm – 5 μm wavelength range. This requires a detector such as indium antimonide, cooled to liquid nitrogen temperatures. However, at higher temperatures, >1000°C, it is possible to use simple uncooled detectors such as CCD arrays because the radiation intensity increases rapidly and moves to shorter wavelengths. The optimum wavelength is ~1 μm. Obviously, care must be taken to avoid radiation from the plasma, such as the strong C I lines at about 908 nm. (Above this wavelength there appears to be little significant radiation.)

The temperature distribution is normally very non-uniform on limiters because of the exponential decrease in power flux along the fields with radius (see Section 3.4) and because of the shaping of the limiter (Section 7.2). It is thus particularly important to have a system which will allow the spatial distribution of temperature to be observed over as large a surface as possible [143]. Such systems have been used and have provided valuable data in the distribution of temperature and power flux [144, 145]. However, they are not used as routinely as they should be. One important aspect of these infra-red systems is their calibration. The emissivity of the radiating surface can change markedly as a result of different types of conditioning, deposition of thin films, etc. The window transmission can also change, for the same reasons. One of the simplest ways of calibration is to have a thermocouple embedded in the surface which is being viewed. Thus, at any time, the temperature measured by the infra-red system and the thermocouple can be compared under steady state conditions and the calibrations checked. An inbuilt heater, allowing calibration over a range of temperatures, is advantageous.

From the time dependence of the surface temperature it is possible in principle to get the incident power flux. In the case of a semi-infinite surface with constant power flux there is the well known equation for the temperature rise ΔT in terms of the power flux density P [146]

$$\Delta T = \frac{2Pt^{1/2}}{\sqrt{\pi \kappa_t s_h \rho}} \qquad (2.33)$$

where κ_t is the thermal conductivity, s_h is the specific heat, ρ is the density of the surface material and t is the pulse length. The condition for the surface to act as semi-infinite is that the thickness d must be greater than the diffusion time

$$d > \left(\frac{4\kappa_t t}{\rho s_h}\right)^{1/2} \qquad (2.34)$$

For the case of a power flux density P(t) which is varying with time, the surface temperature rise is

given [146] by

$$\Delta T(t) = \frac{1}{\sqrt{\pi \kappa_t S_h \rho}} \int_0^t \frac{P(t'-t)}{(t')^{1/2}} dt' \qquad (2.35)$$

Thus, if the temperature is measured as a function of time, the incident heat flux can be calculated by numerical techniques. A significant amount of computing time is necessary to do this for a 2-D array. However, such techniques have been successfully used to obtain contours of power deposition [144].

Direct measurement of the power flux can be made with a bolometer probe. Small robust probes made from refractory metals of known heat capacity with a temperature sensitive element have been used [58]. However, the complication of putting this in the tokamak boundary and their vulnerability to very large heat fluxes makes them unsuitable for general use. Measurements in the main limiter components are preferable. Nevertheless, heat flux probes are valuable for special purposes, such as measuring the sheath power transmission coefficient (see Section 3.3).

3. ANALYTIC MODELLING OF THE SOL

This section is devoted primarily to simple analytic modelling of the SOL. In Section 3.2, 1-D fluid models for the plasma flow along the SOL are reviewed, with the source terms due to cross-field transport being taken as specified. At the limiter, a thin electrostatic positively charged layer, the sheath, separates the solid plasma and the quasi-neutral plasma. The properties of the sheath control the particle and energy removal rates from the SOL. These properties are reviewed in Section 3.3. The derivations in Sections 3.2 and 3.3 are also generally applicable to Langmuir probe interpretation (Section 2.2.1). In Section 3.4, the measured scrape-off lengths for density, λ_n, and temperature, λ_T, are related to the cross-field transport coefficients, namely the particle diffusion coefficient $D_\perp$ and the thermal conduction coefficient $\chi_\perp$, thus permitting the values of these quantities to be inferred in different tokamaks. In Section 3.5, edge plasma conditions are related to the central plasma parameters. The limiter sink is not always the dominant one for the SOL, and in Section 3.6 the 'complex SOL' is considered for cases where other sinks, such as radiation, and localized sources (ionization) are important. Two-dimensional plasma code modelling [147] and neoclassical [7, 148–152] SOL theory are not discussed.

3.1. Introduction

A cut through the magnetic flux surfaces in a poloidal plane (assuming toroidal symmetry, Fig. 25a), makes evident the important role of the LCFS. Plasma outside of the LCFS is in direct contact with a solid surface, unimpeded by the magnetic field. The plasma can flow at high speed to the solid surfaces which thus act as strong particle and energy sinks for the plasma. The plasma density and temperature therefore decrease rapidly outside the LCFS, with decay lengths typically 0.1-5.0 cm (see Section 2.1). When the magnetic flux surfaces are of relatively simple shape and the LCFS is defined by plasma–solid contact with one of these surfaces, the solid object is termed a 'limiter', since its strong sink action limits the radial extent of the plasma quite effectively. The relatively complex magnetic flux surface configurations associated with divertors are considered in Section 7.3.

In general, the shape of the magnetic flux surface does not conform to that of the solid container, and the LCFS is generally defined by a localized point or line of contact with a solid surface. For limiter defined plasmas, three configurations may be distinguished (see Figs 25b, 25c):

(a) *Toroidal limiters.* In the absence of magnetic field ripple, the lines of contact are generally circles in a toroidal plane. A toroidal limiter may involve simply resting the plasma against the outer wall or, more typically, the inner wall. In at least one case, that of JET, special toroidal 'belt limiters' have been installed on the outer wall.

(b) *Poloidal limiters.* One or more poloidal aperture rings are inserted in the vessel.

(c) *Local limiters.* In principle, the plasma can be limited by even a small, localized protrusion since, for non-rational q-values, the magnetic line touching the solid eventually maps out the entire magnetic surface, allowing plasma drainage to the protrusion (where $q \equiv rB_T/RB_p$ is the tokamak safety factor and B_p is the poloidal field). Such limiters can take the shape of 'rails' or 'mushrooms', etc. This configuration lacks toroidal and poloidal symmetry.

The strength of the limiter sink action is inversely dependent on the average distance, called the connection length L_c, the plasma must travel along $\vec{B}$ within the SOL to reach a limiter. This distance is one of the key parameters characterizing a SOL and its properties. For toroidal and poloidal limiters it is straightforward to define this connection length: the distance along a $\vec{B}$-line in the SOL measured from one point of

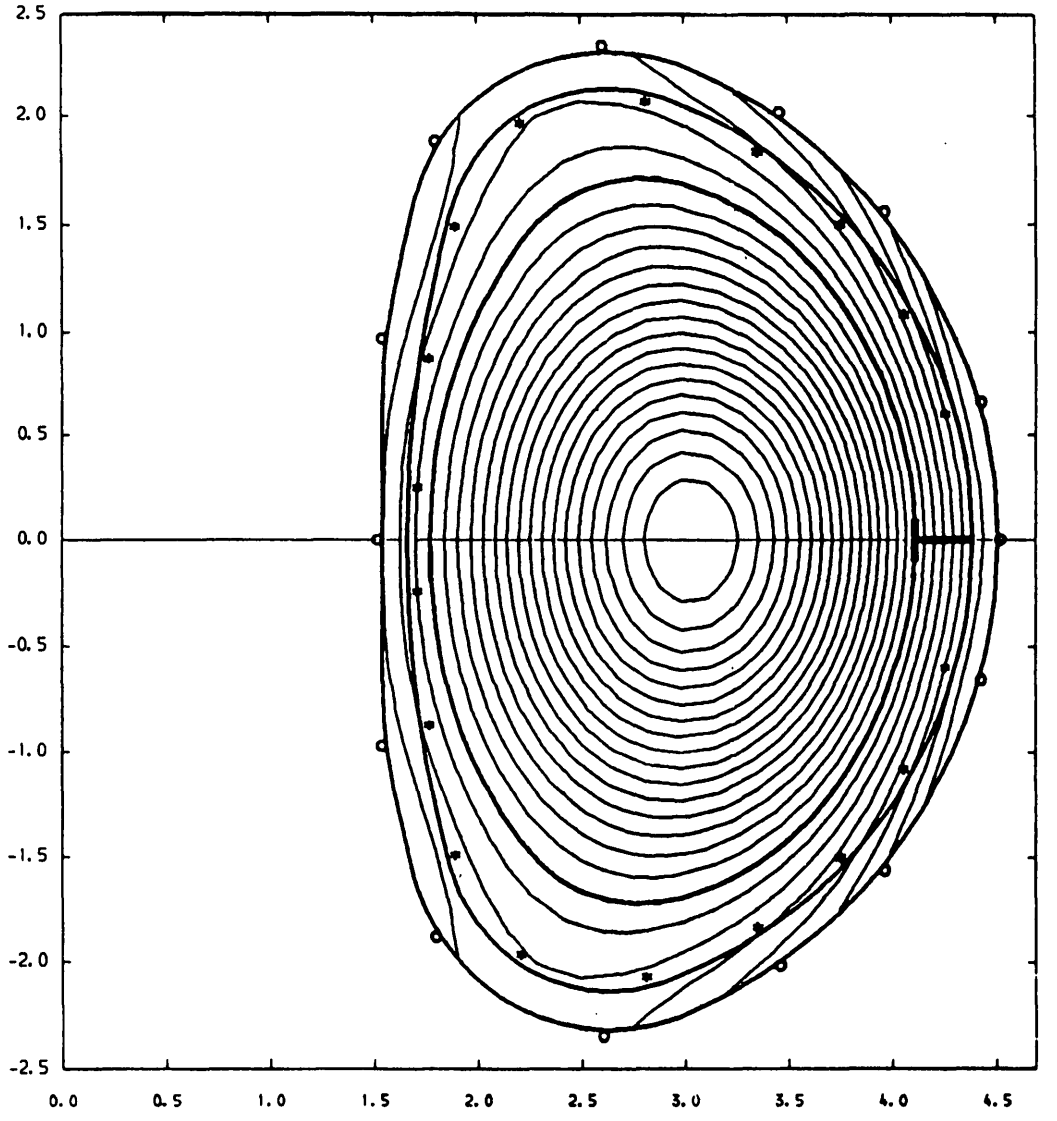

FIG. 25a. JET: Example of poloidal flux surfaces. The limiter is a T-shaped object inserted at the outside midplane. The LCFS is the surface touching the limiter.

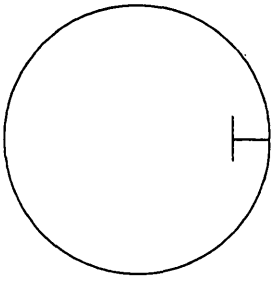

FIG. 25b. Example of a toroidally symmetrical limiter projected onto a poloidal plane. The figure also represents a rail limiter located in a particular plane.

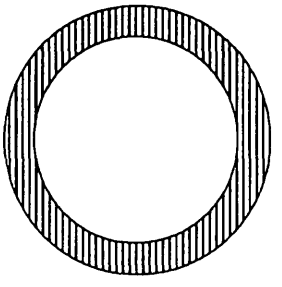

FIG. 25c. Example of a poloidal ring limiter located in a particular plane.

contact with a limiter to the next is, by convention, $2L_c$. Thus, for a tokamak with a single toroidal limiter, $L_c \approx \pi Rq$, while for a tokamak with a single poloidal limiter, $L_c \approx \pi R$ (assuming that a magnetic flux surface coincides with the poloidal limiter). For localized limiters it is more difficult to define L_c; indeed, different values exist for different points on the limiter surface. Resonances between the periodicity of the magnetic field configuration and the configuration of the limiter(s) occur and, for some values of q, $L_c \to \infty$. To a degree, such structure can be blurred by various effects and in some circumstances an effective or average value of L_c may be estimated.

In most SOL modelling, the toroidal geometry of the SOL and the associated neoclassical effects are ignored. It is not clear that this is justified for all SOLs, or that it is justified at all as regards certain SOL phenomena such as e-side/i-side asymmetries (Section 10) and H-mode thresholds (Section 7.3.5); nevertheless, it has turned out to be a useful approximation which has generally resulted in reasonable agreement with observation. The general modelling approach [147] is to 'straighten out' the SOL, forming a long-thin plasma, of length $2L_c$ along $\vec{B}$ (typically 1–100 m) and of width equal to the SOL width (typically ~ 1 cm). The SOL plasma is bounded at each end by the solid limiter surfaces and at the outside by the vessel wall, with the LCFS forming the inside boundary (see Fig. 26). The plasma is assumed to be free to stream parallel to $\vec{B}$, the total magnetic field, while cross-field transport of particles and heat is assumed to occur at specified anomalous rates. Thus, the magnetic field does not appear explicitly in simple modelling. The modelling of the flow along the SOL is usually based on fluid equations, although kinetic formulations are also available.

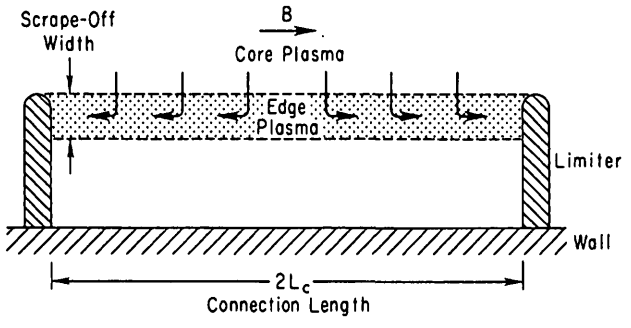

FIG. 26. Schematic of the plasma flow from the core plasma into the scrape-off edge plasma by cross-field diffusion, and of the rapid parallel-field flow of the plasma to the scrape-off surfaces (limiters in this case).

TABLE II. REPRESENTATIVE SOL CONDITIONS

	JET	DITE	ALCATOR C
T_e [eV]	50	15	7
n_e [m^{-3}]	4×10^{18}	3×10^{18}	4×10^{19}
Limiter	Toroidal	One poloidal	Two poloidal
L_c [m]	40	4	1
ν_{*e}	10	52	1500
λ_{ee}, λ_{ii} [m] ($Z_{eff} = 1$)	6	0.8	0.01
$\tau_{\parallel} = L_c/c_s$ [ms]	0.57	0.1	0.04

With regard to justifying this modelling of the SOL, we consider the following points:

(a) *Neglect of toroidal, neoclassical effects:* The SOL conditions are generally collisional so far as banana orbits are concerned, i.e., $\nu_{*e} \gg 1$ (ν_{*e} being the ratio of the effective electron collision frequency to the electron (banana orbit) bounce frequency). Table II gives three representative examples for SOL conditions typical of JET, DITE and ALCATOR-C. Since $\nu_{*e} \gg 1$, one might anticipate that SOLs would be in the neoclassical Pfirsch-Schlüter (P-S, collisional) [479] regime and that the P-S drifts resulting from toroidal geometry would be important in the SOL. Some modelling of the SOL has been carried out on this basis [7, 148–152], but it generally leads to underestimates of the measured cross-field transport rates and of the SOL thickness λ_s, i.e., transport is anomalous. Thus, the more usual procedure is to ignore toroidal and neoclassical effects altogether in the SOL and to invoke anomalous cross-field transport rates for particles and heat, which are adjusted to give agreement with the measured SOL widths for particle and energy density (see Section 3.4). However, since measured scrape-off lengths are not much longer than ion poloidal gyroradii, neoclassical effects may have an influence in the SOL (see, e.g., Section 7.3.5).

(b) *Use of a fluid model for plasma transport along the SOL:* As can be seen from Table II, typically the self-collisional mean free paths, λ_{ee}, λ_{ii}, are smaller than L_c and therefore a fluid model is appropriate. Also, SOL operating regimes are encountered where collisionality is marginal and kinetic analysis is appropriate. It appears, however, that often there is little difference between collisional and collisionless models of plasma flow along the SOL, at least for

most of the quantities of practical interest (see Section 3.2). It should be noted, however, that for situations where T_e varies significantly along the SOL, kinetic effects can be more substantial (see Section 3.6.3).

As will be shown in Section 3.3, the plasma flow velocity along the SOL approaches the ion acoustic velocity $c_s \approx [k(T_e + T_i)/m_i]^{1/2}$. Thus, the SOL particle confinement time $\tau_{\parallel} = L_c/c_s$ is very short, typically < 1 ms (see Table II). The limiter sink strength is therefore very strong and it often dominates over all other sink terms in the SOL, such as impurity radiation, ionization and excitation. This makes for comparatively simple modelling of the SOL, with cross-field transport as the only source and the limiter the only sink of importance. The SOL is therefore easier to understand and model than the radiating layer (RL) just inside the LCFS where atomic processes are dominant and where, of course, no limiter sink action exists.

3.2. Plasma flow along $\vec{B}$ to a surface

Since we are modelling the SOL one-dimensionally, we have the classical case of free plasma flow to two planar surfaces separated by $2L_c$, with a stagnation surface halfway (see Fig. 27). This situation has been modelled many times, employing different assumptions [47, 154–166]. Virtually all models, however, share a number of basic features, which were first clearly elucidated in the 1929 classical paper by Tonks and Langmuir [47]. Before attempting an explanation of these features, we first state briefly what they are:

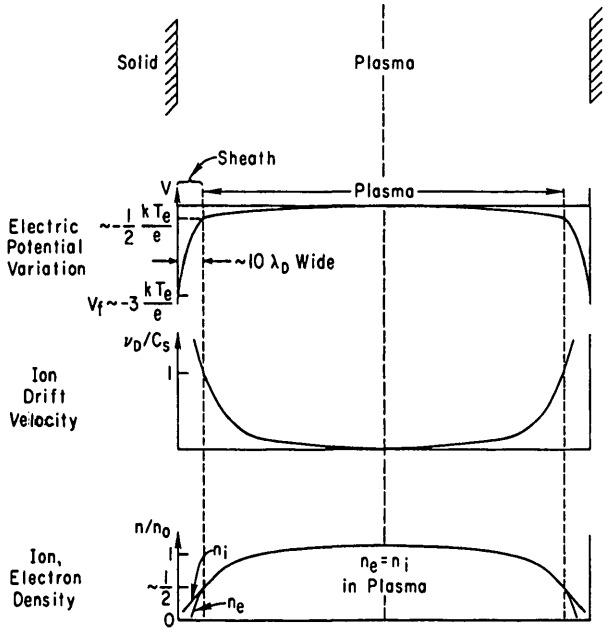

FIG. 27. Schematic of the variation of electric potential, ion drift velocity and ion/electron densities in the plasma between two semi-infinite planes. The thickness of the sheath is exaggerated for clarity.

(a) The solid becomes negatively charged, while an almost equal, positively charged layer — the sheath — forms just in front of the surface. The charge cancellation is imperfect and a small electric field — the pre-sheath — penetrates the plasma all the way to the stagnation point (Fig. 27).

(b) The electrons find themselves in an electrostatic potential, out of which they leak only slowly to the solid surface, i.e. the drift velocity of the electrons is very small compared to their random velocity. Only electrons from the high energy tail of the distribution can reach the surface. Therefore, to a good approximation, the electron density n satisfies a Boltzmann relation; see Eq. (2.2):

$$n = n_0 \exp(eV/kT_e) \tag{3.1}$$

where n_0 is the density at the stagnation point, V is the electrostatic potential, which is taken to be zero at the stagnation point, and T_e is the electron temperature, which is taken to be spatially constant in the 'simple SOL' (see Section 3.6).

(c) Throughout most of the space between the surfaces, quasi-neutrality obtains, $n_e \simeq n_i$ ($Z = 1$). Thus, Eq. (3.1) also gives the plasma density.

(d) The ions are in an accelerating field which causes their drift velocity to reach the ion acoustic velocity c_s just at the plasma/sheath interface. The potential drop in the plasma, i.e. from the stagnation point to the plasma–sheath interface, is $\approx 0.5\ kT_e/e$, while the plasma density drops to $\sim 0.5\ n_0$ (Fig. 27) [47].

(e) The ion density drops further in the sheath, but not as rapidly (in space) as does n_e and, thus, a net, steady-state positively charged sheath exists dynamically. The potential drop through the sheath to the solid is $\sim 3\ kT_e/e$ for hydrogenic plasmas (assuming equal ion and electron currents to the solid, i.e. an electrically floating surface). The latter condition must hold for the simplest arrangements; however, a small object can, of course, be electrically biased so as to collect net ion or electron current. (A large object, such as the limiter which controls the plasma–surface interaction, automatically floats, on average, relative to

the plasma. Frequently, the limiter potential is fixed relative to the outside world, and therefore the plasma floats with respect to the limiter(s).) In that case, and provided the solid is not biased extremely positively relative to the floating potential, all of the foregoing features remain unchanged, except for the potential drop within the sheath, which is less than $\sim 3\ kT_e/e$ for net electron collection and more than that for net ion collection. The sheath thickness, for floating conditions, is of the order of a few Debye lengths [154], $\lambda_D = (\epsilon_0 kT_e/n_e^2)^{1/2}$, and is thus extremely thin; for example: $T_e = 20$ eV, $n_e = 2 \times 10^{18}\ m^{-3}$, $\lambda_D \approx 10^{-5}$ m.

We turn now to the quantitative explanation of the *plasma* part of the foregoing features. The *sheath* aspects are considered in the next section. Since the electron behaviour is fully specified by the Boltzmann relation, Eq. (3.1), the task becomes one of modelling the ions. As mentioned, many different models for the ion transport are available. Probably the simplest model capable of reproducing the principal features of the SOL is the isothermal fluid model [51, 52, 155–158]. Steady-state, 1-D, inviscid, isothermal flow is fully specified by two equations in the two unknowns n(x) and v(x), where v(x) is the ion fluid velocity, x is the space co-ordinate and, here, $n = n_e = n_i$. The two equations represent conservation of particles and momentum:

$$\frac{d}{dx}(nv) = S_p \tag{3.2}$$

$$nm_i v \frac{dv}{dx} = -\frac{dp_i}{dx} + enE - m_i v S_p \tag{3.3}$$

where $p_i = nkT_i$, $E = -dV/dx$, S_p is the source rate of particles due to cross-field transport or ionization, and
Z = 1 ions are assumed (i.e., no impurities).

When S_p is due to ionization, then

$$S_p = n\, n_n\, \overline{\sigma v}_i \tag{3.4}$$

where n_n is the neutral density and $\overline{\sigma v}_i$ is the ionization rate averaged over the electron energy distribution.

When S_p is due to cross-field transport by diffusion, then

$$S_p = \frac{\partial}{\partial r}\left(D_\perp \frac{\partial n}{\partial r}\right) \approx \frac{D_\perp n}{\lambda_n^2} \tag{3.5}$$

where λ_n is the characteristic scale length for plasma density variation in the direction perpendicular to the flow, e.g. the SOL width, and r is in the radial direction.

The Boltzmann relation, Eq. (3.1), gives

$$enE = -kT_e \frac{dn}{dx} \tag{3.6}$$

The simplest closure condition is that the ions are isothermal:

$$\frac{dp_i}{dx} = kT_i \frac{dn}{dx} \tag{3.7}$$

Therefore, the ion momentum equation (3.3) can be written as

$$v \frac{dv}{dx} = -\frac{c_s^2}{n}\frac{dn}{dx} - \frac{S_p v}{n} \tag{3.8}$$

The natural normalization for the ion velocity is c_s, as defined in Section 3.1, and we may define the Mach number as $M(x) = v(x)/c_s$. Combining Eqs (3.2) and (3.8) gives

$$\frac{dM}{dx} = \frac{S_p}{nc_s}\frac{(1+M^2)}{(1-M^2)} \tag{3.9a}$$

We note that, as $M \to 1$, the derivatives of v, n and M with respect to x become infinite and thus the plasma solution fails (i.e. the quasi-neutral assumption fails). This corresponds physically to the termination of the plasma and the start of the sheath with its strong ion acceleration and large electric field. Thus, we have obtained the key result that the ions flow from the plasma at the acoustic velocity. (Assuming that the solid is electrically floating, thus receiving equal electron and ion fluxes, and that $n_e = n_i$, then the electron flow or drift velocity is also c_s.) This is a very general conclusion since it is independent of spatial variations in S_p, and independent of whether the ion flow is assumed to be isothermal or adiabatic.

M starts at zero far from the surface and increases towards it (Eq. (3.9a)). It may be noted that the foregoing only demonstrates that M cannot exceed unity in the plasma. In the next section, however, it is shown that the sheath analysis requires that the entering ions must have an M value of at least unity. Thus, at the plasma–sheath interface, we conclude that $v = c_s$, the so-called Bohm criterion [48].

For either the local ionization source (Eq. (3.4)) or the cross-field diffusion source (Eq. (3.5)) we have $S_p = Cn$ (C being a constant). In this case, Eq. (3.9a) can be integrated to give

$$\left(\frac{\pi}{2} - 1\right)\frac{x}{L} = -M + 2\tan^{-1}M \qquad (3.9b)$$

where L is the system length; the constant has been eliminated by using M(0) = 0, M(L) = 1. For the case of $S_p = S_0$ (constant) the solution is given by integration of Eq. (3.9a)

$$\frac{x}{L} = \frac{2M}{1 + M^2} \qquad (3.9c)$$

where Eq. (3.10) is used together with the same boundary conditions to eliminate S_0.

These two results for M(x) differ little. A more physically realistic approximation for the cross-field source, Eq. (3.5), namely $D_\perp(n_\infty - n)/\lambda_n^2$, would give a value of M(x) between the two solutions.

We may also rewrite the equations to give the distribution for density n(M):

$$\frac{n(M)}{n_0} = \frac{1}{1 + M^2} \qquad (3.10)$$

and, combining Eqs (3.1) and (3.10), for potential V(M):

$$V(M) = -\frac{kT_e}{e}\ln(1 + M^2) \qquad (3.11)$$

independent of spatial variations of S_p, etc. We thus have obtained the further key results that, at the sheath edge, $n_{se} = 0.5\ n_0$ and $V_{se} = -0.69\ kT_e/e$, i.e., $V_{se} \sim -0.5\ kT_e/e$.

As indicated, many other models of 1-D ion transport to a surface are available. One might query the isothermal assumption, for example, or indeed the assumption of a fluid formulation. In fact, changes in these assumptions do not substantially affect the basic conclusions, i.e., $n_{se} = 0.5\ n_0$ and $v_{se} = c_s$, as will now be discussed.

The first collisionless *kinetic* formulation (as distinct from *fluid* formulations such as the foregoing analysis), that of Tonks and Langmuir [47] for cold ions ($T_i = 0$), gives $v_{se} = 1.144\ c_s$ and $n_{se} = 0.425\ n_0$ for the case of plasma production proportional to local electron density, i.e., $S_p \propto n$. For S_p = constant, they obtained $v_{se} = 1.227\ c_s$ and $n_{se} = 0.397\ n_0$.

Of more interest are comparisons with models which do not assume $T_i = 0$, since one of the deficiencies of an isothermal assumption is that the natural ion cooling associated with flow acceleration is not allowed. Of course, in the actual SOL application, such cooling is, at least partially, suppressed by cross-field heat transport, which is generally characterized by a high value of $\chi_\perp$ ($> D_\perp$), see Section 3.4. Nevertheless, we consider next several recent 1-D ion transport models for $T_i \neq 0$:

(a) Emmert et al. [159] (hereafter EWMD) have developed a collisionless kinetic model where the ions are assumed to be created with a velocity distribution:

$$S_p(v) \propto \frac{m_i v}{2kT_s}\exp\left(-\frac{m_i v^2}{2kT_s}\right) \qquad (3.12)$$

where T_s is the ion source temperature.

(b) Bissell and Johnson [160] (hereafter BJ) have developed a model similar to that of EWMD, but they assume:

$$S_p(v) \propto \left(\frac{m_i}{2kT_s}\right)^{1/2}\exp\left(-\frac{m_i v^2}{2kT_s}\right) \qquad (3.13)$$

Although these two models appear to be very similar, they lead to at least one major difference, namely in the strength of the electric field in the plasma near the sheath. The EWMD ion source has the intuitively satisfying property that if the electric field is set to zero, then the resulting ion velocity distribution is found to be Maxwellian everywhere. On the other hand, the BJ source is the one which would actually result if ions were created by electron impact on Maxwellian neutrals.

(c) Zawaideh, Najmabadi and Conn [161] (hereafter ZNC) have published a set of fluid equations, allowing for finite and non-isothermal T_i, and employing the closure condition that the derivative of the ion heat conduction is everywhere zero, $\partial q^i/\partial x = 0$. Bissell [162] applied the ZNC equations to the 1-D problem.

In comparing these three models with the isothermal fluid model, we focus on the case of $T_s = T_e$, i.e. the ion source temperature equals T_e (which is assumed constant in space for all models). Of course, at the sheath edge, the parallel ion temperature $T_\parallel^i$ is lower ($T_\perp^i$ is spatially constant for all models). For example, at the sheath edge, $T_\parallel^i/T_e = 0.16$ for the BJ model

TABLE III. PREDICTIONS OF THE PRINCIPAL QUANTITIES OF INTEREST BY SEVEN MODELS[a]

Quantity	Normalization factor	Model[b]							
		1	2	3	4	5	6	7	Average
Plasma density at sheath edge, n_{se}	n_0	0.50	0.49	0.66	0.52	0.50	0.50	0.43	0.51
Plasma flow velocity at sheath edge, v_{se}	$(kT_0/m_i)^{1/2}$	1.41	1.60	1.35	1.27	1.49	1.46	1.24	1.40
Plasma potential at sheath edge, η_{se}	kT_0/e	-0.69	-0.72	-0.41	-0.65	-0.69	-0.69	-0.86	-0.67
Normalized (floating) wall potential, η_w	kT_0/e	-3.19	-3.08	-2.91	-3.26	-3.13	-3.15	-3.45	-3.17
Particle outflux density, Γ_{se}	$n_0(kT_0/m_i)^{1/2}$	0.71	0.78	0.89	0.66	0.75	0.73	0.54	0.72
Ion heat outflux density, P^i_{se}	$n_0kT_0(kT_0/m_i)^{1/2}$	2.49	2.40	2.08	1.33	2.04	2.01	1.24	1.94
Electron heat outflux density, P^e_{se}	$n_0kT_0(kT_0/m_i)^{1/2}$	3.20	3.40	4.00	3.04	3.33	3.26	2.46	3.24
Total heat outflux density, P_{se}	$n_0kT_0(kT_0/m_i)^{1/2}$	5.69	5.80	6.08	4.37	5.37	5.27	3.70	5.18
Ion cooling rate, P^i_c	$n_0kT_0(kT_0/m_i)^{1/2}$	2.08	1.95	1.78	0.99	1.88	1.83	0.81	1.62
Electron cooling rate, P^e_c	$n_0kT_0(kT_0/m_i)^{1/2}$	3.60	3.85	4.30	3.38	3.50	3.44	2.91	3.57
Ion heat transmission coefficient, γ^i_s	—	2.93	2.50	2.00	1.50	2.72	2.75	2.30	2.39
Electron heat transmission coefficient, γ^e_s	—	5.07	4.96	4.83	5.12	4.44	4.47	4.55	4.78
Total heat transmission coefficient, γ_s	—	8.0	7.46	6.83	6.62	7.26	7.22	6.85	7.18

[a] For the case of $T_e = T^i_\perp(0) = T^i_\parallel(0) \equiv T_0$, temperature at the symmetry point; H^+ ions; no secondary electron emission.

[b] Models: (1) Isothermal, fluid [163]; (2) adiabatic, fluid [163]; (3) kinetic (Emmert et al.) [163]; (4) kinetic (Bissell and Johnson) [163]; (5) fluid, collisionless [164]; (6) fluid, collisional [164]; (7) kinetic, viscid [165].

and 0.18 for the ZNC model. We wish to know what conditions obtain at the sheath edge in terms of remote conditions, for example at the stagnation plane. Thus, we may define the reference ion acoustic velocity as $c_{sr} = [k(T_e + T_i(0))/m_i]^{1/2}$, allowing for the possibility that T_i is not constant. Results for v_{se} are indicated for the four models [163] in Table III for the particular case of $T_e = T^i_\perp(0) = T^i_\parallel(0)$. As can be seen, the calculated values of v_{se} vary only by about $\pm 10\%$ from the isothermal fluid result. The sheath edge density n_{se}/n_0 also varies only slightly among the models, except for the EMWD result, which is $\sim 30\%$ higher than the others. Directly related to n_{se}/n_0 is the plasma potential at the sheath edge, $V_{se}/(kT_e/e)$, which shows similar variation.

Scheuer and Emmert [164] have reported comparisons of other 1-D plasma models (results are also given in Table III):

(i) A collisionless fluid ($T^i_\perp$ = constant) model using either the EWMD source (Eq. (3.12)) or the BJ source (Eq. (3.13)). In the fluid equations, no collision terms in the momentum or energy equations are employed, but the closure condition $dq^i/dx = 0$ is used, which is not strictly correct for collisionless flow and therefore implies some collisionality.

(ii) A collisional fluid ($T^i_\parallel = T^i_\perp$) model using either of the two sources.

The authors reach the same conclusions, namely that variation of the model assumptions — even regarding collisionality — has little influence on the results.

The effect of cross-field viscosity has been included in 1-D plasma flow modelling by Chung and Hutchinson [165], assuming the value of cross-field viscosity $\eta_\perp = mnD_\perp$. The results, given in Table III, are also not greatly different from those of the inviscid models.

We may thus conclude that, as regards the principal quantities of practical interest for the SOL application, there is little difference among the models for these particle flux quantities (or for heat flux quantities, see next section). The isothermal fluid model would therefore appear to be a valid and convenient approximation. It may be noted that the actual situation obtained in the SOL is neither fully collisional nor collisionless. In reality, there is a region distant from the surface where collisionality may hold and where, therefore, fluid models should be applicable. Typically, however, the mean-free-path length, λ_{mfp}, greatly exceeds the sheath thickness, so that there exists a transitional region in front of the sheath where the ion motion changes to collisionless behaviour. Therefore, models

are required which allow for this transition, i.e., for finite λ_{mfp}/L_c. Preliminary results on this topic have been presented and show little change in v_{se} and n_{se}, at least for the moderate levels of collisionality, $\lambda_{mfp} \geq L_c$, so far analysed [166]. When T_e gradients along the SOL are significant, however, then the actual degree of collisionality is probably important (see Section 3.6.3).

It should also be borne in mind that, in real plasma flows to limiters and probes, other effects should be considered, such as 2-D and 3-D effects, cross-field heat transfer, local energy losses and momentum loss due to neutrals. For hydrogenic plasmas, the complex collision processes involving ionization, charge exchange and molecular dissociation may also be important [167]. These effects may cause changes of quantities such as n_{se} greater than the differences among the 1-D, inviscid, adiabatic/isothermal (self-) collisional/collisionless models considered above.

3.3. Role and properties of the sheath

Following Bohm [48], we now consider the modelling of the sheath in front of a solid and look for a sheath constraint on v_{se}. Within the sheath, there is charge imbalance with

$$n_i = n_{se}[V_{se}/V]^{1/2} \tag{3.14}$$

$$n_e = n_{se} \exp[e(V - V_{se})/kT_e] \tag{3.15}$$

where n_i, n_e and V are the densities and the potential at any point within the sheath. Here, $V_{se} = -\frac{1}{2} m_i v_{se}^2/e$ (rather than a factor 0.69); the ions are assumed to have all originated from the same point; they are also cold, $T_i = 0$. Inserting n_i and n_e into Poisson's equation,

$$\frac{d^2V}{dx^2} = -\frac{e}{\epsilon_0}(n_i - n_e) \tag{3.16}$$

giving for the region just inside the sheath:

$$\frac{d^2V}{dx^2} = -\frac{e}{\epsilon_0}(V_{se} - V)\left(\frac{e}{kT_e} - \frac{1}{2|V_{se}|}\right) \tag{3.17}$$

where Eqs (3.14) and (3.15) were used, assuming $|V_{se} - V| \ll 1$. Thus, for monotonic potential, one has the constraint:

$$|V_{se}| \geq \frac{kT_e}{2e} \tag{3.18}$$

or

$$v_{se} \geq (kT_e/m_i)^{1/2} = c_s \quad \text{for } T_i = 0 \tag{3.19a}$$

Since we have from the plasma analysis that $v_{se} \leq c_s$, the final result is $v_{se} = c_s$, the Bohm criterion [48, 168, 169]. (Bohm's original analysis involved integration of Eq. (3.17) to obtain E, plus the constraint that E be real.)

When the ions have a distribution of velocities, $f^i(v)$, then it can be shown [49, 50] that the constraint becomes

$$\int_0^\infty \frac{f_{se}^i(v)dv}{v^2} = \frac{m_i}{kT_e} \tag{3.19b}$$

i.e. the generalized Bohm criterion. Consider, for example, the simple drifting ion distribution [52]:

$$f_{se}^i(v) = \begin{cases} (2c_i)^{-1} & \text{for } v_{se} - c_i \leq v \leq v_{se} + c_i \\ 0 & \text{otherwise} \end{cases} \tag{3.20a}$$

with $c_i \equiv (kT_i/m_i)^{1/2}$. Then, Eq. (3.19b) gives

$$v_{se} = c_s \tag{3.20b}$$

The $f_{se}^i(v)$ distributions calculated by Emmert et al. and Bissell and Johnson also satisfy Eq. (3.19b) [170].

We thus have the important practical result that the ion flux density out of the plasma (thus also the electron flux for a floating solid) is

$$\Gamma_{se}^i = n_{se} v_{se} \simeq 0.5\, n_0 c_s \tag{3.21}$$

We can calculate V_{sf}, the floating potential of the solid relative to the plasma potential V_p, by obtaining an expression for the electron flux and equating the ion and electron fluxes to the surface. Since secondary electron emission (s.e.e.) is generally significant for $T_e \geq 30$ eV, this effect should be included [52, 171–175]. We have the secondary electron flux density

$$\Gamma_{sec}^e = \delta\Gamma_{tot}^e = \delta(\Gamma_{net}^e + \Gamma_{sec}^e) \tag{3.22}$$

where δ is the s.e.e. coefficient, Γ_{tot}^e is the total electron flux striking the surface, and

$$\Gamma_{net}^e = \Gamma_{tot}^e - \Gamma_{sec}^e = (1 - \delta)\Gamma_{tot}^e \tag{3.23}$$

We thus have from Eqs (2.1a), (2.1b), (2.2) and the definition $V_{sf} \equiv V_f - V_p$:

$$\Gamma^e_{net} = \tfrac{1}{4} n_{se} \bar{c}_e (1 - \delta) \exp(eV_{sf}/kT_e) \tag{3.24}$$

Note that V_{sf} in Eq. (3.24) gives only the potential drop across the sheath itself. The actual solid potential relative to the stagnation plane is still lower by the amount of the pre-sheath drop, $\sim 0.69\ kT_e/e$. Equating the electron and ion fluxes, Eqs (3.21) and (3.24), gives the sheath voltage drop [52]

$$\frac{eV_{sf}}{kT_e} = 0.5 \ln\left[\left(2\pi \frac{m_e}{m_i}\right)\left(1 + \frac{T_i}{T_e}\right)(1 - \delta)^{-2}\right] \tag{3.25}$$

Examples of V_{sf} are shown in Fig. 28. As can be seen, the often quoted estimate that $V_{sf} \simeq 3kT_e/e$ can be significantly in error if $T_i > T_e$ and/or if s.e.e. is significant.

The value of V_{sf} in Eq. (3.25) assumes the isothermal fluid model value for v_{se}, i.e., c_s. In Table III, the values of $\eta_w \equiv eV_{sf}/kT_e$ for the case of $T_e = T_i$, H^+ ions and $\delta = 0$ for the various 1-D models are shown for comparison (η_w is defined as the normalized floating wall potential relative to the symmetry plane). The variation among the models is very small, $\lesssim \pm 5\%$.

We turn next to the energy transmission properties of the sheath [51, 52, 171–176] and consider the electrons. Because of the height of the potential barrier, eV_{sf}, the electron distribution is not significantly distorted from Maxwellian; equivalently, $\bar{c}_e \gg c_s$. Since the electrons are in a retarding conservative field, the electron distribution at the solid-sheath interface is still Maxwellian, but of reduced total density with respect to the rest of the sheath and plasma. The power flux associated with a Maxwellian distribution is 2kT times the particle flux. In calculating the electron heat outflux density P^e_{se}, it should be noted that the escaping electrons actually possess a higher kinetic energy as they are removed from the plasma, namely, an energy higher by the amount eV_{sf}. Thus,

$$P^e_{se} = (2kT_e - eV_{sf})\Gamma^e_{tot} + eV_{sf}\Gamma^e_{sec} \tag{3.26}$$

Note: $-eV_{sf} > 0$. The last term in Eq. (3.26) represents the energy injected into the plasma by secondary electrons accelerated through the sheath drop; their thermal energy, a few electronvolts, is neglected. Thus,

$$P^e_{se} = \left(\frac{2kT_e}{1 - \delta} - eV_{sf}\right)\Gamma^e_{net} \tag{3.27}$$

For purposes of modelling the energy balance of the SOL electron population, it is useful to define P^e_c, the energy flux density of cooling the plasma electrons, i.e. $P^e_c = P^e_{se} + P^{ei}_{ps}$, where P^{ei}_{ps} is the power transferred from the electrons to the ions in the pre-sheath (ion acceleration). $P^{ei}_{ps}/\Gamma^e_{net}$ is less than the total pre-sheath potential energy drop, since not all of the ions fall through the entire pre-sheath. Approximately, $P^{ei}_{ps} \simeq 0.5\ kT_e\Gamma^e_{net}$; specific values for each of the models were used in the results given in Table III.

The electron energy transmission coefficient γ^e_s is defined by

$$P^e_c \equiv \gamma^e_s\, kT_e \Gamma^e_{net} \tag{3.28}$$

Thus,

$$\gamma^e_s = \frac{2}{1 - \delta} - \frac{eV_{sf}}{kT_e} + \sim 0.5 \tag{3.29}$$

The exact values for the various models are given in Table III.

We next consider P^i_{se}. Since the ions are accelerated, this quantity is harder to calculate [51] than P^e_{se}. If $f^i_{se}(v)$ were actually a Maxwellian of temperature T_i drifting at c_s, then

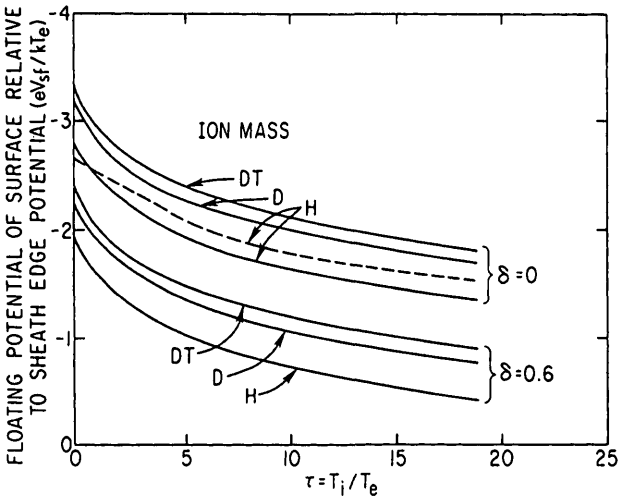

FIG. 28. Voltage difference between a floating surface and the potential at the plasma/sheath interface (normalized), i.e. excluding the pre-sheath voltage, Eq. (3.25). The dotted line is from Emmert et al. [159].

$$P^i_{se} = \left(\frac{5}{2} kT_i + \frac{1}{2} m_i c_s^2\right)\Gamma_{se} = 3.5\ kT_i\Gamma_{se} \qquad (3.30)$$

and thus,

$$\gamma^i_s \approx 3.5\ T_i/T_e \qquad (3.31)$$

In analogy to the electron case, one defines $P^i_c \equiv P^i_{se} - P^{ei}_{ps}$ and, by convention, $P^i_c \equiv \gamma^i_s kT_e\Gamma^e_{net}$, where P^i_c is the energy flux density of cooling the plasma ions, and P^i_{se} is the ion heat outflux density. Such an ion distribution, however, does not satisfy the generalized Bohm criterion, since it has ions with $v \leq 0$ (this would also be intuitively unacceptable, since the solid is assumed to absorb all ions). A collision transition model which completely covers this situation has not yet been developed, but we may again consider the various 1-D models for the example of $T_e = T_i$. Results are given in Table III for P^i_{se}, P^i_c and γ^i_s; they indicate a somewhat wider range than for the particle flux quantities, partly because higher moments of the ion velocity distribution are involved and partly because of different source assumptions. In the absence of a complete theory, it is suggested that an average value of γ^i_s for the models be taken; for $T_e = T_i$, this gives $\gamma^i_s = 2.39$.

The following points should be noted:

- P^i_{se} includes the original ion energy from the source (an amount of 3/2 $kT_i\Gamma$ for the BJ source, Eq. (3.13), and $2kT_i\Gamma$ for the EMWD source, Eq. (3.12)) plus P^{ei}_{ps}.
- P^i_{se} includes both parallel and transverse ion energy.
- The values for P^i_{se}, P^i_c and γ^i_s are calculated in terms of the plasma conditions, such as T_i, *far* from the solid at the stagnation plane. For more sophisticated SOL modelling [147], the value of P^i_{se} is required as a function of conditions at the plasma-sheath interface.

The latter situation, which is an issue of central importance for code simulation studies, is unfortunately not resolved at the present time, since there is no model which spans the range from the collisional region far from the surface, through a collisionally transitional zone, to the collisionless region just in front of the plasma-sheath interface. In the absence of such an analysis, it may be proposed that values of $T_{e,i}$ at the interface be used, i.e. T_{es} and T_{is}, together with γ^e_s and γ^i_s from Eqs (3.29) and (3.31). If the ion flow were genuinely adiabatic, then, presumably, one should use $c_s = (kT_e + (5/3)kT_i)/m_i)^{1/2}$ rather than the isothermal value, which would change both the particle flux boundary value $n_{se}c_s$ and γ^i_s (also γ^e_s through V_{sf}). In general, however, the ion flow along the SOL is subject to cross-field heat input due to finite cross-field heat conduction, and the assumption of an isothermal flow may not be unreasonable.

It may be noted that the total heat transmission coefficient, $\gamma_s \equiv \gamma^e_s + \gamma^i_s$ (Table III), varies little among the various models. On the other hand, the experimental values of γ_s (which are generally more accessible than γ^e_s or γ^i_s separately) span a much wider range, as discussed below. Evidently, modelling questions of collisionality versus non-collisionality, viscid versus inviscid, kinetic versus fluid, etc., are of rather slight consequence compared with other factors, which remain to be better identified.

The existence of the electrostatic sheath, separating the plasma from the solid, has both beneficial and detrimental effects with regard to plasma–materials interactions. Compared to the situation which would obtain in the absence of a sheath, the ion sputtering is increased owing to the higher ion impact energy resulting from the sheath potential drop, but the total heat flux density is decreased, since the increase in heat carried per ion pair is more than offset by the reduction in electron flux density.

The existence of the sheath also tends to bring about non-equality of T_e and T_i in the SOL. This occurs because the sheath acts as a 'high energy pass filter' for SOL electrons, while ions of just average energy are removed. Thus, there is a tendency for $T_i > T_e$ in the SOL [53], although equipartition collisions tend to lead to equal temperatures. An additional factor which can tend to keep T_i high is that the ions are backscattered from the surface, carrying a certain fraction of their impact energy back into the plasma. Depending on the backscatter energy and particle reflection coefficients (Fig. 39, Section 4) and on the ratio T_e/T_i, this process can result in net heating or cooling of the plasma ions.

The choice of limiter material affects the SOL properties directly through the s.e.e. coefficient δ and the ion backscatter distributions. The value of δ, in fact, can vary for a given material as a result of plasma exposure, and thus it is important to use values for material exposed to plasmas in calculating sheath drops, heat transmission coefficients, etc. [54]. The value of δ is also dependent on the incident angle of the electrons. Since, in practice, exposed surfaces tend to be microscopically rough, it is not clear whether a Maxwellian averaged value or a normal incidence value should be employed. Experimental measurements of floating potential as a function of T_e, using a gridded energy analyser in the DITE SOL [54], have shown

a decrease in eV_{sf}/kT_e with increasing T_e, as would be expected, since δ increases with T_e (Eq. (3.25)).

In practice, the surface of the limiter is often inclined at a shallow angle to $\vec{B}$ in order to decrease the deposited heat flux density. The ions do not actually strike the surface at this angle, owing to gyro-motion and sheath effects; nevertheless, the incidence is, on average, rather oblique. The sheath analysis [71–81, 89, 177, 178] for oblique ion incidence indicates that the total potential drop between the plasma and the (floating) surface is little changed compared to the case of normal ion incidence. Ion sputtering yields are dependent on the angle of incidence; calculations [179] have been carried out which average this effect over the ion angular distribution, also allowing for an oblique angle between $\vec{B}$ and the surface. For example, for a surface with a tangent of 10° to $\vec{B}$, $T_i = T_e = 100$ eV, $n_e = 10^{18}$ m^{-3}, the average D^+ ion impact angle is ~60°; for a pyrolytic graphite surface, the yield of ~300 eV D^+ ions would be increased by a factor of about four for this incidence angle [180]; for technical grade graphites, the enhancement factor is less (about two) [181]; roughness effects may result in further reductions of enhancement, as has been calculated for the related effect of ion backscatter [182]. At shallow angles of incidence, the effective secondary electron emission is expected to be reduced owing to recapture on the first Larmor orbit [89].

For surfaces which are almost exactly parallel to $\vec{B}$ (angle of incidence $\ll (m_e/m_i)^{1/2}$), it is calculated that the floating sheath potential reverses, and the surface becomes electron attracting, since the Larmor radius of electrons is less than that of ions. Flux densities have been computed to be about 1% of $n_e c_s$ [90]. Experimentally, however, it has been found that cross-field particle and heat fluxes onto parallel surfaces of probes are about 10% of the flux onto normal surfaces [183, 184]. This result implies interpretation problems for probes whose collectors are at shallow angles to $\vec{B}$.

The value of γ_s can be established experimentally by measuring the particle flux density (e.g. measuring I_s^+ using a Langmuir probe), the electron temperature (e.g. using a Langmuir probe) and the heat flux density P (e.g. using infrared detection of surface temperature changes), together with the relation $P = \gamma_s kT_e \Gamma_{net}^e$.

The reported values of γ_s obtained experimentally span a considerable range; Microtor and Macrotor [185]: 25–100; JFT-2 [27]: 3.5–20; TFR [186]: ~15; DIVA [187]: 7–20; DITE [188–190]: 10–20; ISX [191, 192]: ~4–6; PDX [93]: 2–40; ASDEX [193]: <6. Since the inference of γ_s requires three separate measurements, errors can be significant, particularly regarding T_e (Section 2.2.1(b)) and P, where the ion energy reflection coefficient has to be allowed for. (If $T_i \neq T_e$, then a fourth quantity must also be measured, namely T_i.) High values of γ_s probably indicate the presence of fast, non-thermal ions or electrons [100, 176, 185, 194]. A proper testing of models for γ_s requires measurement of the ion and electron energy distribution and of the secondary electron emission and the ion reflection coefficients of the contaminated and roughened surface. Such detailed experiments have not yet been carried out in tokamaks.

3.4. Scrape-off lengths and evaluation of $D_\perp^{SOL}$, $\chi_\perp^{SOL}$

In this section we consider the relation between the scrape-off lengths of the SOL (the characteristic radial scale lengths) and the connection length L_c, etc., for the 'simple SOL', i.e. the situation where cross-field transport is the only source term and the limiter is the only sink term. As shown in Section 2.1, radial scale lengths in the SOL are short — of the order of centimetres or less. This is a matter of considerable practical consequence, since it means that heat fluxes to edge structures are highly concentrated. For the purpose of predicting this critical aspect of future devices, it is thus of the greatest importance to know the scrape-off lengths, and the (anomalous) cross-field transport coefficients ($D_\perp^{SOL}$, $\chi_{\perp,e}^{SOL}$, $\chi_{\perp,i}^{SOL}$) which control them.

A first estimate of the density scrape-off length λ_n is obtained by equating the total cross-field particle flux into a SOL of length L_c and (poloidal) depth w:

$$D_\perp \left.\frac{dn}{dr}\right|_{LCFS} L_c w \approx D_\perp \frac{n}{\lambda_n} L_c w \qquad (3.32)$$

to the particle flux reaching the limiter:

$$w \int_{LCFS}^{wall} n_e(r)\, c_s(r) dr \approx 0.5\, n_0 c_s w \lambda_n \qquad (3.33)$$

where n_0 is the density on the LCFS far from the limiter and the radial variation of c_s has been neglected. Thus [195-197],

$$\lambda_n \simeq (2 D_\perp L_c / c_s)^{1/2} \qquad (3.34)$$

Probes and other SOL diagnostics provide measurements of λ_n and T_e (from which one can estimate c_s, assuming $T_e = T_i$), thus allowing $D_\perp$ to be estimated.

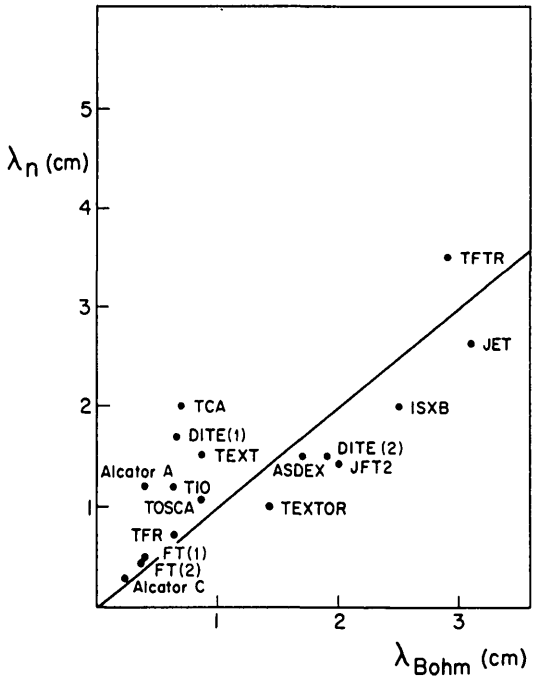

FIG. 29. Comparison of experimentally measured density scrape-off lengths, λ_n, with the theoretical value, $\lambda_{Bohm} = (2D_\perp L_c/c_s)^{1/2}$, where $D_{\perp\,Bohm}[m^2 \cdot s^{-1}] = 0.06\ T[eV]/B[T]$. The JET and TFTR points are averages of the values given in Table I. For JET, $\overline{\lambda}_n = 0.5\ \lambda_{n\,probe}$ has been used [198].

Figure 29 shows results [198] from a variety of tokamaks, comparing $D_\perp$ with the empirical Bohm [48] diffusion value $D_\perp^{Bohm}$ $[m^2 \cdot s^{-1}] = 0.06$ T [eV]/B[T]. As can be seen, SOL values of $D_\perp$ are often close to the Bohm value [185, 199].

Considering both particle and energy balance [37, 74, 200, 201] yields estimates of the ion and electron temperature scrape-off lengths λ_i and λ_e. We assume

$$n_e(r) = n_0 \exp(-(r - a)/\lambda_n) \tag{3.35}$$

$$T_{e,i}(r) = T_0 \exp(-(r - a)/\lambda_{e,i}) \tag{3.36}$$

where it is arbitrarily assumed that $T_e = T_i$ at the LCFS. It is also assumed that T_0 is constant along the LCFS, while n_0 is the density on the LCFS far from the limiter (dropping to 0.5 n_0 on the LCFS at the limiter).

The values of λ_n and $\lambda_{e,i}$ are given by the three conservation equations for mass, electron energy and ion energy:

$$L_c \frac{d}{dr}\left(D_\perp \frac{dn}{dr}\right) = \frac{1}{2} nc_s \tag{3.37}$$

$$L_c \frac{d}{dr}\left[n\chi_\perp \frac{d(kT_e)}{dr} + \frac{5}{2} kT_e D_\perp \frac{dn}{dr}\right] = \frac{1}{2} nc_s \gamma_s^e kT_e \tag{3.38}$$

$$L_c \frac{d}{dr}\left(\frac{5}{2} kT_i D_\perp \frac{dn}{dr}\right) = \frac{1}{2} nc_s \gamma_s^i kT_e \tag{3.39}$$

where electron (anomalous) convection and conduction is included; however, ion conduction is assumed to be neoclassical and is neglected. The use of the factor 5/2 is uncertain; factors of either 3/2 or 2 may be appropriate. Since cross-field transport is anomalous, it is not clear whether the normal factor of 5/2 for convected heat applies or whether an energy density factor of 3/2 is appropriate, or some factor in between.

Assuming $\gamma_s^i = 2.5\ T_i/T_e$, then $\lambda_i \to \infty$, since each ion entering the SOL brings with it $\frac{5}{2}kT_0$ while $\frac{5}{2}kT_i(r)$ is removed per ion at the sheath; thus, $T_i(r) = T_0$. We may therefore make the convenient approximation throughout most of the SOL that $T_i \gg T_e$; thus,

$$c_s(r) \simeq (kT_i/m_i)^{1/2} = c_{so} \tag{3.40a}$$

$$c_s(0) \equiv (kT_0/m_i)^{1/2} \tag{3.40b}$$

Equations (3.37)–(3.39) are integrated from the LCFS to ∞, i.e. the wall is assumed to be at a position $(r_w - a) \gg \lambda_n$, then, evaluated at r = a, giving:

$$\frac{D_{\perp 0}}{\lambda_n} = \frac{c_{so}\lambda_n}{2L_c} \tag{3.41}$$

$$\frac{D_{\perp 0}}{\lambda_n}\left(\frac{5}{2} + \frac{\chi_{\perp 0}}{D_{\perp 0}}\frac{\lambda_n}{\lambda_e}\right) = \frac{\gamma_s^e c_{so}}{2L_c}\left(\frac{1}{\lambda_e} + \frac{1}{\lambda_n}\right)^{-1} \tag{3.42}$$

where $D_{\perp 0}$, $\chi_{\perp 0}$ are the values at r = a. Thus, λ_n is again given by the simple relation, Eq. (3.34), while λ_e can be obtained from combining Eqs (3.41) and (3.42) to give:

$$\left(\frac{5}{2} + \frac{\chi_{\perp 0}}{D_{\perp 0}}\frac{\lambda_n}{\lambda_e}\right)\left(1 + \frac{\lambda_n}{\lambda_e}\right) = \gamma_s^e \tag{3.43}$$

Results are displayed in Fig. 30, where λ_n and λ_e are expressed in terms of a reference value, $\lambda_{ref} \equiv (2L_c D_{\perp 0}/c_{so})^{1/2}$. As can be seen, the value of λ_e is strongly dependent on both the sheath electron heat transmission coefficient γ_s^e and the ratio of $\chi_{\perp 0}/D_{\perp 0}$.

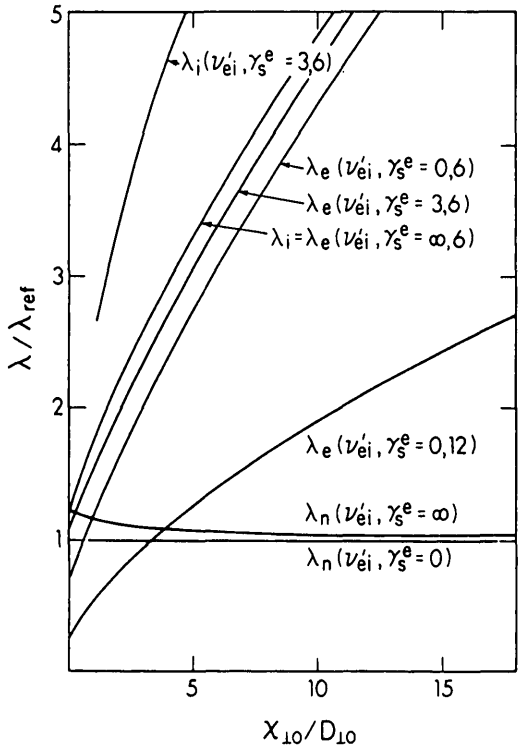

FIG. 30. Theoretical values for the density scrape-off length λ_n, the electron temperature scrape-off length λ_e, and the ion temperature scrape-off length λ_i, as a function of the ratio of the cross-field electron heat conduction to the diffusion coefficient, $\chi_{\perp o}/D_{\perp o}$, at the LCFS, the sheath electron heat transmission coefficient γ_s^e, and the normalized e–i equipartition collision frequency, $\nu'_{ei} \equiv 2L_c\nu_{ei}/c_{so}$. The reference SOL length $\lambda_{ref} \equiv (2L_cD_{\perp o}/c_{so})^{1/2}$. $\chi^i_{\perp o} = 0$ is assumed.

The latter quantity is often found to be in the range 1–10 for the *main* plasma [74, 202, 203].

Experimentally, it is in fact often found that $\lambda_e \gtrsim \lambda_n$ in the SOL [53]. Measurements of T_i and λ_i in the SOL are very sparse, but they tend to show $\lambda_i > \lambda_e$ [53].

The foregoing simple treatment which yielded the result that λ_i tends to be large is, in reality, often modified by various effects:

— The ion heat conductivity, $\chi_{\perp i}$, may not be negligible;
— Just as the pre-sheath electric field (along $\vec{B}$) transfers energy from the electrons to the ions, any electric field perpendicular to $\vec{B}$ also transfers energy. For ambipolar conditions in the SOL, this field is such as to transfer energy from ions to electrons [204], thus more or less offsetting the effect of finite $\chi_{\perp i}$;
— The electron–ion equipartition collisions can be important.

Regarding the latter, we may partially relax the definition of the 'simple SOL' to allow for such internal plasma heat transfer, while still excluding all net sources and sinks. We can no longer assume $T_e \ll T_i$ throughout most of the SOL. We consider first the extreme case of $T_e = T_i$; thus, $c_s(r) = (2kT(r)/m_i)^{1/2}$. Following the same procedure as before, it can be shown that this gives the following two relations which can be solved for λ_n and $\lambda_T \equiv \lambda_e = \lambda_i$:

$$\lambda_n = (2L_cD_{\perp 0}/c_{so})^{1/2}(1 + \lambda_n/2\lambda_T)^{1/2} \tag{3.44}$$

$$(\gamma_s^e + \gamma_s^i)(1 + \lambda_n/2\lambda_T) = (1 + 3\lambda_n/2\lambda_T) \times \left(5 + \frac{\chi_{\perp 0}}{D_{\perp 0}}\frac{\lambda_n}{\lambda_T}\right) \tag{3.45}$$

We now compare the two extreme cases, namely the results of Eqs (3.41)–(3.43), assuming that T_e and T_i are fully decoupled (and that $T_i \gg T_e$ throughout most of the SOL), with the results of Eqs (3.44) and (3.45), assuming $T_e = T_i$ throughout the SOL. From Fig. 30, it can be seen that λ_n and λ_e are scarcely changed, while λ_i goes from ∞ to some finite value. Since the change in the ion behaviour is so dramatic, it is of interest to consider the situation for various values of ν_{ei}, the electron–ion equipartition collision frequency. The analysis, now somewhat cumbersome, gives the results presented in Fig. 30, showing that $T_e \simeq T_i$ for the normalized collision frequency $\nu'_{ei} \equiv 2L_c\nu_{ei}/c_{so} \gtrsim 3$. This result is a useful one for Langmuir probe interpretation of I_s^+ in terms of n_e since, generally, values of T_i are not measured. Inserting the values of ν_{ei} and c_{so} for a D^+ plasma with some contamination, $Z_{eff} > 1$, where $Z_{eff} \equiv \sum_j n_jZ_j^2/n_e$ and the sum is over all ion species j of charge Z_j, gives the result [74, 205] that equipartition occurs, $T_e \simeq T_i$, when $\nu'_{ei} \gtrsim 3$, i.e.

$$\frac{L_cn_eZ_{eff}}{T^2} \gtrsim 6 \times 10^{17}\ [m^{-2}\cdot eV^{-2}] \tag{3.46}$$

for L_c [m], n_e [m^{-3}], T [eV].

For the SOL data examples of Table II, we find that the LHS of Eq. (3.46) for JET, DITE and ALCATOR-C has the values 2, 1.5 and 6×10^{17}, respectively, assuming $Z_{eff} = 3$. Thus the attainment of equipartition in the edge is generally marginal — at least when the sheath is the dominant sink.

As indicated earlier, the inference of $D_\perp$ from measurements of λ_n can be carried out using Eq. (3.34)

and, as can be seen from Fig. 30, this is not significantly dependent on uncertainties about the value of γ_s^e and/or the degree of equipartition in the SOL. When the value of $\chi_\perp$ is inferred from measurements of λ_n and λ_e (Fig. 30), however, a problem is encountered if there is uncertainty concerning γ_s^e, since this significantly alters the relation between λ_e and $\chi_\perp$ (Fig. 30). One source of uncertainty in γ_s^e is the effectiveness of secondary electron emission when the limiter surface is nearly tangential to $\vec{B}$, as is often the case for reasons of heat load. If the angle is small enough, then the secondary electrons return to the limiter after completing only part of a Larmor orbit and are recaptured. The returning fraction of electrons is difficult to calculate for real (roughened) surfaces, thus introducing uncertainties in $\delta_{effective}$ and γ_s^e, and thus also in the inference of $\chi_\perp$. An experimental approach to the problem would involve estimating γ_s^e for the actual surface by separately measuring T_e, Γ and P. At present, there is little reliable experimental information on this critically important quantity, $\chi_{\perp e}^{SOL}$. Further experimental data are urgently required for predictions of edge conditions in future devices such as ITER.

Turning to the ion heat conduction coefficient $\chi_{\perp i}^{SOL}$, there is essentially no experimental information at all. In many tokamaks, it has been reported for the *core* plasma that $\chi_{\perp i}^{core} = \alpha\chi_{\perp i}^{neo}$, where α = 1-5 and $\chi_{\perp i}^{neo}$ is the neoclassical value [203, 206, 207]. If it were assumed that this also holds in the SOL, then $\chi_{\perp i}$ would generally not be an important term. There is, however, recent evidence from large tokamaks such as JET and TFTR that $\chi_{\perp i}^{core} \approx \chi_{\perp e}^{core}$ [208] — a situation which therefore cannot be ruled out for the SOL. It is difficult to establish $\chi_{\perp i}^{SOL}$ experimentally, for two reasons: the lack of T_i diagnostics and the weak sheath effects on ions. Few diagnostic measurements of T_i in tokamaks have been reported, and no systematic studies at all; for T_e, by contrast, such studies have been performed. The most reliable probe diagnostic for T_i, the gridded energy analyser [138], is considerably less robust than the Langmuir probe.

The sheath tends to strongly cool the electrons, making for a short λ_e. This is offset in proportion to $\chi_{\perp e}/D_\perp$, which therefore makes it possible, in principle, to infer values of $\chi_{\perp e}/D_\perp$ from measurements of λ_e/λ_n. The sheath does not, however, cool the ions in the simplest model and, therefore, $\lambda_i \to \infty$. In this situation, there is no comparable way to infer $\chi_{\perp i}/D_\perp$ from the measured λ_i/λ_n. One could, in principle, obtain $\chi_{\perp i}$ by measuring T_i at various points along the length of the flux tube, since the ion acceleration tends to reduce T_i along $\vec{B}$. This cooling will be offset by finite values of $\chi_{\perp i}$, which could therefore be inferred.

In practice, a number of complicating effects can influence the inference of $D_\perp$ from λ_n. If the SOL is not simple (Section 3.6), then various processes, such as local ionization of neutrals within the SOL, can affect λ_n, independent of $D_\perp$. Non-symmetry of limiters and non-circularity of the plasma poloidal cross-section can also significantly alter the relation between λ_n and $D_\perp$ [11, 209, 210].

Detailed analysis [209] of the JET limiter configuration, including the effect of (a) non-circular plasma cross-section and (b) discrete rail limiters, yields the relation between λ_n and $D_\perp$:

$$\frac{c_s\lambda_n^2(0)}{fD_\perp\pi(R_m + a)} = \begin{cases} q_s(0) & \text{for } q_s(0) > q_s^*(0) \\ q_s^*(0) & \text{for } q_s(0) < q_s^*(0) \end{cases} \quad (3.47)$$

where $\lambda_n(0)$ is measured at the outside midplane (limiter) location (θ = 0), f is a shape factor of order 0.5, $q_s(0)$ is the normalized pitch of $\vec{B}$ at the limiter: $q_s(0) \equiv r(0)\, B_T(0)/R(0)\, B_p(0)$, $q_s^*(0) \equiv 2\pi a/h_w N$, where h_w is the wetted height of each of the N rail limiters. This expression gives values of $D_\perp$ which are, typically, a factor of four higher than those in the simple expression, Eq. (3.34). It should be noted that Eq. (3.47) makes no allowance for 2-D plasma flow effects, ionization within the SOL, etc. Results for $D_\perp$ for a range of Ohmic discharges in JET are shown in Fig. 31. For medium to high density operation, the SOL values of $D_\perp$ are not greatly different from that found in INTOR and ALCATOR, $D_\perp \simeq 10^{19}/\bar{n}_e$ (although based on $\bar{n}_e$, not on local $\bar{n}_e(r)$); these values are also not greatly different from those measured [202] in the central part of the plasma (see Fig. 44, Section 4). Finally, since it is observed on JET [12] that $T_e(a)$ decreases with increasing $\bar{n}_e$, these results for $D_\perp$ are also Bohm-like, $D_\perp \propto T$.

The particle flux and heat flux scrape-off lengths, λ_Γ and λ_P, are directly related to λ_n and λ_T: $\lambda_\Gamma = (\lambda_n^{-1} + 0.5\,\lambda_T^{-1})^{-1}$, $\lambda_P = (\lambda_n^{-1} + 1.5\,\lambda_T^{-1})^{-1}$. One expects $\lambda_\Gamma \simeq \lambda_n$, and, as indicated by the JET examples of Fig. 31, the H_α footprint values of λ_Γ are, in fact, close to the Langmuir probe values of λ_n. H_α viewing of the inside (column) limiter on TFTR [211] provides a direct, rather precise and convenient measurement of λ_Γ, since the small difference in the poloidal radii of curvature of the plasma and the limiter makes the wetted height quite sensitive to the value of λ_Γ. Infrared thermography of the limiters

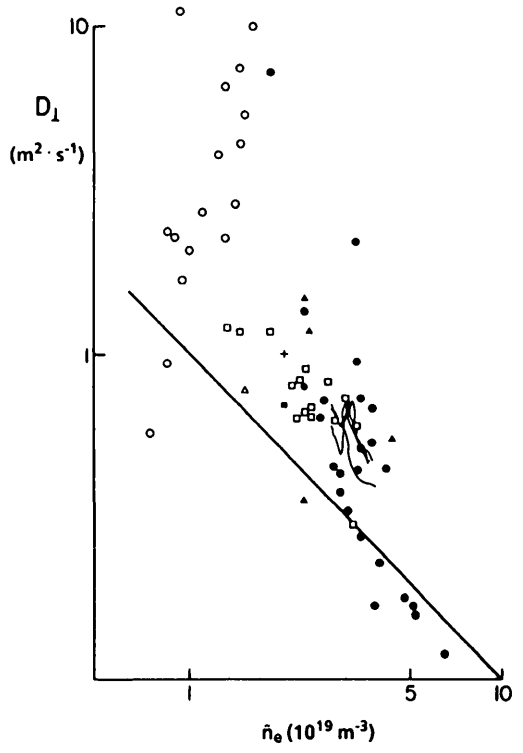

FIG. 31. Values of $D_\perp$ obtained from measurements of λ_n on JET [209]. Probe data: o 1 MA, ▵ 2 MA, ▲ 3 MA, □ 4 MA, ● 5 MA. H_α camera viewing of limiter: wavy lines, four 5 MA discharges. Solid line: $D_\perp = 10^{19}\,\bar{n}_e^{-1}$, INTOR-ALCATOR scaling (but for average n_e, not local n_e). The highest four density points are for He discharges, otherwise for D_2. Error bars: a factor of two to three.

(Section 2.2.8) provides measurements of λ_p. In some cases (PLT [212], T-10 [213]), non-exponential power profiles have been reported.

3.5. Relation between the core plasma and the edge plasma conditions

How are the edge plasma and the core plasma conditions linked? The Lawson criterion specifies the core conditions which must be achieved. What edge conditions will this create? Indeed, since the edge conditions may well have a strong controlling influence on the central conditions, the question is perhaps best put as: What central and edge conditions are mutually compatible? Unless we can explain the observed conditions, our ability to predict reactor conditions will be uncertain.

Such an analysis can be carried out at different levels of sophistication and self-consistency. In this section we consider the conceptually simplest approach in which the particle and energy confinement times, τ_p and τ_E, of the main plasma are taken as given. In reality, the edge conditions influence the confinement times — particularly τ_p, but also τ_E through the radiative loss rate P_R — and therefore a self-consistent analysis is desirable. In Section 4.6, τ_p is related to the edge conditions; in Section 6, P_R is related to the edge conditions.

Values of τ_E for the main plasma are deduced from measurements of the density and temperature in the main plasma and from the total power input. τ_p is deduced [214] from measurements of the main plasma density, plus either (a) the refuelling rate given by H_α measurements, or (b) the ion flux to the limiters measured by edge probes, or (c) charge exchange neutral fluxes to the edge. For many tokamaks, τ_E is found to follow the Goldston empirical (L-mode) scaling [215]:

$$\tau_E\,[s] = 3.7 \times 10^{-2}\, I_p\, P_T^{-1/2}\, R_m^{1.75}\, a^{-0.37}\, \kappa^{1/2} \qquad (3.48)$$

where $\kappa = b/a$ is the plasma elongation, I_p is in MA, P is in MW, and R_m and a are in m. Values of τ_p have not been scaled as systematically, but they have been measured on several machines as a function of $\bar{n}_e$ [198, 214]. For ohmically heated, deuterium, limiter discharges in JET, for example, it is found [216] that

$$\tau_P\,[s] = 1.26 \times 10^{14}\, R_m a^2\, \bar{n}_e^{-0.8} \qquad (3.49)$$

from both H_α and SOL probe measurements [70].

With the exception of deep fuelling, e.g. by neutral beam or pellet injection, the method of measuring τ_p makes it clear that this quantity is not purely a central plasma property, and it is therefore not fully consistent to relate edge quantities to central ones, with τ_p taken to belong to the latter group. Nevertheless, as a first approach, we make this simplifying assumption.

The total particle flux out of the main plasma in steady state is given by

$$\frac{\int n\,dV}{\tau_p} = \frac{\bar{n}V}{\tau_p} = \frac{1}{2}\, n_0 c_{so} A_{L\Gamma} \qquad (3.50)$$

where $A_{L\Gamma} = \lambda_\Gamma w$, the wetted limiter area for particle flux, and V is the plasma volume. The total heat into the SOL, allowing for radiation loss to the walls, P_R, is given by

$$\left(1 - \frac{P_R}{P_T}\right)\frac{\int 3nkT\,dV}{\tau_E} = \left(1 - \frac{P_R}{P_T}\right)\frac{3\bar{n}k\bar{T}V}{\tau_E}$$

$$= \frac{1}{2}\, n_0 c_{so} \gamma_s k T_0 A_{LP} \qquad (3.51)$$

where $A_{LP} = \lambda_P w$, the wetted limiter area for heat flux, and P_T is the total input power. In this first simplified treatment, P_R is treated as a specified central plasma parameter; in Section 6, it is made part of a self-consistent relation between edge and central conditions.

Equations (3.50) and (3.51) thus constitute two equations relating the two edge quantities n_0 and T_0 (i.e., $n_{LCFS}(a)$ and $T_{LCFS}(a)$) to the central plasma quantities $\bar{n}$, $\bar{T}$, τ_p, τ_E, P_R/P_T. The values of λ_Γ and λ_P are functions of n_0 and T_0 (also of $\chi_{\perp 0}$ and $D_{\perp 0}$, which must be assumed as known, or, alternatively, the measured values of $\lambda_{\Gamma,P}$ or $\lambda_{n,e,i}$ are taken as input). We thus have the simple relation [187, 217, 218] between the edge temperature T_0 and the average temperature $\bar{T}$ in the main plasma:

$$\frac{T_0}{\bar{T}} = \frac{3}{\gamma_s} \frac{A_{L\Gamma}}{A_{LP}} \frac{\tau_p}{\tau_E} \left(1 - \frac{P_R}{P_T}\right) \tag{3.52}$$

Typically, $A_\Gamma \approx A_P$ and $P_R/P_T \simeq 0.5$ on JET [219], yielding for $\gamma_s = 10$ (Section 3.3):

$$\frac{T_0}{\bar{T}} = 0.3 \left(1 - \frac{P_R}{P_T}\right) \frac{\tau_p}{\tau_E} \tag{3.53}$$

For example: $\bar{n}_e = 2 \times 10^{19}\,m^{-3}$, $P_T = P_\Omega = 2.1$ MW, $\tau_p \simeq 0.2$ s and $\tau_E \simeq 0.65$ s; then, $T_0/\bar{T} \simeq 0.05$, which is close to the observed ratio for such a discharge, where $T_0 \simeq 100$ eV and the central (peak) $T \simeq 3$ keV [12, 70]. Ignoring the difference between $A_{L\Gamma}$ and A_{LP}, and using the fact that the energy to the edge, $P_T - P_R$, equals the product of $\gamma_s k T_0$ and the particle outflow, $\bar{n}_e V/\tau_p$, one obtains

$$T_0 \approx \frac{(P_T - P_R)\tau_p}{\gamma_s V \bar{n}_e} \tag{3.54}$$

Thus, using Eq. (3.49) for τ_P and assuming $\gamma_s = 10$, $P_R = 0.5\,P_T$, $R_m = 3$ m, $a = 1.2$ m, $\kappa = 1.45$, we obtain $V = 2\pi R\,\pi a^2 \kappa$ and

$$T_0 = 3.2 \times 10^{11}\, P_T \bar{n}^{-1.8} \tag{3.55}$$

Figure 2 gives a comparison of model results with experimental measurements of T_0 on JET, showing not only that the trends of the T_0 dependence on $\bar{n}_e$ and I_p, i.e. P_T, are reproduced, but also that the absolute magnitude is modelled to within a factor of two or better. The empirical relation for Ohmic discharges in JET has been used, $P_T \approx 0.7\, I_p^{1.15}$, with P_T in MW and I_p in MA [12].

Turning to n_0, the edge density at the LCFS far from the limiter, $n_0 \equiv n_{LCFS} \equiv n_e(a)$, Eqs (3.49) and (3.50) may be grouped to give

$$n_0 = \frac{4\pi^2 \bar{n}^{1.8}}{1.26 \times 10^{14}\, c_{so} A_{L\Gamma}} \tag{3.56}$$

Using Eq. (3.55) for T_0 provides a value for c_{so}. For the JET limiters, $A_{LT} \approx 0.1$ m^2, although there is some variation of $A_{L\Gamma}$ with $\bar{n}_e$ and I_p, particularly at the lowest $\bar{n}_e$ and I_p values [12, 46, 70]. Thus,

$$n_0 = 1.6 \times 10^{-31}\, P_T^{-0.5}\, \bar{n}_e^{2.7} \tag{3.57}$$

This result is compared in Fig. 3 with the experimental [12] results. Again, both the absolute magnitudes and the trends of the n_0 dependence on $\bar{n}_e$ and I_p (i.e., P_T) are approximately reproduced.

These strong, comprehensible relations between edge and central conditions observed on JET are rather a rarity. On DIVA [187], T_0 was found to scale in a similarly explicable way, but, for most tokamaks, no comprehensive surveys of these relations have been published. A large number of limited surveys have been published, however, and for the most part they do not exhibit simple, readily explained trends. For example, on many tokamaks the SOL temperature remains in the 10–20 eV range, virtually independent of central conditions including heat input [13–22] (Section 2.1). With regard to the relation between $n_e(a)$ and $\bar{n}_e$: in some cases a square-power dependence is found, but in other cases little variation is seen, and in still other cases the dependence varies from linear to approximately fourth power, depending on conditions [13–20] (Section 2.1). Comprehensive surveys of edge–centre relationships on other large, long-pulse tokamaks are required for progress in this critical matter.

3.6. Simple versus complex SOL

The complex SOL [51, 74] can be defined to be one in which cross-field transport is not the only important source, or the limiter is not the only sink, or parallel field gradients are strong. The processes introducing further complexity which we now consider are: (a) neutral related, (b) impurity related and (c) parallel field temperature gradients. Neutral and impurity effects are dealt with in detail in Sections 4 and 5. In the following, they are considered only with regard to the influence they have on the particle, momentum and energy balance of the SOL plasma. Other effects

which introduce 'complexity' in the SOL are: asymmetries, possibly due to $\nabla\vec{B}$ drifts; variation of the SOL scrape-off lengths along $\vec{B}$ due to flow acceleration (rarefaction); and other effects. These are reviewed in Section 10.

3.6.1. *Effects of neutrals in the SOL*

For tokamak pulse lengths greater than τ_p the plasma is generally refuelled in a quasi-steady-state way by neutrals recycling from the limiters and walls (Section 4). Thus, the neutral density is highest in the SOL. A simple estimate of edge atomic and molecular densities for the simple SOL can be made assuming toroidal and poloidal symmetry, and that all particles recycle from the limiters and do so as molecules (neglecting wall influxes, backscattered atoms, etc.). The incoming flux density of neutrals is given by

$$\Gamma_n = n_{D_2} v_{D_2} = D_\perp n_e(a)/\lambda_n \qquad (3.58)$$

where the right hand side is the ion flux density out of the main plasma which, for the simple SOL, is the only source of ions; $v_{D_2} = (8kT_w/\pi m_{D_2})^{1/2}$, where T_w is the wall/limiter temperature. Take an example for JET: $D_\perp = 1\ m^2 \cdot s^{-1}$, $\lambda_n = 0.03$ m [46] and $T_w \approx 0.1$ eV; then, $n_{D_2}/n_e(a) \simeq 10^{-2}$. This simple

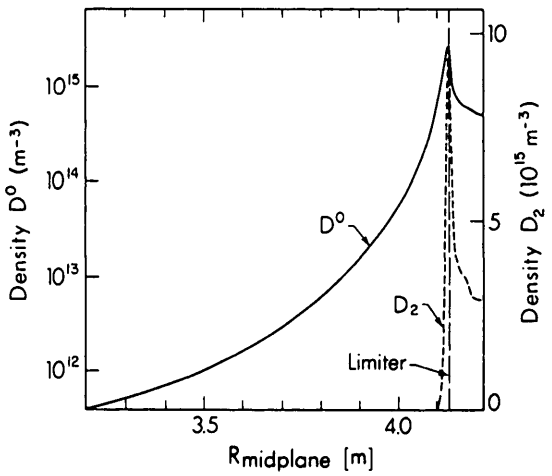

FIG. 32. Neutral code (NIMBUS) calculations of neutral density, and of atomic and molecular radial profiles for a JET case [23]. The profiles give the density integrated for poloidal flux surfaces (see Fig. 25a, whose intercepts with the midplane are $R_{midplane}$). JET discharge 17280 at 11.6 s, 3 MA, B_T = 3.1 T, Ohmic heating, $\bar{n}_e = 2.2 \times 10^{19}\ m^{-3}$. From probe data: T_{LCFS} = 35 eV, $n_{LCFS} = 0.94 \times 10^{18}\ m^{-3}$, λ_n = 0.65 cm, λ_T = 1.0 cm (λ's at the midplane).

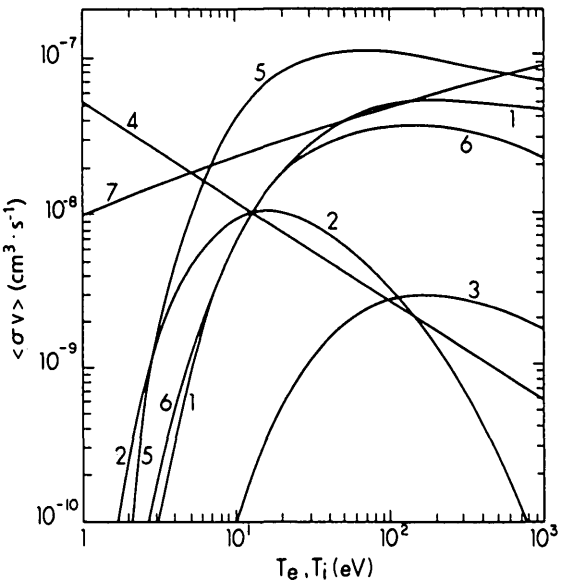

FIG. 33. Rate coefficients for volume processes involving atomic and molecular hydrogen [239]. The numbered reactions are: (1): $e + H_2 \rightarrow H_2^+ + 2e$, (2): $e + H_2 \rightarrow 2H^0 + e$, (3): $e + H_2 \rightarrow H^0 + H^+ + 2e$, (4): $e + H_2^+ \rightarrow 2H^0$, (5): $e + H_2^+ \rightarrow H^0 + H^+ + e$, (6): $e + H^0 \rightarrow H^+ + 2e$, and charge exchange (7): $H^0 + H^+ \rightarrow H^+ + H^0$.

estimate compares well with the results from sophisticated 3-D Monte Carlo neutral codes such as DEGAS [220] and NIMBUS [221] (Section 4), as can be seen from a NIMBUS example for JET (Fig. 32), giving the poloidal/toroidal average radial profiles of n_{D_2} and n_{D^0}. The atoms are largely created by Franck-Condon dissociation of the molecules, producing ~3 eV atoms, and thus, n_{D^0} is smaller than n_{D_2} by $\approx v_{D_2}/v_{D^0} \simeq 0.15$, which is also in reasonable agreement with code results, Fig. 32. For smaller, colder machines, e.g. DITE, with $T_w \simeq 0.03$ eV and $\lambda_n \simeq 0.01$ m, both Eq. (3.58) and the DEGAS code [222] predict higher (relative) edge neutral densities, $n_{D_2}/n_e(a) \sim 10^{-1}$.

Neutrals in the SOL can influence the plasma mass, momentum and energy balance. Consider mass balance. Ionization within the SOL is insignificant when

$$n_e n_D \overline{\sigma v}_i L_c \ll n_e c_s \qquad (3.59)$$

i.e. when

$$n_D \overline{\sigma v}_i L_c / c_s \ll 1 \qquad (3.60)$$

which, using Eqs (3.34) and (3.58), can be rewritten as the intuitively obvious criterion [198]

$$\lambda_n \ll \lambda_{iz}^D \qquad (3.61)$$

where $\lambda_{iz}^D \equiv v_D(n_e\overline{\sigma v}_i)^{-1}$ is the deuterium ionization length.

The reaction rates for the most important neutral processes are given in Fig. 33. As can be seen for $T_e \lesssim 20$ eV, Franck-Condon (F-C) breakup of D_2 into atoms is as important as molecular ionization, while, above 20 eV, direct ionization dominates. Thus, for a first estimate of λ_{iz}^D, one can use $v_D \simeq 2 \times 10^4$ m·s^{-1} (F-C D^0) for $T_{LCFS} < 20$ eV and $v_D \simeq 2 \times 10^3$ m·s^{-1} (thermal D_2) for $T_{LCFS} > 20$ eV. We take the JET example [70], with $n_{LCFS} = 3 \times 10^{18}$ m^{-3} and $T_{LCFS} = 100$ eV; then, $\lambda_{iz}^D \approx 0.024$ m, which, being comparable to $\lambda_n = 0.015$ m at the limiter, implies that ionization is not negligible in the JET SOL. Comparison with NIMBUS code results [23] shows that this simple approach somewhat overestimates the importance of SOL ionization: for this JET case, the code calculates that only 20% of the total ionization in the plasma occurs within the SOL. DEGAS code calculations for a smaller machine (DITE [223]) give: case (i) $n_{LCFS} = 6 \times 10^{18}$ m^{-3} and $T_{LFCS} = 13$ eV, with 86% of the total ionization occurring inside the LCFS; case (ii) $n_{LCFS} = 1.5 \times 10^{18}$ m^{-3} and $T_{LFCS} = 20$ eV, with 93% occurring inside the LCFS. A collection of code calculations are given in Table IV.

The SOL ionization criterion, Eq. (3.61), has been applied to edge data reported for a wide range of tokamaks [198] (Fig. 34) and shows that, generally, SOL ionization is not an important influence on particle balance for limiter tokamaks operated to date. However, projected cases for high power JET operation (also shown in Fig. 34) indicate significant SOL ionization. We therefore consider the properties of SOLs where ionization is an important particle source. The principal effect is to increase λ_n [195, 201, 217, 224] since a weaker radial density gradient is now required to bring in particles from the main plasma to supply the limiter sink. For the case of significant ionization in the SOL, it can be shown [224] that

$$\lambda_n \approx (2L_c D_{\perp 0} F_R / c_{so})^{1/2} \qquad (3.62)$$

where F_R is the recycle factor, i.e., for each ion pair entering an elemental volume of the SOL via cross-

TABLE IV. FRACTION OF IONIZATION OCCURRING WITHIN THE SOL OF LIMITER TOKAMAKS (multidimensional neutral codes)[a]

Tokamak	Refs	Code	$\bar{n}_e$ (10^{19} m^{-3})	n_{LCFS} (10^{18} m^{-3})	Ionization fraction in SOL
PLT (rail limiters)	Ruzic et al. [137]	DEGAS	5.5	5	31%
DITE (poloidal limiter)	Maddison et al. [222, 223]	DEGAS	2 2	5 2	14% 7%
JET (eight rail limiters)	Simonini et al. [23]	NIMBUS	1.4 1.6 2.1 2.1 2.6 3.25 1.79 2.6 3.05 3.63 3.95	1.2 1.7 2.2 2.2 3.0 4.1 2.8 4.0 5.5 7.5 10	21% 26% 30% 25% 25% 24% 28% 30% 31% 31% 36%
T-10	Pigarov and Vershkov [238]	TNG	2.6 (1.8)	4.5 (14.5)	43% 63%

[a] For Ohmic heating; the two values in brackets are for ECH.

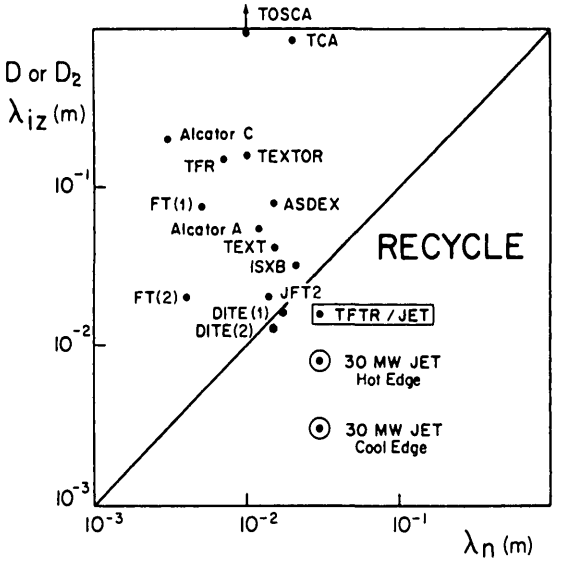

FIG. 34. Penetration distance of neutral deuterium molecules (case of $T_e(a) \geq 20$ eV) or atoms (case of $T_e(a) \leq 20$ eV) compared with the SOL thickness λ_n. When $\lambda_{iz}^D \leq \lambda_n$, ionization and recycle occur in the SOL [198].

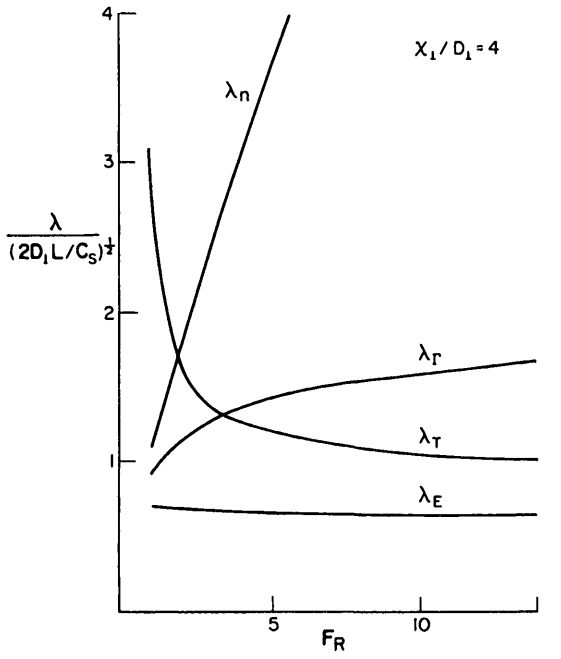

FIG. 35. Normalized values of the density, temperature, particle flux and heat flux e-folding lengths as a function of the recycle factor F_R for the case of $\chi_\perp/D_\perp = 4$ [224].

field diffusion, there are $(F_R - 1)$ SOL ionizations per volume; e.g., if 20% of the total ionization occurs within the SOL, then $\bar{F}_R = 1.25$. (Equation (3.62) is obtained by noting that the total source strength is $L_c D_\perp (n_0/\lambda_n)(1 + F_R - 1)$ while the sink strength is, as before, $0.5\, n_0 c_{so} \lambda_n$.) Equation (3.62) assumes that F_R is constant throughout the SOL, which is not generally realistic (see below). At the same time, λ_T decreases, since the energy removed by the limiter is now $\gamma_s F_R$ per ion pair leaving the main plasma. The variations of λ_n, λ_T, λ_Γ and λ_P are given in Fig. 35.

On the basis of this simple approximation, one would not expect significant changes to occur in the SOL widths unless $F_R \gg 2$, i.e. unless much more than 50% of the total ionization occurred in the SOL. In reality, however, F_R varies greatly with radius in the SOL and, even if $F_R = 2$, there are regions where locally $F_R \gg 2$ can occur, causing the SOL width to increase substantially, according to both code [225] and analytic [224] calculations.

Such SOL broadening would be most beneficial from the viewpoint of heat load concentrations at the limiter and would also improve impurity screening (Section 5). Present limiter design is not optimized to enhance SOL ionization since, precisely owing to heat concentration problems, limiters are generally shaped to be nearly tangential to $\vec{B}$. This geometry, in contrast to straight slab limiter geometry, projects recycling neutrals directly into the main plasma, reducing the probability of ionization within the SOL.

Consider next the influence of SOL neutrals on plasma momentum balance. In flowing towards the limiters, the plasma suffers frictional drag due to charge exchange [226, 227]. Since the sheath condition still requires that the drift velocity approach c_s, the result is that an extra pre-sheath potential drop, $e\Delta V_{cx}$, develops. This additional potential drop can be estimated:

$$e\Delta V_{cx} \approx m_i c_s \nu_{cx} L \tag{3.63}$$

or

$$\frac{e\Delta V_{cx}}{kT} = 2Ln_D{}^0\sigma_{cx} \tag{3.64}$$

The significance of this effect can be gauged by comparing the normalized drop $e\Delta V_{cx}/kT$ with the basic pre-sheath drop of ~ 0.5, Eq. (3.11). We take as an example the same JET (NIMBUS) case [23]: $Ln_D{}^0 = \int n_D{}^0 d\ell$ integrated along the LCFS gives $Ln_D{}^0 = 1.6 \times 10^{17}$ m^{-2} and thus $e\Delta V_{cx}/kT \simeq 0.1$. DEGAS calculations for DITE [222, 223] give: case (i) $Ln_D{}^0 = 3.7 \times 10^{17}$, $e\Delta V_{cx}/kT = 0.25$; case (ii) $Ln_D{}^0 = 7.4 \times 10^{16}$, $e\Delta V_{cx}/kT = 0.05$. Thus, it would appear that charge exchange friction may sometimes play a significant role in limiter tokamak SOLs. Such an extra pre-sheath potential drop,

concentrated near the limiter, would be beneficial since it would constitute an enhanced impediment to the escape of impurity ions released at the limiter, i.e. it would aid impurity screening of the central plasma (see Section 5).

Finally, turning to the influence of SOL neutrals on energy balance, consider first the charge exchange energy loss to the ions. The ratio of the charge exchange energy loss to the ion heat flow to the limiter is

$$ER_{cx} = \frac{\frac{3}{2}kT_i L n_{D^0} n_i \sigma_{cx} c_s}{2kT_i n_i c_s} = L n_{D^0} \sigma_{cx} \qquad (3.65)$$

The numerator of Eq. (3.65) represents the loss of energy by the ions to neutrals recycled from the walls and limiters, under the assumption that the neutrals are cold compared to the ions; since this is not necessarily true, Eq. (3.65) represents an upper limit to ion heat loss. The energy loss is integrated along the SOL, at the LCFS, over a unit cross-sectional area of the SOL. The denominator of Eq. (3.65) is an approximation to the ion heat loss per unit area at the sheath. Using the same values of Ln_{D^0} as above, we have for the JET example: $ER_{cx} = 0.05$; for the DITE examples: case (i) $ER_{cx} = 0.12$; case (ii) $ER_{cx} = 0.024$. It would thus appear that charge exchange energy loss may not be significant in the SOL.

Turning now to electron heat loss due to ionization: The energy loss due to excitation and ionization is ~ 50 eV per ionization at $T_e \simeq 10$ eV, and ~ 30 eV at $T_e \simeq 100$ eV [228]. Each new ion pair, however, carries $\gamma_s kT \sim 10$ kT of energy to the limiter. Thus, except for very low edge temperatures, SOL ionization cannot re-direct significant amounts of energy away from the limiter, no matter how large the recycle factor F_R. (A code analysis of a strongly recycling INTOR divertor SOL [229], for example, found $F_R \simeq 10^3$, but, since the temperature at the plate remained above 10 eV, the sheath was still calculated to remove most ($\sim 85\%$) of the SOL energy.) Ionization in the SOL can affect the electron energy balance if the SOL density is so high that the SOL temperature drops below ~ 10 eV. At 5 eV, for example, the energy loss per ionization event is ~ 100 eV [228] and thus, for $F_R \gg 1$, a substantial fraction ($\sim 2/3$) of the SOL energy would be converted into photon energy (wall loading) rather than appearing as limiter loading. The achievement of such a desirable regime, however, may not be attainable for limiter tokamaks.

In conclusion, it appears that neutrals have not played a major role in the mass, momentum or energy balance of most limiter SOLs to date. From the viewpoint of reducing sputtering, reducing limiter heat loading and increasing impurity screening, it would be very beneficial if the role of SOL neutrals could be enhanced. It may be that high power, high density operation of large tokamaks such as JET will allow this advantageous regime to be reached by using high edge densities.

3.6.2. *Effects of impurities in the SOL*

Impurities in the SOL can affect the mass, momentum and energy balance of the SOL plasma. However, because of the strong radiative power of impurities, the principal concern may be for their influence on energy balance. Unfortunately, there are virtually no direct measurements of the impurity density in the SOL, and bolometer (total radiation power) measurements are generally of inadequate spatial resolution to distinguish SOL radiation from that generated by plasma just inside the LCFS. An estimate of n_{imp}^{SOL} can be made by assuming diffusive cross-field impurity transport at a rate proportional to the impurity density gradient:

$$\Phi_{total}^{imp} \simeq A_p D_\perp^{imp} n_{imp}^{SOL} / \lambda_{imp} \qquad (3.66a)$$

where Φ_{total}^{imp} is the total impurity influx and λ_{imp} is the impurity density e-folding length in the SOL;

$$\Phi_{total}^{imp} \approx Y_{tot} \Phi_D \qquad (3.66b)$$

where Φ_D is the total hydrogenic flux striking the limiters and walls (other sources of impurities may also be important, Section 5), and Y_{tot} is the effective yield, including self-sputtering and other impurity sputtering (Section 5).

Assuming

$$\Phi_D = A_p D_\perp^D n_e(a) / \lambda_n \qquad (3.67)$$

the impurity fraction in the edge may be estimated as

$$\frac{n_{imp}(a)}{n_e(a)} \simeq Y_{tot} \frac{D_\perp^D}{D_\perp^{imp}} \frac{\lambda_{imp}}{\lambda_n} \qquad (3.68)$$

If we assume $D_\perp^D \simeq D_\perp^{imp}$, $\lambda_{imp} \simeq \lambda_n$, then $n_{imp}(a)/n_e(a) \simeq Y_{tot}$, which is typically 0.02–0.2 (Section 5). It is thus evident that the mass, momentum and Z_{eff} of the SOL can be appreciably influenced by the presence of impurities.

Consider also the energy balance: Electron cooling by impurity radiation will be significant when

$$n_{imp} n_e L_z(T_e) L_c \gtrsim \gamma_s^e kT\, n_e c_s \qquad (3.69)$$

where $L_z(T_e)$ is the radiative cooling rate, which attains a maximum value of $\sim 10^{-31}$ W·m^{-3} for light impurities (C and O) at low temperatures [230, 231]. Using this extreme value, the criterion [74, 198, 205] becomes

$$n_{imp}(a) L_c / T_e^{1.5}(a) \gtrsim 5 \times 10^{16}\ [m^{-2} \cdot eV^{-1.5}] \qquad (3.70)$$

Examples calculated from reported edge conditions [198] for a range of limiter tokamaks and assuming carbon impurity $n_{imp} = 0.1\ n_e$ are shown in Fig. 36, indicating that for high field/high density tokamaks, such as FT and ALCATOR, impurity radiative cooling of the SOL can be significant. Large (and therefore large L_c) tokamaks, particularly when operated at high density, may also access this attractive region where distributed heat loading of the walls replaces highly localized limiter loading. The effect of charge exchange between impurities and neutral hydrogen can also increase radiative cooling [232].

With regard to the influence of impurities on other aspects of the SOL, consider the example of $n_c = 0.1\ n_D$, a rather strong level of contamination, and assume that all the carbon ions are C^{4+} (see Section 5). In this case, the deuterium dilution in the SOL is not negligible, $n_D/n_e = 0.714$, and Z_{eff} is appreciable, $Z_{eff}^{SOL} = 3.28$. Assuming that the ions are sufficiently collisionally

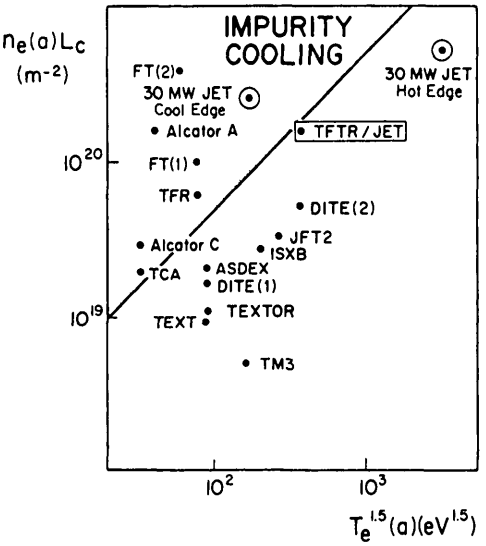

FIG. 36. Impurity radiation cooling of the SOL is significant when $n_e(a)L_c \gtrsim 5 \times 10^{17} T_e^{1.5}(a)$. The assumed SOL carbon/oxygen impurity density is 0.1 $n_e(a)$ [198].

coupled so as to have a common fluid velocity, it can be shown that the acoustic velocity c_s is given [233] by

$$c_s^2 = \left(kT_j \sum_j n_j + kT_e \sum_j Z_j n_j\right)\left(\sum_j m_j n_j\right)^{-1} \qquad (3.71)$$

where the sums are over all ion species. For $T_e = T_j$ and the foregoing example, one obtains $c_s = 0.88\ (kT/m_H)^{1/2}$, compared with a numerical value of unity for a pure D^+ plasma. Thus, the plasma momentum is not greatly altered. The C^{4+} *current* to solid surfaces, however, is 40% of the D^+ current, which has implications for the interpretation of Langmuir probes.

3.6.3. Parallel-field T_e gradients

Because of the great strength of the limiter heat sink for electrons, $\gamma_s^e \gtrsim 5$, and the considerable length of the SOL, there is the possibility of substantial T_e gradients developing along the SOL (even for compact plasmas, T_i^i drops along the flow direction because of acceleration, see Section 3.2). Such a development is generally very advantageous since it will lead to low plasma temperatures at the limiter surface and hence reduced sputtering. (It will be shown that the SOL conditions which lead to substantial T_e gradients also lead to equipartition, $T_e \simeq T_i$, so that the temperature of all species near the limiter would tend to be low.) In addition, assuming pressure constancy along $\vec{B}$, a low temperature at the limiter implies increased plasma density, thus facilitating the development of a high recycling regime; this results in increased volume energy losses at low temperature, leading to a further reduction in T and an increase in n, etc. Such a desirable state has been achieved in divertor tokamaks (Section 7), but, for some of the reasons given in Section 3.6.1, it is hard to achieve in the limiter configuration and has not been reported to date. The presence of parallel-field T_e gradients can also lead to complex, 2-D and 3-D, SOL phenomena such as Marfes (Section 6)

When the electron scattering mean free path is smaller than L_c, then parallel-field temperature gradients can occur in the SOL. Assuming uniformly distributed energy input into the SOL, one can show that the difference between T_m, the value of T_e midway between limiters, and T_{sh}, the value of T at the sheath, is given [37, 74, 171] by

$$T_m^{7/2}(r) - T_{sh}^{7/2}(t) = 7L_c P_e(r)/4\kappa_0 \qquad (3.72)$$

where $\kappa_0 T^{5/2}$ is the electron heat conduction coefficient, λ_P is the power scrape-off thickness and

$$P_e(r) = \tfrac{1}{2} n_0 c_{so} \gamma_s^e k T_{so} \exp\,[-(r - a)/\lambda_P] \quad (3.73)$$

Now the difference between $T_m(r)$ and $T_{sh}(r)$ will not be great, provided

$$T_m(r)^{7/2} \simeq 7 L_c P_e(r)/4\kappa_0 \quad (3.74a)$$

For example, if

$$T_m(r) > 1.1\ (7 L_c P_e(r)/4\kappa_0) \quad (3.74b)$$

then

$$1 \geq T_{sh}(r)/T_m(r) \geq 0.5 \quad (3.74c)$$

Thus, gradients may be neglected, provided

$$\frac{T_0^{7/2} \exp[-7(r - a)/2\lambda_T]}{(7L_c/4\kappa_0)\ \tfrac{1}{2} n_0 c_{so} \gamma_s^e k T_0 \exp[-(r - a)/\lambda_P]} \geq 1 \quad (3.74d)$$

For illustration, we assume

$$\lambda_P = [\lambda_n^{-1} + 1.5\lambda_T^{-1}]^{-1} \quad (3.75)$$

and $\lambda_n = \lambda_T$. Relation (3.74d) then becomes

$$\frac{8\kappa_0 T_0^{5/2} \exp[-(r - a)/\lambda_n]}{7 L_c n_0 c_{so} \gamma_s^e} \geq 1 \quad (3.76)$$

Thus, throughout the first e-folding thickness of the SOL, relation (3.76), for hydrogen, gives

$$Z_{eff}^{SOL} L_c n/T_e^2 \lesssim 10^{17} \quad (3.77)$$

where L_c is in m, n in m^{-3} and T_e in eV.

Results for SOL data published for a variety of limiter tokamaks [198] are given in Fig. 37. It can be seen that the high-field tokamaks are most susceptible to the formation of parallel-field T_e gradients, although the large tokamaks are also rather susceptible. For the results in Fig. 37, $Z_{eff}^{SOL} = 1$ is assumed and so, clearly, even at moderate contamination levels, most limiter tokamaks can develop T_e gradients. Generally, however, the gradients are not as strong as can be achieved in divertor tokamaks (Section 7.3), and the other requirements for achieving a high recycling regime are not readily achieved (Section 3.6.1). Thus the benefits of T_e gradients have not been major ones in limiter devices to date.

When T_e gradients are significant, kinetic effects can also become significant [234–237]. For example, the majority of the electrons may be collisional and for them it may be the case that $T_{sh} \ll T_m$. The high energy electrons in the distribution, however, may be collisionless, and such electrons reach the sheath still with the high energies associated with T_m. This can make the sheath potential drop primarily depend on T_m rather than on T_{sh}, thus increasing sputtering. Such 'epithermal' electron (also ion) effects require kinetic analysis with regard to calculating corrections to parallel heat flux, sheath drops, etc. [234–237].

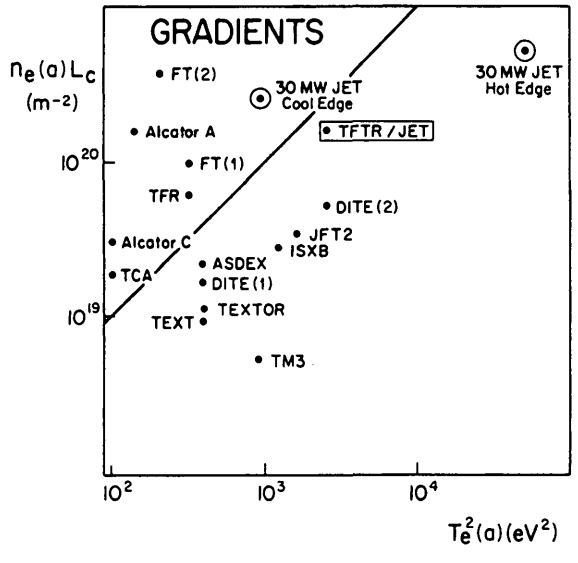

FIG. 37. The T_e gradients along $\vec{B}$ in the SOL are predicted to be substantial when $n_e(a)L_c \geq 10^{17}\ T_e^2(a)$. $Z_{eff}(a) = 1$ [198].

4. EDGE REFUELLING AND RECYCLING

This section deals with plasma particle behaviour, particle confinement time, plasma density profiles, and related topics. Section 4.1 discusses the generally substantial conceptual difference between particle confinement time and energy confinement time; also discussed is the recently identified strong influence of the density profile and the spatial ionization distribution on energy confinement for several high performance modes of tokamaks. Section 4.2 deals with measurements of the particle confinement time τ_p and its distinction from the plasma density decay time τ_p^*. Since hydrogen largely recycles as a molecule and also since it has a high charge exchange cross-section, the hydrogenic recycling behaviour is rather complex; the basic atomic/molecular processes are reviewed in Section 4.3. This complexity necessitates the use

of multi-dimensional neutral transport codes, which are described in Section 4.4. Direct neutral-wall interactions occur owing to the charge exchange process; implications are discussed in Section 4.5. A simple model can often describe the basic characteristics of particle balance; this is discussed in Section 4.6, including comparisons of the model with experimental measurements of τ_p on a number of tokamaks. Finally, Section 4.7 discusses the distribution of particles between the wall surfaces and the plasma volume, i.e. the issues of fuelling efficiency, wall pumping and tritium inventory.

4.1. Introduction

Generally, less attention has been paid to particle balance than to energy balance, to particle confinement time τ_p than to energy confinement time τ_E. Superficially, this would appear to be justified since net energy production is the objective of fusion research. Particle behaviour, however, strongly influences the overall properties — including the energy confinement properties — of the plasma, and thus the achievement of net energy production conditions may be as dependent on the understanding and control of particle flow as it is on the control of energy flow.

The (fuel) particle 'confinement time' τ_p is defined [214] by

$$\tau_p = N/\Phi \tag{4.1a}$$

where N is the total fuel particle content of the plasma and Φ is the total outflux of the fuel ions. τ_p is also sometimes called the 'average confinement time'; the preferred term for this quantity is 'replacement time'. It is important to note that confinement times — whether of particles, momentum or energy — are strongly dependent on the source location (the sink is assumed to be fixed at the edge). Since energy sources are usually near the centre of the plasma while particle (neutral ionization from recycle) sources are near the edge, τ_p and τ_E can be quite different, even if the cross-field transport coefficients $D_\perp$, $\chi_\perp$ are numerically the same.

This point is illustrated by the following simple example. Consider slab geometry and heat transport due to conduction only, with $\chi_\perp = D_\perp$ = constant, and $T_{LCFS} = n_{LCFS} = 0$. Let the power P_ℓ [W·m^{-2}] input per unit length toroidally occur at the plasma centre r = 0 while the neutral particle source influx Φ [m^{-2}·s^{-1}] is ionized at r = a — λ_{iz} (where λ_{iz} is the ionization depth into the plasma); for simplicity, we assume $\lambda_{iz} \ll a$. Then the plasma n(r) profile is flat inside $r = a - \lambda_{iz}$, dropping linearly to zero at r = a, while the T(r) profile is triangular:

$$n(r) = \begin{cases} n(0) = \lambda_{iz}\Phi/D_\perp & \text{for } r \le a - \lambda_{iz} \\ \dfrac{n(0)}{\lambda_{iz}}\, a \left(1 - \dfrac{r}{a}\right) & \text{for } a - \lambda_{iz} \ll r \ll a \end{cases} \tag{4.1b}$$

and

$$T(r) = \frac{aP_\ell}{n(0)\chi_\perp}\left(1 - \frac{r}{a}\right) \tag{4.1c}$$

Thus, the particle confinement time is

$$\tau_p = n(0)a/\Phi \approx a\lambda_{iz}/D_\perp \tag{4.1d}$$

while the energy confinement time is

$$\tau_E = 3n(0)\,(0.5\ kT(0))\ a/P_\ell \simeq \frac{3a^2}{2\chi_\perp} \tag{4.1e}$$

and the ratio $\tau_E/\tau_p \simeq a/\lambda_{iz} \gg 1$.

The term 'particle replacement time' is preferable for τ_p since a typical particle actually in the plasma, say at r = 0.5a, will require a time to escape from the plasma of about $a^2/D_\perp$, i.e., $\gg \tau_p$.

As discussed in the next section, typical τ_p values range from 10^{-3} s to 1 s and are always short compared to the discharge times. Thus, on average, fuel particles must be replaced many times during a discharge and the mechanism of *refuelling* is therefore critical.

The simplest refuelling situation — and a rather common one for graphite (although not for metals) — is when the edge structures (particularly the limiters and divertor plates) quickly attain an equilibrium where they return neutrals to the plasma at the same rate as they receive ions. Thus, external neutral sources, such as a gas inlet, can be turned off and a *recycling coefficient* of unity maintains a constant plasma density. This is the case of complete *edge refuelling*.

Edge refuelling tends to result in rather flat plasma radial profiles. On the other hand, achievement of fusion conditions in the core plasma can be facilitated by the creation of peaked n and T profiles [240]. *Core refuelling* is therefore of great importance. This can be achieved using fast pellets of frozen hydrogen or by

neutral beam injection (NBI). For steady state, strong *edge pumping*, i.e. an edge recycle coefficient of < 1, is required in order to maintain constant density.

Before proceeding to a detailed consideration of refuelling and recycling, we consider several examples of the influence of these processes on overall tokamak performance.

4.1.1. Influence of recycling on the H-mode

For divertor tokamaks subject to strong auxiliary heating (Section 7.3), two energy confinement times can exist at about the same operating conditions (L- and H-modes for 'low' and 'high' energy confinement, τ_{EL} and τ_{EH}), i.e., a bifurcation exists. The mechanism for achieving the H-mode is still not entirely understood, but there is considerable evidence that edge recycling can play a critical role. On PDX [241], for example, the H-mode was achieved when the divertor was configured to minimize the amount of fuel recycle which occurred within the main plasma chamber. Apparently, recycling at the edge of the main plasma cools it, thus compromising the H-mode which requires high temperatures at the edge of the main plasma [242], possibly for reasons related to magnetic shear stabilization [243].

4.1.2. TFTR supershots and edge recycling

A high performance mode has been achieved in a *limiter* tokamak, TFTR, by increasing wall pumping together with NBI core fuelling [244]. The toroidal graphite limiter is pre-conditioned by low density deuterium and helium discharges [245]. This reduces the recycling coefficient from 100% to $< 50\%$ for the discharge which follows and results in discharges characterized by highly peaked plasma density profiles and a high τ_E, about $2\tau_{EL}$. While the peaked profiles are in contrast to the flat H-mode profiles, there is a common element to obtain high τ_E, namely the need to suppress edge recycling.

4.1.3. Peaked profiles to achieve energy breakeven

Assuming an L-mode expression for the τ_E dependence on a, R, etc., it can be shown [240] that the central fusion parameter $\hat{n}\hat{T}\tau_E$ is given by

$$\hat{n}\hat{T}\tau_E = 3 \times 10^{18}\, f_n f_T f_g^2\, a^{1.26}\, R_m^{0.5}\, \epsilon^2\, B^2\, q^{-2} \qquad (4.2)$$

where $f_n \equiv \hat{n}/\bar{n}$ and $f_T \equiv \hat{T}/\bar{T}$ are the profile peaking factors, and $f_g \equiv \tau_E/\tau_{EL}$ allows for enhancement due, for example, to an H-mode. This indicates that for a given device configuration, improvements in fusion conditions can only be achieved by raising the f-values. With regard to f_n, this appears only to be achievable by a combination of core fuelling and strong wall pumping. In this context, it may be noted that for the record $n\tau$ value achieved in ALCATOR-C, pellet fuelling was required [246].

4.1.4. Fuel recycle and the density limit

Experimentally it is known that when $\bar{n}_e$ is increased, a limit can be reached that results in a 'density disruption' of the discharge [247, 248] (see Section 6). This density limit is generally thought to be due to edge energy loss associated with impurity radiation [249–251]. However, for very clean discharges, this limit is only a little higher, and it has been suggested that in this case the energy loss due to fuel re-ionization [252] at the edge may impose the density limit. Manipulation of the gas puffing toroidal distribution on JFT-2M [253] has been found to influence the density limit, although marginally. On T-10 [11, 254], at high values of $\bar{n}_e$ the power flow to the limiters abruptly drops — an effect which has been attributed [255] to strong localized recycling at the limiter; a similar observation has been made on DIII [256]. (These observations may, however, indicate detached plasmas or Marfes [257], see Section 6.)

4.1.5. Improved Ohmic confinement (IOC)

In Ohmic discharges a most advantageous $\tau_E \propto \bar{n}_e$ scaling exists [258, 259], but, unfortunately, this regime saturates [215] (saturated Ohmic confinement, SOC) at higher $\bar{n}_e$. On JFT-2M [253] it was shown that this degradation could be diminished by optimization of gas puff fuelling, keeping low peripheral gas pressures. A clear-cut IOC regime was reported from ASDEX [260] which was achieved by reducing the gas puff early in the discharge; the $\tau_E \propto \bar{n}_e$ dependence could be fully restored to $\bar{n}_e$ levels twice as high as the SOC limit. It is suggested [260] that the linkage between particle and energy confinement in such high performance modes (IOC, pellet injection, supershots) may be as follows: For some reason, high neutral density levels at the edge, such as occur for gas puff fuelling where the fuelling efficiency is low (see Section 4.6), change the plasma particle transport properties ($D_\perp$ and v_{in}, the inward drift velocity of the plasma). When neutral densities are kept low, plasma transport changes, making $v_{in}/D_\perp$ larger and thus

giving more peaked $n_e(r)$ profiles — as observed in IOC, pellet injection and supershot modes; these density profiles are thought to stabilize ion temperature gradient modes which may be the cause of high cross-field heat conductivity and low τ_E. An apparently related effect was reported on T-10 [261], where reduction of the gas inflow caused a transition to an enhanced impurity confinement regime.

4.2. Measurements of τ_p

The total particle content of the plasma, N, is generally obtained from microwave measurements of $n_e(r)$ in the main plasma. For a pure hydrogenic plasma, this also gives the ion content. For impure plasmas, appropriate corrections are made, generally on the basis of measured values of Z_{eff}. When external fuel sources such as a gas inlet are turned off, then N(t) is observed to decay with a characteristic time τ_p^*, i.e. as $\exp(-t/\tau_p^*)$. However, edge recycle fuelling continues and the confinement/replacement time τ_p is given [214] by

$$\tau_p = (1 - \bar{R})\tau_p^* \tag{4.3}$$

where $\bar{R}$, the global recycling coefficient, is defined by this equation (since τ_p and τ_p^* are experimentally measurable).

Experimentally, it is often observed that N(t) scarcely decays when external sources are turned off, $\tau_p^* > 10$ s not being uncommon, implying $\bar{R} \simeq 1$ [245, 262, 263]. In order to precisely establish the value of $\bar{R}$, and of τ_p , it is necessary to measure Φ as well as N (Eq. (4.1)). Typically, the method of measuring the neutral influx Φ_{in} is based on counting the H_α photons released in the plasma near the walls, limiters, etc., which are proportional to the neutral influx [126, 127, 214]. Typically, the ionic outflux is measured using Langmuir probes or other edge diagnostics which give $n_e^{SOL}(r)$, $T_e^{SOL}(r)$, λ_n, λ_T and thus, by calculation, the total ion flux out of the plasma [70, 264].

The H_α method of measuring Φ_{in} requires absolute calibration of the spectroscopic instrumentation together with calculations of the number of H_α photons produced per neutral entering the plasma [126, 265, 266]. The latter quantity is generally given in the inverse form, as the 'ionization events per photon' (Fig. 19, Section 2). This result only accounts for H_α photons produced by electron impact on neutral atoms. While some of the recycling hydrogen actually leaves the solid already as atoms (the backscattered fraction), many of the recycling particles are molecular.

Two types of correction are required for molecules [127]:

(a) Some molecules initially undergo dissociative ionization:

$$e + D_2 \rightarrow D_2^+ + 2e \rightarrow D^+ + D^0 + 2e \tag{4.4}$$

rather than dissociation:

$$e + D_2 \rightarrow 2D^0 + e \tag{4.5}$$

and so part of the influx never has an opportunity for H_α emission from (isolated) atoms.

(b) Both of these ionization and dissociation processes have a finite probability of creating H_α photons promptly at the time of molecular breakup. The H_α yield for each of the breakup pathways has been either measured or estimated [127, 266].

The Langmuir probe technique of obtaining Φ_{out} [186] uses

$$\Phi_{out} = \Gamma_\parallel(a)\lambda_\Gamma w \tag{4.6}$$

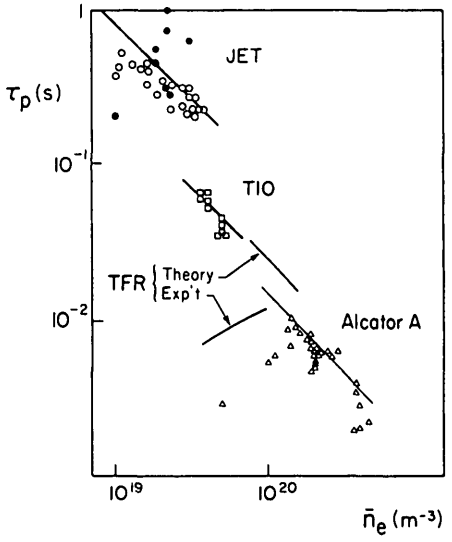

FIG. 38. Particle confinement time. The straight lines are for $\tau_p = 3 \times 10^{19}\, a/(D_\perp \bar{n}_e)$, where values of $D_\perp$ are obtained from measurements of λ_n. Experimental points: JET: o — H_α, • — edge probes; T-10: □ — edge probes; TFR: edge probes; ALCATOR-A: △ — H_α. For JET, T-10, ALCATOR-A: $\dot{\bar{n}} = 0$ during measurements; for TFR: $\dot{\bar{n}} \neq 0$ [198].

$$\Gamma_{\parallel}(a) = I_s^+/e \qquad (4.7)$$

i.e. the probe ion saturation current at the LCFS, λ_Γ is the e-folding length of I_s^+ and w is the total wetted length of the limiter.

In long pulse tokamaks such as JET, operating with graphite limiters, it is found that [70, 262] $\bar{R} \simeq 1$ and $\Phi_{in} \simeq \Phi_{out}$. Thus, values of τ_p measured on JET [198] by H_α or by Langmuir probes give agreement to within experimental errors — about a factor of two for each technique. Values of τ_p measured in several tokamaks [198] are given in Fig. 38. As can be seen, there is a tendency on some tokamaks for τ_p to decrease with increasing $\bar{n}_e$. However, there are numerous exceptions: the case of TFR (Fig. 38); in TEXTOR [13], $\tau_p \propto \bar{n}_e$; in TEXT [267], τ_p first increases with $\bar{n}_e$ and then decreases. Overall, it is difficult to identify a consistent pattern of the $\tau_p(\bar{n}_e)$ dependence (see, however, Section 4.6). For JET ohmically heated deuterium plasmas it is found [216] that

$$\tau_p\,[s] \simeq 2 \times 10^3\, R_m\,[cm]\,(a\,[cm])^2/(\bar{n}\,[cm^3])^{0.8} \qquad (4.8)$$

4.3. Atomic and molecular processes

The recycling processes for hydrogen are rather complex since both atomic and molecular states must be followed. These processes are briefly reviewed in the following. For a more extensive discussion, the reader is referred to the recent review by Harrison [268].

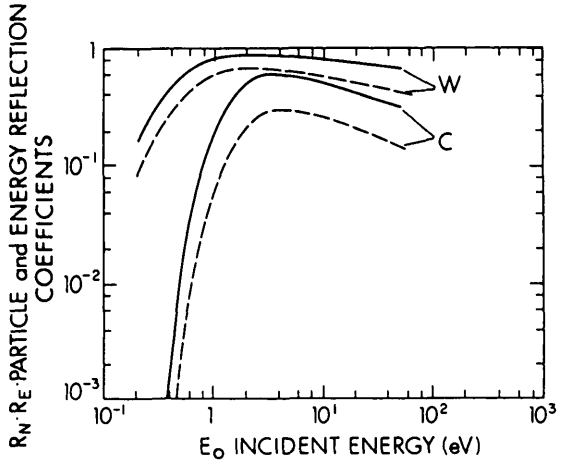

FIG. 39. Calculated particle and energy reflection coefficients, R_N (solid lines) and R_E (broken lines), versus the incident energy E_0 for bombardment of C and W at normal incidence and for a surface binding energy E_s = 1 eV [269, 270].

The probability that an impacting ion will be directly reflected from a surface is R_N (see Fig. 39), which is dependent on the impact energy E_0, the incident angle, and the mass of the substrate and the reflected particle. The backscattered particle is generally neutral and has, on average, an energy of $(R_E/R_N)E_0$. Figure 39, giving calculated results for low energy impact, is for illustration only. More extensive tabulations of R_N and R_E are given in Refs [269, 270]. For flat surfaces, R_N is a strongly increasing function of the angle of incidence α. Since limiter and divertor surfaces are, for heat dispersal reasons, often arranged to be at shallow angles to the magnetic field, shallow incident angles for the impacting ions are implied (even allowing for the tendency of the electrostatic sheath and of gyromotion to move the ions towards normal incidence [179]). It appears, however, that, in practice, angle of incidence effects are not very important since the working surfaces are highly roughened. Calculations using the TRIM reflection code, together with a realistic simulation of the surface roughness through the use of fractals, indicate [182] little dependence of R_N or R_E on α.

Those particles which are not directly backscattered are assumed to recombine on the surface, leading to their eventual release as a molecule. Upon entering the plasma, the molecule is subject to a variety of electron impact processes. The reaction rates for the most important processes are given in Ref. [271] and in Fig. 33 (Section 3). As can be seen, for low edge temperature tokamaks, the first step is molecular breakup into two Franck-Condon (F-C) atoms, while, at higher edge temperatures, direct ionization to form a molecular ion is the more likely first step, rapidly followed by breakup.

The two main paths for creation of F-C neutral atoms have different fragment energies [271] E_f:

$$e + H_2 \rightarrow e + H(1s) + H(1s), \quad E_f \simeq 3\ eV \qquad (4.9)$$

$$e + H_2 \rightarrow e + H(1s) + H^*(2s), \quad E_f \simeq 0.3\ eV \qquad (4.10)$$

with the first reaction being the more likely for low edge temperatures. The principal molecular ionization reaction

$$e + H_2 \rightarrow e + H_2^+ \qquad (4.11)$$

is followed by prompt breakup, either into $H^+ + H(1s)$ with $E_f \simeq 4.3$ eV or into $H^+ + H^*$ (n=2) with $E_f \simeq 1.5$ eV, with approximately equal probability.

Thus, hot edge tokamaks can be expected to have less extended or tighter ionization and H_α distributions around limiters than cold edge devices since direct ionization of (slow) molecules is more probable than formation of F-C atoms, and such molecular breakup into F-C atoms as occurs tends to produce slower atoms (Eq. (4.10)). The tokamaks with hot edges also happen to be the large devices, such as JET and TFTR, which have very large limiters with surfaces at shallow angles to $\vec{B}$. As a consequence of all of these factors, the H_α distributions on the limiters of these large tokamaks rather faithfully reproduce the footprints of the impinging ions — thus providing a diagnostic method for measuring the ion flux density scrape-off length λ_Γ [209, 272], from which $D_\perp$ can be derived [209]. This technique can generally not be used on smaller tokamaks with cooler edges and smaller limiters which are less tangential to $\vec{B}$; in such cases, the H_α clouds around the limiter are rather diffuse and no clear-cut correlation with the incident ion footprint is evident [103].

For modelling neutral particle behaviour in the plasma edge, it is necessary to know the backscatter or sticking probability for the F-C atoms with energies in the range 0.1–10 eV. This information is particularly important for assessment of the gas pumping capability of pumped limiters and divertors. Unfortunately, there are only few experimental data in this energy range [273]. However, a number of rather sophisticated theoretical treatments are available [274–277]. It is probably important that surface roughness [182] and contamination effects be allowed for. Experimental data are available in the energy range down to ~10 eV (see Refs [789, 790]).

4.4. Neutral transport codes

Because hydrogen can exist in both molecular and atomic form, and because atomic hydrogen has a large charge exchange cross-section, it is particularly challenging to model neutral hydrogen transport in a plasma. The incentives to do such calculations reliably are, however, substantial:

(a) The spatial distribution of the ionization source must be known with some precision in order to establish the plasma transport properties, $D_\perp$ and the convective ion drift velocity v_{in} . Since half or more of the electrons can be produced from impurities, one should also know this source.
(b) The prediction of the capability of divertors, pumped limiters and wall pumping to remove neutral hydrogen (for density control) requires detailed modelling of neutral transport.
(c) Charge exchange neutral losses to the walls can constitute a significant power loss for the plasma (as a whole, although not necessarily for the SOL, see Section 3.6.1), a major source of impurity generation by wall sputtering and a route for tritium loss.
(d) The absolute magnitude and the spatial distribution of H_α radiation as well as the H_α line shape constitute diagnostics of major importance in understanding the plasma. Interpretation of such measurements is dependent on detailed modelling of the neutrals.

Ideally, a neutral transport code should include (see Ref. [220]:

— All neutral-plasma interactions for hydrogen, for example those of Eqs (4.9–4.11), but including many others and especially charge exchange;
— All neutral-plasma interactions for impurity neutrals;
— Neutral-neutral and neutral-ion elastic collisions;
— Realistic wall reflection coefficients over the entire energy range of interest, 10^{-1} to 10^4 eV, and allowing for surface roughness and contamination;
— Wall sputtering by fast neutrals;
— Full geometry (at least 2-D).

To date, it appears that, while no neutral code completely satisfies this ideal, a number of Monte Carlo codes, using techniques from neutronics codes, have reached very advanced levels. DEGAS [220, 278] — the 3-D Princeton code developed by Heifetz — is perhaps the most sophisticated code and has been the most widely applied. In some versions the complex breakup pattern of CH_4 is also included [279, 280]. Many of the applications of DEGAS have focused on the pumping capability of divertors, pumped limiters, etc. [220]. The neutral codes can be used in a stand-alone mode, where the plasma density and temperature profiles are provided as code inputs. DEGAS has also been combined with 2-D plasma codes for fully self-consistent solutions. NIMBUS [221], a 3-D code developed for JET, has been employed in a stand-alone mode [23] and has also been incorporated in a plasma code. A number of other Monte Carlo models [281–289] and non-Monte Carlo models [290-301] have also been employed.

Although neutral codes executed on supercomputers have attained a high level of sophistication with regard to their ability to follow multiple, complex pathways,

the reliability of their results is limited by significant uncertainties in basic input assumptions. Some of these relate to the basic reactions within the plasma. Most of the uncertainty, however, relates to neutral-wall interactions where there are virtually no experimental data for very low energy impact (≤ 10 eV) [273]; the effects of surface roughness and of impurities are also difficult to assess. The implication of this situation is that neutral code results are probably the more reliable the less plasma-wall interactions are a factor. Thus, calculations of ionization sources, H_α patterns, etc., for conventional limiters are probably more reliable than pumping calculations for relatively closed geometries such as pumped limiters, where multiple wall interactions are important. Even regarding code interpretation of H_α patterns on limiters, the reliability of the sophisticated neutral code results is often undermined by a deficiency — sometimes even a total absence — of plasma measurements of n_e and T_e in the H_α emission zone. It thus appears that there is often a mismatch in the sophistication and power of the neutral codes and in the relative weakness of the basic data upon which their reliable use depends.

4.5. Charge exchange neutral fluxes

Neutral hydrogen atoms charge exchange with hydrogenic ions throughout the volume of the main plasma. The energy distribution of the charge exchange (cx) neutrals reaching the wall provides information on $T_i(r)$, and diagnostic techniques based on this effect are widely used in tokamaks [302-305]. The angular distribution of the neutrals impacting on the walls is also of importance, but little experimental information is available. Typically, cx neutral detectors do not have sensitivity in the low energy range (several hundred eV or less), where the distribution peaks. Cohen and co-workers on PLT [136, 137, 214, 306, 307] and Verbeek and co-workers on ASDEX [135, 308, 309] have developed low energy cx neutral detectors extending measurements down to ≈ 10 eV (Section 2.2.7). On PLT [137], the energy spectrum (Fig. 40a), the total outflux density and the average energy (Fig. 40b) are found to be dependent on $\bar{n}_e$. Since the detector measures the outflux at a particular poloidal/toroidal location, it is necessary to take poloidal/toroidal variations into account to reach global conclusions. This was achieved [137] by using the DEGAS code, with the absolute levels being set by the cx neutral measurements at the specific detector location (Figs 40a, 40b). In this way, a number of important quantities were deduced:

(a) The particle confinement time was obtained. τ_p decreased from 0.3 s at $\bar{n}_e = 0.18 \times 10^{19}$ m^{-3} to 0.1 s at 5.5×10^{19} m^{-3}, showing the same tendency to decrease with $\bar{n}_e$ as observed in some other tokamaks (Fig. 38).

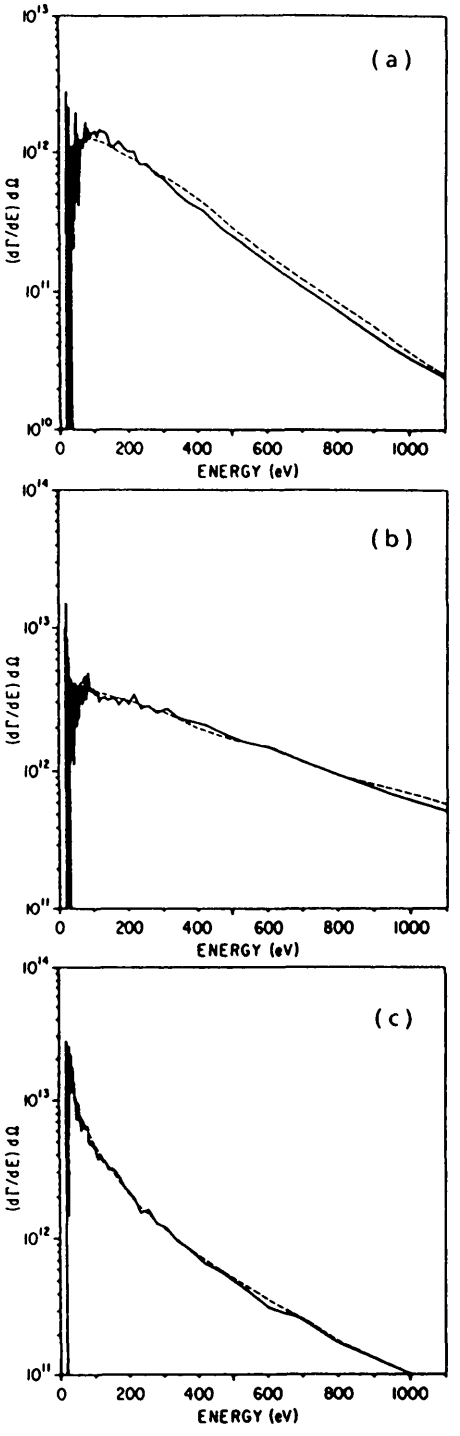

FIG. 40a. PLT: Measured (solid lines) and calculated (dashed lines) charge exchange spectra, $(d\Gamma/dE)d\Omega$, for the cases: (a) $\bar{n}_e = 1.8 \times 10^{18}$ m^{-3}, (b) 1.0×10^{19} m^{-3} and (c) 5.5×10^{19} m^{-3}. The spectra were measured by the LENS detector at the toroidal position of the active limiters [137].

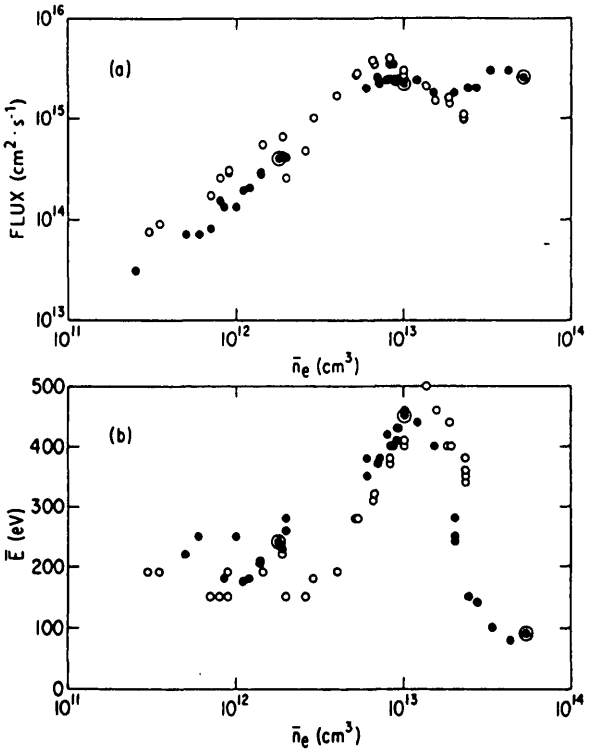

FIG. 40b. PLT: Total measured fluxes Γ (a) and average energies $\bar{E}$ of the detected neutrals (b) as functions of $\bar{n}_e$, for B_T = 1.6 T (open dots) and B_T = 3.2 T (closed dots) [137].

(b) Both the total ion flux to the limiters, Φ_L^+, and the total neutral flux to the walls, Φ_w^0, increased with $\bar{n}_e$: Φ_L^+ = 0.15, 1.5, 10 × 10^{20} s^{-1}, while Φ_w^0 = 0.18, 0.88, 1.8 × 10^{20} s^{-1} for the three values of $\bar{n}_e$ considered. The wall fluxes were thus seen to be of diminishing importance with regard to recycling as $\bar{n}_e$ increases. Taking the energy distributions into account, the wall fluxes were also found to be of relatively small importance for sputtering.

(c) The total ion fluxes to the wall, Φ_w^+, were small compared with either Φ_L^+ or Φ_w^0.

(d) The total neutral fluxes to the limiter, Φ_L^0, were small compared with the total ion fluxes, Φ_L^+, but, at high $\bar{n}_e$, Φ_L^0 was larger than Φ_w^0, indicating the strong localization of the cx processes.

(e) The power deposition on the walls and limiters due to cx neutrals was deduced to be negligible compared with the measured power deposition; for example, at the highest $\bar{n}_e$ the limiter cx neutral power was 800 W and the wall flux was 140 W·m^{-2}. The discrepancy in power balance observed on PLT, and also on many other tokamaks, could therefore not be accounted for by cx neutrals.

(f) Physical sputtering of the carbon limiters due to ions was 94–97%, with cx neutrals contributing the small residual. Sputtering of iron from the walls was entirely due to cx neutrals, with negligible ion sputtering.

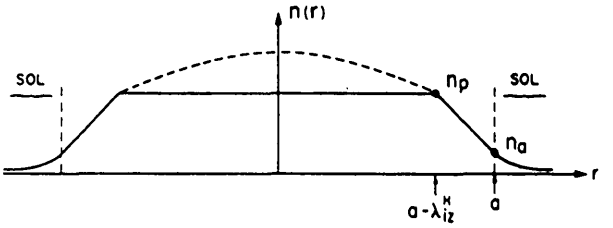

FIG. 41. Schematic of plasma density profile. Solid line: diffusion only; dotted line: pinch plus diffusion.

4.6. A simple model for particle balance

Engelhardt et al. [310, 311] have presented a simple but powerful 1-D model for recycling, refuelling and the resulting density profile. Neutrals launched inward from the boundary at r = a are assumed to penetrate a distance λ_{iz} before being ionized. The ions then diffuse outward with a flux density $-D_\perp dn_i/dr$, giving, in slab geometry, a linear density profile within [a – λ_{iz}, a]. Inside r = a – λ_{iz}, the plasma is replenished such that, in steady state, $n_i(r) = n_i(0)$ = constant there (see Fig. 41). We thus have the simple result:

$$n_i(0) = \Phi_{in}\lambda_{iz}/D_\perp A_p \qquad (4.12a)$$

where Φ_{in} is the total neutral influx and $A_p = 2\pi R_m 2\pi a$ is the plasma surface area. (This relation also assumes the hard boundary condition $n_i(a) = 0$.) If one assumes that the neutrals all have radial inward velocity v_0, then

$$\lambda_{iz} \approx v_0/0.5\, n_i(0)\overline{\sigma v_i} \qquad (4.12b)$$

where $\overline{\sigma v_i}$ is the average ionization rate coefficient in the radial region (a – λ_{iz}, a) and v_0 is the effective atom penetration velocity which ought to allow for both molecular and atomic ionization and for cx processes. Combining Eqs (4.12a) and (4.12b) gives the two simple and valuable results [198]:

$$\Phi_{in} = \overline{\sigma v_i}\, D_\perp A_p\, n_i^2(0)/2v_0 \qquad (4.13a)$$

and

$$\tau_p = a v_0 / D_\perp \overline{\sigma v_i}\, n_i(0) \qquad (4.13b)$$

where $\tau_p = \pi a^2 \, 2\pi R_m n_i(0)/\Phi_{in}$ is the particle confinement time. We thus have the prediction that the recycling flux (thus also, for example, the H_α light) varies as the square of the plasma density and τ_p varies inversely as n (assuming $D_\perp$, etc., constant). Such observations have in fact been reported, at least on large tokamaks such as TFTR [272] and JET [262].

The simple model has been extended in a number of ways:

(a) $n_i(r)$ is often observed to be peaked and, generally, a small anomalous, inward pinch velocity is implied, $v_{in} = -SD_\perp r/a^2$ being typical, with the plasma inward drift parameter (a shape factor) $S \simeq 2$. The pinch simply forces the $n_i(r)$ profile into a Gaussian shape imposed on top of the 'plateau' density given by Eq. (4.12a) (provided $\lambda_{iz} \ll a$), see Fig. 41. We obtain

$$n_i(r) = n_{pi} \exp[0.5S\,(1 - r^2/a^2)] \qquad (4.14a)$$

where

$$n_{pi} \equiv n_i(a - \lambda_{iz}) \qquad (4.14b)$$

is the 'plateau' density given by Eq. (4.12a). Thus,

$$\bar{n}_i/n_{pi} = f(S) \qquad (4.14c)$$

$$\bar{u}_i/n_{pi} \equiv 2(\exp(S/2) - 1)/S \qquad (4.14d)$$

and so Φ_{in}, Eq. (4.13a), is divided by f^2, while τ_p, Eq. (4.13b), is multiplied by f^2.

(b) The hard boundary condition (which assumes an infinitely strong sink strength in the SOL) can be relaxed [147, 311], i.e., $n_i(a) \neq 0$. By equating the perpendicular flow across the field with the parallel flow in the SOL, the value of $n_e(a)$ can be obtained. Then the ion outflux density becomes

$$\Gamma^i_\perp = D_\perp (n_{pi} - n_i(a))/\lambda_{iz} \qquad (4.14e)$$

$$= D_\perp n_i(a)/\lambda_n \qquad (4.14f)$$

Thus, assuming $n_i(a) \ll n_{pi}$, one has the useful result (see Ref. [198]):

$$n_i(a) \simeq (\lambda_n/\lambda_{iz}) n_{pi} = \frac{\lambda_n \, \overline{\sigma v_i} \, \bar{n}_i^2}{2 f^2 v_0} \qquad (4.15a)$$

i.e. we now have the edge density predicted to vary as $\bar{n}^2$. Such behaviour has also been observed on JET [12] and on some smaller tokamaks such as T-10 [11]. A number of other refinements of the simple model have been made [147], including relaxation of the assumption of a delta function ionization source [311]. The same result has also been developed independently and in a somewhat different form by Alexander et al. [21].

The most extensive testing of this simple model to date appears to be the one recently reported for JET [12]. Figure 3 (Section 2) shows a collection of measured JET $n_e(a)$ values (from Langmuir probes) as a function of line averaged density $\bar{n}_e$ and plasma current I_p. The results are taken for Ohmic deuterium plasmas with discrete limiters on the outside midplane, approximating a quasi-toroidal limiter; further experimental details are given in Ref. [12]. The dash-dotted line in Fig. 3 is for the model of Eq. (4.15a), with $\overline{\sigma v_i} = 3 \times 10^{-14}$ m^3·s^{-1}, $v_0 = 3 \times 10^4$ m·s^{-1}, $\lambda_n = 3$ cm and $S = 2$. The edge temperatures in JET [12] are higher than in most tokamaks (T_{LCFS} = 25–250 eV) and so ionization tends to occur at nearly the maximum value of $\overline{\sigma v_i}$, i.e. $\simeq 3 \times 10^{-14}$ m^3·s^{-1}. The measured JET scrape-off lengths [46] vary somewhat with I_p, although they vary little with $\bar{n}$: (I_p [MA], $\bar{\lambda}_n$ [mm]) = (2, 40), (3, 30), (4, 24), (5, 20), where $\bar{\lambda}_n$ are the poloidally averaged values. Because of the non-circular JET poloidal cross-section, the magnetic field line compression at the outside midplane reduces λ_n there to about half $\bar{\lambda}_n$. A key element in the model is the establishment of a value for the effective neutral penetration velocity v_0. Since the effects of molecular dissociation, molecular ionization, atomic ionization, charge exchange, etc., must be included in establishing v_0, the use of a full neutral code (Section 4.4) is needed. The value of $v_0 = 3 \times 10^4$ m·s^{-1} is a first estimate; it was proposed originally [198] on the basis of simple estimates obtained by assessing DEGAS Monte Carlo neutral code modelling results for DITE [222]. A value of $v_0 \simeq 4.4 \times 10^4$ m·s^{-1} (20 eV) has been estimated employing a 1-D Monte Carlo neutral code for T-10 [312], and a value of 2×10^4 m·s^{-1} has been measured spectroscopically (Doppler shift) for TEXTOR [103] (although the cx particles were not included).

In the analytic formulation of Alexander et al. [21] the simplifying assumption is made that in hydrogen recycling the most probable interaction of neutral atoms with the plasma is charge exchange. Molecular

ionization, etc., is neglected. The inward motion of neutral atoms is treated as a diffusion process, and at the first cx event the neutral acquires the temperature of the plasma ions. Alexander et al. define the neutral penetration length λ_{pen} (not to be confused with λ_{iz}):

$$\lambda_{pen} = (\Sigma n)^{-1} \tag{4.15b}$$

where Σ is an average cross-section given by

$$\Sigma = (\overline{\sigma v_i}(\overline{\sigma v_i} + \overline{\sigma v_{cx}}))^{1/2}/(kT/M)^{1/2} \tag{4.15c}$$

an expression similar to that employed by Podesta and Engelmann [313], Tendler and Agren [314], Lehnert [315, 316] and Harrison et al. [229]. Alexander et al. point out that Σ only varies by a factor of ~ 3 for 10 eV $\leq T \leq$ 1000 eV, and so they take $\Sigma = 3 \times 10^{-19}$ m^2, constant for hydrogen. Using Eq. (4.15a) with 0.5 λ_{pen} in place of λ_{iz} then gives

$$n_i(a) = 0.5\ \Sigma\ \lambda_n n_i^2 \tag{4.15d}$$

where n_i is the central plasma ion density. Not only is the quadratic relation the same as that of Eq. (4.15a), but also the numerical factors are fairly close: in Eq. (4.15d) the factor is 1.5×10^{-19}, while in Eq. (4.15a) it is 5×10^{-19} (for S = 0, i.e. no pinch, so that $n_{pi} = n \simeq \bar{n}$; for the more typical S = 1 case, the correspondence to the factor in Eq. (4.15a) [198] is even closer, becoming 1.7×10^{-19}).

One of the principal tasks of edge modelling is to relate edge conditions and central ones, and the results shown in Fig. 3 (Section 2) make an encouraging contribution to this. At least for these JET conditions there does appear to be a simple and readily understandable link between edge density and central density. A number of questions and problems, however, are evident; for example:

- As indicated, establishing a correct value of v_0 is of central importance. Presumably, the effective penetration velocity of the neutrals is dependent on $\bar{n}_e$ and I_p.
- Not all tokamaks obey simple relations such as in Eq. (4.15a) and the question is why this is so. Clearly, if ionization were actually quasi-uniform throughout the plasma — as might occur for small devices — then a model which assumes localized ionization would not be expected to apply very well.

A number of further problems also have to be addressed: (a) Frequently, impurities contribute about half the main plasma electrons (e.g. at $Z_{eff} \simeq 3.3$ for carbon) and thus the central $n_i^D \simeq 1/2\ n_e$ (the SOL dilution should be less, assuming lower charge states of the impurities). (b) Variation of S and λ_n with I_p should be allowed for. (c) The plasma may be non-circular, as in JET and DIII-D. (d) If a significant fraction of the total ionization occurs within the SOL, then the simple model fails in several respects.

In order to deal in a reliable way with these questions — and particularly to put v_0 and λ_{iz} on a properly quantitative basis — a full neutral code such as DEGAS and NIMBUS must be employed. Results [23] obtained using NIMBUS and the JET geometry as well as measured plasma conditions are summarized in the following.

For a spatially distributed source of ionization, the effective ionization depth is defined to be that depth where, if all the ionization occurred there, the central density would be the same as for the distributed source. Consideration of Eq. (4.12a) then shows that in slab geometry the effective λ_{iz} is

$$\lambda_{iz} = \sum_j \left(\frac{\delta\Phi_j}{\Phi_{in}}\right) \lambda_{iz}^j \tag{4.16}$$

where λ_{iz}^j is the ionization depth of a poloidal ring volume j wherein the total (molecules, backscattered atoms, F-C atoms, cx atoms) ionization fraction is $(\delta\Phi_j/\Phi_{in})$. A number of Ohmic JET discharges were analysed to give values of λ_{iz} (Fig. 42). A reasonable fit is provided by $\lambda_{iz} = 0.11\ (\bar{n}_e)^{-0.7}$ for λ_{iz} in m and $\bar{n}_e$ in 10^{19} m^{-3}. From Eq. (4.15a)

$$n(a) = n_{pi}\bar{\lambda}_n/2\lambda_{iz} = 4.6\ \bar{n}_e^{1.7}\bar{\lambda}_n/f \tag{4.17}$$

in convenient units (n [10^{19} m^{-3}], $\bar{\lambda}_n$ [m]); the factor 2 is due to impurity dilution, assumed to be a constant 1/2 for all conditions. Using f $\simeq$ 1, Eq. (4.17) gives good agreement with the data in Fig. 3 (Section 2). Even the tendency on JET for n(a) to increase somewhat less steeply than the square of $\bar{n}_e$ for fixed I_p is reproduced. It may also be noted that results from T-10 [21] indicated $n(a) \propto \bar{n}^{1.8}$.

The values of $D_\perp$ and S for each discharge were obtained using the measured $n_e(r)$ profiles and the local ionization source calculated with NIMBUS, together with the continuity equation. The values of $D_\perp$ are shown in Fig. 43 and compared with measurements made in JET using measurements of λ_{SOL} [209]. These

values are also quite close to the INTOR-ALCATOR scaling $D_\perp \simeq 10^{19}/\bar{n}_e$ (although based on $\bar{n}_e$ rather than on local $n_e(r)$). They are also very close to the values found in JET on the basis of localized $D_\perp$ measurements [317] for discharges where auxiliary heating caused n_e to change temporally. The present $D_\perp$ values are compared in Fig. 44 with values obtained from temporal variation experiments on JET [317]; since, operationally, $\bar{n}_e$ and I_p are coupled, the present $D_\perp$ results appear to scale either with $\bar{n}_e$ (Fig. 43) or with I_p (Fig. 44). Inserting the specific values of f, averaged for each I_p, into Eq. (4.17) gives the dashed lines in Fig. 3, in good agreement with the experimental results.

Significant contributions of λ_{iz}^{j} to λ_{iz}, Eq. (4.16), come from deep zones. Let $\lambda_{½}$ be the depth for which half of the contributions to λ_{iz} are deeper than the other half. Then it is found [23] that $\lambda_{½} \simeq 046/\bar{n}_e$ [m]. If we define 'edge refuelling' to imply $\lambda_{½}/a \leq 0.1$, say, then this criterion, $\bar{n}_e a \gtrsim 5 \times 10^{19}$ m^{-2}, can only be satisfied in the very large tokamaks and the high field tokamaks. Within the framework of expressions (4.15b, c), Alexander et al. [21] also consider the issue of 'tokamak transparency' and quantitatively

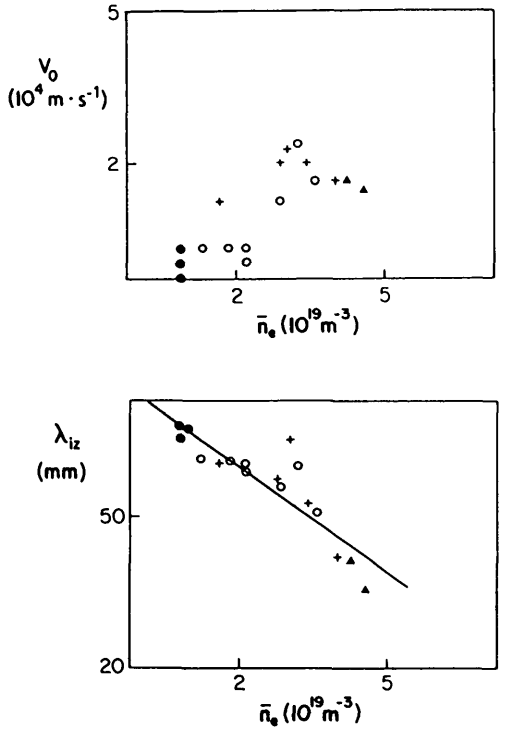

FIG. 42. Calculated values of v_0 and λ_{iz} for JET, using the NIMBUS neutral code. Solid lines: $\lambda_{iz} = 10.8\,(\bar{n}_e)^{-0.7}$, $v_0 = 0.75 \times 10^4\,(\bar{n}_e)^{0.8}$ [23].

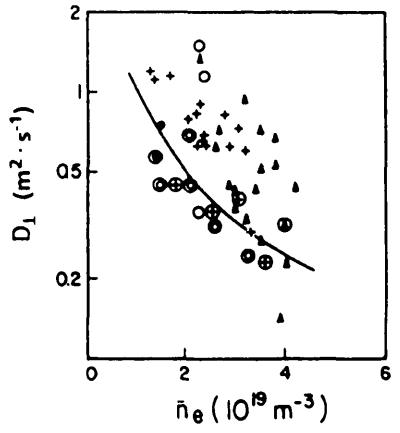

FIG. 43. Values of $D_\perp$ calculated by the method based on a calculated ionization source [23] (circled points) compared with values obtained from Langmuir probe measurements of λ_n on JET [209]. Solid line: INTOR-ALCATOR scaling; $D_\perp = 10^{19}/\bar{n}_e$ (but based on average n_e, not local n_e).

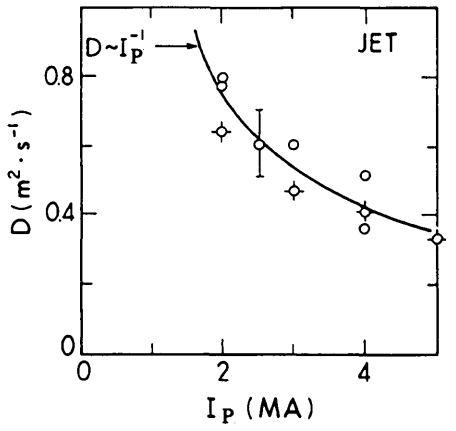

FIG. 44. Average diffusion coefficient $D_\perp$ ($r/a \geq 0.5$) versus plasma current I_p. Results of perturbation studies (○), Ref. [317]; static profile analysis ⊕ [23].

assess the transition from a quadratic n(a)-$\bar{n}$ dependence to a linear one.

Finally, turning to the effective penetration velocity v_0, which in this approach must now be *defined* by $v_0 = \bar{n}_e \overline{\sigma v}_i \lambda_{iz}/(2f)$, values from the NIMBUS calculation are given in Fig. 42. The best correlation, for this limited data set, is again with $\bar{n}_e$. The average value of $\bar{v}_0 = 1.55 \times 10^4$ m$^2\cdot$s^{-1} (2.5 eV) is almost precisely half the value estimated in the earlier work by Stangeby [198], which, when the impurity effect is accounted for (as is done here, but was not done in Ref. [198]), gives the same result as before. This explains the good fit of the dash-dotted line (simple model) in Fig. 3 with experiment.

The following conclusions may be drawn:

(1) The relation between edge and central density conditions appears to be quantitively explained — at least for large, long-pulse tokamaks such as JET, operated in the simplest mode (Ohmic heating, no limiters, no pellets, etc.), Eq. (4.17).

(2) While a tendency for $\tau_p \propto \bar{n}_e^{-1}$ and for $n_{LCFS} \propto \Phi \propto H_\alpha \propto \bar{n}_e^2$ exists (Eqs (4.13a), (4.15a)), these dependences on $\bar{n}_e$ can easily be obscured since, generally, $D_\perp$, v_0, v_{in}, λ_n and λ_{iz} also have $\bar{n}_e$ dependences. Thus, when these simple $\bar{n}_e$ relations for τ_p, n_{LCFS}, etc., are observed, as on JET [12], TFTR [272] and JT-60 [318], they are to some degree a coincidence. There is no a priori reason to anticipate any particular dependence on $\bar{n}_e$, and the details have to be worked out in each case using a neutral code to find v_0, etc.

(3) It is essential to establish the ionization source distribution for each case. Without this information, it is not possible to arrive at useful conclusions about particle behaviour, τ_p, $D_\perp$, v_{in}, etc., or to make meaningful comparisons of $\tau_p(\bar{n}_e)$, etc., between different tokamaks.

(4) Since impurities sometimes contribute half or more of the electrons, this source must also be modelled or measured with some precision.

(5) With regard to medium/small sized tokamaks, $\bar{n}_e a \lesssim 5 \times 10^{19}$ m^{-2}, an extra complication is encountered so far as the applicability of simple formulas such as Eqs (4.13a) and (4.15a) is concerned. The effective ionization is then so deep that there is no longer a meaningful distinction between 'edge' and 'core' plasmas as far as refuelling is concerned. In this case, one would not necessarily expect to see even a tendency to the simple trends, $\tau_p \propto \bar{n}_e^{-1}$ or $n_{LCFS} \propto \bar{n}_e^2$.

(6) It appears that $D_\perp$ does not vary greatly across the plasma from the centre to the SOL (e.g. JET [23], TEXT [319, 320] and ASDEX [321, 322]). In some tokamaks, however, $D_\perp$ varies significantly, e.g. in TFTR [323], where $D_\perp(0) \simeq 0.1$ m$^2 \cdot$s^{-1} and $D_\perp(a) \simeq 2$ m$^2 \cdot$s^{-1} for Ohmic conditions, and in FT-1 [324], where $D_\perp$ increases from $\simeq 0.1$ m$^2 \cdot$s^{-1} at the centre to $\simeq 1$ m$^2 \cdot$s^{-1} at the edge (Ohmic heating, $\bar{n}_e \simeq 2.3 \times 10^{19}$ m^{-3}). There is also some evidence that $D_\perp$ varies inversely as the *average* density, rather than as the *local* density [23, 319, 322, 325].

(7) This area of recycle ionization remains in an early state of development and firm conclusions would seem to be premature. It is necessary to make more detailed assessments of various tokamaks operating under a wider variety of conditions, employing full neutral transport codes to establish the spatial ionization distribution and properly accounting for impurity effects.

Notwithstanding these caveats, we may attempt to correlate and approximately explain quantitatively the $\tau_p(\bar{n}_e)$ relations reported for various tokamaks. Wootton et al. [326] pointed out that the $\tau_p(\bar{n}_e)$ results from JET, ALCATOR-A, JT-60 and TEXT can be superimposed, using certain arbitrary normalizations for τ_p and $\bar{n}_e$ (Fig. 45). The empirically found normalizations τ_p' and $\bar{n}_e'$ are given in Table V. It may be noted from

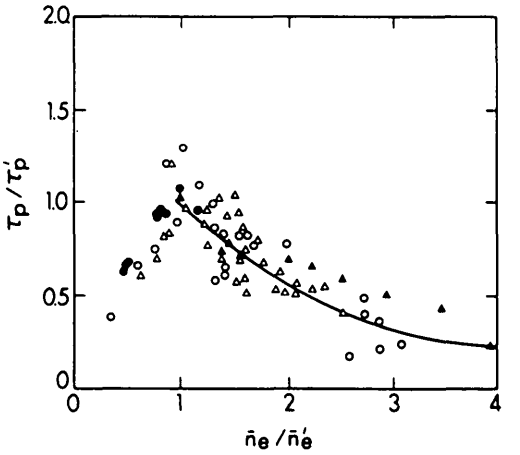

FIG. 45. Dependence of the global particle confinement time τ_p on the density $\bar{n}_e$ for four ohmically heated tokamaks [326]. Both τ_p and $\bar{n}_e$ are normalized to the values at which τ_p is a maximum. Relevant normalization parameters for each machine are given in Table V.

TABLE V. DEPENDENCE OF PARTICLE CONFINEMENT TIME ON PLASMA DENSITY[a]

	JET	ALC	JT-60	TEXT
Machine parameters				
a [m]	1.2	0.10	0.8	0.27
$D_\perp$ [m$^2 \cdot$s^{-1}]	0.5	0.2	(1)	2.6
Empirically found normalizations [326]				
τ_p' [ms]	950	7.8	140	7.3
$\bar{n}_e'$ [10^{19} m^{-3}]	1.1	14	1.0	3.9
Model results of Section 4.6				
τ_p' [ms]	1000	15	(220)	8
$\bar{n}_e'$ [10^{19} m^{-3}]	0.8	10	1.2	3.7

[a] Observed by Wootton et al. [326] and related to the simple model of Section 4.6.

Fig. 45 that for small $\bar{n}_e/\bar{n}_e'$, τ_p/τ_p' tends to increase to a maximum and then drops. On the basis of the JET analysis, we may quantitatively explain the change of regime which occurs at $\bar{n}_e/\bar{n}_e' = 1$; edge fuelling requires $\lambda_{n_e} \ll a$, and thus a transition from distributed fuelling to edge fuelling could be considered to occur when $\lambda_{n_e} = 0.5a$, say. Taking $\lambda_{n_e} = 0.46\ \bar{n}_e^{-1}$ then gives $\bar{n}_e'\ [10^{19}\ m^{-3}] \approx a^{-1}\ [m^{-1}]$, which values agree well with the empirical values of $\bar{n}_e'$ found by Wootton et al. [326], Table V. We assume a typical value of $S = 2$, thus giving $\tau_p = 3 \times 10^{18}\ a/\bar{n}_e D_\perp$ for the high $\bar{n}_e$ branch. Defining $\tau_p' \equiv 0.3\ a^2/D_\perp$ then gives the prediction

$$\tau_p/\tau_p' = (\bar{n}_e/\bar{n}_e')^{-1} \qquad (4.18)$$

for the upper branch, which agrees well with the results, Fig. 45. The values of $\tau_p' = 0.3\ a^2/D_\perp$ are also in fair agreement with the empirically established ones (Table V). The $D_\perp$ values were calculated in Ref. [198] on the basis of λ_n measurements in the SOL. For JT-60, no λ_n values are available and the value of $D_\perp = 1\ m^2 \cdot s^{-1}$ is an estimate. The good quantitative agreement between this simple model and measurements of $\tau_p(\bar{n}_e)$ must be, in large part, fortuitous considering that, undoubtedly, $D_\perp$, S, Z_{eff}, etc. vary with $\bar{n}_e$ and the relation $\lambda_{n_e}(\bar{n}_e)$ must depend somewhat on the limiter shape. Nevertheless, it appears that the $\tau_p(\bar{n}_e)$ behaviour observed on a wide range of tokamaks can be at least approximately explained quantitatively.

4.7. Fuelling efficiency, wall pumping, inventory

Up to this point, it has been assumed that a steady state exists, with $\Phi_{in} = \Phi_{out}$, for the walls and limiters. Such conditions can exist during the flat-top ($\bar{n}_e$, I_p) part of discharges with a global recycling coefficient of about unity [262] (carbon limiters). During start-up and ramp-down of the discharge, however, $\Phi_{in} \neq \Phi_{out}$, generally [262]. In addition, it can be very advantageous (for high τ_E modes, Section 7.2) to suppress wall recycling during the flat-top by net wall pumping. We are therefore interested in the ability of wall materials to pump and retain hydrogen. This is also a matter of importance as regards tritium inventory.

An earlier generation of tokamaks employed metal walls and limiters. The hydrogen retention/release properties of metals appear to be reasonably well understood [1] and will not be further considered here. During the 1980s, many tokamaks [263] employed carbon extensively for limiters, divertor plates and walls;

TABLE VI. AMOUNT OF CARBON ON TOKAMAK WALLS [263]

Tokamak	Material of limiter/divertor plate	Wall material	Proportion of C on walls
JET (1987)	carbon	Inconel	55% to ≈100% after carbonization (including self-carbonization)
TFTR (1987)	carbon	Inconel	10% C + 10% TiC
TEXTOR (1987)	carbon	Inconel	100% after carbonization
DIII-D (1988)	carbon	Inconel	50%
JT-60 (1987)	carbon	Inconel/TiC	40%

TFTR and JET, for example, each contained more than two tonnes of graphite, and the majority of the plasma exposed surface area was covered by carbon. Table VI indicates the carbon coverage in a number of devices [263]. The hydrogen retention properties of carbon are quite complex and are still imperfectly understood [216, 263].

When large areas in TFTR and JET ($\gtrsim 20\ m^2$) were covered with carbon tiles, a most valuable effect was discovered: the graphite can permanently and strongly pump the hydrogenic plasma. Pumping rates of order $100\ torr \cdot L \cdot s^{-1}$ have been measured in TFTR, with saturable capacities of order 100 torr·L [327]. Considering the importance of edge pumping for density control in the presence of auxiliary heating and pellet injection, and the cost and complexity of pumping with divertors and pumped limiters, such pumping is most valuable. In both tokamaks the rather small outboard limiters ($\lesssim 1\ m^2$ wetted area) generally have near-unity recycle. The inner walls ($\sim 20\ m^2$ area), however, can be operated for a few seconds at a pumping rate of about $100\ torr \cdot L \cdot s^{-1}$ in Ohmic discharges. In TFTR [245] the inner wall normally runs in a saturated mode, with $\bar{R} \simeq 1$ and $\tau_p^* \gtrsim 10$ s (Fig. 46). $\bar{R}$ can be lowered to ~ 0.3 by conditioning the graphite by a series of helium discharges (Fig. 46). (Subsequent fiducial discharges in deuterium then achieved supershot conditions of record high values of T_i, and $n_e T_i \tau_E \gtrsim 3 \times 10^{20}\ m^{-3} \cdot keV \cdot s$,

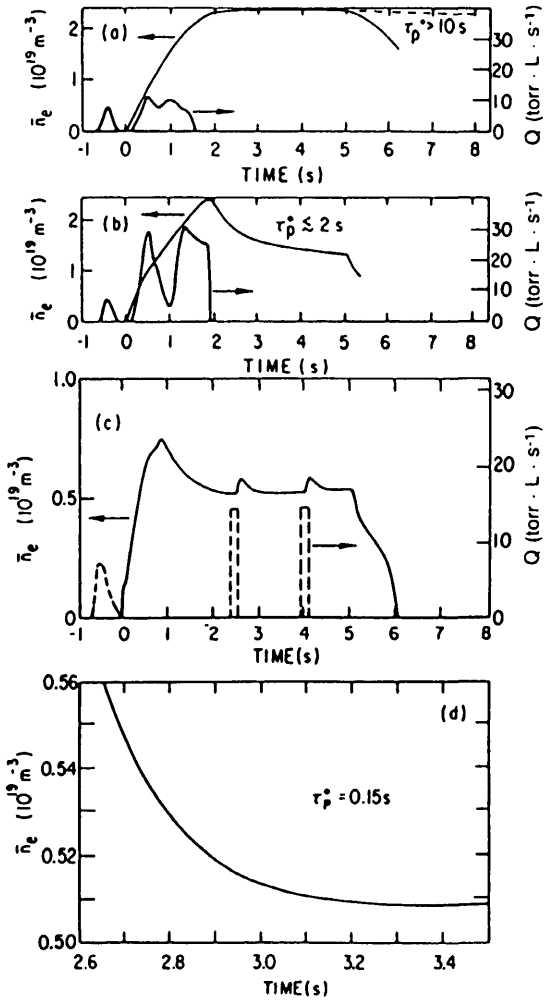

FIG. 46. TFTR: Plasma density and gas input behaviour for three operational cases [327].
(a) Standard conditions on the movable limiter or the bumper limiter when recycling is close to one and the density decay constant τ_p^* is > 10 s.
(b) 1.4 MA discharge on the bumper limiter (R_m/a = 2.45 m/0.80 m) after the initial conditioning with ten low density helium discharges.
(c) 0.8 MA discharge on the bumper limiter after extensive conditioning.
(d) Lowest observed value of τ_p^* (0.15 s) for the 0.8 MA discharge.

Section 4.1.) In JET [216, 263] the pumping power of the inner wall becomes available simply by first operating the plasma on the outer, small area limiters and then abruptly moving it to the inner wall (Fig. 47). The inner wall pumping is greater still after helium conditioning.

The TFTR wall pumping has been quantitatively explained [327] by the simple process of depletion of the saturable layer. Under hydrogenic ion bombardment, carbon saturates at a level of about 0.4 H/C, down to the depth of ionic penetration [328, 329] (on a longer time-scale, migration to greater depths also occurs — see later). Assuming a D^+ impact energy of 200 eV, an implantation depth of ~10 nm is calculated, giving a saturation level of about 100 torr·L for 20 m^2. The helium conditioning discharges are highly contaminated with carbon ($Z_{eff} \simeq 6$) and so most of the deuterium removal is apparently by carbon ion impact desorption (this would also explain why low density *hydrogen* conditioning discharges can also be used to deplete the hydrogen in the tiles).

Wall pumping in JET does not appear to be explicable by the same *saturable* mechanism as that for helium conditioning since the wall is not saturable. A number of hypotheses [216, 263] have been advanced to explain the JET case, and the matter remains in an evolving state. The basic problem is to explain the ability of apparently hydrogen saturated surfaces to absorb further hydrogen while being exposed to plasma. One would expect that the fuelling ratio $F = N_e^p/N_e^{in}$ (N_e^p is the number of electrons in the plasma and N_e^{in} is the total external electron input, e.g. gas puff) would quickly settle to a value of unity. Values of F measured on JET [263], however, show that F can be well below unity, particularly for large N_e^{in} (Fig. 48). On TFTR [330] and JT-60 [331], similar results are obtained. By contrast, in helium discharges on JET [263], F values near to unity are found for all but the lowest values of N_{in}^e (Fig. 49). The pumping ability of the JET inner wall (Fig. 47) also points to this problem, since it would again be expected to be saturated; helium discharges in JET [263] do not exhibit any change in pumping at the inner wall similar to that shown in Fig. 47. It is thus evident that there is an unidentified mechanism for temporary (i.e. 'dynamic') retention [332] of hydrogen by carbon under plasma exposure. It is also known that this retention ability differs between plasma exposure conditions and post-exposure conditions [216, 263, 332], since the wall retention time of particles, τ_w, as deduced from the pumping experiments of Fig. 47, is $\lesssim 1$ s, while the hydrogen desorption time after the discharge in JET has a time constant at least an order of magnitude larger [263].

Co-deposition of carbon and hydrogen constitutes a plasma activated pumping mechanism which can explain part of the observations, but the reversibility of the inner wall pumping on JET (evident from Fig. 47) is not explained, since co-deposition would cause permanent loss [263].

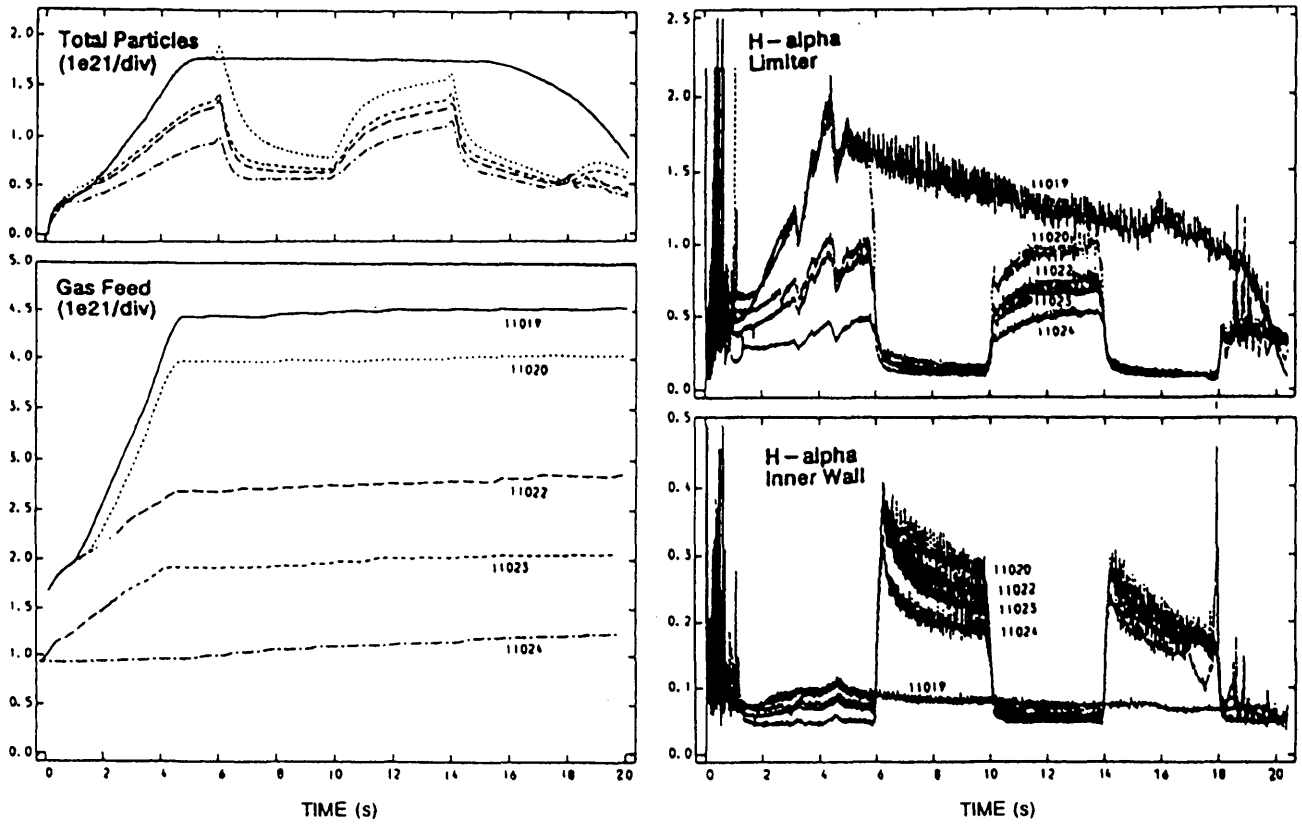

FIG. 47. Time evolution of four parameters for five JET discharges [216]: 11019, 11020, 11022, 11023 and 11024. Discharge 11019 was always positioned on the outer limiters; the other discharges were started on the outer limiter, moved to the inner wall at 6 s, moved back to the limiter at 10 s, back to the inner wall at 14 s, and back to the limiter at 18 s.

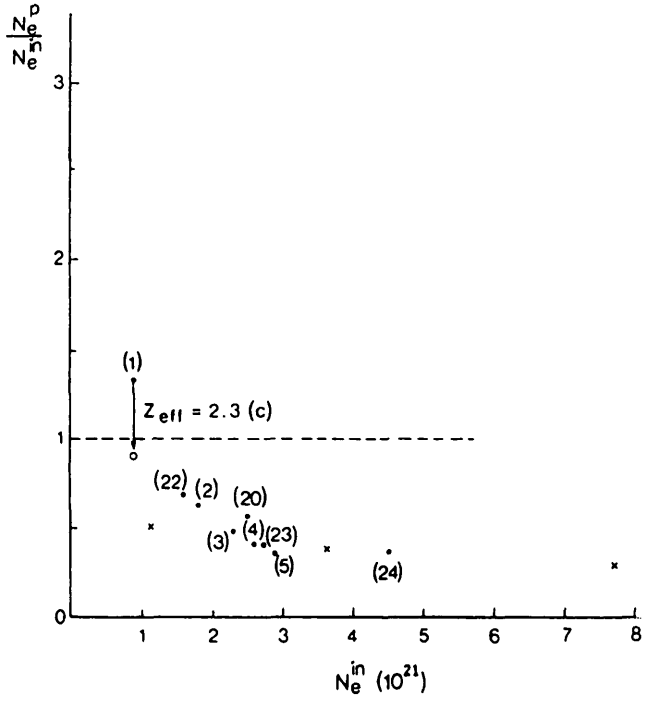

FIG. 48. JET deuterium discharges: Fuelling ratio N_e^p/N_e^{in} for JET Ohmic limiter discharges at T_L = 100°C and T_w = 200°C. The numbers in brackets denote the order of the discharge within the discharge series. The correction for Z_{eff} decreases the ratio relatively stronger at smaller N_e^{in}. The N_e^p data were taken at the end of the current flat-top (16 s in the discharge). I_p = 2.1 MA, B_T = 2.2 T [263].

Despite the lack of an explanation of the basic mechanism of dynamic trapping of hydrogen in carbon, the pumping processes can be modelled phenomenologically using values of τ_w deduced from experiments. Such modelling has provided a number of valuable results:

(1) On JET, the inner wall pumps more strongly than the outer limiter (Fig. 47); when the plasma is moved onto the graphite tiles at the top/bottom of the

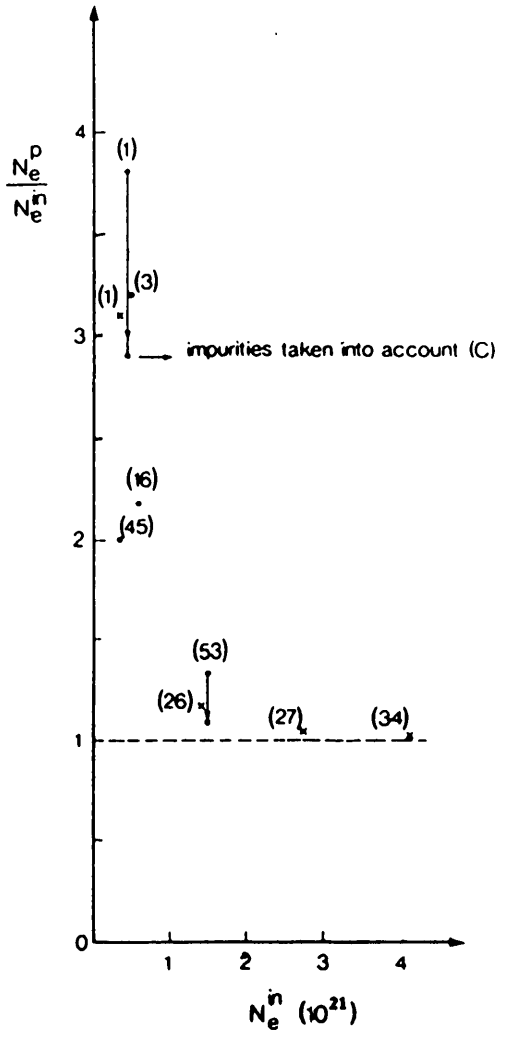

FIG. 49. JET helium discharges: Fuelling ratio N_e^p/N_e^{in} as a function of N_e^{in} for JET Ohmic helium fuelled discharges. The numbers in brackets denote the sequence numbers [263].
•: $T_L = T_w = 200°C$, $I_p = 2.2$ MA, $B_T = 3.4$ T;
×: $T_L = T_w = 300°C$, $I_p = 3.2$ MA, $B_T = 2.2$ T.

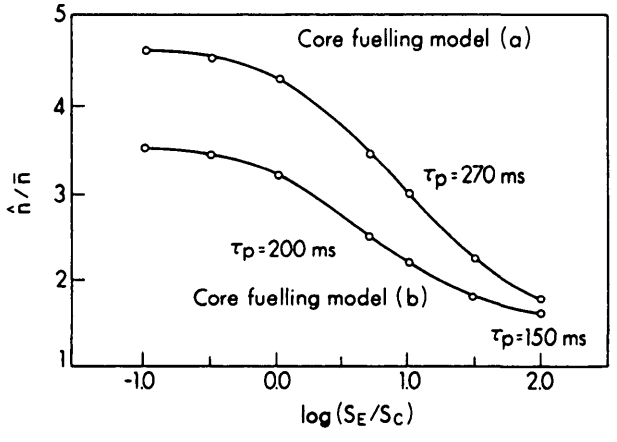

FIG. 50. JET: Variation of the density profile peakedness, $\hat{n}/\bar{n}$, with the ratio of edge and core sources, for two models of the core source (see text and Ref. [332]).

vessel, the pumping is still stronger. Using the measured value of τ_w, it has been shown [263] that these differences can be at least partially explained by the different fractions of SOL ionization which are associated with the different values of λ_n at the three locations (non-circular plasma shape).

(2) It has already been pointed out that it is advantageous to obtain high values of $\hat{n}_e/\bar{n}_e$ in order to maximize the fusion power. The model has been used to calculate [332] density profiles for JET at full power, operating with pellets, NBI (20 MW), ICRH (20 MW), a pump limiter, and a conditioned inner wall for recycling control. Results (Fig. 50) show that $\hat{n}_e/\bar{n}_e$ values in the range 3 to 4 are achievable for sufficiently low values of the ratio of the core fuelling rate S_C to the edge fuelling rate S_E.

(3) The phenomenological model [216, 263, 332] gives the following fuelling ratio

$$F = \frac{\tau_p}{\tau_w + \tau_p} \tag{4.19}$$

(τ_p can also be corrected in order to allow for prompt ion reflection from the surfaces.) For JET, with carbon limiters the pumping experiments show that, typically, $\tau_w \simeq \tau_p \approx 0.2$ s.

In an attempt to explain the form of the F versus N_e^{in} curve in Fig. 48, four hypotheses were tested [263] regarding the N_e^p dependences of τ_w and τ_p:

- τ_w = constant or $\tau_w \propto 1/\Phi_{out}$; the former hypothesis would be appropriate for diffusion limited release of hydrogen from the carbon and the latter hypothesis would be appropriate for recombination-limited release [329].
- τ_p = constant or $\tau_p \propto 1/N_e^p$, as in the model giving Eq. (4.13b).

The calculated dependences of F on N_e^{in} are shown in Fig. 51. Comparison with Fig. 48 indicates that only the case with $\tau_p \propto 1/N_e^p$ and τ_w = constant reproduces the observed functional dependence. A similar conclusion regarding τ_p was reached in TFTR refuelling studies [330].

With regard to the key question of how carbon wall pumping will behave in the presence of auxiliary (NBI) heating and pellet injection, the capacity under NBI on TFTR [327] is substantially increased, to more than 1000 torr·L, presumably due to the higher edge temperatures and therefore greater penetration depths, although it may also be due to greater co-deposition; the capacity during pellet injection is also substantially above 100 torr·L·s^{-1}.

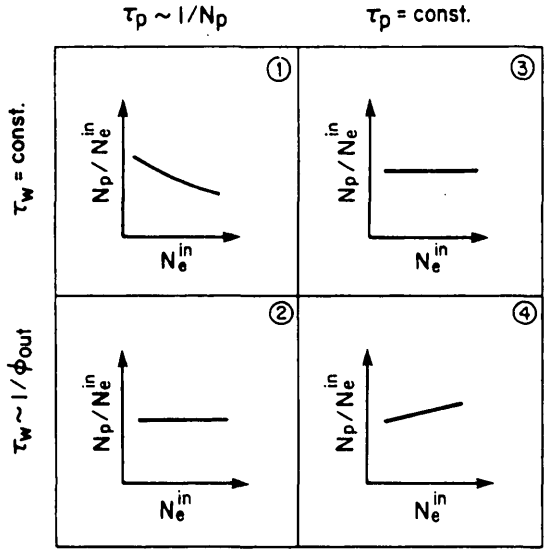

FIG. 51. JET: Calculated qualitative dependence of the fuelling ratio on the total electron input for different combinations of τ_p and τ_w (see text and Ref. [263]).

Möller [333] has provided a recent comprehensive review of hydrogen trapping and transport in carbon, which focuses on the implanted layer, i.e. the depth range where the injected atoms are deposited.

Turning to other, generally slower and saturable, mechanisms of hydrogen retention and the implications for tritium inventory, three important mechanisms have been identified [334]:

(a) *Co-deposition of tritium and carbon:* Carbon sputtered from limiters and walls traps hydrogen as it redeposits. H/C ratios are found to be of order 0.5; however, unlike for the conventional saturable layer, there appears to be no limit to the thickness of co-deposited layers, and up to 10^{19} D per cm^2 has been found in JET and TFTR deposits. It is believed that up to 25% of the hydrogen let into TFTR is lost in co-deposited layers. The implied tritium inventory is therefore significant — about 2.1 g has been estimated for TFTR [334], compared with only 0.3 g for the saturated layer. Co-deposited tritium is calculated to represent the bulk of the first wall tritium inventory in TFTR and in future devices such as CIT.

(b) *Tritium retention on pore surfaces.* Technical grade graphites have substantial internal porosity, 0.25–1.0 $m^2 \cdot g^{-1}$, and up to 10^9 pores per cm^3, with pores from 1 nm to 1 mm in diameter. Hydrogen slowly migrates through this porous graphite via internal surface diffusion; Causey [334] has measured a diffusion coefficient of 1.2 exp(–0.9 eV/kT) [$cm^2 \cdot s^{-1}$] for POCO AXF-5Q. An absolute upper limit of capacity can be estimated assuming a monolayer coverage of a surface area of 1 $m^2 \cdot g^{-1}$, thus giving 2×10^{19} atoms per cm^3. For 20 m^2 of graphite, a tritium content of 2 g to a depth of 1 cm is indicated; however, experimentally, such high levels of retention have not been possible to achieve.

(c) *Solubility and trapping of tritium in graphite.* Hydrogen diffuses through the graphite lattice with an estimated diffusivity [334] of

$$D[cm^2 \cdot s^{-1}] = 0.93 \exp(-2.8 \text{ eV/kT}) \quad (4.20)$$

and a solubility of

$$\text{Sol [atom fraction/atm}^{1/2}] = 6.44 \times 10^{-5} \exp(0.2 \text{ eV/kT}) \quad (4.21)$$

Diffusion eventually fills the 4.3 eV traps which are present in unirradiated graphite at a level of about 20 at. ppm. Thus, the 2 tonnes of graphite in TFTR or JET could eventually retain about 5 g of tritium by this process. For neutron irradiated devices such as ITER, where traps might be 500 times more abundant, greatly increased tritium inventories are indicated; with regard to safety design, this very strongly trapped tritium, however, might not be counted as being vulnerable to accidental release.

5. IMPURITIES

This section deals with the two principal elements of impurity behaviour — impurity *sources* and impurity *transport* into the main plasma and subsequently to the sink at the edge. Section 5.2 reviews the experimental information on measured impurity influxes and out-fluxes. Section 5.3 discusses the principal impurity production mechanism, i.e. limiter and divertor plate sputtering, particularly focusing on the case of carbon. Section 5.4 extends Section 5.3, considering the requirements for further progress in explaining the observed impurity influxes more reliably. Section 5.5 describes models for 1-D and 2-D impurity transport in the plasma. Section 5.6 deals with the implications of how the impurities return to the edge surfaces, i.e. net erosion/deposition patterns and the pumping of hydrogen by the co-deposition of carbon and hydrogen. Section 5.7 deals briefly with recent experience using beryllium limiters.

5.1. Introduction

Plasma-surface interactions produce impurities which contaminate the plasma. Unfortunately, this is generally a multiplicative and potentially runaway process, since the plasma impurity ions have higher sputtering and desorption yields than the hydrogenic ions [335-340, 791]. Contamination makes it more difficult to achieve net fusion energy conditions, for the following reasons:

— Impurities in the core of the plasma, particularly medium/high-Z elements, generate strong line and bremsstrahlung radiation [341], thus reducing the central temperature and hence the fusion power output P_F, potentially preventing ignition [342].
— Impurities in the outer part of the main plasma, particularly low-Z elements such as O and C, generate powerful line radiation (the 'radiating layer') which appears to destabilize the magnetic equilibrium [343-345]. The radiation power increases as $n_e n_{imp}$ so that density limits arise which are associated with Marfes [256, 346-349], detached plasmas [350-352], and a disruptive density limit [251] (see Section 6). Therefore, this also sets an upper limit to P_F for the high density approach to net fusion power.

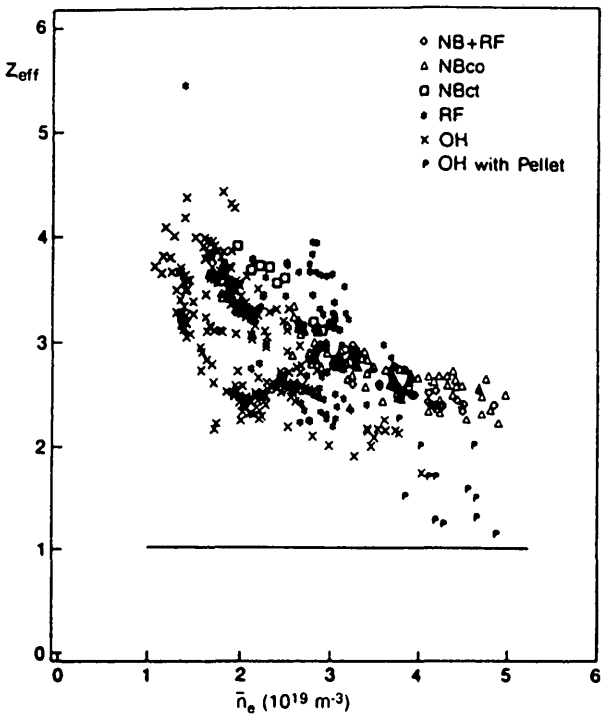

FIG. 52a. JET: Z_{eff} from bremsstrahlung for shots in 1986 (until April) as a function of $\bar{n}_e$ [354].

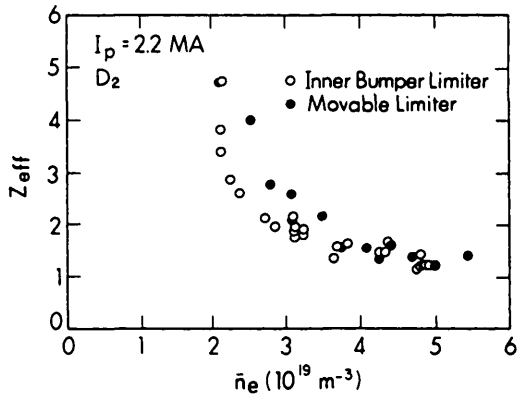

FIG. 52b. TFTR: Z_{eff} versus line averaged electron density $\bar{n}_e$ for high current (2.2 MA) and large radius (a = 0.82 m) Ohmic discharges [330].

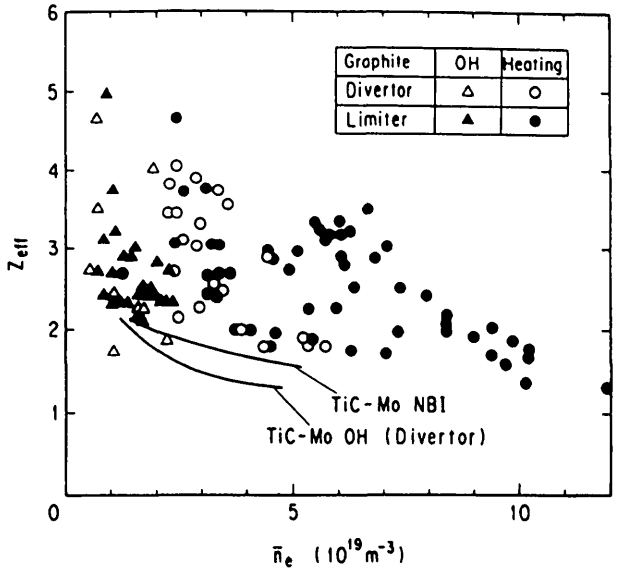

FIG. 52c. JT-60: Z_{eff} versus line averaged electron density $\bar{n}_e$ for various discharge conditions [355].

— In addition to this density limit, there is separately a pressure limit for a given field B due to MHD instabilities, for example, the Troyon beta limit [353]:

$$\bar{\beta}[\%] \leq \frac{2.8\ I_p[MA]}{B[T]\ a[m]} \qquad (5.1)$$

where $\bar{\beta}$ is the ratio of average plasma pressure to magnetic pressure. Thus, the impurities in the core plasma which add to the total plasma pressure effectively reduce the total core density n_{DT} and thus also the fusion power through fuel dilution. Fuel dilution also reduces the heating power available to the DT ions.

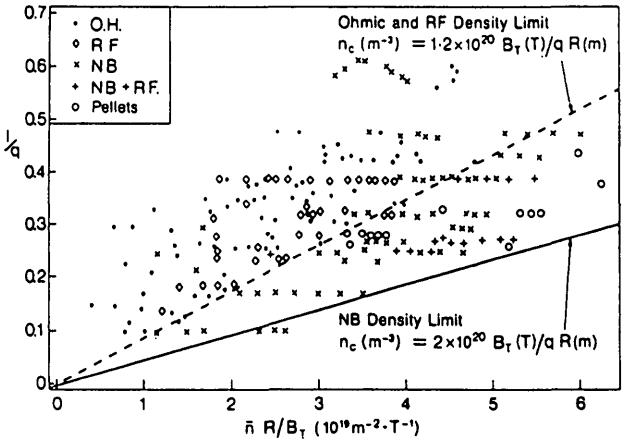

FIG. 53. JET: Plot of operating conditions in the normalized current, normalized density plane, the Hugill diagram [240].

Values of Z_{eff} generally decrease with $\bar{n}_e$ [330, 354, 355] (see Figs 52a–52c), approaching unity for some but not all tokamaks. The fuel dilution problem is generally seen as particularly serious; for example, 4% carbon ($n_c/n_e = 0.04$) implies $Z_{eff} = 2.2$ and $n_{DT}/n_e = 0.76$, thus reducing the fusion power by $(0.76)^2 = 0.58$. The high density disruptive limit can also be related to Z_{eff} [356]. This density limit is displayed on the Hugill diagram [247] for JET [240] in Fig. 53. Here, q_{cyl} is defined as $q_{cyl} = 5A_{cp}B/\pi R_m I_p$, where A_{cp} is the cross-sectional area of the plasma and the units are m, T, MA. The Murakami parameter [248], defined as Mur $\equiv \bar{n}R_m/B$, where $\bar{n}$ is the average electron density [10^{19} m^{-3}], has been found empirically to correlate with the upper density limit of tokamaks. On JET [240], values of up to Mur ~ 7 have been achieved at low q, while the design value for NET [357] is Mur $\simeq$ 16, and for economic reactors [240] Mur $\simeq$ 30. It has been shown [356] that the disruptive limit associated with $P_R/P_T \rightarrow 1$ gives

$$\text{Mur} = \frac{3.5}{B}\left(\frac{P_T R_m q}{(Z_{eff} - 1)\,ab(q - 2a/b)}\right)^{1/2} \qquad (5.2)$$

Thus, improvements in reducing Z_{eff} are as effective as increasing the input power to the tokamak, and probably less expensive.

We consider now the question of how the impurity behaviour is controlled. It is intuitively obvious that the edge plays a key role in certain aspects of this problem such as the impurity influx rate. It is perhaps less obvious that the edge can be the dominant factor with regard to impurity behaviour altogether. As with the other two primary quantities of interest in fusion plasmas — the fuel particle balance and the energy balance — the impurity behaviour is set by (a) the source, (b) the sink, and (c) the transport mechanism linking the two:

(a) *Source.* Generally, the impurity source is purely an edge effect arising from plasma-surface interactions [1], most typically sputtering [336] of the limiters/divertor plates.

(b) *Sink.* Most impurities eventually return to the limiters/plates where they are re-deposited. Some reach the walls; only a small portion is permanently removed by the pumps.

(c) *Transport.* Often, impurity transport is dominated by the edge plasma, and the core impurity density can be largely determined by processes occurring within a few centimetres of the LCFS. First, there is the prompt *screening* effect of the SOL: Impurity neutrals originating from the wall or limiters can be ionized within the SOL and, as a result of friction, they flow to the limiters with the fuel ions. Second, for those impurities which are ionized inside the LCFS, the exact ionization depth is critically important since the core density is proportional to this depth [310] (see Section 5.5). Because ionization distances are typically about 1 cm [358, 359], the edge plasma conditions also govern this aspect of the transport.

5.2. Measurements of impurity influx and outflux

Clearly, the first and principal quantity that must be measured in order to understand impurity behaviour in a fusion plasma is the impurity source(s). One needs to know:

- the locations of all significant sources — walls, limiters, wave antennas, divertor plates, etc.;
- the impurity species;
- the absolute magnitude of the influxes;
- the location of first (neutral) ionization.

Traditionally, such impurity measurements have not been made in tokamaks, and spectroscopic impurity studies have focused on the central plasma to measure impurity densities there. Such impurity information is essential, but it provides limited information on the cause of the impurity problem and little indication of how to solve it. First on ASDEX [360] and then on JET [128], Behringer has developed the technique of measuring impurity influxes on the basis of visible wavelength emission spectroscopy; this powerful technique is employed in a number of tokamaks: ASDEX

TABLE VII. ISX [363]
INTEGRATED INFLUXES FROM THE WALL AND LIMITER[a]

Conditions	Ion	Φ_w (s^{-1})	Φ_L (s^{-1})	Φ_w/Φ_L	Time (ms)
Before	Be I	1.6×10^{17}	1.1×10^{18}	0.14	280
melting	Cr I (a^7S)	1.2×10^{19}	1.7×10^{18}	6.9	280
(115 kA)	Ti II (a^4F)	4.7×10^{18}	4.7×10^{17}	10.0	280
	Ti II (a^2F)	2.0×10^{18}	1.6×10^{17}	12.8	280
	D I	5.0×10^{21}	1.5×10^{21}	3.3	280
	O II			19.0	280
Melting	Be I	2.9×10^{18}	1.2×10^{19}	0.25	150
sequence	Cr I	1.1×10^{19}	3.6×10^{17}	32.0	150
(150 kA)	Be I	5.0×10^{18}	1.3×10^{20}	0.04	340
	Cr I	7.3×10^{18}	3.2×10^{17}	24.0	340
After	Be I	4.5×10^{18}	1.39×10^{19}	0.3	150
fluence test	Cr I	5.5×10^{18}	8.3×10^{17}	6.6	150
(115 kA)	Be I	3.3×10^{18}	7.2×10^{19}	0.05	290
	Cr I	3.9×10^{18}	4.6×10^{17}	8.4	290

[a] The electron temperature is assumed to be 30 eV.

[361, 362], ISX [363, 364], TEXTOR [38, 350], DITE [122–124, 142, 365, 366], JET [367, 368]. The method involves absolute measurement of the photon intensity I_{ph} of specific lines of C I, C II, ..., O I, O II, ..., Cr I, etc., in the immediate vicinity of the sources. The particle influx of impurities Φ_{in} is then given [364, 369, 370] by

$$\Phi_{in} = 4\pi \frac{\overline{\sigma v}_i (T_e)}{\overline{\sigma v}_{\ell m}(T_e)} I_{ph}/b_r \qquad (5.3)$$

where $\overline{\sigma v}_i(T_e)$ and $\overline{\sigma v}_{\ell m}(T_e)$ are the average ionization and excitation rate coefficients, and b_r is the branching ratio. Examples of calculated photon efficiencies, $\overline{\sigma v}_i/\overline{\sigma v}_{\ell m} b_r$, given in Fig. 19 (Section 2), emphasize the importance of knowing the local electron temperature in the emission zone. The technique can require sophisticated corrections when densities of atoms in the metastable state are comparable with ground state densities; for Be I, for example, 50–70% of the population can be in metastable states [363]. Table VII gives examples of measured influxes of Be, Cr, Ti, D and O from both walls and limiters in the ISX-B tokamak [363] using Be limiters. It is noted that the limiters are, not surprisingly, the main source of Be influx, although the walls are significantly contaminated by Be, causing some influx; the influx from the wall increased by more than an order of magnitude after the limiters suffered melting, indicating that a large fraction of the wall was covered by Be. It may also be noted that the ratio $\Phi_{in}^{Be}/\Phi_{in}^{D} \sim 7 \times 10^{-4}$ for the limiters corresponds to the physical sputtering yield for BeO at 40 eV D^+ impact [363]. The wall is seen to be the dominant source of oxygen. Examples of spectroscopically measured Ti influxes from the ASDEX divertor plate [361] are presented in Fig. 54. The influxes can be explained as resulting from sputtering

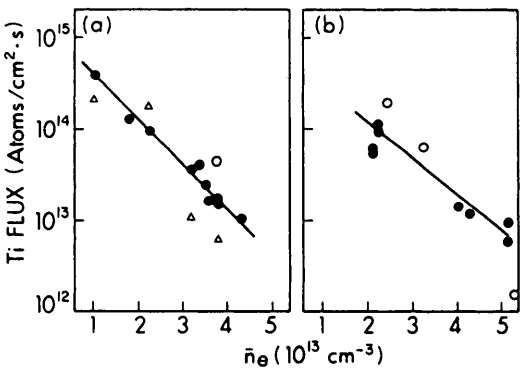

FIG. 54. ASDEX: Measured Ti fluxes (●) in front of the neutralizer plate versus $\bar{n}_e$ for (a) D^+ and (b) H^+ discharges. Calculated values for sputtering by thermal ions (△) and suprathermal ions (○) are also shown (Ref. [362]).

TABLE VIII. ASDEX [361]
SPECTROSCOPICALLY DETERMINED IRON DENSITIES AND CALCULATED AND MEASURED IRON FLUXES[a]

	$\bar{n}_e$ (cm^{-3})	Iron central density (cm^{-3})	Iron influx (calculated) ($cm^{-2} \cdot s^{-1}$)	Iron outflux to the divertor (measured) ($cm^{-2} \cdot s^{-1}$)
Helium				
Limiter	4.7×10^{13}	1.2×10^{10}	1.3×10^{13}	
	3×10^{13}	1.2×10^{10}	1.3×10^{13}	
Divertor	4.7×10^{13}	4.1×10^{9}	4.4×10^{12}	8×10^{12}
	3×10^{13}	5.3×10^{9}	5.6×10^{12}	9×10^{12}
Deuterium				
Limiter	3×10^{13}	1.5×10^{9}	1.6×10^{12}	
	4.7×10^{13}	1.9×10^{9}	2×10^{12}	5.2×10^{12}
Divertor	3×10^{13}	2×10^{9}	2.1×10^{12}	4×10^{12}
	3.6×10^{13}	1.2×10^{9}	2.4×10^{12}	
Hydrogen				
Divertor	3.6×10^{13}	3×10^{8}	8×10^{11}	1.1×10^{12}

[a] ASDEX divertor collector probe.

due to (a) the local 'thermal' plasma at the plates, and (b) fast, collisionless 'epithermal' ions which penetrate to the divertor from the main SOL; influxes and yields have been calculated using local measurements of T_e and T_i.

In ASDEX, iron is a critically important impurity, since the H-mode (Section 7.3) can be terminated by radiation collapse due to high core levels of metals [361, 371-373]. The metal walls were the evident source, and a comprehensive effort was made to establish the actual source mechanism by measuring Φ_{in} and Φ_{out} by several methods. Table VIII gives results [361] for the *measured* (from Fe XVI and Fe XVII) central impurity densities n_{Fe}, and for the *calculated* influxes Φ_{Fe} which would give rise to these densities (see Eq. (5.8), assuming $D_\perp = 0.4\ m^2 \cdot s^{-1}$, $v_{in} = -2D_\perp r/a^2$, $\lambda_n = 2$ cm, and ionization near the LCFS, see Section 4.6). It is noted that the Fe influxes for H_2 discharges are about one-third of those for D_2 discharges, as expected from the sputtering ratio. Regarding the absolute values of Φ_{Fe}, these have been explained in the case of the H and D discharges on the basis of the measured charge exchange (cx) flux density to the walls and the measured cx energy distribution [135, 374]. The calculated sputtering rates are also shown in Table VIII; generally, they agree well with the (indirect) spectroscopically measured Φ_{Fe}. The discrepancies for He, evident in Table VIII, have been explained as follows: a small fraction of the ions, about 5%, strike the protective plates at the divertor entrance; in the case of He^{2+}, the sputtering yield is sufficiently high to explain the extra influx.

The accuracy involved in the spectroscopic method of measuring Φ_{in} has not been systematically assessed, but it appears that it may not be high. Generally, calculated values of $\overline{\sigma v}_i(T_e)$ and $\overline{\sigma v}_{\ell m}(T_e)$ are used. Errors of less than a factor of two are estimated for each of $\overline{\sigma v}_i$ and $\overline{\sigma v}_{\ell m}$ separately, with uncertainties becoming particularly large when T_e is less than the ionization potential [375]. When experimental values of $\overline{\sigma v}_i$ and $\overline{\sigma v}_{\ell m}$ were used, e.g. for Cr [376], the disagreement with the calculated value of $\overline{\sigma v}_i/(\overline{\sigma v}_{\ell m} b_r)$ was found to be about a factor of four. Clearly, what is required is that calibration experiments be carried out, making injections of known influxes of impurity atoms into plasmas where T_e is accurately measured and where absolutely calibrated spectroscopy is used to measure the intensity of photon emission, so that purely experimental values of $\overline{\sigma v}_i(T_e)/\overline{\sigma v}_{\ell m}(T_e) b_r$ can be obtained. No such work appears to have been reported.

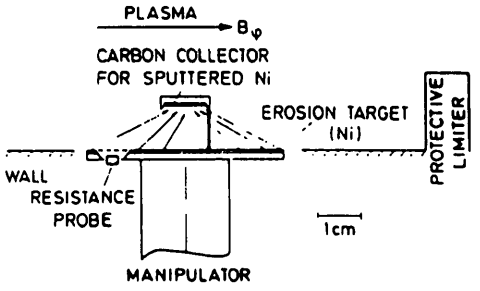

FIG. 55. ASDEX: Erosion probe (schematic) consisting of the erosion target (Ni) and a carbon collector (Papyex) in front of the target. The carbon resistance probe is placed behind a diaphragm (1.3 cm dia.) and views the whole visible plasma surface [374].

While spectroscopic techniques for measuring Φ_{in} are, in principle, of general applicability, other techniques can be employed in special circumstances. Staudenmaier and Wampler [374] demonstrated the use of an erosion probe on ASDEX for discharges similar to those just discussed (see Fig. 55). The wall metal sputtered onto the collector was subsequently measured by electron induced X-ray analysis. The results, presented in Table IX, are in excellent agreement with theoretical sputtering yields based on the D(He) cx fluxes and energies measured by a resistance probe [374]. Because of the low erosion rates, the effect had to be integrated over a number of discharges. Thus, the iron wall influx in H and D discharges is confirmed as being due to cx sputtering.

We turn now to the measurements of impurity outfluxes, Φ_{out}. This is one of the most often used diagnostic techniques in edge physics, and impurity deposition probes have been deployed in virtually all tokamaks [377]. These probes readily provide qualitative information, e.g. identification of species, correlation with auxiliary heating and the time dependence of the outflux (start-up, flat-top, ramp-down), and asymmetries. A considerable array of surface analysis techniques are available [1, 377]; these are capable of identifying very small surface deposits, even down to sub-monolayers. There is a variety of deposition 'probes', e.g. post-mortem analysis of portions of limiters [378–380] and walls [381, 382], etc., long-term samples fixed to the walls [379, 383, 384], removable probes which integrate over several discharges [196, 385–391], removable probes which integrate over a complete single discharge [392, 393], and probes which time-resolve during a single discharge [394–407]. The extensive literature on deposition probes was recently reviewed by Zuhr et al. [377], by Taglauer [408] and by Staudenmaier [409]. Despite their extensive use, deposition probes have a number of deficiencies and there are not many publications giving information on such probes which can be quantitatively related to other quantifiable aspects of tokamak operation. The relation between the (measured) deposition areal density [atoms/m^2] and the impurity density in the plasma [ions/m^3] in the absence of a probe was not generally considered in deposition probe analysis; recently, a simple probe model [410] was

TABLE IX. ASDEX [374]
EROSION YIELDS AND SPUTTERING YIELDS[a]

Discharge		Measured erosion (Ni/cm^2)	CRP		Erosion yield, Ni/D(He)	Sputtering yield, Ni/D(He)
Gas	No.		Neutrals ($at./cm^2$)	E (eV)		
D_2	17998-18017	8.3×10^{13}	1.6×10^{15}	350	5.2×10^{-2}	3.9×10^{-2}
He	17951-75	7×10^{13}	3.6×10^{14}	360	0.19	0.17
He	17852-98	6×10^{13}	3.7×10^{14}	270	0.16	0.16

[a] Experimental erosion yields evaluated from simultaneous measurements of the eroded nickel fluence and the impinging neutral particle fluence as measured with the carbon resistance probe (CRP). The sputtering yield calculated from the measured average particle energy and the sputtering data of Ref. [335] agree well with the experimental erosion yields.

produced for this situation, including the effects of subsequent removal of the deposited layer by ongoing plasma exposure. Deposition probes generally provide no information on the impurity charge state nor on the impact energy, although Larmor radius effects have occasionally been employed to estimate these quantities [55, 377].

The results of one quantitative study (the above-mentioned comprehensive ASDEX study [361] of iron) are given in Table VIII. In this work the time-resolved deposition probe was located in the divertor, where it could receive a calibrated fraction of the entire Fe production in the SOL of the main chamber as the Fe ions flowed, presumably with toroidal symmetry, into the divertor sink [408]. As can be seen in Table VIII, the measured iron outflux values agree to within a factor of two with the iron influx values calculated as being necessary to account for the spectroscopically measured iron core densities. It may be noted that in this case an impurity flux rather than a density was measured, thus minimizing interpretation [55] problems.

The ASDEX study of iron impurities illustrates what can be achieved by a comprehensive and quantitative examination of all sources, using complementary techniques for measuring Φ_{in} and Φ_{out}. The mechanisms of impurity generation were clearly and quantitatively established, which is the first and necessary step to finding a solution to an impurity problem. It appears [372], in fact, that the only solution to the problem of the impurity accumulation/radiation collapse in ASDEX H-modes (and also in pellet discharges) is to reduce the impurity influx, particularly that of metals, since long particle confinement/accumulation appears to be fundamentally coupled to long energy confinement. It is concluded that metal concentrations must not exceed $\sim 10^{-4}$ before the onset of the H-mode, while the tolerable C and O concentrations can be much higher ($\lesssim 2\%$), since these low-Z impurities were found not to experience accumulation in ASDEX. Carbonization of the ASDEX walls was found to suppress the central iron densities by an order of magnitude, and counter-injection neutral beam heating experiments could then be made without radiation collapse occurring.

Part of the difficulty of interpreting deposition probe measurements of intrinsic impurities is that "... the fluxes of intrinsic impurities detected by deposition probes near the wall do not necessarily represent the impurity efflux from the core plasma only, but rather seem to be a superposition of the impurity flux from the core plasma with intrinsic impurities originating from additional sources at the wall, limiters, etc." [411]. Thus, deposited fluxes often differ, depending on whether the probe is in the ion or the electron drift direction, and other asymmetrical phenomena are observed (see Section 10). These difficulties were avoided when extrinsic impurity sources, such as laser blow-off, were used in conjunction with temporal and spatial (radial) resolving deposition probes [411–414]. Time-resolving deposition probes on T-10 registered particle confinement times for injected K and Li of about 100 ms [411], which is indicative of core confinement; a spatially resolving probe [412] registered radial decay lengths for Li at the edge of 7 mm, corresponding to a value of $D_\perp$ at the edge of $\simeq 0.7\ m^2 \cdot s^{-1}$, close to the Bohm value.

Post-mortem analysis of limiters and divertor plates after their exposure in tokamaks can also yield valuable information. While it can be difficult to quantitatively relate the observed deposits to Φ_{out}, owing to complex re-deposition processes (see Section 5.6), the measurements are directly useful since they indicate the limiter's effective material composition for plasma–surface interactions. In a series of studies of limiters used in several tokamaks, Behrisch and co-workers obtained the following results for graphite limiters from ASDEX [415], TFR [416, 417] and JET [379, 418, 419]:

- A metal layer on the limiters, from Inconel and stainless steel components of the vessel, can reach very high levels, 5–500 atomic layers equivalent.
- The metal is often in the form of droplets of a diameter of up to 100 μm. It appears that the droplets agglomerate thermally.
- Since the metals are concentrated in droplets, the plasma still mainly 'sees' a carbon surface. This was confirmed experimentally by using Auger surface analysis which is only sensitive to the actual surface composition.
- The spatial distribution of metals tends to show minima where the heat flux onto the limiter is highest; maxima are on surfaces radially further out (see Section 5.6).

Similar studies have been reported for graphite limiters on T-10 [254], TFTR [420-423], TEXTOR [424], JIPP T-IIU [425] and PDX [426]. In a recent post-mortem analysis of the TFTR bumper limiter and wall [427], it was found that the surface morphology and composition varied greatly among regions of little plasma contact, purely eroded regions, regions with strong impurity deposition, and regions with both erosion and deposition occurring at different times. The

implications of such surface changes for gas pumping, tritium retention, etc., may be substantial.

Returning to the techniques for measuring Φ_{out}: Recently, Matthews [142] has developed a real-time impurity analysis probe which discriminates between species on the basis of Z_{imp}/m_{imp}; ; details of the probe are discussed in Section 2.2.7. While systematic studies have yet to be undertaken, it has been shown in the DITE SOL that C and O fluxes can constitute a substantial fraction of the fuel (H, He) fluxes. The charge states I to IV are approximately equally represented in edge fluxes — a situation which has been reproduced by a Monte Carlo code impurity model [428].

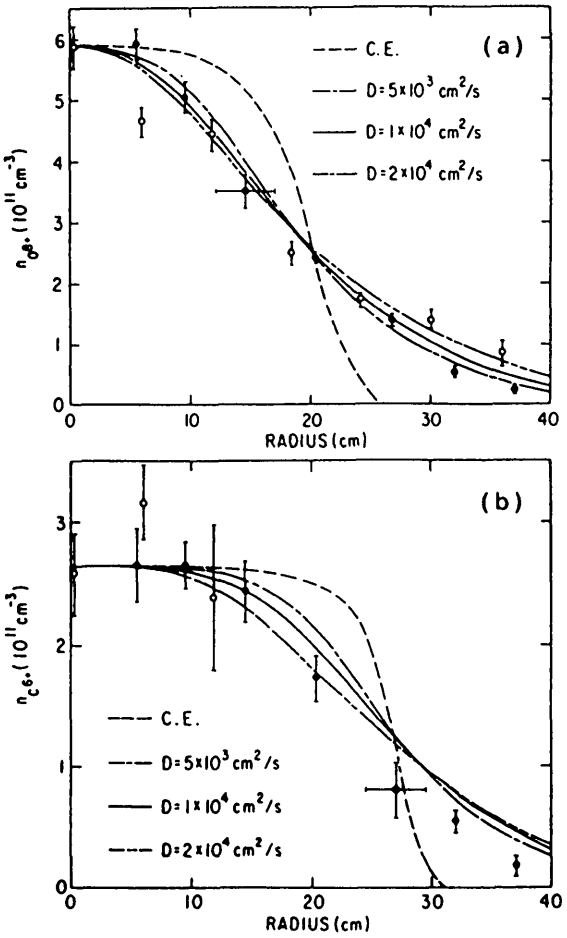

FIG. 56. PDX: Radial profiles of fully ionized oxygen (a) and carbon (b) during the steady state phase of the discharge. The limiter radius is at 30 cm. The solid lines are profiles of C^{6+} and O^{8+} calculated from an impurity transport code. C.E. is the distribution expected from coronal equilibrium assuming a constant impurity density; D is the constant impurity diffusion coefficient [432].

Laser induced fluorescence [103, 131, 191, 429–431] (see Section 2.2.6) is a powerful technique for measuring Φ_{in} . Indeed, this technique measures separately the impurity number density in front of the source and the velocity distribution (via Doppler shifts), from which Φ_{in} can be calculated. On TEXTOR, iron densities of 3×10^{16} [atoms/cm^3] were measured [103] at the limiter, with an average velocity of 2×10^5 cm·s^{-1}; at the liner, the density was 3×10^{13} [Fe/m^3], giving a total wall influx Φ_{in} of 2×10^{18} [Fe/s], for a liner area of 40 m^2.

Although not measuring Φ_{in} directly, charge exchange spectroscopy [103] can provide a measure of $n_{imp}(r)$ across the plasma, including the SOL. Figure 56 shows results for C^{6+} and O^{8+} on PDX [432], measured with a collimated, 25 keV, H^0 beam. The densities at the limiter radius are about 10^{17} m^{-3} and, when the edge electron density is estimated to be a few 10^{18} m^{-3}, Z_{eff}^{SOL} can be significant (>2).

5.3. Impurity production mechanisms

5.3.1. Physical and chemical sputtering

Although impurities can be released from limiters and divertor plates by arcing and evaporation, ion sputtering (both physical and chemical) is the most general cause [1]. Wall impurity release processes are less clear; they can include charge exchange neutral sputtering and desorption (see Section 5.2) and possibly chemical processes involving atomic hydrogen [433]. Impurities can also be produced by pathological operating modes such as disruptions; the latter phenomenon has recently been reviewed [434] and will not be discussed further here.

In steady state conditions the impurity influx and outflux are equal, $\Phi_{in} = \Phi_{out}$, and the effect of self-sputtering can be very important since the impurity ions returning to the surface are multiply charged and can be accelerated to high impact energy by the sheath potential drop (Eq. (3.25)). In addition, for a given impact energy, self-sputtering yields generally exceed hydrogenic sputtering yields (see, for example, Figs 57a, 57b). For the case of hydrogenic sputtering, with yield Y_H, and self-sputtering, with yield Y_S, in steady state the globally averaged result is

$$\Phi_{in}^{imp} = \Phi_H Y_H + \Phi_{out}^{imp} Y_S \quad (5.4a)$$

Thus,

$$\Phi_{in}^{imp} = \Phi_H Y_H/(1 - Y_S) \quad (5.4b)$$

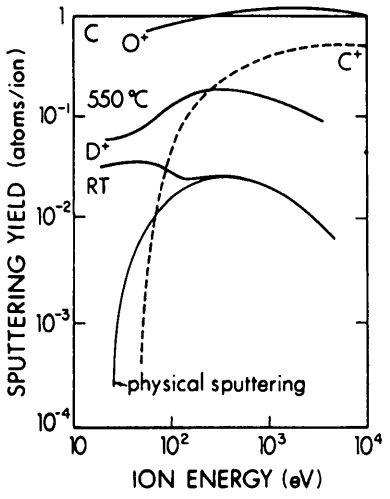

FIG. 57a. Energy dependence of the sputtering yield of carbon at room temperature with deuterium, oxygen and self-ions. The deuterium yields at elevated temperatures are also given. The beryllium self-sputtering data were calculated by the TRIM code. In the case of graphite sputtering with deuterium, the values for a SiC doped graphite are also given [335].

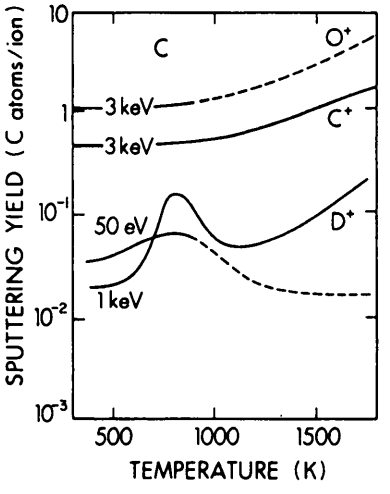

FIG. 57b. Temperature dependence of the sputtering yield of carbon at different energies for D, O and self-ions [335].

Therefore, self-sputtering is multiplicative rather than additive and there is the possibility of catastrophic influxes if $Y_S \rightarrow 1$ (see Section 5.3.2).

An earlier generation of tokamaks employed metal limiters. For carbon dominated devices such as JET, TFTR and TEXTOR in recent operation, metals on the limiter can be present owing to contamination from RF antenna screens or other metal wall components. Metal sputtering appears to be well understood [1, 336].

Figure 58 shows Ni concentration levels measured in OH deuterium JET [435] discharges as a function of $\bar{n}_e$ and I_p . The trends are quite explicable in terms of known edge temperatures (Fig. 2, Section 2), with lower edge temperatures leading to reduced sputtering since the yield is lower. The JET metal influxes have also been quantitatively explained [198]. Studies of metal impurity production have been reported for a number of tokamaks, and the influx rates have generally been accounted for by known sputtering processes: Tuman-3 (Fe, Ni) [436], ISX-B (Be, Cr, Ti, Fe) [191, 363], ALCATOR-C (Mo) [437], TEXTOR (Cr, Fe) [38, 131, 438], UNITOR (Cr) [429], ASDEX (Fe, Ti) [359, 361], DIII (Ti) [439].

In the case of tokamaks with graphite limiters and graphite or carbonized walls, the impurity production mechanism is quite complex and is still not conclusively established. We consider first the carbon sputtering database from laboratory experiments employing ion beams [181, 335, 440–446] (see Figs 57a, 57b):

- Deuterium physical sputtering reaches a peak yield of ~ 0.025 atoms/ion for an impact energy E_0 of hundreds of eV, assuming normal incidence ions;
- Deuterium chemical sputtering results in a peak yield of ~ 0.2 at a substrate temperature of ~ 550°C; at room temperature and for low values of E_0, it also contributes to the yield, preventing the yield fall-off that is associated with physical sputtering alone;
- Carbon self-sputtering reaches quite high levels, $\gtrsim 0.5$ (normal incidence ions), for $E_0 \gtrsim 1$ keV; this source can be important since multiply charged carbon ions are accelerated to very high energies by the sheath; e.g., for $T_{LCFS} = 50$ eV, $E_0(C^{6+}) \approx 1$ keV;
- Oxygen sputtering, to produce CO and CO_2, has a very high yield (~ 1), virtually independent of E_0 and surface temperature;
- Radiation enhanced sublimation (RES) occurs for all impacting species for $T \gtrsim 1300$ K. Yields for carbon self-sputtering exceed unity for energies of 200 eV and surface temperatures of 1900 K.

The question is whether such accelerator-based data are relevant to tokamak edge conditions. Effects which have to be considered are:

- The relation between ion flux density and yield [440–447]; accelerator ion flux densities are $\lesssim 10^{16}$ cm$^{-2}\cdot$s^{-1}, whereas typical limiter flux densities are two to three orders of magnitude higher; there is (non-tokamak) evidence from the

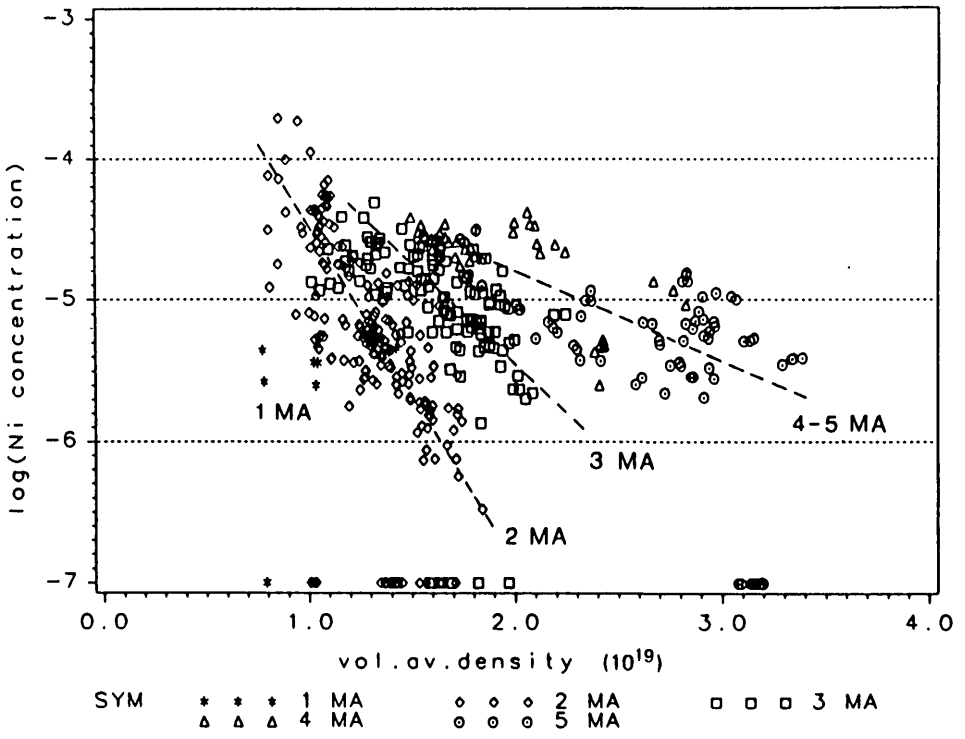

FIG. 58. JET: Nickel concentrations for 1986 limiter discharges with Ohmic heating [435]. The dependence on $\bar{n}_e$ and I_p is characteristic of physical sputtering (see Fig. 2, Section 2, for the edge temperature dependence on $\bar{n}_e$ and I_p).

high flux PISCES plasma facility [448, 449] that the yield decreases by a factor of about two at $\sim 10^{18}$ H·cm^{-2}·s^{-1}, compared with 5×10^{14} H·cm^{-2}·s^{-1};

— Metal impurities may suppress chemical erosion [423, 450, 451];

— Multi-species interactions may be significant; the role of oxygen in particular appears to be very important, although it is difficult to assess.

Carbon impurities, not surprisingly, dominate the Z_{eff} of carbon tokamaks, and the resulting values (generally >2) are not acceptable from the point of view of fuel dilution. It is therefore of primary importance to understand the source of carbon. Since RES can result in carbon yields greater than unity, this sets an absolute upper limit to the temperature at which operation with graphite in tokamaks is possible. Such a limit is effectively equivalent to the melting limits of metals, but, since RES only occurs for graphite at relatively elevated temperatures, there is still an operating advantage over most (low-Z) metals. (Nevertheless, local hot-spot problems have been encountered in JET and TFTR at the edges of the graphite limiter and wall tiles, resulting in high carbon influxes, evidently due to RES.) While RES can, in principle, be controlled by avoiding extreme operating temperatures, the H-C chemical sputtering peak of graphite occurs at relatively low temperatures (~600-900 K), which operating regime is otherwise attractive. Oxygen chemical sputtering is strong (yield ≃ unity) for virtually all conditions. It is therefore of particular importance to establish whether chemical sputtering (by D and O) is important in actual tokamak operating conditions.

The evidence from different tokamaks which bears on this question is organized here under four categories: comparisons of He and H/D discharges, quantitative accounting of absolute carbon influx/density levels, effect of varying the carbon temperature, and special tests of chemical sputtering; these are discussed in the following subsections.

5.3.1.1. Comparisons of He and H/D discharges

Such comparisons can provide clear indications for strong chemical effects (H-C and/or O-C). For ASDEX limiter discharges, the carbon influx (C III signal at 120° toroidally from the limiter) was dramatically greater for D/H discharges than for He discharges [335, 361, 452] (Fig. 59); unfortunately, oxygen levels were not measured and so the role of

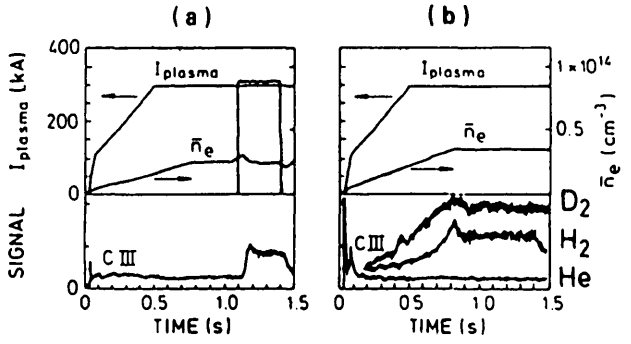

FIG. 59. ASDEX: Time dependence of the C III line intensity in divertor discharges with D_2 (a) and in limiter discharges with He, H_2 and D_2 (b), with otherwise identical parameters [361].

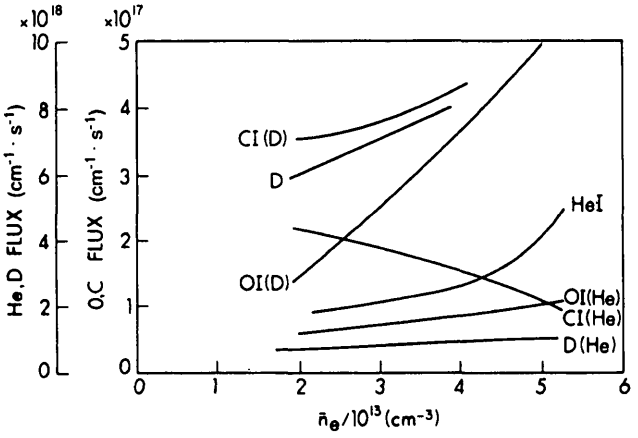

FIG. 60. TEXTOR: Fluxes from the main limiter for discharges in helium (He); curves for deuterium discharges (D) are shown for comparison (I_p = 480 kA) [350].

O-C sputtering cannot be assessed. Pospieszczyk et al. [350] found that, on TEXTOR, the carbon influx (limiter C I) was significantly lower for He than for D (Fig. 60); the oxygen influx (limiter O I) was also measured in this case; they concluded that their results indicated D-C chemical sputtering. Roth [335], however, pointed out that the C/O influx ratio was approximately unity for the D discharges on TEXTOR and proposed that oxygen sputtering is the main cause of carbon influx — a view now shared by the TEXTOR authors [453–455]. It appears that the TEXTOR results can be explained on the basis of D-C sputtering plus self-sputtering together with oxygen sputtering, although more information on T_{edge} is needed to assess this. The TEXTOR study of Ref. [350] showed that a fresh carbonization of the walls lowered the O and C influxes by approximately the same amount, apparently confirming the strong role of oxygen.

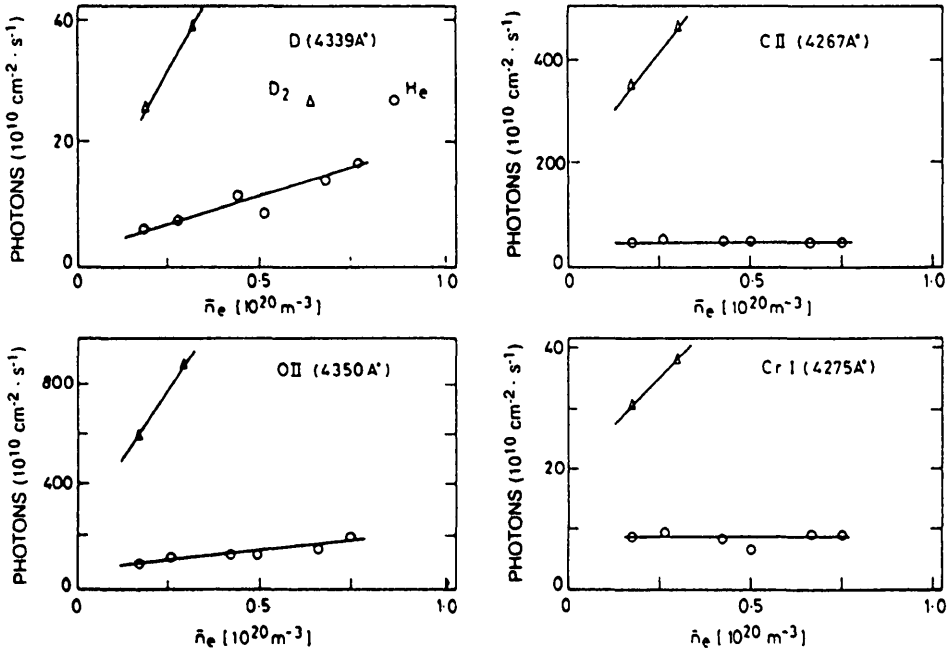

FIG. 61. DITE: Impurity and deuterium line intensities at the wall, measured in deuterium and helium discharges with I_p = 100 kA and B_T = 2.0 T [433].

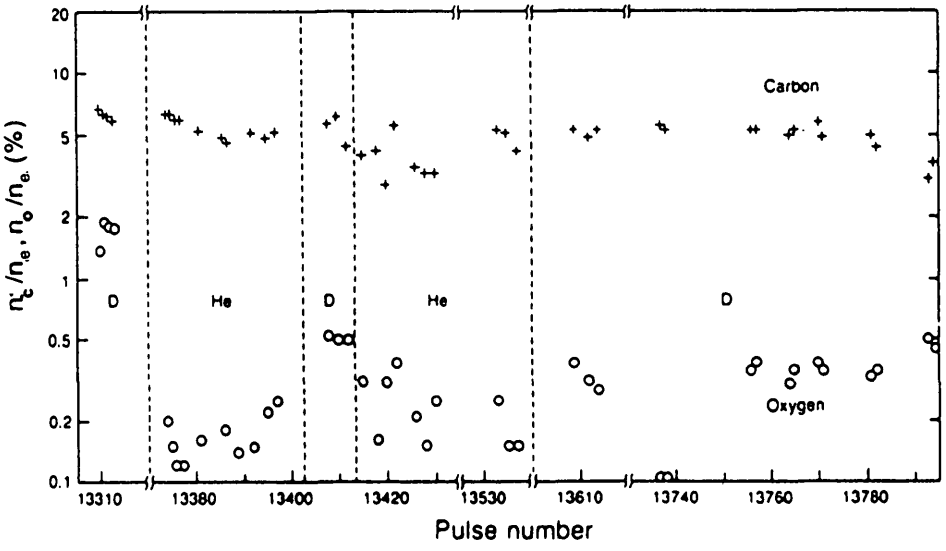

FIG. 62. JET: Carbon and oxygen concentrations (characterized by C VI/$\bar{n}_e^2$ and O VIII/$\bar{n}_e^2$) for 1987/1988 JET deuterium and helium plasmas (Ohmic heating) [435]. The carbon levels in these discharges are very similar. Longer helium operation leads to a lasting reduction of oxygen.

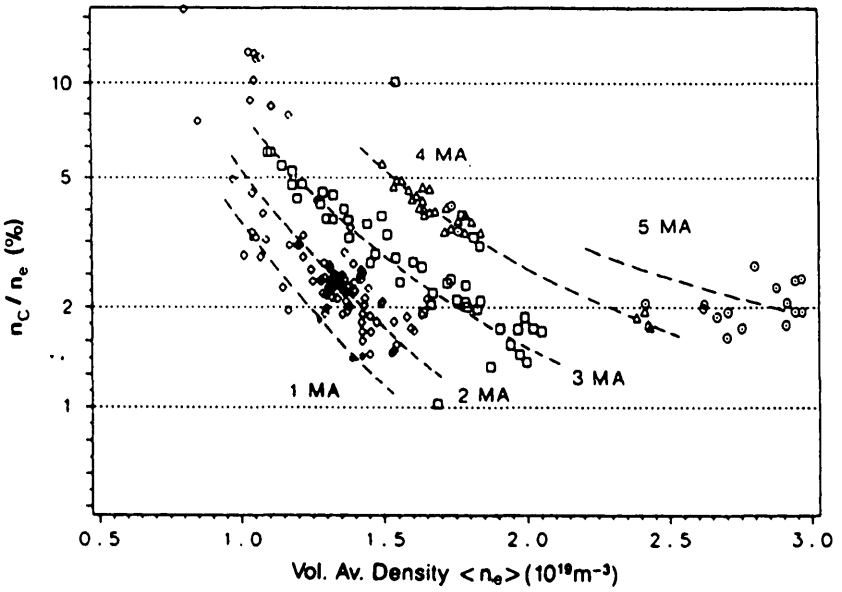

FIG. 63. JET: Carbon concentrations for 1986 JET limiter discharges in deuterium with Ohmic heating [435]. The dependence on $\bar{n}_e$ and I_p is characteristic of physical sputtering (see Fig. 2, Section 2).

On DITE [433], *wall* influxes (C II) were measured to be much higher in D discharges than in He discharges (Fig. 61), as were the O influxes (O II). The D influxes from the wall (He discharges always contain some D) indicate that the source of the oxygen itself may be chemical reactions with hydrogenic atoms at the wall. A suggested reaction route [456] for the production of oxygen and carbon is:

$H_2 + e \rightarrow 2H$	dissociation in plasma;
$2H + O(\text{surface}) \rightarrow H_2O$	reaction on the wall surface;
$H_2O + e \rightarrow 2H + O$	dissociation in plasma;
$O + C(\text{surface}) \rightarrow CO$	reaction on the graphite limiter surface.

For all-carbon machines, Phillips et al. [454] propose direct release of CO from the walls by impact desorption of oxygen lightly bound to the carbon through the impact of cx or F–C hydrogen atoms. It is further postulated that the CO is ionized in the SOL and is convected to the limiters, causing oxygen sputtering and self-sputtering, followed by oxygen recycling at the limiters. Evidence for the last effect may be indicated by JET data [367] which typically show oxygen limiter influxes slowly increasing during the discharge, over a period of ~ 10 s. Central carbon impurity levels on JET, however, show little difference between He and D discharges [435], although the central oxygen levels are significantly lower in He discharges (Fig. 62). Furthermore, the central JET carbon levels rather faithfully follow the measured T_{edge} values (Fig. 63 compared with Fig. 2) as a function of I_p and $\bar{n}_e$, i.e. their behaviour is similar to that of metals (Fig. 58). This is taken as evidence that physical (D–C and C–C) sputtering dominates. (It should, however, be pointed out that H–C chemical sputtering yields are also sensitive to ion impact energy E_0: at 550°C, the H–C chemical sputtering yield [449] increases from $Y = 0.025$ to $Y \approx 0.06$ as E_0 increases from 50 to 200 eV. Furthermore, central density levels reflect not only changes in influx but also changes in transport: impurity 'screening' improves as n_{edge} increases.) On TFTR [457] the central carbon levels (inferred from Z_{eff}, allowing for the contribution of metals and the measured C/O ratio) are actually lower in D discharges than in He discharges again indicating that physical sputtering is dominant.

Thus, with regard to comparisons of He and D/H discharges, unfortunately a wide range of carbon behaviour appears to be possible; the oxygen behaviour may be critical, but it is not always monitored; firm conclusions do not appear to be possible at this time.

5.3.1.2. Quantitative accounting of absolute carbon influx rates or density levels in the main plasma

A quantitative accounting of the absolute influx or density levels in the plasma would appear to be the most straightforward means of establishing which sputtering processes are important. Unfortunately, there are rarely enough data for any given experiment to be able to reach firm conclusions, since factors of only about two are involved. In the first place, the preferred measurement would be of influx (C, O, D) rather than central density if one wishes to avoid the uncertainties of transport (Section 5.5) and of the role of other sources in the tokamak. Spectroscopic influx measurements are probably not more accurate than a factor of two or worse [375]; in particular, the all-important D influxes are uncertain since molecular effects should be accounted for (see Section 4.2); often, however, they are not accounted for [435]; also, there are uncertainties in the molecular rates [129]. Second, edge plasma conditions at the location of the source must be known accurately — particularly T_e; such information is critical to the interpretation of the spectroscopic measurements of particle influxes and to calculation of the D–C and C–C sputtering rates, which can be strongly energy dependent; such plasma measurements are rarely available.

In a TFTR study [457], the central carbon levels are explained quantitatively as being due to physical sputtering (He or D), including self-sputtering together with oxygen chemical sputtering; however, the considerable uncertainties involved allow for other interpretations. On JET [128], the Φ_C/Φ_D ratios (typically ~ 0.1), are only estimated to within a factor of about two, which precludes any precise accounting of the sputtering mechanisms. On TEXTOR [350], the carbon influxes are open to different quantitative interpretation, partly because detailed edge temperature data were not available at the time.

Further uncertainties related to the evaluation of D–C and C–C sputtering rates are associated with the sheath voltage drop at the limiters, which accelerates the ions. Secondary electron emission can reduce the sheath drop [51, 138] significantly. The TFTR study [457] invoked this effect in order to obtain a fit. The effective value of secondary electron emission for actual limiter surfaces (nearly tangential to $\vec{B}$) is, however, uncertain (Section 3). With regard to self-sputtering, a further uncertainty is associated with the charge state mix, which is generally unknown, since the impact energy will vary greatly between C^+ and C^{6+}.

A large uncertainty is associated with surface roughness as it affects the strong increase in yield with increasing ion incidence angle as observed in laboratory accelerator experiments using samples with highly oriented, smooth surfaces. Increases of the yield by an order of magnitude were reported for pyrolytic graphite samples when the ion incidence angle was increased from normal to nearly tangential [181, 458]. For technical grade graphite samples, however, a much weaker dependence of yield on incidence angle was found [181]. Whether surfaces subject to the roughening influence of tokamak exposure will show a still weaker dependence is not known.

It thus appears that experiments are required with more comprehensive and accurate measurements of influxes, edge plasma conditions, sheath voltage drops and incident carbon charge states, in order to make progress along this avenue. Laboratory measurements of the yield are required for samples cut from tokamak exposed limiters and divertor plates and subjected to ion impact at high angles of incidence.

5.3.1.3. Effect of varying the carbon temperature

Since chemical D–C sputtering is expected to show a strong dependence on the graphite temperature (Figs 57a, 57b), this is obviously a relationship to look for. One of the arguments for D–C chemical sputtering not being important in JET Ohmic discharges [367] is the lack of any observed change in limiter carbon influx as the limiter heats up to ~1400 K. In contrast, for JT-60 NBI discharges it has been concluded that D–C chemical sputtering is important [459], although this conclusion is based on C VI radiation and on inferred graphite temperatures. On T-10 [460], the radiation from the limiter did not rise when the measured limiter temperature was in the interval for maximum D–C chemical sputtering, ~800 K, although this radiation level did show a rise in close correspondence with RES above 1500 K (Fig. 57b).

At any given instant, a large range of surface temperatures will exist across the face of a limiter under plasma exposure. Thus, at all times, there may be some points at the limiter where maximum D–C chemical sputtering occurs and a simple clear-cut thermal signature therefore might not be expected. Thus, in order for this type of test to be conclusive, detailed mappings of the surface temperature are required together with an assessment of the impacting spatial distribution of flux and energy. Since such analyses have not as yet been reported, these tests are inconclusive.

In the all-graphite TM-G tokamak, the vessel temperature was varied from 20°C to 350°C; virtually no change was observed in the spectroscopically measured carbon influxes [461]. The effective yields were observed to remain at approximately 0.03 (ratio of C influx to H outflux). Although this temperature variation would not be expected to result in significant variation of H–C chemical sputtering for low energy ion impact (Figs 57a, 57b), the authors of Ref. [461] "concluded that chemical sputtering was apparently unimportant in the sputtering of the graphite during the discharge" and that, within experimental uncertainties regarding the influxes, outfluxes and ion impact energies, the observed carbon influxes could be accounted for by physical sputtering, including self-sputtering. The TM-G plasma was found to be remarkably clean [380], with oxygen levels an order of magnitude below the carbon levels, and $Z_{eff} < 1.4$ for the entire density range $2 \leq \bar{n}_e \leq 8 \times 10^{19}$ m^{-3}. It is also noted that these low Z_{eff} values were obtained at rather low values of $\bar{n}_e/j$, (1–4) $\times 10^{19}$ MA$^{-1}\cdot$m^{-1}; in this range, JET, for example, has significantly higher levels of Z_{eff} (Fig. 52a). The edge temperatures on TM-G [461], however, are rather low (~10–15 eV at $\bar{n}_e \simeq 5 \times 10^{19}$ m^{-3}) compared with those of JET (Fig. 2, Section 2).

5.3.1.4. Special tests of chemical sputtering

Each of the foregoing type of tests for chemical sputtering could, in principle, decide the issue if sufficient experimental information were obtained. At the present time, the most convincing evidence has been obtained from special tests, which are reviewed below.

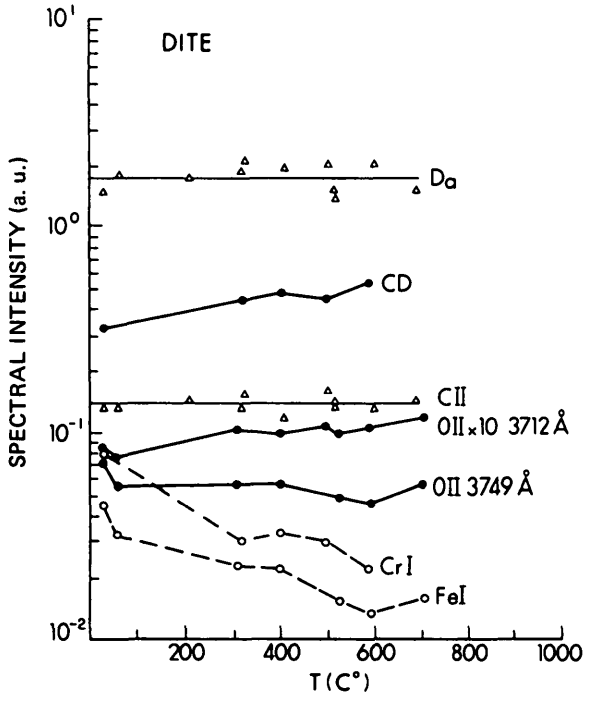

FIG. 64. DITE: Integrated spectral line intensities as a function of the probe limiter temperature in successive similar deuterium discharges at t = 210 ms. The probe limiter is at r_{PL} = 25.5 cm, where heating by the plasma is insignificant [365].

(a) Heated probe/limiter in DITE

Pitcher et al. [365] deployed a graphite probe limiter in DITE, incorporating an internal heating element and surface Langmuir probes. The probe limiter, maintained at various temperatures, was viewed spectroscopically during deuterium discharges, and the results are shown in Fig. 64. Heating of the surface by the plasma was insignificant for the case shown, with the probe limiter at the same radius as the main limiters, and so the entire graphite probe was at the same temperature. The Langmuir probes provided information on the local plasma conditions. No change in the D or C influxes was observed as the graphite temperature was changed over the range 30–400°C where D–C chemical sputtering is found to be strong in laboratory tests. The CD signal, presumably indicative of hydrocarbon formation, increased by a factor of ~ 1.7 as the temperature was raised, indicating the existence of chemical sputtering but at an insignificant level compared with total carbon sputtering (as evidenced by the C II signal). Metal influxes dropped with increasing graphite temperature, evidently due to some clean-up process. The calculation of $\Phi_{in}^{C}/\Phi_{in}^{D}$ was complicated by interpretative uncertainties regarding Φ_{in}^{D}, but it was as low as 0.02 (assuming corrections to Φ_{in}^{D} for the H_α signal from cx neutrals outside the field of view) or as high as 0.08 (assuming the traditional Johnson–Hinnov H_α factor).

The absence of significant chemical sputtering was attributed to (a) the high fluxes compared with those found in laboratory experiments, since the yield is known to decrease with flux [440, 449], or (b) surface metal impurities; such impurities are also known to decrease the yield [335, 423, 450, 451].

In discussing this DITE study, the authors of the PISCES high flux chemical sputtering study [449] conclude that the DITE observation of an increase of the CD signal by a factor of 1.7 as the temperature was raised corresponds closely to the PISCES result for low impact energy (see also Ref. [440]) and that, therefore, H–C chemical sputtering actually occurred. This still leaves unexplained the lack of change in the C II signal with temperature in the DITE experiment. Possible explanations are that the contribution of C–O sputtering was underestimated or that metal contamination suppressed the H–C chemical sputtering. A third possible explanation is that the carbon returns to the limiter before the CD_4 has been broken down to C^+. Langer and Ehrhardt [280] have modelled the CD_4 breakup for the conditions of the DITE experiment. They find that a significant fraction of the CD_4 returns to the limiter as neutrals (CD_3, CD_2, CD, C), simply due to geometry. CD_4 ions are produced quite near the limiter and, although ion transport is not modelled, it is possible that much of the CD_4 which is ionized is swept back to the limiter (as CD_4^+, CD_3^+, CD_2^+, CD^+) by the SOL frictional and electrostatic forces before breaking down to C^+.

(b) Sniffer probe in TEXTOR

Phillips et al. [453, 454] deployed a special sniffer probe in TEXTOR, incorporating a heatable and biasable graphite element inside the sniffer head, placed in the SOL so as to receive a high plasma flux ($\sim 10^{18}$ cm$^{-2}\cdot$s^{-1}) along $\vec{B}$. The gases produced in the graphite element were detected by a quadrupole mass analysing detector. For the sniffer probe located just outside the LCFS, the main product was found to be CO, although TEXTOR is virtually an all-carbon tokamak. The yields were $(4–6) \times 10^{-2}$ CO/D(H). The methane production was lower: 8×10^{-3} CH_4/H and 1.5×10^{-2} CD_4/D for graphite at room temperature and at floating potential; at temperatures of around 500°C, methane production increased by a factor of two. Biasing the graphite element (change of the ion impact energy) decreased the methane yield at room temperature and increased it in the highest temperature range.

These tests demonstrate that even in a tokamak with very high internal surface coverage by carbon, the oxygen level can be sufficiently high to dominate chemical sputtering. With regard to hydrogenic chemical sputtering, Phillips et al. conclude that the chemical sputtering yield can be comparable to the hydrogenic physical sputtering yield [454].

(c) The H_α line profile as evidence of CH_4 in DITE

Fielding et al. [129] recorded the H_α line profiles which resulted from puffing of H_2, D_2 and CH_4 into the DITE edge. The profiles resulting from H_2 and D_2 showed a characteristic 'shoulder' associated with ~ 3 eV neutrals, presumably F–C atoms, while the H_α profile resulting from CH_4 puffing showed no shoulder. When the graphite limiter was viewed in natural (no puff) H_α light, a strong shoulder (3 eV) was observed — evidence that H_2 rather than CH_4 determined the shape of the H_α line. It was concluded that methane production did not dominate the recycle. Since the chemical sputtering yield recorded in laboratory experiments can reach ~ 0.1 CH_4/H^+, i.e. 0.4 H/H^+ (Figs 57a, 57b), it is clear that such high

chemical sputtering rates were not present in this tokamak experiment.

(d) Measured oxygen fluxes in the SOL of DITE

Matthews [142] has developed a real-time impurity ion analyser and deployed it in the DITE SOL. He has recorded oxygen fluxes about equal to carbon fluxes, implying that oxygen chemical sputtering can be strong in the DITE SOL, a point noted variously above.

(e) Effect of limiter biasing

In T-3M [462], the C III signal from the graphite limiter was found to change insignificantly when the limiter was biased to increase the ion impact energy. This observation would appear to imply that chemical sputtering was more important than physical sputtering, but, since oxygen signals were not recorded, the type of chemical sputtering (O or D/H) is not clear.

5.3.1.5. Conclusions regarding the carbon production mechanisms

It is evident that the carbon production mechanisms in carbon tokamaks are complex, contradictory and unresolved. A large part of the difficulty in understanding this situation is the lack of basic data on the SOL conditions of the different machines. The edge temperature is undoubtedly a major factor and may explain much of the difference between machines. For tokamaks with high edge temperature, such as JET, physical sputtering is likely to be very important — particularly since self-sputtering by highly charged carbon ions will be quite strong. The role of oxygen can clearly be a major one. Assuming that the oxygen is initially released at the walls by some chemical process [433, 463, 464], on might expect considerable variation among tokamaks operating with different wall temperatures; also, the precise form of carbon on the wall, the degree of metal deposition and other chemical variables of the surface would be important factors. The recycle pathways of oxygen will be dependent on the specific SOL plasma conditions; oxygen released from the wall will reach a steady state balance in its distribution between wall, limiter, SOL plasma and main plasma — in a way which will be largely governed by the SOL quantities of n_e, T_e, λ_n, λ_T.

In principle, all of these complexities can be resolved by the acquisition of sufficient edge data, and it is certainly necessary to implement such investigations. For the present time, with regard to carbon *sources* at limiters (note that *transport* must also be considered before assessing the overall importance of an impurity mechanism, Section 5.5), the following tentative conclusions can be put forward:

- In most tokamaks, hydrogenic chemical sputtering of carbon is not dominant, although it may be comparable to hydrogenic physical sputtering.
- Oxygenic chemical sputtering of carbon is often important, particularly in tokamaks with low edge temperatures, or in tokamaks which have high oxygen levels due to, for example, poor conditioning.
- Physical (D–C and C–C) sputtering tends to be dominant in tokamaks with high edge temperatures.

Taking into consideration that carbon is quite susceptible to oxygenic sputtering and, to some degree, also to hydrogenic chemical sputtering, there is a clear incentive to explore the potential of other low-Z materials for edge surfaces such as B, Be and Li (see Section 7).

5.3.2. Carbon impurity production at high temperature

As discussed above, a process known as RES occurs at high operating temperatures (>1200°C) [465]. The mechanism has been extensively studied with ion beams and is quite well understood. Energetic ions produce interstitials in the lattice which migrate to the surface and sublimate at temperatures much below that normally occurring during simple thermal processes [466]. Thermal sublimation relative to sputtering becomes important only at higher temperatures (≥2300°C). In large tokamaks, such as JET and TFTR, additional heating leads to very high power loadings on the limiters, and surface temperatures in the range 2000–3000°C have been observed [339, 465]. These high temperatures have been found to be accompanied by very high influxes of carbon, termed the 'carbon bloom'. These influxes lead to plasma dilution and also to reduced neutral beam penetration. Since the carbon influx occurs within one or two seconds after the start of heating, it can lead to a rapid decrease in the D–D fusion reaction rate. So far, the surfaces have not been sufficiently well diagnosed to know whether the onset of the carbon influx is due to RES or to thermal sublimation. It is possible that the problem becomes progressively worse as the temperature increases, with the two processes overlapping. It seems clear, however, that the high surface temperature is the main cause of the high carbon influx. These high temperatures occur principally at the edges of

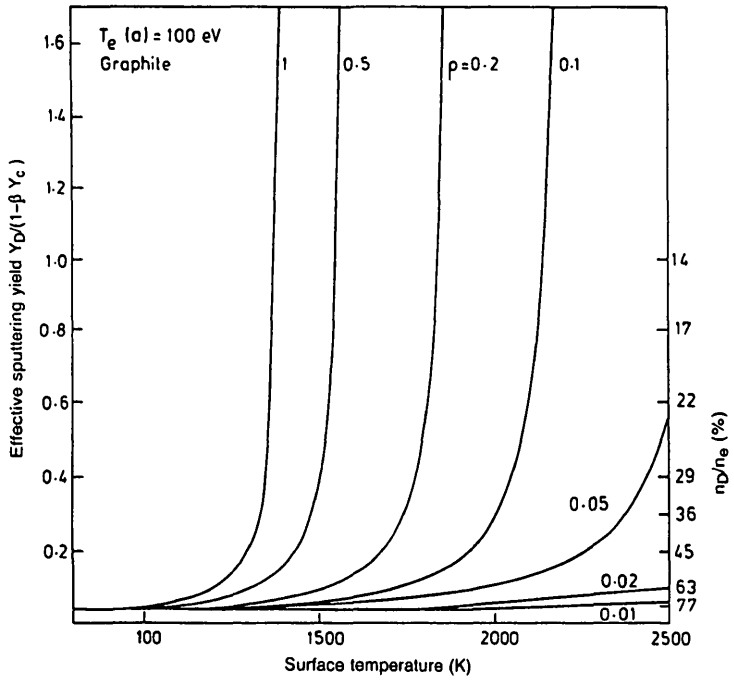

FIG. 65. Approximate effective sputtering yield for carbon at high temperatures, taking into account self-sputtering and radiation enhanced sublimation. T_e = 100 eV. ρ is the fraction of the impurity ions which return to the high temperature area ('hot spot') were the self-sputtering yield can exceed unity.

limiter tiles, where the gaps between the tiles constitute an area which is normal to the magnetic field lines. The carbon bloom was observed both in the configuration with the inner wall as a limiter [339] and in the divertor configuration in JET. The problem is aggravated when the alignment of the tiles is imperfect. Very high tolerances are required, with alignments better than 0.5 mm being necessary to avoid excessive heat loads.

The high carbon self-sputtering yields ($Y_C > 1$) due to RES can, in principle, lead to a runaway effect [467], since in steady state the effective sputtering yield Y is given approximately by

$$Y = \frac{Y_D}{1 - \rho Y_C} \tag{5.4c}$$

where Y_D is the deuteron sputtering yield, Y_C is the self-sputtering yield, and ρ is the fraction of the impurity ions which return to the area at high temperature, i.e. the area where the self-sputtering yield can exceed unity. As the RES yield increases with temperature, the effective yield reaches infinity. The result obtained using the data from ion beam experiments [466] for different values of ρ are shown in Fig. 65 for an edge temperature of 100 eV. It is assumed that the fraction ρ at the surface is of high temperature, while the rest of the surface is assumed to remain at a temperature below that at which RES takes place. It is to be noted that ρ is strictly defined as the fraction of the incident flux which hits the surface with the high sputtering yield, not as the geometrical fraction of the limiter surface. When the whole surface is heated, the effective sputtering yield increases rapidly at ~1400 K; when the fraction of the surface which is heated is less than 1%, then it has virtually no effect on sputtering.

In practice, no runaway effect occurs, since the additional radiation from the injected impurities leads to reduced edge temperature, which results in lower ion energies and reduced power flow to the limiter. This is discussed in more detail in Section 6.2. The same effect will, in principle, occur for thermal sublimation. Nevertheless, the increased impurity influxes clearly have deleterious effects.

Since in present devices the problem of carbon impurity production occurs locally, it could be substantially alleviated by obtaining a more uniform power loading on the limiters or the divertor target plates. It is notable that no evidence of a carbon bloom has been reported from DIII-D or JT-60, despite the fact that

the power densities in the plasma of these devices are equal to or greater than those in JET and TFTR. Nevertheless, the engineering problems of achieving the high tolerances necessary in large devices are formidable. Another approach suggested as a solution to the problem is the sweeping of the plasma contact point across the surface; however, this also poses significant engineering difficulties. The high power loadings on limiters or divertor target plates are recognized to be one of the major engineering obstacles to the successful operation of fusion reactors.

5.4. Explanation of the observed impurity influxes

Much of the preceding part of Section 5 has already dealt with attempts at a quantitative explanation of the magnitude of the observed impurity influxes in terms of sputtering and other release mechanisms. For further progress, a number of developments will be required:

- Quantitative influx spectroscopy should be made more accurate by calibration, using known influxes of impurities (from puffing, etc.) into the edge region of tokamaks, with exactly measured local plasma conditions.
- The charge state distribution of impurity ions striking the surfaces should be measured [142]. The energy of the impacting ions should also be measured, since there are uncertainties concerning the sheath potential drop and the amount of energy gained by the impurity ions in the pre-sheath.
- Physical and chemical sputtering yields need to be established more accurately for actual tokamak operating conditions. This requires the use of: high flux densities ($\gtrsim 10^{18}$ cm$^{-2}\cdot$s^{-1}); materials samples taken from tokamaks, which are roughened and have redeposited layers, surface impurities, etc.; and combined measurements of fluxes of D, C and O. The effects of the angle of incidence on the yield need to be established under realistic conditions of surface roughness, etc.
- For any impurity source of interest in a tokamak, it is essential that the local plasma conditions be accurately measured for a distance of the order of 5 cm inside of the source. The influxes of D, C, O and metals are required, plus an indication of whether steady state has been attained ($\Phi_{in} = \Phi_{out}$). Since the incident fluxes of each species may vary spatially across the limiter in different ways, the e-folding lengths of each species are required.

The spatial distribution of the ionization source is as important as the magnitude of the influx, since it controls the central impurity levels (see Section 5.5). The source mechanism can be expected to significantly influence the velocity distribution of the neutral influx. Consider, for example, the case of carbon:

(a) *D-C physical sputtering.* Experiments [133], employing a 1.5 keV argon ion beam bombarding a graphite target and using laser induced fluorescence to measure the atom density and velocity, confirm that such physically sputtered carbon atoms have a velocity distribution that is remarkably well approximated by a Thompson [468] distribution with a surface binding energy $U_0 = 8.3$ eV. For light ion sputtering, simple momentum transfer considerations [336] indicate that the Thompson distribution would be expected to have a rather low energy cut-off, $E_{max} = E_0(1 - \gamma)\gamma - U_0$, where E_0 is the impact energy and $\gamma = 4\, m_1m_2/(m_1 + m_2)^2$. Thus, for example, for D^+ on C, with $T_{LCFS} = 50$ eV, $\lambda_T = 4$ cm, $\lambda_n = 2.7$ cm (it is necessary to allow for the fact that not all of the sputtering occurs at the LCFS), and assuming an ion impact of $E_0 = 2$ kT + 3 ZkT, one finds a maximum carbon atom energy of 54 eV and an average energy of 9.5 eV. For lower edge temperatures the carbon energies can be very low indeed; example: for H^+ on C, $T_{LCFS} = 10$ eV, $\lambda_T = \infty$, $\lambda_n = 2$ cm, then $E^C_{max} = 1.9$ eV and $\bar{E}^C = 0.81$ eV.

(b) *C-C physical sputtering.* The Thompson velocity distribution would now be expected to have a cut-off at $E_{max} \simeq E_0$. This can result in substantially higher sputtered atom energies; example: for C^{4+} on C, $T_{LCFS} = 50$ eV, $\lambda_T = 4$ cm, $\lambda_n = 2.7$ cm, then $E^C_{max} = 700$ eV and $\bar{E}^C = 34$ eV.

(c) *Evaporation and radiation enhanced sublimation.* It is known [441] that the average carbon atom release has a temperature comparable to the substrate temperature, i.e. ~ 0.1 eV.

(d) *Chemically sputtered carbon as CH_4, CO, etc.* The effective velocity distribution of the neutrals is not clear in this case. If only direct molecular ionization is taken into account, the neutral energy is presumably very low. Simple molecular breakup would be expected to lead to carbon energies of ~ 0.3 eV, in the case of methane [280]. The actual breakup pathway, however, will, to some degree, involve charged radicals which will be efficiently heated by ion collisions before their final breakup, partly into neutrals, which may therefore be quite hot. Attempts to model these complex pathways are in progress [280].

It is evident that if the impurity generation mechanism is uncertain, then the neutral velocity distribution (and thus the ionization spatial distribution) will be as uncertain as the magnitude of the expected influx. Nevertheless, it is of interest to compare observations of spatial distributions with calculations. An example of a radial profile of C I in DITE [123, 428] has been given in Section 5.3. In the physical sputtering model, D^+ on C only (no self-sputtering) was assumed and $\bar{E}^C = 4$ eV was calculated for this case ($T_{LCFS} = 15$ eV, $\lambda_T = \infty$, $\lambda_n = 3$ cm). Inclusion of self-sputtering would increase $\bar{E}^C$, making the predicted radial distribution more extended. For 'chemical sputtering', $\bar{E}^C = 0.5$ eV was assumed (0.2 eV gave about the same result). It is possible that chemical sputtering involves higher energies than this; considering the important role of oxygen sputtering as indicated in DITE (see Section 5.3), this might even turn out to be a necessary conclusion.

A non-spectroscopic measurement related to the neutral velocity distribution was carried out using the impurity control limiter experiment on DITE [142]. In this case, the carbon sputtered onto the walls behind the impurity control limiter was measured and was found to be in good accord with model calculations based on physical sputtering and on a Thompson distribution (Fig. 66). Since the discharges in which this effect was observed were mainly in helium, this experiment was presumably not complicated by the uncertainties of chemical sputtering.

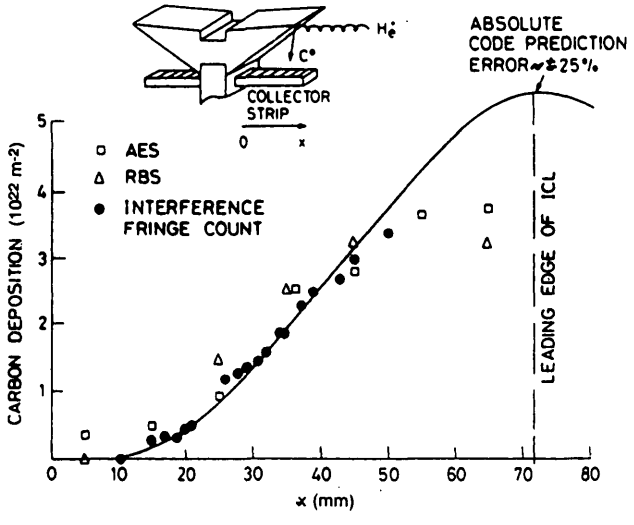

FIG. 66. DITE: Thickness of the carbon film deposited on a collector underneath an impurity control limiter (ICL) tile, obtained from a variety of measurements and from the code prediction [142].

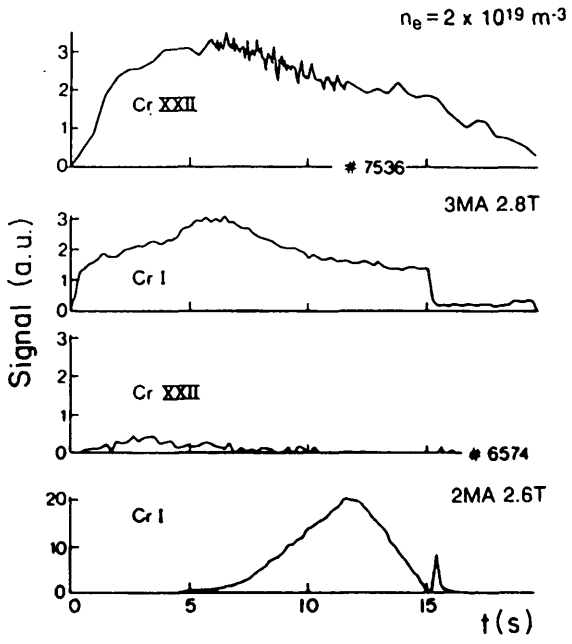

FIG. 67. JET: Intensities of Cr I (∝ chronium influx) and Cr XXII (∝ Cr density in the plasma) for the cases of sputtered Cr (top pair) and evaporated Cr (bottom pair) [128].

5.5. Impurity ion transport

5.5.1. One-dimensional modelling

Impurity generation is not necessarily damaging to tokamak operation. If the impurities are ionized near the source and return to it directly, then there is no net erosion and the main plasma is not contaminated. That such situations can exist is indicated in Fig. 67 [128]. For JET discharge 6574, the carbon limiter, contaminated with Cr, became hot late in the discharge and Cr evaporated from it, as shown by the Cr I signal directly from the limiter; however, virtually no Cr (Cr XXII) was seen in the centre of the plasma. By contrast, shot 7536 — a more conventional case characterized apparently by physical sputtering only — showed low (Cr I) influx throughout, but relatively high central levels (Cr XXII). The qualitative explanation is that the slow evaporated atoms were ionized in the SOL near the limiter, where they were subject to drag and electrostatic forces associated with the SOL plasma flow to the limiter and promptly returned to the surface. The faster sputtered atoms, by contrast, penetrated the plasma to greater distances where the limiter directed forces were weak or absent, and the resulting ions had a greater probability of reaching the core plasma before eventually returning to the edge. A

quantitative description of these processes is difficult, but clearly necessary.

First, we briefly consider the overall impurity transport picture of the tokamak. Impurity transport within the *main* plasma is a much studied subject [469–478] and will not be dealt with in any detail here. Such studies are based either on natural impurities or on injected ones, e.g. from laser ablation. These studies generally start from a point fairly far into the plasma radially, i.e., the complex processes near the edge and in the SOL are essentially ignored, and the intensity and radial location of successive rings of the different ionization stages are measured and modelled. Such studies provide information on $D_\perp$ and v_{in} for the main plasma. In some circumstances, a very high v_{in} is measured, associated theoretically with neoclassical impurity transport [479], and experimentally with impurity accumulation, non-steady-state conditions and even radiation collapse. Often, however, v_{in} is found to be low and the transport is dominated by diffusion with $D_\perp^{imp} \approx D_\perp^{fuel} \simeq 1\ m^2 \cdot s^{-1}$ and $v_{in} \simeq -D_\perp r/a^2$ [469–478]. Whatever the form of the central transport, however, the boundary conditions must always, in a sense, be controlling — and it is therefore critical to understand the latter in order to deal with the ultimate question of relating the central impurity density $\hat{n}_{imp}$ to the neutral impurity influx Φ_{in}^0. For the case of low v_{in}, this relation appears, in principle, to be quite simple and dominated by conditions near the edge; the conditions within a few centimetres of the LCFS set the level of $\hat{n}_{imp}$, with little sensitivity to processes elsewhere in the plasma.

We consider the work of Engelhardt and Feneberg [310], which provides a simple and powerful model for relating central impurity levels to edge conditions. The same model was applied in Section 4.6 to the fuel species. Consider, therefore, Fig. 41 (Section 4). Over a plasma surface area A_p, a uniform neutral influx of impurities, Φ_{in}^0/A_p, is assumed. All the neutrals are assumed to be ionized at a distance λ_{iz}^0 inside the LCFS.

Assuming perpendicular transport to be governed by diffusion, the resulting impurity ion density profile is very simple: a linear (in slab geometry) decay to a level $n_{imp}(a)$ at the LCFS and a profile inside $r = a - \lambda_{iz}^0$ which only gradually 'backfills' up to a constant value in reaching steady state. One thus has

$$\Phi_{in}^0/A_p = \Gamma_{out}^+ \approx D_\perp \hat{n}_{imp}/\lambda_{iz}^0 \qquad (5.5)$$

Using the same boundary conditions as discussed in Section 4.6 [147], we can show that for the impurities

$$\Gamma_{out}^+ = D_\perp(\hat{n}_{imp} - n_{imp}(a))/\lambda_{iz}^0 = D_\perp \frac{n_{imp}(a)}{\lambda_{SOL}} \qquad (5.6)$$

where λ_{SOL} is the characteristic decay length of impurities in the SOL. Thus,

$$\hat{n}_{imp} = \frac{\Phi_{in}^0(\lambda_{iz}^0 + \lambda_{SOL})}{D_\perp A_p} \qquad (5.7)$$

and the edge plasma properties are seen to play a further role. If ionization is in the SOL, $\lambda_{iz}^0 < 0$, then it can be shown that

$$\hat{n}_{imp} = \Phi_{in}^0 \lambda_{SOL} \exp(\lambda_{iz}^0/\lambda_{SOL})/D_\perp A_p \qquad (5.8)$$

These simple models often give a reasonable prediction. Consider, for example, a typical JET case where carbon sputtered from the limiter governs Φ_{in}^0. Spectroscopic measurements [128] (C II, C III light) of influx (also approximately confirmed by sputtering calculations based on the Langmuir probe measurements of the JET SOL properties [198]) give Φ_{in}^0/Φ of order 10^{-1} and thus Φ_{in}^0 of order $10^{21}\ s^{-1}$. For JET, $D_\perp^{SOL} \sim 0.5\ m^2 \cdot s^{-1}$ is typical [209] and $A_p \simeq 200\ m^2$. From the Langmuir probe measurements, one can measure or calculate $\lambda_{iz}^0 \simeq \lambda_{SOL} \simeq 2$ cm [46]. These values of $D_\perp$ and $\lambda_{SOL}(\lambda_n)$ are for the D^+ plasma, but are presumably indicative of impurity behaviour. Inserting these values into Eq. (5.7) gives $\hat{n}_c \simeq 4 \times 10^{17}\ m^{-3}$, i.e. a few per cent of $\bar{n}_e$, which is, in fact, of the order of the central carbon levels measured in JET [128].

As in the case of the fuel ions, a number of further refinements to the simple model can be readily incorporated. A weak, anomalous pinch, $v_{in} \simeq -2SD_\perp r/a^2$ (with $S \simeq 1$), often appears to be necessary to explain slightly peaked $n_{imp}(r)$ profiles. For a pinch of this form, the flat part of the profile is simply multiplied by a factor $\exp[S(1 - r^2/a^2)]$ (Fig. 41). For stronger pinches the plasma may never attain a steady state, since the impurity accumulation can cause sufficiently high radiation levels in the core to disrupt the discharge. Assuming, however, that a steady state is reached, edge processes may still establish a 'base level', given by Eq. (5.7) or (5.8), on which the inward convection builds the central impurity density profile. This would require that the diffusive velocity at the edge, $D_\perp/\lambda_{iz}^0$, exceed local convective velocities, which seems plausible considering the small value of λ_{iz}^0.

The 1-D analytic formulations have been summarized and extended by Fussmann [470] to their most

complete form to date, including definitions which clearly distinguish quantities such as the particle replacement/confinement time from the decay time (characteristic decay time of the central impurity density following injection).

5.5.2. *Two-dimensional modelling*

The simple 1-D model is valuable and powerful. The principal deficiency of the approach is, however, the assumption of toroidal/poloidal symmetry of both source and sink. Consider first the sources. For a wall impurity source, due for example to charge exchange sputtering, the assumption of a uniformly distributed source may be a good approximation. For a limiter discharge, however, the limiter is often the dominant source and it is highly localized. At a first glance, this fact would seem to totally invalidate the use of the simple formulas, Eqs (5.7) and (5.8). Fortunately, however, the localization of the source only changes the dwell time of impurities in the SOL, τ_{SOL}, which results in a fairly weak influence on the value of $\hat{n}_{imp}/\Phi^0_{in}$ calculated from Eq. (5.7): λ_{SOL} only varies as $\tau^{1/2}_{SOL}$ and the effect is further diluted, since λ_{SOL} is added to λ^0_{iz}. Thus, provided the neutral ionization occurs fairly deeply inside the LCFS, the impurity ions can distribute themselves somewhat along $\vec{B}$ before they have significantly diffused outward to reach the SOL. In this sense, a limiter source can be effectively uniform (to within a factor of two or so of the result from calculating $\hat{n}_{imp}/\Phi^0_{in}$ using Eq. (5.7)). This can be the case for the physically sputtered light impurities C and O, for which λ^0_{iz} may be 1–2 cm. The time required for the ions to reach the SOL is $\sim(\lambda^0_{iz})^2/D_\perp \sim 1$ ms, which can, depending on L_c, be comparable to the time required for an ion to move a significant distance along $\vec{B}$ around the torus. There are cases, however, where the ionization is not deep enough for any homogenization to occur and then the source is not even approximately uniform. A dramatic illustration of such a case — the JET chromium case — is given in Fig. 67. Consider also the divertor case and the impurities generated at the plates. This source is clearly non-uniform and, while in some circumstances there may be such a bad impurity 'leakage' out of the divertor plasma, into the main SOL and hence into the plasma inside the LCFS that the source is effectively uniform, this undesirable case should be rare.

Even if the source is uniform, the sink may not be. The simplest assumption for the sink is that the impurity continuity equation has a constant sink term for ions in the SOL of n_{imp}/τ_{SOL}, with $\tau_{SOL} = L_c/c_s$, c_s being the fuel acoustic velocity and L_c the connection length. The assumption of the simple term $\tau_{SOL} \sim L_c/c_s$ representing the SOL sink action for such uniform influxes was tested using the Monte Carlo impurity code LIM [480]. It was found that, for a wide range of SOL conditions and for the example of carbon as an impurity, the average dwell time of the ion in the SOL was (1 - 1.5) L_c/c_s for uniform influx.

At the other extreme of complexity is the case of a divertor plate impurity source (Section 7.3). Of lesser, but still considerable, complexity is the case of the limiter as a source and a sink. Experimentally, the simple model can, under some circumstances, for example for physically sputtered light impurities and low edge n_e, successfully relate the measured $\hat{n}_{imp}$ and Φ^0_{in} values to within a factor of two or three (see the JET carbon example in Section 5.5.1). At the present time, it is probably not possible to be more precise. There is also the problem that, for a limiter source, the plasma conditions just near the limiter are of great importance — much more so than for a wall source. The region just near the limiter, unfortunately, is complex and not well understood:

- Strong 2-D effects arise which are related to the abrupt transition from zero plasma flow velocity just inside the LCFS to the sonic velocities just outside the LCFS;
- The ambipolar electric field in the SOL, just approaching the limiter, is calculated to have radically different values in different models (see Section 3);
- The plasma flow to the limiters is often not ambipolar (see Section 10);
- Strong recycling of hydrogen at the limiters creates further 2-D effects, charge exchange recombination of impurities, charge exchange friction for the hydrogenic flow (thus changing the ambipolar electric field near the limiter), etc.;
- The impurity ionization is highly localized to the limiter region which can change the plasma background itself with 2-D Z_{eff} effects, impurity–impurity collisions, etc.;
- All of the above effects may change the local cross-field transport coefficients $D_\perp$ and v_{in}.

5.5.3. *Experimental tests of 2-D modelling*

It would appear that the best way forward may be to focus experiment and modelling on the limiter region itself, and to leave the ultimate, but more ambitious,

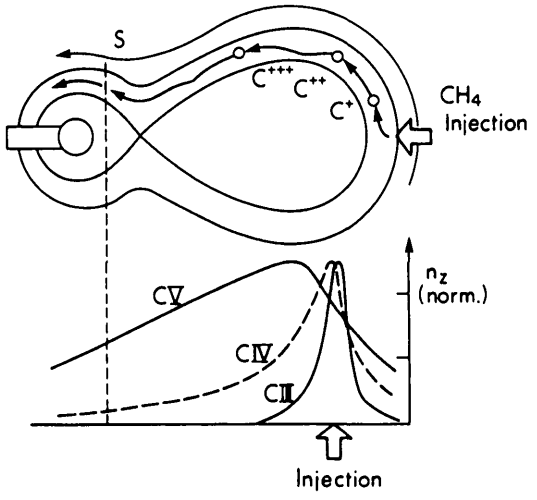

FIG. 68a. DIVA: Result of Monte Carlo calculation of a CH_4 injection experiment [187]. Boundary layer assumptions: flow velocity = 0.3 c_s, $D_\perp$ = 0.1 $D_{\perp\ Bohm}$, E = 0.5 T_{edge}/L, T_{edge} = 30 eV. Code results: T(C IV) = 50 eV, T(C V) = 70 eV; experimental results: T(C IV) = 40 eV, T(C V) = 80 eV.

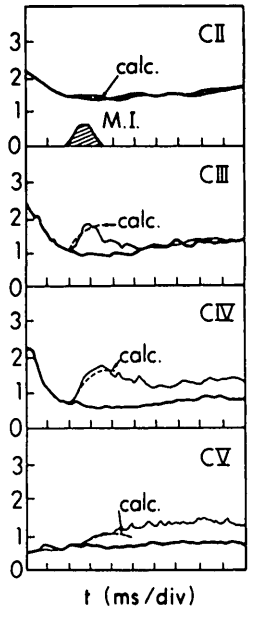

FIG. 68c. DIVA: Temporal behaviour of C II, C III, C IV, C V in a divertor, compared with calculation [187].

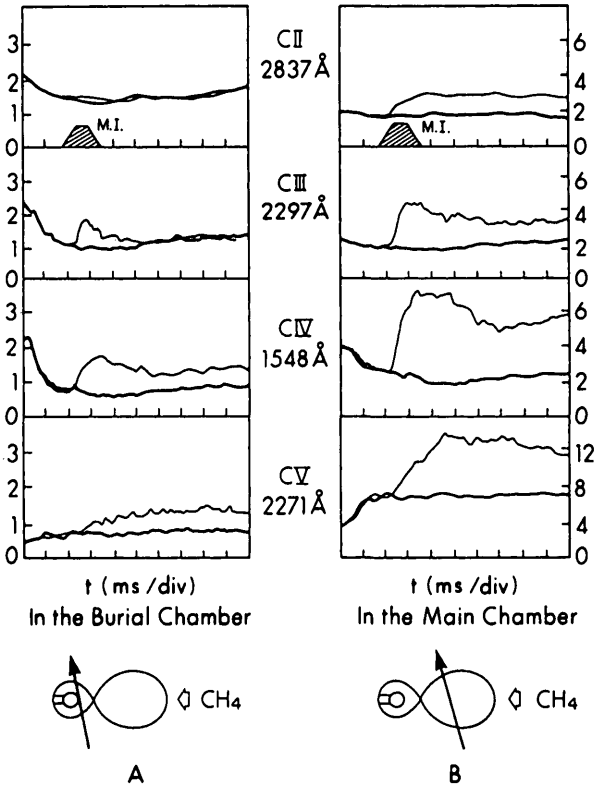

FIG. 68b. DIVA: Time development of the increase of the line intensity from ionization states of carbon ions in the burial chamber and the main plasma with methane injection (M.I.) for a diverted discharge. Thick lines without injection, thin lines with injection [187].

task of more precisely relating $\hat{n}_{imp}$ to Φ^0_{in} until impurity behaviour near the limiter is better understood. Appropriate experiments would include spectroscopic viewing of limiters in C I, C II, ..., O I, O II,..., etc., to establish the radial, toroidal and poloidal extent of each ionization cloud, the average impurity ion temperatures in each cloud, the relative and absolute intensities of each cloud, etc. These studies should include natural limiter impurity influxes as well as injected or puffed impurities from the limiter. Measurements of the charge states [142] and impact energies of impurity ions striking the limiter would provide much information on the limiter region, although processes occurring throughout the entire plasma are also significant.

Early experimental and modelling work in this area applied to the case of a divertor tokamak was reported by the DIVA Group [187, 481, 482]. Impurities such as CH_4 were puffed into the main chamber (Fig. 68a). The C II, C III, C IV and C V emission was measured in both the main and the divertor chambers as a function of time after the puff (Fig. 68b). As can be seen from Fig. 68a, no C II appears in the divertor chamber, because the parallel transport along the SOL requires a time longer than the ionization time of C^+. The case has been modelled using a Monte Carlo impurity transport code [482] (results are shown in Figs 68a and 68c). As can be seen, the experimental

observations are well reproduced by assuming in the code that the boundary temperature is 30 eV, the parallel plasma flow velocity is 0.3 c_s, the parallel electric field in the SOL is 0.5 T/L_c and the cross-field diffusion coefficient is 0.1 $D_\perp^{Bohm}$. This experimental/modelling work appears to provide the first direct evidence that impurities are transported along the SOL with velocities of the order of the hydrogenic ion acoustic velocity.

In DITE, spectroscopic experiments have been carried out in which impurity radiation in the vicinity of the limiter has been viewed, establishing the radial and toroidal extents of the different impurity neutral and ion clouds both for natural [123, 142] and puffed [122, 366] impurities (Figs 69). Figure 69a shows the measured [123] radial distribution of natural C I, C II and C III light at the DITE fixed limiter for 150 kA, 2 T, 5 × 10^{19} m^{-3} helium discharges. Also shown are LIM Monte Carlo impurity code [428, 480] results. A comparison of the experiment and modelling indicates that $D_\perp \simeq 0.5$ $m^2 \cdot s^{-1}$, a value similar to hydrogenic values found in SOLs, for example in JET [209].

Helium was puffed from the tip of a movable probe limiter (PL) on DITE (Fig. 69e) into helium discharges, and the toroidal extent of the He I and He II clouds was measured (Fig. 69b) [122]; the fixed limiters were at r = 0.26 m. Plasma conditions were measured with Langmuir probes. When the probe limiter was at r_{PL} = 0.23 m, the impurity clouds were less extended in the toroidal direction than for r_{PL} = 0.255 m, since the local plasma density was higher for the deeper location. Different tests were carried out, using the LIM code [483]. The importance of including in models the finite thermalization rate

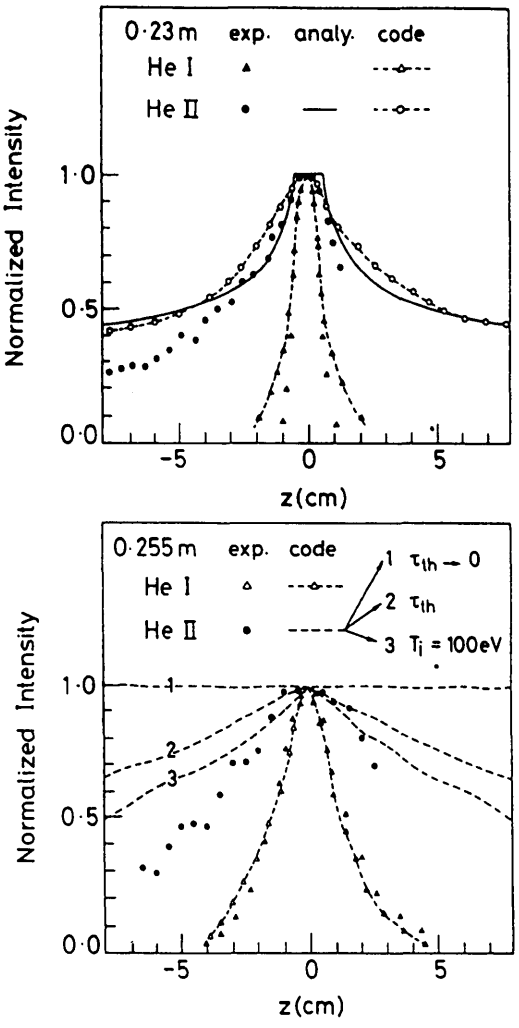

FIG. 69b. DITE: Toroidal viewing of He I and He II resulting from puffing of helium into helium plasmas from a probe limiter [122]. The radial locations of the probe limiter are: r_{PL} = 0.23 and 0.255 m. Fixed limiters are at r = 0.26 m. LIM code results [483] with different assumptions.

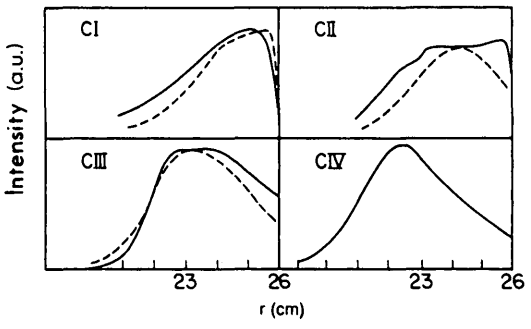

FIG. 69a. DITE: Radial spectroscopic profiles observed at the fixed limiter (solid lines) in a helium discharge. Code simulation (broken lines) assumes $D_\perp$ = 0.5 $m^2 \cdot s^{-1}$ [123, 428, 480]. Arbitrary vertical scale with experimental and code results matched at peaks. No experimental results for C IV.

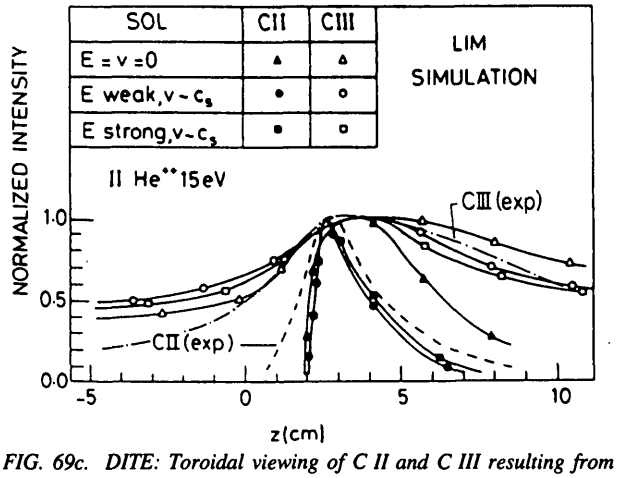

FIG. 69c. DITE: Toroidal viewing of C II and C III resulting from puffing of CH_4 from the side of the probe limiter into the SOL. Helium plasma [122]. LIM code results for different assumptions of the SOL plasma flow velocity and electric field [366].

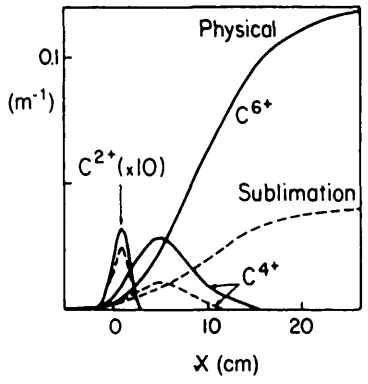

FIG. 69d. DITE: LIM code calculations. Complete radial profiles (toroidally integrated), showing that physical sputtering is approximately three times more effective at contaminating the centre than sublimation [484]. The vertical scale is for influx of one C atom per second per metre of poloidal length of the limiter.

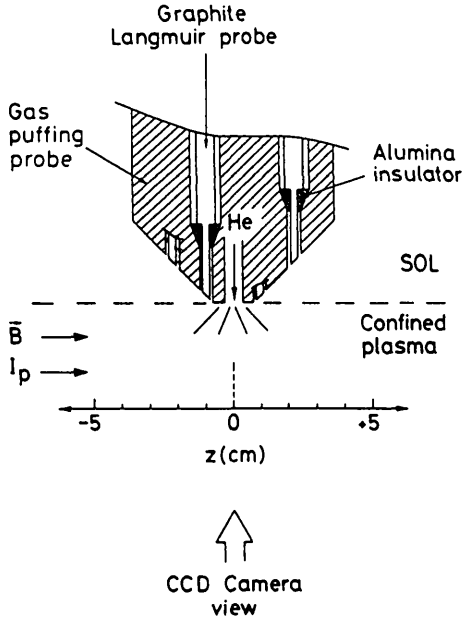

FIG. 69e. Camera view of the probe limiter puffing experiments (results in Fig. 68b).

for impurity ions was demonstrated by assuming instant thermalization ($T_{imp} = T_{plasma}$, taken to be the measured T_e). As can be seen for the case of r_{PL} = 0.255 m, this assumption results in very poor agreement with the observed He II radiation. Allowing for a finite (Spitzer) thermalization process and assuming a background ion temperature (unmeasured) equal to the measured background T_e, gave much better agreement for the case of r_{PL} = 0.255 m and excellent agreement for the deeper puffing. Since (background) ion temperatures in the edge have often been found to exceed T_e, the impact of using in the LIM code a background value of T_i = 100 eV was tested, with T_e as measured and allowing for finite thermalization; the results for the case of r_{PL} = 0.255 m showed a further improvement in the agreement with observation.

CH_4 was puffed from the side of the DITE probe limiter, and the toroidal C I, C II, C III radiation was measured [366] (Fig. 69c). Reasonable agreement with the experiment was obtained from the LIM code for the C II and C III distributions, assuming that the CH_4 inflow was effectively ~0.1 eV neutral carbon atoms. Different assumptions used in the code concerning the background plasma flow velocity in the SOL and the SOL electric field showed the importance of frictional force for impurity behaviour (Fig. 69c).

The measurements of the charge state distributions of C and O in the DITE SOL [142] have also been modelled using the LIM code (Table X). The discharges were Ohmic, 100 kA, D^+, $\bar{n}_e \sim 2 \times 10^{19}$ m^{-3}, with the probe about 15 mm behind the limiter. The plasma conditions were not measured for these particular discharges, but from similar discharges it was estimated that T_{LCFS} = 19 eV, $n_{LCFS} = 2.4 \times 10^{18}$ m^{-3}, λ_n = 1.6 cm, λ_T = 3.3 cm. Other plasma properties assumed in the LIM code were: $D_\perp = 0.5$ m$^2 \cdot$s^{-1}, inward pinch $v_{in} = -2D_\perp r/a^2$; geometry: a = 0.24 m, connection length = 3.5 m, slab-sided probe, cylindrical plasma shape. Charge exchange recombination was included. Since the sources of the C and O impurities were not known, a number of source options were tested in the code (Table X). Case A is for physical sputtering from the limiter due to D^+ bombardment (with the code, an average neutral energy $\bar{E} \approx 4$ eV was computed); as can be seen, there is a rough correspondence with the observed flux ratios, in that the lower 4(5) C(O) states are roughly equally represented, with the higher states being less common. Case B is for sublimation from the limiter ($\bar{E}$ = 0.1 eV) (e.g. for radiation enhanced sublimation and possibly also representative of chemical sputtering of the limiter); the agreement with the experiment is very poor: three quarters of the flux are calculated to be singly ionized. For cases C, D and E, a uniform wall influx of different neutral energies is assumed (1, 3, 6 eV, respectively) — possibly representing Franck-Condon molecular breakup of CO into energetic neutrals; again, broad agreement is found with experiment. Case F is simply the average of Cases A and D, i.e. wall and limiter sources of equal strength; this gives perhaps the closest agreement

TABLE X. DITE [142]
IMPURITY ION FLUXES OF DIFFERENT CHARGE STATE Z[a]

Impurity	Experimental model, case	Z = 1	Z = 2	Z = 3	Z = 4	Z = 5	Z = 6	Z = 7	Z = 8
Carbon		18	24	29	24	5			
	A	29	28	15	19	2	1		
	B	75	16	4	3	4	1		
	C	12	26	22	28	3	9		
	D	8	21	22	33	3	13		
	E	5	15	22	37	5	16		
	F[b]	20	27	20	28	3			
Oxygen		16	13	18	31	15	6	1	
	A	27	20	15	12	9	14	2	1
	B	77	11	4	3	2	3	0.4	0.2
	C	13	20	18	18	11	14	3	2
	D	8	14	18	21	14	20	4	2
	E	5	12	17	20	15	22	5	3
	F[b]	18	18	17	17	12	17	3	

[a] Experimental values from Matthews' probe in DITE edge plasma compared with LIM impurity code results for different source assumptions (cases defined in text).
[b] Case F is the average of cases A and D, with C^{6+} and O^{8+} omitted (to compare with experiment where these states were not measured).

with experiment, possibly confirming the conclusion drawn in Ref. [433] that wall and limiter sources are about equally important in DITE.

With regard to the relation between Φ_{in}^0 and $\hat{n}_{imp}$, the LIM code results [484] are shown in Fig. 69d, comparing the case of physical sputtering with chemical sputtering/sublimation from the DITE carbon limiter. The limiter shape is as follows: a blunt-nose poloidal limiter with a flat tip, 1.5 cm across, 45° on the sides, to 2.75 cm outside the LCFS, then radially outward to the walls. The physical sputtering production rate was calculated to be 3.3×10^{19} neutral carbon atoms per second per metre poloidal length; the sublimation rate was set to be equal. For a given influx, physical sputtering is about three times more effective at contaminating the centre than chemical sputtering/sublimation. Similar results have been obtained on ASDEX [335].

A similar LIM calculation of $\hat{n}_{imp}/\Phi_{in}^0$ was made for the JET chromium cases (Fig. 67). The nearly tangential limiter shape and the spatial distribution of metals deposited on the graphite limiters were allowed for [379, 418, 419]. For a value of $\Phi_{in}^0 = 10^{20}$ s^{-1} (Case A: JET discharge No. 7536, assuming physical sputtering; Case B: No. 6574, assuming $\bar{E} = 0.15$ eV), taking plasma edge parameters from probe measurements in each case and assuming different values of $D_\perp$, the code gave the results: Case A: $\hat{n}_{imp} = (7.6, 4.5 \times 10^{15}$ m$^{-3})$ for $D_\perp = (0.3, 1$ m$^2 \cdot$s$^{-1})$; Case B: $\hat{n}_{imp} = (0.097, 0.39 \times 10^{15}$ m$^{-3})$ for $D_\perp = (0.3, 1$ m$^2 \cdot$s$^{-1})$. (Note from Eq. (5.8) that for a source sufficiently deep in the SOL, as in Case B, $\hat{n}_{imp}$ is expected to increase with $D_\perp$.) Thus, the observed difference in contamination efficiency of two orders of magnitude or more (Fig. 67) can be quantitatively accounted for by assuming a value of $D_\perp \approx 0.3$ m$^2 \cdot$s^{-1} in the vicinity of the limiter. The contamination efficiency is highly sensitive to both the value of $D_\perp$ and the impurity production mechanism, thus providing a means of experimentally establishing these two critical aspects of impurity behaviour.

In conclusion, with regard to impurity ion transport in the edge: The situation for a limiter source/sink is rather complex and the applicability of simple expressions such as Eqs (5.7) and (5.8) is questionable. Progress can be made in unravelling the uncertainties associated with edge impurity ion transport, in addition to the impurity generation mechanism, by coupled experimental and modelling studies which focus on the

limiter region itself. Models available for such work [485] include analytic formulations [412, 486–492] as well as test particle [493] and Monte Carlo codes [124, 142, 424, 482, 494–501]. Fluid impurity codes [502–510], developed for divertor studies, could also be employed, but their assumption of high collisionality and instant thermalization of impurity ions is less applicable for limiter situations. More experimental measurements are required in well characterized SOLs, employing known calibrated impurity injections.

5.5.4. *Impurity screening*

Clearly, it would be desirable to establish quantitative definitions of concepts such as 'contamination efficiency' and 'impurity screening'. This objective has proven to be rather elusive and, while a number of definitions have been offered in the literature, none have gained widespread acceptance so far.

A simple and common definition of 'screening efficiency' is the fraction η_{sc} of the neutrals which are ionized within the SOL [205]; approximately,

$$\eta_{sc} = 1 - \exp(-\lambda_n/\lambda_{iza}) \tag{5.9}$$

where

$$\lambda_{iza} = v_0/\overline{\sigma v_i} n_e(a) \tag{5.10}$$

While large values of η_{sc} ($\rightarrow 1$) would generally be expected to correspond to small values of $\hat{n}_{imp}/\Phi^0_{in}$, there is no direct quantitative relationship between the two quantities. Furthermore, this definition makes too great a distinction between neutrals which are ionized just inside and just outside the LCFS; in fact, a source of neutrals ionized just inside the LCFS results in virtually the same value of $\hat{n}_{imp}$ as a source of neutrals ionized just outside the LCFS (compare Eqs (5.7) and (5.8)).

Claassen and Repp [486] extended the definition of η_{sc} to allow for both ion penetration of the LCFS and neutral penetration of the LCFS. The quantitative relation between η_{sc} and $\hat{n}_{imp}/\Phi^0_{in}$ remains unclear.

Fussmann [470] defines the 'penetration probability' $P_{pen}(r)$:

$$\Phi^+_{out}(r) = \Phi^0_{in} P_{pen}(r) \tag{5.11}$$

where $\Phi^+_{out}(r)$ is the *absolute* ion outflux through radius r (one may note that if the neutrals are all ionized outside radius r, then the *net* ion flux must be zero at r, with $\Phi^+_{out}(r) = \Phi^+_{in}(r)$). In particular, $P_{pen}(a)$ is the probability of penetration of the LCFS; Fussmann [470] defines the 'screening efficiency of the SOL' as

$$\eta^F_{sc} \equiv 1 - P_{pen}(a) \tag{5.12}$$

These definitions have the advantage of bringing the ion transport into the picture; however, there is again no simple connection between η^F_{sc} and $\hat{n}_{imp}/\Phi^0_{in}$. Indeed, for certain cases, a decreasing η^F_{sc} can correspond to a decreasing $\hat{n}_{imp}/\Phi^0_{in}$ [470].

One also wishes to be able to encompass the effects associated with the 2-D and 3-D aspects of impurity transport near the source/sink. For this purpose, one can define an impurity 'reduction factor' Rf [480]:

$$Rf \equiv \hat{n}_{imp}/\hat{n}^{ref}_{imp} \tag{5.13}$$

where $\hat{n}^{ref}_{imp}$ is the value calculated from Eq. (5.7) (which assumes uniform neutral influx) and $\hat{n}_{imp}$ is the value calculated for the actual (spatially localized) source (the same values of Φ^0_{in}, $D_\perp$, A_p are assumed in each case). The LIM impurity transport code was used to generate sample values of Rf [480]. For example, for $T_{LCFS} = 25$ eV, $n_{LCFS} = 8 \times 10^{18}$ m^{-3}, $\lambda_n = \lambda_T = \infty$, $D_\perp = 1$ m$^2\cdot$s^{-1}, $v_{in} = 0$, $a = 1.2$ m, $L_c = 40$ m, a value of Rf = 0.013 was obtained for a source of neutrals that are all ionized at a depth of 1 cm outside the LCFS and 2 cm along $\vec{B}$, away from a flat-sided limiter ($\hat{n}^{ref}_{imp}$ was thus calculated for $\lambda^0_{iz} = -1$ cm and $\lambda_{SOL} = (D_\perp L_c/c_s)^{1/2}$ in Eq. (5.8)). This means that such a localized source would be only ~1% as effective as a uniformly distributed source, both located at the same distance outside the LCFS (i.e., an approximation to the JET Cr cases described in Section 5.5.3). The Rf has to be calculated for each case of interest (T_{LCFS}, n_{LCFS}, λ_n, λ_T, $D_\perp$, v_{in}, L_c, limiter shape, ionization source location). One may eliminate the source location as a required input by calculating instead the spatial distribution of neutral ionization. The LIM code has been used to carry out such calculations, giving values of $\hat{n}_{imp}$; the appropriate definition of $\hat{n}^{ref}_{imp}$ now requires rethinking, since the ionization does not all occur at one radius. An arbitrary but convenient re-definition of $\hat{n}^{ref}_{imp}$ is

$$\hat{n}^{ref}_{imp} = \Phi^0_{in}\, \lambda_{SOL}/D_\perp A_p \tag{5.14}$$

with

$$\lambda_{SOL} = (L_c D_\perp/c_{sa})^{1/2} \tag{5.15}$$

i.e. the reference case assumes that all ionization

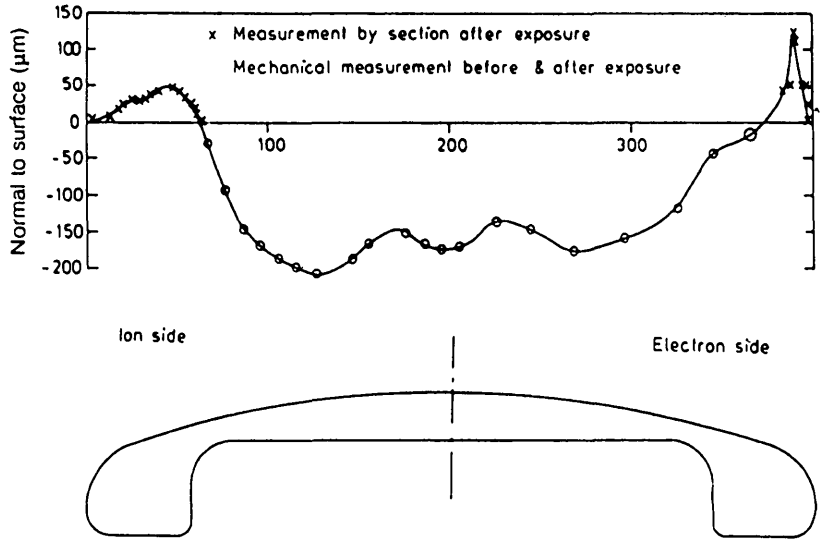

FIG. 70a. JET: Experimental measurements of erosion and re-deposition of carbon on the JET limiter tile 4, octant 4, exposed in 1986 [433].

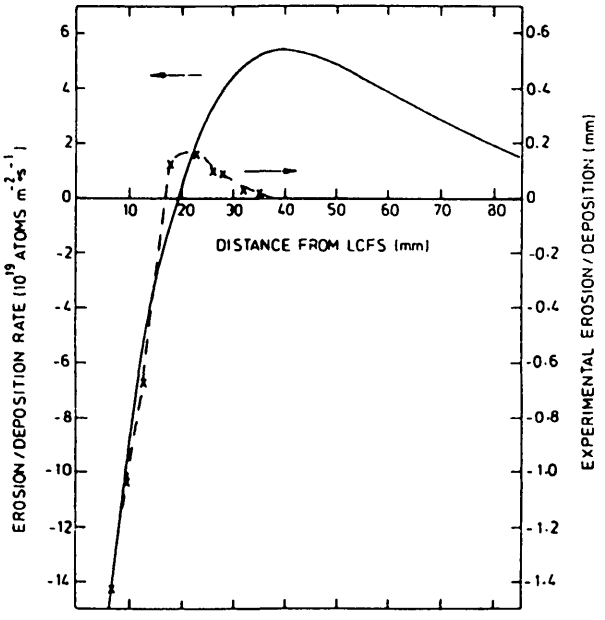

FIG. 70b. JET: Comparison of the theoretical erosion rate, calculated from Eq. (5.16), with the experimental erosion measured in the direction of the field lines [433]. Conditions assumed: T_{LCFS} = 50 eV, $n_{LCFS} = 10^{18}$ m^{-3}, λ_T = 0.04 m, λ_n = 0.02 m, D^+ ions, C limiter, impurity charge = 4. Normal incidence ion yields.

occurs uniformly along the LCFS. Values of Rf $\ll 1$ correspond to sources located deep in the SOL, near the limiter; values of Rf $\gg 1$ correspond to sources deep in the main plasma. Values of Rf have been tabulated for a variety of plasma conditions and impurity source assumptions [511].

5.6. Net erosion and re-deposition

The wall structure is gradually eroded by plasma contact, compromising the physical integrity of the fusion device. Fortunately, most of the removed material re-deposits elsewhere in the vessel, with only a small fraction being permanently removed by the vacuum pumps. Whether the re-deposition will occur where it is needed and whether the plasma erosion properties of the re-deposited material are as good as the original remains to be demonstrated.

It has been observed on JET [433, 491, 512, 513], TFTR [420, 421] and T-10 [254] that the limiters often suffer net erosion in the region closest to the LCFS, with net deposition further out (Fig. 70a) [433]. A qualitative explanation is that the sputtering is relatively stronger near the LCFS, where the temperature is higher, than further out; thus, assuming a simple re-deposition pattern, the material tends to be moved radially outward. A simple quantitative model has been developed [491] for this situation. For a carbon limiter, the *net* deposition flux density $\Gamma_{net}^{dep}(r)$ at a distance r from the LCFS is given by

$$\frac{\Gamma_{net}^{dep}(r)}{\Gamma_{D^+}(a)} = \frac{n_C(a)}{n_D(a)} (1 - Y_C(r)) \exp(-(r - a)/\lambda_{dep}) - Y_D(r) \exp(-(r - a)/\lambda_\Gamma) \quad (5.16)$$

where $\Gamma_{D^+}(a)$ is the fuel ion flux density at the LCFS, $n_C(a)/n_D(a)$ is the impurity fraction at the LCFS, Y_C is the C–C (self-) sputtering yield, Y_D is the fuel–C

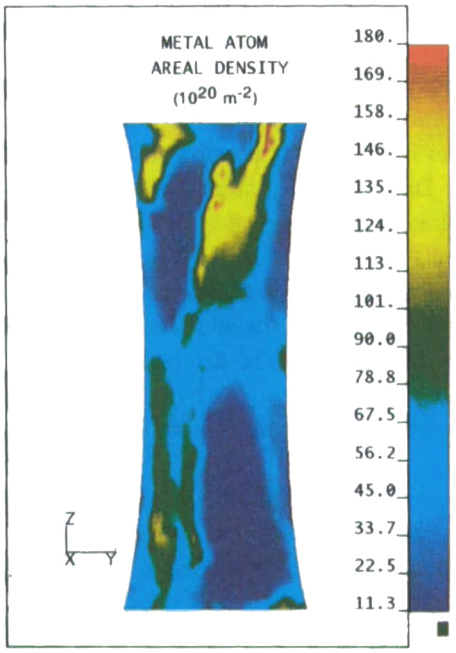

FIG. 71a. Beta backscatter measured spatial profile for metal deposits on a sector of the inner (graphite) bumper limiter of TFTR at the end of July 1987 after 9922 discharges, 70% of which were Ohmic [499].

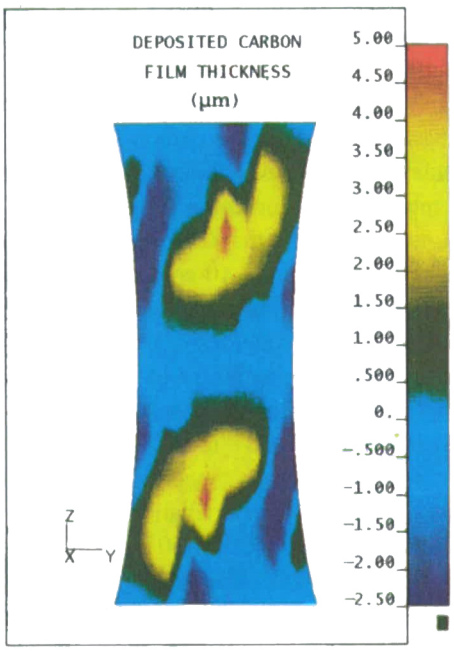

FIG. 71b. REDEP calculations of the spatial profile for carbon erosion and redeposition on the surface of the inner bumper for plasma conditions approximating those in the discharges resulting in the pattern of Fig. 71a [499].

yield, λ_{dep} is the deposition e-folding length and λ_Γ is the fuel flux e-folding length. One may note that other sputtering, e.g. by O, is neglected. It is not evident what value should be used for λ_{dep} (perhaps $\lambda_{dep} = \lambda_\Gamma$?). Equation (5.16) assumes a steady state and that all carbon removed from the limiter returns to the limiters, i.e. there are no other C sources or sinks in the system. Both Y_C and Y_D vary with r because of T(r) variations (the latter being taken from probe measurement, with the Y's then calculated). The use of a density ratio $n_C(a)/n_D(a)$ assumes that the impurities move with the fuel ion velocity; the actual value of this ratio is directly calculated from the assumption of C influx = C outflux.

Results are given in Fig. 70b; for the values of λ_Γ, λ_{dep}, λ_T, T(a) shown, these results are in rather good agreement with the JET measurements — regarding both the basic pattern (of net erosion near the LCFS, crossing over to net deposition at about 2 cm radially outward) and the absolute levels. However, the absolute levels require calculating fluences from fluxes integrated over a year's exposure to many different discharges and is therefore subject to more uncertainty.

Thus, an encouraging agreement is found, at least for this case, between measurements of net erosion and a simple model. It is clear, however, that the situation cannot always be so simple, for the following reasons:

- Oxygen sputtering can be important, even dominant;
- Wall-limiter exchanges of carbon should be included;
- 2-D effects such as ionization within the SOL should be included, particularly for high values of n_{LCFS} and for metals;
- λ_{dep} will, in general, differ from λ_{SOL}.

More sophisticated treatments of the problem of net erosion/re-deposition are therefore called for. Brooks et al. [494–500] have developed the REDEP and ZTRANS codes for the analysis of this problem and have applied the codes to both limiter and divertor cases. The REDEP code has been applied to the analysis of erosion and re-deposition of the TFTR bumper limiter [499]. Figure 71a shows the measured spatial profile of metal deposits on the inner graphite wall (bumper limiter) of TFTR after exposure to 9922 discharges, 70% of which were Ohmic; the Z-direction here is poloidal, with the mid-point of the figure being at the inside midplane; the y-direction here is toroidal. The REDEP code was used to calculate the carbon (spatial profiles of erosion and re-deposition (Fig. 71b). Given that the experimental results are integrated over a range of exposure conditions and that

the modelled deposition patterns were for carbon rather than for metals, the degree of agreement between Figs 71a and 71b is quite encouraging.

The LIM code was also applied to the limiter net erosion problem [484, 512, 513] and it was demonstrated that the entire carbon limiter erosion pattern (of net erosion near the LCFS, with net deposition further out) can be suppressed and then inverted as n_{LCFS} is increased from 1×10^{18} m^{-3} to 5×10^{18} m^{-3}, due to increasing ionization within the SOL. Figure 72 shows the experimental net erosion pattern on a JET belt limiter tile removed in May 1988 after exposure to a campaign of high power discharges. As can be seen, the pattern has indeed become inverted, with net deposition now being observed near the tangency point, followed by regions of net erosion and then again net deposition at the limiter edges. The LIM code results (Fig. 72) closely duplicate the observed pattern when edge parameter values are used which are characteristic of the high power discharges. Such prompt ionization and re-deposition is thus doubly valuable: (a) it constitutes a screening action, so far as contamination of the main plasma is concerned, and (b) it reduces the net erosion of the limiter.

In addition to the above-mentioned uncertainties, an additional uncertainty is associated with any effect in a tokamak which is integrated over many different discharges and, for each discharge, over the start-up, flat-top and ramp-down phases. It may be that the basic limiter erosion pattern is governed by non-standard discharges or by the transitional portions of discharges or by cleaning procedures, etc. In order to clarify this, time-resolved measurements of deposition are required, rather than just post-mortem analysis of limiters.

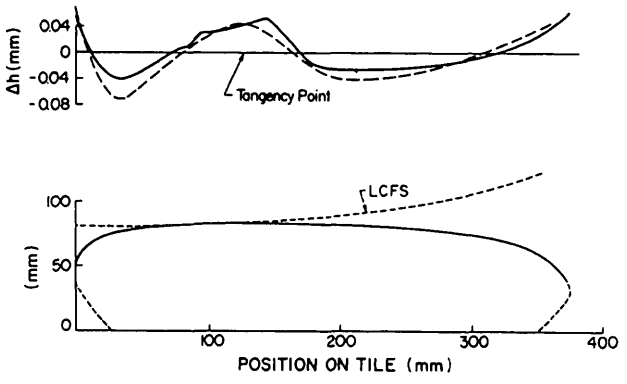

FIG. 72. JET: Net erosion/deposition pattern measured (solid line, top) on a belt limiter tile, removed in May 1988 after a campaign of high power discharges. LIM code results (broken line, top); assumed edge conditions: $n_{LCFS} = 5 \times 10^{18}$ m^{-3}, $T_{LCFS} = 50$ eV, $\lambda_n = 1.35$ cm, $\lambda_T = 2$ cm, $D_\perp = 1$ m$^2 \cdot$s^{-1}, characteristic of high power discharges.

As discussed in Section 4.7, the recently identified *co-deposition* effect is a critical one from the viewpoint of tritium inventory and possibly also for gas pumping/recycle. This process is intimately associated with the net erosion/re-deposition, and further progress on the two effects will be linked. If the SOL ionization were optimized to reduce the net erosion of the limiter, it is likely that co-deposition would also be minimized, although this remains to be demonstrated.

5.7. Beryllium limiter operation

Because of the susceptibility of carbon to chemical sputtering (Section 5.3.1) and the runaway influxes due to radiation enhanced sublimation (Section 5.3.2), it is of interest to explore the use of other low-Z structural materials. Experiments have been carried out using beryllium limiters on the Unitor [514], ISX-B [515] and JET [516] tokamaks. On ISX-B, very low oxygen levels were achieved owing to the gettering action of Be, i.e. plasma interaction with the limiter resulted in Be deposition on the wall, trapping oxygen. On JET [517], the oxygen levels during the early part of 1989 using carbon limiters were relatively high compared with those in 1988 discharges (owing to a major vent). The use of Be evaporative gettering in mid-1989 immediately resulted in a dramatic reduction of oxygen influxes, by a factor of ~ 20; at the same time the carbon influxes were reduced by a factor of ~ 2, presumably because of the elimination of oxygen sputtering and the associated carbon self-sputtering. Replacement of the carbon limiters by beryllium ones in September 1989 reduced the oxygen influxes to unmeasurable levels (at the same time, the Be influxes increased by a factor of ~ 10 compared with those in the Be evaporation/C limiter phase, and the C influxes decreased by a further factor of ~ 10).

Because of the elimination of oxygen as well as the lower radiative power of Be compared to C, the P_R levels were reduced in JET to $\lesssim 25\%$ of P_T, typically, from the $\sim 40\%$ of the P_T range typical of C limiter operation [516]. The lower radiation levels raised the density limit by a factor of 50–60% for otherwise similar conditions [518]. The density limit with Be is softer and the density rise is terminated by formation of Marfes (Section 6.5) rather than hard disruptions. With carbon limiters, P_R rose with the application of ICRH power and prevented the achievement of H-mode operation (Section 7.3.5) when only ICRH auxiliary heating was used [519]. For $P_{ICRH} = 10$ MW,

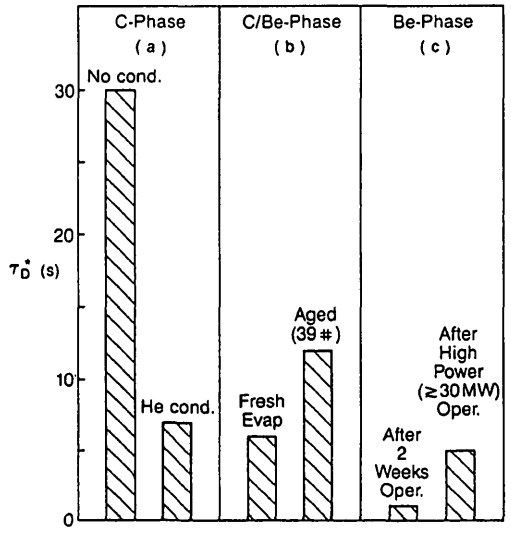

FIG. 73. JET: Measured deuterium decay time τ_D^* for the case where gas influx is stopped, for different operating conditions: (a) carbon limiters, with and without helium discharge conditioning, (b) carbon limiters with beryllium evaporative gettering, immediately after a fresh evaporation and after 39 discharges; (c) beryllium limiters after two weeks of low-to-medium power operation and after high power operation at ≥30 MW [520].

the rate of rise of P_R was ~ 10 MW·s^{-1}. With Be (either evaporative gettering or using Be limiters), $\dot{P}_R$ was reduced to $\simeq 2$ MW·s^{-1} at $P_{ICRH} = 10$ MW, and the H-mode could be achieved with ICRH alone.

An extra benefit of the use of Be in JET was very strong hydrogenic pumping [520]. Figure 73 shows the measured deuterium decay times τ_D^* (see Section 4.2) for the three operating phases: (a) C limiter phase, (b) C limiter/Be evaporation phase, (c) Be limiter phase. The Be operation results in pumping rates greater than can be achieved even with a carbon limiter subjected to helium discharge conditioning (Sections 4.7, 7.1). Such strong pumping is advantageous from the viewpoint of density control, particularly for neutral beam heating, and also for the achievement of peaked density profiles (Section 4.7). In addition, the pumping is strong enough to permit the puffing of extra deuterium gas into the plasma edge without significantly changing the central density [521]. Such additional puffing was found to reduce the central impurity levels, as was also reported for T-10 [261]. This was also frequently observed in other tokamaks gettered with titanium [247]. The hydrogenic content of the walls was largely recovered after each discharge in the vacuum exhaust [522]. Such efficient recovery may be related to the further observation on JET that little conditioning is reqired after a disruptive discharge compared with the case for C limiter operation [516]. The efficient hydrogen recovery will also be valuable for tritium operation. The ability of Be to strongly pump hydrogen at JET operating temperatures of 300°C is currently not understood; it is inconsistent with the high diffusion coefficient for H in Be at such temperatures [523].

The edge plasma density and temperature were not found to vary greatly between C limiter and Be limiter operation on JET [524].

The behaviour of Z_{eff} varied greatly between the C-limiter operation on JET of early 1989 and the Be limiter operation of September 1989, with reductions of approximately two units at $\bar{n}_e = 1.5 \times 10^{19}$ m^{-3} [516, 517]. Comparisons with the cleaner C limiter conditions of 1988, however, showed only a slight reduction of Z_{eff}, particularly at higher densities, $n \geq 3 \times 10^{19}$ m^{-3}. Deuterium dilution was improved to levels of $n_D/n_e \geq 0.8$ using Be on JET, permitting the achievement of record high values in H-mode plasmas of $\hat{n}_i \tau_E \hat{T}_i = 7 \times 10^{20}$ m^{-3}·keV·s [525].

On the negative side, the Be limiters, both on ISX-B and JET, were found to suffer melting damage, which may be a concern for long term operation. The effect of neutrons on Be also raises questions regarding use in reactors.

6. THE RADIATING LAYER

The total fraction of the radiated power P_R which is emitted within the SOL is generally small, and although impurity radiation can be significant in the energy balance of the SOL, typically it is not (see Section 3.6.2). In small tokamaks, or tokamaks dominated by metals, $P_R(r)$ can be substantial throughout the plasma. For large tokamaks, particularly with carbon limiters and walls, $P_R(r)$ is generally only large in a relatively thin layer ($r \sim 0.1$ m) just inside the LCFS. Thus, impurity radiation is not directly important for the energy balance of the core plasma. The edge radiation, however, appears to determine the maximum plasma density at which a tokamak can operate. In all tokamaks, there is usually a rather well defined upper density limit at which P_R rises rapidly with increasing $\bar{n}_e$, reaching levels close to the total input power. At the density limit the plasma usually disrupts, with I_p collapsing extremely rapidly, ≤ 1 ms. At densities just below this level, the plasma may 'detach' from the limiter (see Section 6.4) or it may form a localized

radiating zone or Marfe (see Section 6.5). In some cases, the density limit is associated with Marfes or with another, more gentle, collapse of the plasma, rather than hard disruptions.

The power loss of the radiating layer appears to interact in a rather complex way with the MHD stability of the tokamak. It is believed that when the temperature gradients near the q = 2 surface are substantially altered, owing to radiation losses, growth of magnetic islands occurs because of m/n = 2/1, 3/2 tearing modes, and overlapping of magnetic islands results in strong radial energy losses, disrupting the plasma [344, 345].

Understanding the behaviour of the radiating layer is as important as understanding the SOL. Unfortunately, the radiating layer is less accessible for diagnostics than the SOL, and the experimental database for this region is quite sparse. The following sections therefore review only briefly the gross experimental observations associated with the radiating layer. It is to be hoped that in future research of the edge, much greater attention will be given to this region, particularly to the detailed measurement of plasma density and temperature profiles, and their correlation with local radiation profiles, $P_R(r)$. The precise values of $n_e(r)$, $T_e(r)$, $T_i(r)$ and $P_R(r)$ in the radiating layer are probably critical to the establishment and stability of this region and determine whether disruptions, detached plasmas or Marfes occur. These quantities also establish the boundary conditions for the core plasma — the confinement region. They are therefore also critical for the linkage between the conditions in the core plasma and the conditions in the SOL plasma, and therefore the linkage between the fuel/impurity influxes and the operating conditions in the core.

6.1. Local radiation

The radiation occurring locally in the plasma is due to the excitation and subsequent de-excitation of atoms with bound electrons and also due to bremsstrahlung. In both cases the radiated power increases rapidly with the atomic number and, therefore, impurities are much more deleterious than hydrogen isotopes. The amount of radiation at any point can be characterized by an expression of the form

$$P_R(r) = n_e(r)\, n_{imp}(r)\, L_z(T) \qquad (6.1)$$

where $n_e(r)$ and $n_{imp}(r)$ are the local electron and impurity densities, and $L_z(T)$ is the radiation function which can be calculated from known atomic physics processes for any given impurity as a function of local electron temperature [231]. The form of $L_z(T)$ as a function of temperature is shown in Fig. 74 for a number of impurities for the case of coronal equilibrium. These values may be considerably increased if the product of density and confinement time $n\tau$ is low [230].

Local radiation results in local cooling, changing the temperature gradients and in general causing more heat to be conducted to the radiating region. The general 1-D power balance equation can be written

$$P(r) = \frac{d}{dr}\left(\kappa_\perp \frac{dT}{dr}\right) + n_e n_{imp} L_z(T) \qquad (6.2)$$

where P(r) is the deposited power at radius r and $\kappa_\perp$ is the cross-field thermal conductivity (neglecting heat convection, for simplicity).

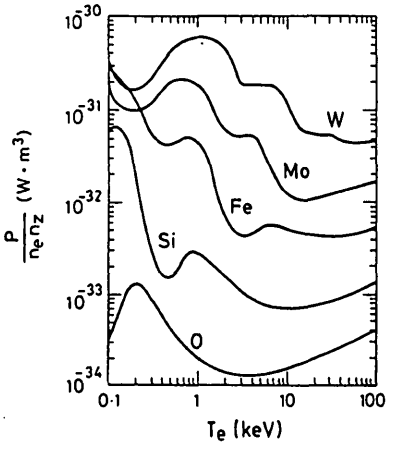

FIG. 74. Temperature dependence of the total radiated power for typical impurities, showing the increase with the nuclear charge Z [231].

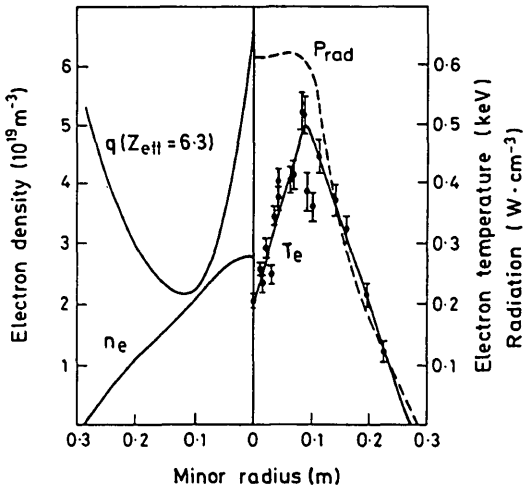

FIG. 75. DITE: Profiles of T_e, n_e, q and radiated power for a discharge with high central molybdenum concentration [526].

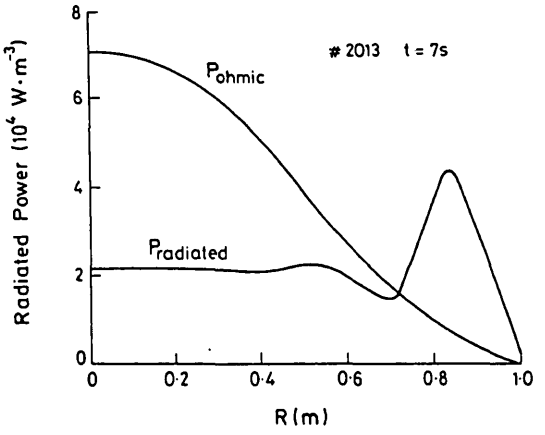

FIG. 76. JET: Radial distribution of Ohmic input and radiated power at t = 7 s, shot 2013, with Ohmic heating [527].

It has been observed that radiation from the centre of a tokamak discharge due to high-Z impurities can actually lead to formation of a hollow temperature profile (Fig. 75) [526]. Such a profile can only occur in tokamaks where the central temperature is relatively low so that the high-Z impurities are not fully stripped of electrons. In large tokamaks with high central temperatures and mainly low-Z impurities, radiation is predominantly from the plasma boundary, cooling the edges and steepening the temperature gradient at large radii. A typical radiation profile from JET with Ohmic heating is shown in Fig. 76 [527].

The presence of edge radiation has the advantage of spreading the power used to heat the plasma uniformly over the wall rather than conducting it outward and depositing it locally at the limiter or the divertor plate. Gibson and Watkins [528] first pointed out the advantage of having a cold, high density radiating layer at the boundary of the plasma. If all the energy can be emitted in the form of radiation and the edge temperature can be kept arbitrarily low, then impurity production due to ion sputtering might be eliminated. Such an arrangement has been called a 'cold plasma mantle'. If the product of the edge density and the blanket thickness can be maintained above 10^{19} m^{-2}, then the blanket will also be impermeable to charge exchange neutrals, thus reducing sputtering due to charge exchange neutrals at the walls. In practice, in order to get adequate radiation, the levels of impurities of $Z \sim 10$ (e.g. neon) must be $\geq 10^{18}$ m^{-3}; this gives rise to self-sputtering, which has a very low temperature threshold. There is also the problem that, at present, it is not known how to prevent the transport of the radiating impurity into the centre of the plasma, which causes fuel dilution.

6.2. Role of radiation in determining the edge temperature

The overall energy balance in a tokamak can be given as

$$P_T = P_R + P_c \tag{6.3}$$

where P_T is the total energy input, P_c is the energy conducted and convected to the edge, and P_R is the total energy radiated.

$$P_c = \gamma_s A_L c_s(a)\, n_e(a) k T_e(a) \propto n_e(a) T_e(a)^{3/2} \tag{6.4}$$

$$P_R = 4\pi^2 R_m \int_0^a n_e(r)\, n_{imp}(r)\, L_z(T)\, dr \tag{6.5}$$

where A_L is the surface area of plasma interacting with the limiter and γ_s is the sheath power transmission factor. γ_s is about 10 for $T_e = T_i$ (Section 3).

If we consider that a pure plasma is formed initially, then the radiation will be due only to hydrogen and, hence, it will be small. Most of the power will be transported to the edge and the edge temperature will be high. As discussed in Section 5.3, a high edge temperature will result in high physical sputtering and other impurity processes leading to an influx of impurities. These impurities will radiate, leaving less energy to be conducted to the edge and so the edge will cool. Since the physical sputtering yield increases with increasing energy, a negative feedback loop is set up, and such a process will regulate the edge temperature. An approximate description can be presented in the following way [529]. The ion energy E_0 arriving at the surface of a limiter is given by

$$E_0 = 2T_i + 3ZT_e \tag{6.6}$$

where T_i is the local ion temperature (assumed in the following to be equal to T_e) and Z is the average ion charge state. The sputtering yield Y is well known from experimental data (see Section 5.3) and can be given by a number of empirical formulas [458]. One of the simplest formulas [530] is

$$Y = \frac{A(E_0 - E_T)}{(E_0 - E_T + B)} \tag{6.7}$$

where E_T is the threshold impact energy for sputtering, and A and B are constants. We can write the total neutral impurity influx as

$$\Phi_{in}^{0} = 0.5\, A_L\, n_e(a)\, c_s(a)\, Y(E) \qquad (6.8)$$

To obtain the central impurity density, we use the model described in Section 5.5:

$$n_m = \frac{\Phi_{in}^{0}(\lambda_{iz}^{0} + \lambda_n)}{A_p\, D_\perp} \qquad (6.9)$$

where $A_p = 2\pi R_m 2\pi a$ is the surface area of the confined plasma.

Using Eqs (6.5) and (6.9), the radiated power P_R can now be expressed as

$$P_R = \bar{n}_e \frac{V_p}{A_p} \frac{\bar{L}_z(T_e)}{D_\perp} \Phi_{in}^{0} (\lambda_{iz}^{0} + \lambda_n) \qquad (6.10)$$

where $V_p = 2\pi R_m \pi a^2$ is the plasma potential, and $\bar{n}_e$ and $\bar{L}_z(T_e)$ are volume averaged values of the density and the radiation function, respectively. It has been shown experimentally that $L_z(T_e)$ is approximately constant in JET over a wide range of operating parameters [354]. An approximately constant value is expected from non-coronal calculations of radiation [230]. The dependence of $D_\perp$ on density or temperature can be specifically included if this is considered to be justified. We use the relationship between edge density $n_e(a)$ and average density $\bar{n}_e$ from Eq. (4.15a) together with Eqs (6.5) and (6.8) to obtain Φ_{in}^{0} in terms of P_c. Then, using Eq. (6.10), we substitute for P_R in the global energy balance Eq. (6.3) and solve for P_c.

A numerical procedure, using trial values of P_c is found to be the simplest method of solving the equations. It is found that the edge temperature increases as the total power input increases and that the edge temperature decreases as the density increases. A comparison of this simple model with experimental results from JET is presented in Fig. 77 [12]. Also, the model predicts that the edge temperature decreases as the atomic number of the injected impurity increases.

6.3. Effect of radiation on stability

It is found experimentally that when the radiation exceeds a certain fraction F_{rad} of the input power, a disruption of the plasma current occurs. This is generally assumed to be a consequence of the peripheral plasma region radiating to such an extent that the temperature profile collapses [248–250]. Rewriting Eq. (6.5), removing the integral by using volume averaged values of n_e, n_{imp} and $L_z(T)$, we obtain the upper (disruption) limit to plasma density $\bar{n}_{ec}$

$$\bar{n}_{ec} = \frac{F_{rad} P_T}{V_p \bar{n}_{imp} \bar{L}_z(T_e)} \qquad (6.11)$$

where the fraction F_{rad} is typically between 0.5 and 1.0. As the density limit is approached, P_R generally rises rapidly, often tending to approach P_T. An example from JET is shown in Fig. 78.

For a fixed impurity fraction and an ohmically heated plasma, Eq. (6.11) leads to a critical density

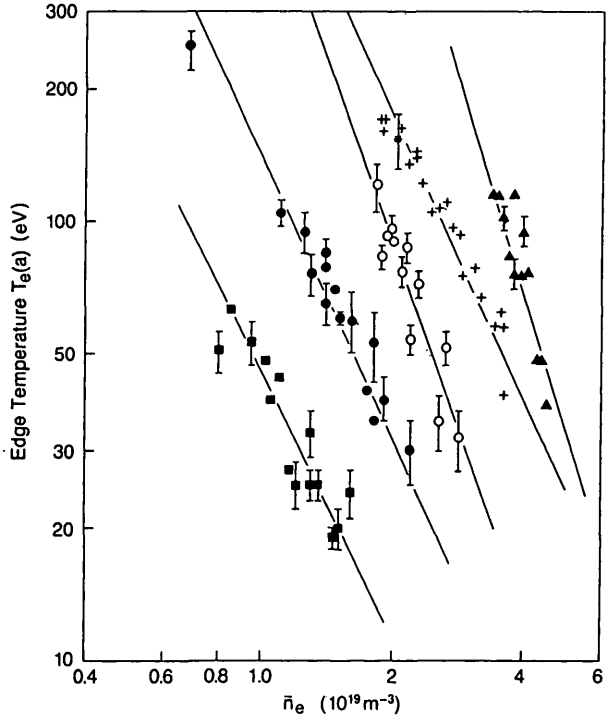

FIG. 77. JET: Experimental and theoretical edge temperatures. The solid lines are least-squares fits through the experimental points. The dotted lines are from the global theory [12].

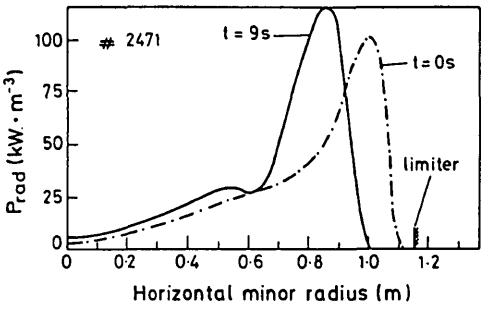

FIG. 78. JET: Radiated power against radius before disruption [251].

proportional to the plasma current, which is in turn proportional to B/R_m for a fixed q value. This is the behaviour derived from experimental data by Murakami et al. [248] and which is incorporated in the scaling laws of Hugill (see Fielding et al. [247]) (Fig. 53). If the input power is increased owing to additional heating, the critical density would be expected to rise, provided the impurity content does not change. Such an increase does occur, particularly when there are high impurity levels. However, there appears to be an absolute limit for all tokamaks, given by

$$\bar{n}_{ec}\ [m^{-3}] \approx \frac{2 \times 10^{20}\, B}{R_m q} \qquad (6.12)$$

where R_m is the major radius in m, B is the magnetic field in T and q is the safety factor. As the density increases, the edge temperature decreases; this leads to reduced impurity production, and the overall picture becomes more complicated.

A 1-D model of the situation has been presented by Ashby and Hughes [531], who point out that the temperature collapses when the local radiation at the boundary exceeds the heat flux conducted to that radius. The plasma is divided radially into two regions — a central region where $T > 2$ keV and the input power is deposited, and a peripheral region where $T < 2$ keV and no net power is generated. Integrating Eq. (6.2), the criterion for preventing thermal collapse is that the power conducted from the centre, Q, must be given by

$$Q^2 = \left(\kappa_\perp \frac{dT}{dr}\right)^2 > 2 \int_0^T \kappa_\perp n_e n_{imp} L_z(T_e)\, dr \qquad (6.13)$$

The thermal stability of this criterion depends on how the n_e and n_{imp} profiles change and how the temperature gradient steepens as the temperature profile collapses. The stability is discussed at the end of Section 6.4.

6.4. Detached plasmas

Detached plasmas have been observed in many ohmically heated tokamaks [351, 352, 532–535]. The term 'detached plasma' has been applied to the state where the temperature profile has contracted in the way expected from the simple analysis discussed in Section 6.3. However, the interesting thing about the experimentally observed detached plasmas is that the contracted temperature profile is stable. The detachment can be obtained by increasing the plasma density to a value near the density limit at constant current [351], or by decreasing the current at constant density [352]. This behaviour is what would be expected on the basis of Eq. (6.11). In both cases, the equilibrium is rather delicate, with a slight increase in density leading to a density limit disruption and a slight decrease in density leading to a reversion to the attached state. It has also been demonstrated that the equilibrium can be changed by the application of additional heating such as ICRH or NBI [533, 536]. The increase in heating power makes detachment more difficult to achieve.

Experimentally, the detached plasma can be most easily observed by viewing the plasma tangentially in the visible region of the spectrum, for example using a TV camera. As the density is raised, the radiation from the edge of the plasma — corresponding to the H_α light from the plasma atoms and the low ionization states of the impurities — gradually moves concentrically inwards. At any arbitrary value of density the radiating

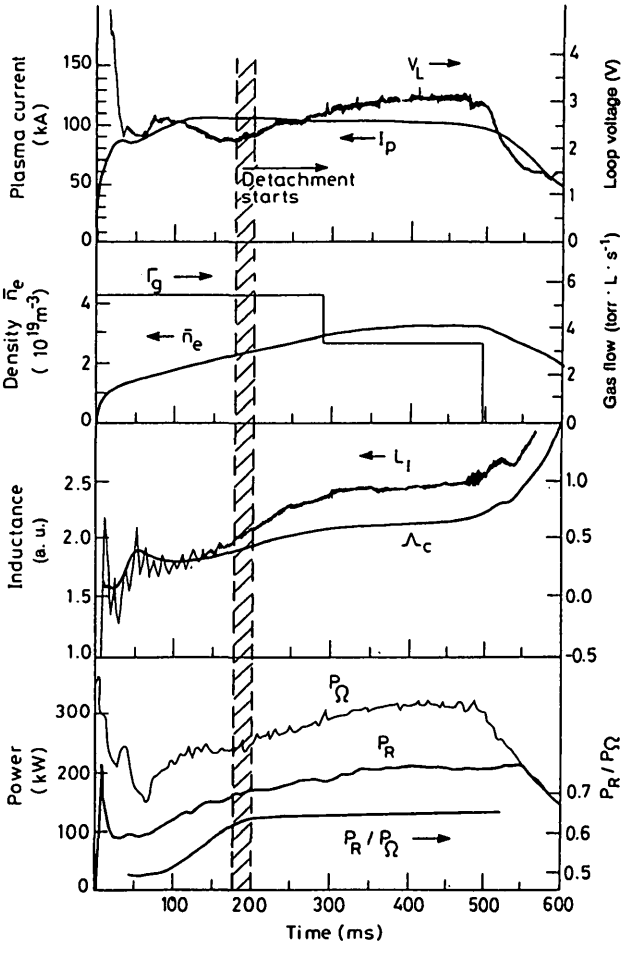

FIG. 79. DITE: Plasma parameters for a typical detached discharge [351].

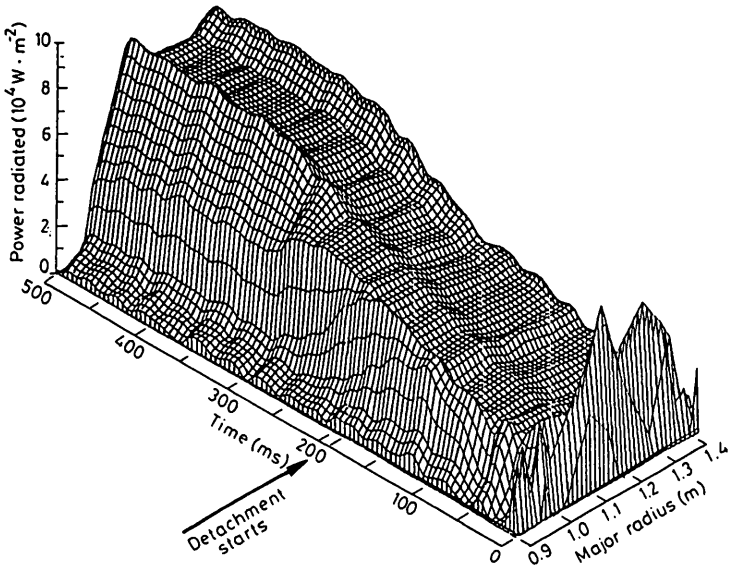

FIG. 80. DITE: Chord integrated radiation intensity for a detached discharge with I_p = 100 kA and $\bar{n}_e = 3 \times 10^{19}$ m^{-3} [351].

layer is spatially stable. The other characteristics of the plasma are shown as a function of time in Fig. 79 for DITE. At a constant current of 105 kA, the density is raised approximately linearly to a value of 3×10^{19} m^{-3} at 340 ms and then kept constant until 500 ms. Between 150 and 250 ms, the plasma detaches, as observed with the bolometer array (Fig. 80). Before detachment, the uninverted profile is relatively flat, with a slight peak on the inside edge. On detachment, the radiation profile shrinks and moves radially inward approximately 50 mm (Fig. 80). On larger machines such as TFTR the detachment is even more striking because the plasma can shrink as much as 300 mm from the limiter before disruption occurs [352]. As the plasma detaches, the poloidal beta, β_θ, remains constant at 0.4, while the plasma inductance increases from 2.0 to 2.4. This implies that the current channel is shrinking. However, the sawtooth inversion radius, as determined from the X-ray diode array, increases from <23 mm at 115 ms to 47 mm at 400 ms. The loop voltage increases from 2.2 V to 2.8 V, and the Ohmic power increases by a similar factor. The fact that β_θ stays constant as the Ohmic power increases indicates that the energy confinement time decreases.

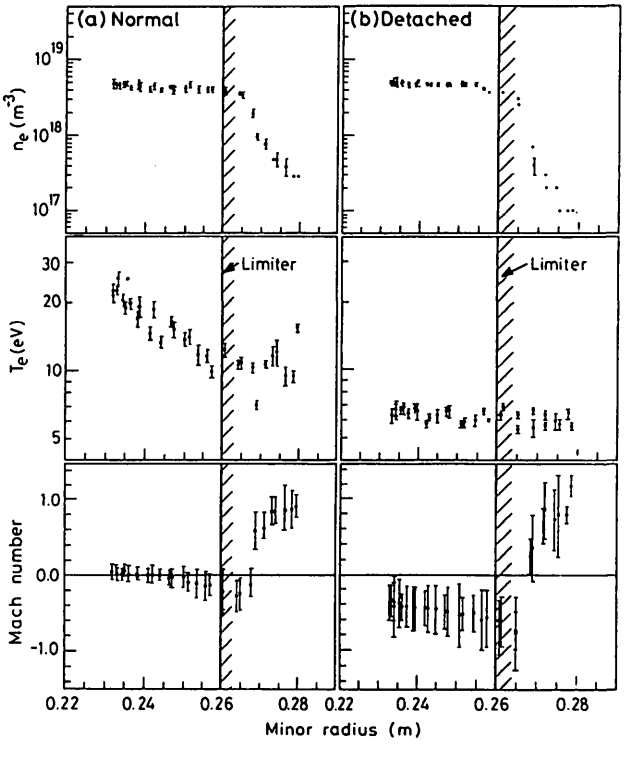

FIG. 81. DITE: Plasma edge profiles for normal and detached discharges. Measurements at 0.455 s, for (a) 100 kA and (b) 130 kA [351].

The edge parameters are shown in Fig. 81. On detachment, the edge temperature decreases, typically from 10–15 eV to 6–7 eV. The profile also becomes much flatter inside the limiter radius. In DITE, the edge density does not change significantly, but in other machines it has been observed to decrease on detachment [533]. Measurements of the Mach number reveal the presence of strong, large-scale convection on the boundary between the edge of the detached plasma and the radius of the LCFS.

We have previously discussed the fact that impurity densities decrease as the plasma density increases. Measurements of the impurity level at different stages of detachment show that there is no abrupt change in the general trend of impurity behaviour on detachment. Measurements of the central impurity confinement time, using aluminium injection by laser ablation, show that this confinement time is not affected by detachment [351].

In general, detachment is most easily induced at a high safety factor q. As q is decreased, the margin between the density at which detachment occurs and the density disruption limit becomes gradually smaller. It seems probable that when the low temperature region moves inward to the radius at which q = 2, the temperature gradients induce MHD activity which starts the disruption.

The stability of the detached plasma is not yet fully understood. It seems that at the collapse of the temperature profile, the temperature gradient increases and the amount of heat conducted to the radiating layer also increases. For a circular plasma of radius a_p with a limiter radius a_L, the energy balance can be written [251] as

$$\frac{d}{dt}(\pi a_p^2 \bar{\epsilon}) = I_p^2 R_\Omega(a_p) + 2\pi \times \left[-Cn_e(a_p)a_p - \kappa_\perp \frac{T_R}{(a_L - a_p)} a_p\right] \quad (6.14)$$

where $\bar{\epsilon}$ is the average plasma energy density and R_Ω is the plasma resistance per unit length. The second term on the right hand side gives the radiation loss and the third term the thermal conduction loss, T_R being the temperature at which $L_z(T_e)$ is a maximum. Linearization of Eq. (6.14) with constant I_p leads to a stability equation [251], but it is difficult to determine a stability criterion because it is not possible to predict the behaviour of a number of the plasma parameters, e.g. the density profile, during the temperature collapse.

Experimentally, the detached plasma is observed to be stable; however, contraction of the temperature profile leads to an increasingly unstable current profile and, ultimately, a disruption can result (Fig. 78) [251].

6.5. Marfes

The multifaceted asymmetric radiation from the edge (Marfe) is another form of intense edge radiation. It was first identified on ALCATOR [346] and was later observed on a number of machines [537]. Although the Marfe is toroidally symmetric, it is, unlike a detached plasma, concentrated at one poloidal position, normally on the high field side of the tokamak. In ASDEX, FT and DIII the Marfe was found to be on the inside midplane, whereas in ALCATOR, JET and TFTR it was observed to be above the midplane [537].

The generally accepted explanation of the Marfe [346–349, 537] is that it is a temperature instability which is induced by the T_e dependence of the radiation function of low-Z impurities such as oxygen and carbon. In Fig. 74 we see that above a local temperature of 20 eV the radiation constant for carbon decreases with increasing temperature. If there is a cool spot at one poloidal location in the edge plasma, then this spot will radiate more and so cool further. Such a situation is unstable as long as the temperature decreases until the peak of the radiation function is reached, where it then stabilizes. As the volume cools, the temperature gradient increases, and more and more heat is conducted along the field lines [346–348, 537] or across the field [349] to balance the radiated power. It is only at the edge, where the parallel conductivity is low, that such a phenomenon is possible. The radiation from Marfes is dominated by the low ionization states of oxygen and carbon, consistent with the observation of very low temperatures. After the onset of a Marfe, the amplitude of the density fluctuations increases by two orders of magnitude. The density rise within a Marfe is typically 0.5 to 1.0 times the central density. The density threshold for the appearance of a Marfe has been found to be given for a wide range of machines by the simple relationship [537]

$$\bar{n}_{em} = CI_p/\pi a^2 \quad (6.15)$$

The constant C can vary from 0.4 to 0.7, but is typically 0.55. The Marfe normally precedes a detachment. If the density is raised after the occurrence of a Marfe or if the plasma current is lowered, the radiation from the Marfe spreads poloidally and plasma detachment starts.

The reason why the Marfe occurs on the inside midplane is not obvious. It has been suggested that it is because the cross-field thermal conductivity is greater on the low field side midplane and that it is more difficult for a cold spot to form there [346, 347].

7. CONTROL OF BOUNDARY CONDITIONS

The objective of studies of the plasma edge is the control of the boundary conditions with the aim of optimizing the performance of the confined plasma. For present devices, methods are required for (a) reducing impurities in the confined plasma and (b) controlling recycling in order to maintain the desired density and density profiles. For reactors, the erosion rates must also be kept at a minimum and the helium product of the fusion reactions must be pumped away. Methods of controlling the boundary conditions are reviewed under three categories: (i) modification of surfaces, e.g. by discharge cleaning (Section 7.1), (ii) use of limiter and/or magnetic field shaping, e.g. pumped limiters (Section 7.2), and (iii) use of divertors (Section 7.3).

Surface modification methods such as discharge cleaning, carbonization and gettering are relatively inexpensive and effective at reducing impurities and controlling recycling. Their effectiveness is, however, temporary and periodic replacement and maintenance of apparatuses, etc., is required; the reactor relevance of these methods is therefore in question. Reactor relevant methods, capable of steady state operation, such as the use of divertors and pumped limiters, are more expensive and in some cases less effective than the surface modification methods. In the following sections we will attempt to survey the principal methods currently used. The reader is also referred to earlier reviews of conditioning techniques (Refs [1, 214]).

7.1. Surface modification

7.1.1. Discharge cleaning

Discharge cleaning or conditioning is a technique that is used to remove loosely bound gases adsorbed on the inner surfaces of vacuum systems. Typically, the adsorbed species are H_2, H_2O, CO and CO_2. This method is used in various guises to reduce impurity fluxes from the wall, after exposure to the atmosphere and before initial tokamak operation. Early work was reviewed by McCracken and Stott [1] and by Dylla [539]. The discharge can be of many types, e.g. a glow discharge, a pulsed discharge or an electron cyclotron resonance (ECR) discharge, but, in each case, energetic atoms, ions and electrons are produced which bombard the walls of the vacuum vessel. Atoms and molecules adsorbed on the wall are removed by momentum transfer, electronic excitation and chemical interaction. These processes are much more effective than baking of the vacuum vessel alone, since more energy can be transferred to adsorbed impurity species. In some cases, the cleaning efficiency can be further enhanced by using the discharge when the vessel is hot. Few comparisons of the relative effectiveness of the different techniques have been made because it is difficult to bring a tokamak into an initial 'reproducibly dirty' state. Comparisons of glow discharge cleaning (GDC), Taylor discharge cleaning (TDC) [540] and cleaning with plasmas produced by ECR were made by Matsuzuki et al. on JFT 2M [541]. These techniques were compared by examining the resulting tokamak plasmas, by Auger analysis of surface samples exposed to the cleaning process and by residual gas analysis. It was found that TDC and ECR cleaning were much more effective at reducing oxygen than GDC. Residual gas analysis showed that water molecules were produced in TDC and in ECR cleaning, whereas mainly hydrocarbons were produced in GDC. The relative advantages and disadvantages of the different types of discharge cleaning have been summarized by Cohen [214].

The most widely used cleaning technique is GDC, because it is reasonably effective and very simple to carry out. A variation of GDC has been developed at KFA Jülich [542–544], where RF radiation at 10–20 MHz is used together with GDC to excite the discharge (RF–GDC). By providing more ionization with the RF radiation, the glow discharge can be operated at lower pressures (typically 5×10^{-4} torr), and this causes the discharge to expand throughout the vessel. The lower pressures result in higher ion energies owing to reduction of collisions in the sheath, and the presence of RF allows the insulating layers to be removed. This type of discharge has been adopted on TEXTOR, JET, DITE and Tore Supra. Evidence from TEXTOR indicates that RF–GDC is effective at reducing the oxygen levels in the plasma to $\lesssim 0.3\%$ [543].

Many gases have been used for GDC [1]. Using a heavy rare gas, such as argon, results in physical sputtering of the surface. While this is effective at removing adsorbed gas, it can also lead to thick layers of sputtered material being deposited on windows, insulators, etc. For many years, the trend has been to use light gases, in particular hydrogen isotopes. In this case, the cleaning is enhanced by chemical action, with the formation of hydrocarbons, CH_4, C_2H_4, etc., as

well as H_2O, CO and CO_2. Since these species are volatile, the impurities can be pumped away by the vacuum system. More recently it has been found that in machines where a large area of the wall is covered by carbon, discharge cleaning in hydrogen is dominated by hydrocarbons. It has been found empirically that discharges in helium reduce the hydrocarbon production but still clean up the oxygen — mainly by production of CO [545]. In JET, the use of helium RF-GDC has enabled oxygen levels as low as 0.1–0.5% to be realized. Use of helium is less satisfactory if there are larger metal wall areas, since the sputtered metal contaminates the carbon limiters. Helium discharges have a further advantage in that helium ion bombardment releases hydrogen isotopes from carbon [546, 547], thus reducing recycling (see Section 4.7).

7.1.2. Carbonization and boronization

Carbonization was introduced as a method of reducing contamination of metal surfaces [548]. The technique has recently been reviewed by Winter [544]. It consists basically of running a GDC (or RF-GDC) in hydrogen or helium with typically 20% CH_4. The methane is dissociated in the plasma, and carbon atoms are deposited on metal surfaces. A layer of carbon is built up. The type of layer produced depends on the wall temperature, on the pressure in the discharge and on the percentage of methane used. The optimum wall temperature is about 300°C and at this temperature a hard adherent layer of amorphous carbon (referred to as a-C:H) is formed [549]. The layer has typically 0.4 hydrogen atoms per carbon atom incorporated in its structure. The use of carbonization together with carbon limiters has allowed tokamaks to be operated with virtually all-carbon walls. A marked reduction in both the metal contamination (10–20 times) and the oxygen level (5–8 times) compared with those in machines where RF-GDC was applied is observed [544].

A drawback of carbonization is that the high concentration of hydrogen in the a-C:H layer can lead to hydrogen release into the tokamak discharge, with uncontrolled recycling [544]. A large number of discharges is required before the wall becomes adequately conditioned. The conditioning can be accelerated by the use of helium GDC after carbonization. There are two further potential difficulties. One difficulty is that the right substrate has to be used for a well adhered layer. Nickel, stainless steel and Inconel are satisfactory, but copper does not form a carbide and is less good [550]. The other difficulty is that, in practice, carbonization alone is effective only for a limited time. In TEXTOR, after a 0.1 μm carbon layer had been deposited, the iron concentration was suppressed for about 120 discharges [548]. The lifetime of carbonization increases in proportion to the thickness, but layers which are thicker than a few micrometres are expected to have reduced adhesion.

Boronization is a technique similar to carbonization. When boranes (B_2H_4, B_2H_6) are introduced into a vacuum vessel which is at a temperature of $\sim$400°C, they decompose and deposit a layer of boron on the wall. Boron can act as a getter, forming an oxide, and thin boron films will pump both oxygen and hydrogen at temperatures of $<$100°C [551]. Boronization as a technique for surface treatment was proposed as early as 1976 by Veprek et al. [552], and the results of such treatment were reported recently by Winter et al. [553]. An RF-GDC helium discharge was used, with a mixture of 10% boranes and 10% methane. This resulted in deposition of a mixture of boron, carbon and hydrogen on the walls. Boronization was demonstrated to be effective at reducing the oxygen level in TEXTOR, and it was found that the beneficial effects lasted even after opening the vacuum vessel to the atmosphere. This result is attributed to the low affinity of boronized surfaces for water vapour [553].

7.1.3. Gettering

Gettering is the term used to describe the sublimation of a chemically active metal onto the walls of a vacuum system so that this metal can act as a pump. The fresh layer of metal reacts chemically with many active gases (O_2, CO, H_2, CO_2, etc.), binding them tightly to the surface [554]. Sequential deposition of gettered layers results in the gas being buried, and in the case of hydrogen the gas can also be removed by diffusion into the bulk. There are many suitable getters, but those which have been used most frequently are titanium [1] and chromium [555, 556] because of their relatively high vapour pressure at modest temperatures (Cr, 1300–1600 K; Ti, 1500–1850 K). These metals are effective at reducing oxygen levels, though titanium is more effective than chromium in pumping hydrogen. Other getters, such as Zr, Nb, Al, B, Be and Li, should be equally effective. Beryllium was recently tested on JET [516, 557] because of its low atomic number and its suitable evaporation rate (see Section 5.7). Earlier experiments using Be as a limiter showed the effects of Be gettering when the limiter was heated to temperatures at which Be evaporated [558]. The alkali and alkaline earth metals (e.g. Li) are good getters, but their relatively high vapour pressures at operating

temperatures (~300°C) may be a disadvantage. Getters do not pump inert gases (He, Ne, etc.) or saturated hydrocarbons (e.g. CH_4).

There is some difference of opinion on the extent of the surface to be covered for gettering to be effective. Dylla et al. quote data from TFTR [556] which indicate that it is necessary to cover a large proportion of the surface. It is argued that the gettered layer reduces the local outgassing. In other experiments, gettering of a relatively small proportion (~30%) of the surface area was sufficient to produce a marked improvement, and gettering a larger area did not result in significant improvement [247]. In PLT it was possible to reduce the plasma oxygen concentration to ≤0.5% in an unbaked machine, compared with an oxygen concentration of 1-2% after TDC [559]. Typically, in most tokamaks using gettering, Z_{eff} was reduced to ≤1.5 [538].

The disadvantage of gettering is that it relatively quickly saturates, and in some machines it was necessary to getter between all consecutive pulses [559]. This may be even more of a problem in long-pulse machines such as JET. A further difficulty is that the thin films of deposited metal tend to flake off when they reach thicknesses of ~10–100 μm. This results in impurities entering the plasma in a random manner and can cause disruption. Thus, gettering is not a long term solution to removing oxygen, but it can be an effective short term solution with which reduced oxygen levels, better density control and access to much higher density limits can be achieved.

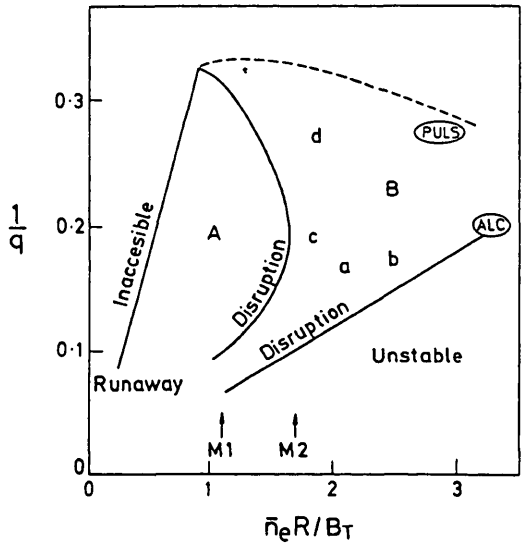

FIG. 82. Stable operating region in (I, $\bar{n}_e$) space with normalized co-ordinates, $1/q \propto I$ and $\bar{n}R/B_T$; region A without gettering and region B with gettering in DITE [247]. The density limits in ORMAK without and with gas feed are marked M1 and M2. The high density regimes in ALCATOR and PULSATOR are marked ALC and PUL.

The reduction in impurity levels allows access to a wide operating regime [560] (results for DITE are shown in Fig. 82). However, the use of titanium, which reduces the recycling rate for the fuel ions, necessitates strong gas puffing in order to reach the density limit. It may be speculated that this strong puffing reduces the edge temperature and further reduces impurity production via sputtering. There is, however, a generally clearly defined upper limit to the plasma density which applies to all tokamaks (Eq. (6.12)).

Non-evaporable getters have also been used in tokamaks [538]. Usually, they consist of a layer of Zr–Al deposited on a metal substrate which can be heated. They have a high effective pumping speed for most active gases. While the pumping speed for hydrogen can be recovered by heating to 700°C, the speed for other gases (O_2, CO, H_2O, etc.) saturates and the pumping cartridge has to be replaced. While these gases are useful for obtaining a high pumping speed, they have not been very effective in tokamaks. A possible application of non-evaporable getters is for the pumping of tritium [561]. It is clearly advantageous that tritium is tied up locally and is not exhausted into the atmosphere.

7.1.4. Discharge conditioning with helium

When NBI is applied, it is desirable to maintain low plasma densities to obtain high plasma temperatures for a given input power. This requires strong wall pumping and thus low recycling rates. On TFTR [245] it was found that by operating helium discharges on the inner carbon wall of the vessel, a high proportion of the trapped hydrogen isotopes can be desorbed from the wall. In subsequent deuterium discharges, the walls pump by trapping the deuterium, and low densities can be maintained (see Section 4.7). The mechanism of desorption of hydrogen from carbon is thought to be energy transfer to the lattice atoms by the incident ions. Both helium and carbon ions have been shown to be effective when using ion beams [546, 547]. The desorption efficiency increases with the ion mass and the ion energy, which is consistent with the calculated energy loss to the lattice. Unfortunately, this technique is time consuming (more than 100 discharges were required in TFTR to fully condition the wall). Also, it is effective only for a limited time, since after a few deuterium discharges the walls are again saturated.

Similar results were obtained in JET [562], but because of the longer pulse length, conditioning with helium does not take quite so long as in TFTR. It was found advantageous to use long-pulse ICRH to increase the efficiency of conditioning [563]. This mechanism should not be confused with the more long term pumping observed in JET which is attributed, at least in part, to erosion and re-deposition of carbon with co-deposition of hydrogen and carbon [263].

7.2. Limiter and magnetic field shaping

7.2.1. *Role of the limiter shape: the impurity control limiter*

Conventional limiters are usually curved so that field lines intersect them at grazing incidence (Fig. 83(a)). This allows the heat flux to be spread out over a larger area than for normal incidence and minimizes the possibility of cracking, melting or evaporation. However, such a limiter geometry causes the impurities released from the surface to directly enter the plasma, since they tend to be expelled in a direction normal to the limiter surface. A proposal to change the geometry in order to reduce the impurity flux from the limiter was put forward by Bieger et al. [564]. A similar design was suggested by Schivell [565]. A more detailed design for an impurity control limiter (ICL) was published recently by Matthews et al. [566]. The field lines intersect the limiter on surfaces which do not face the plasma (Fig. 83(b)). This results in impurity trajectories being predominantly towards the wall. Some atoms will reach the wall without ionization. The fraction which is ionized will be in the SOL and thus it will have a lower probability of entering the confined plasma. A disadvantage of this geometry is the requirement for a narrow leading edge which receives the maximum heat flux at normal incidence. In order to maximize impurity control, this edge must be small compared with the power scrape-off length and it must be comparable with the ion Larmor radius. Such a design is satisfactory in short-pulse machines, and its capability to reduce the influx of impurities due to limiter sputtering was demonstrated on DITE [15]. It was shown that in helium discharges where limiter sputtering is the dominant impurity process, the total radiation from the plasma could be reduced by a factor of two over a wide range of plasma densities. The operation of the ICL also demonstrates the importance of correct shaping of the divertor plates to minimize ionization of impurities. However, because of the high local power loading at the leading edge, it is unlikely that the ICL can be used in steady state operation.

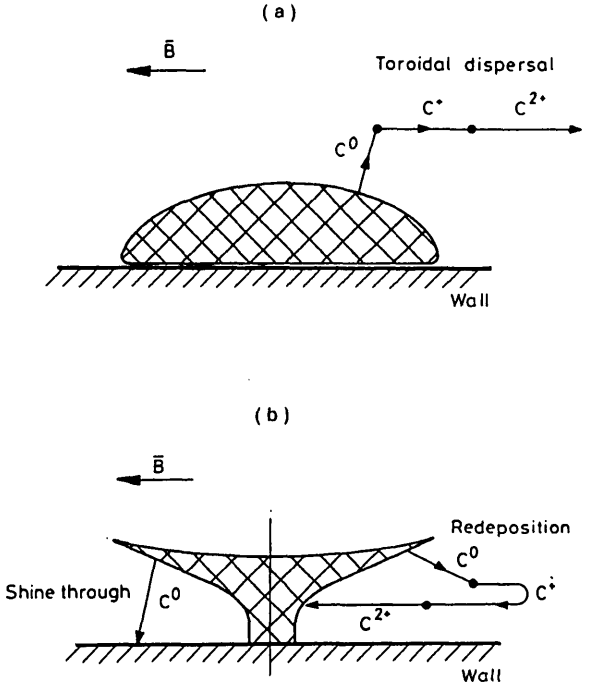

FIG. 83. Schematic of alternative limiter geometries.
(a) Conventional limiter which directs impurities onto closed flux surfaces.
(b) The ICL which controls impurities by improved screening and shine-through [15, 566].

7.2.2. *Pumped limiters*

The objective of pumped limiters is to achieve density control and, if possible, to achieve pumping of helium in a tokamak reactor with limiters [567]. A schematic view of a pumped limiter is shown in Fig. 84. The pumped limiter is superficially similar to the ICL, but

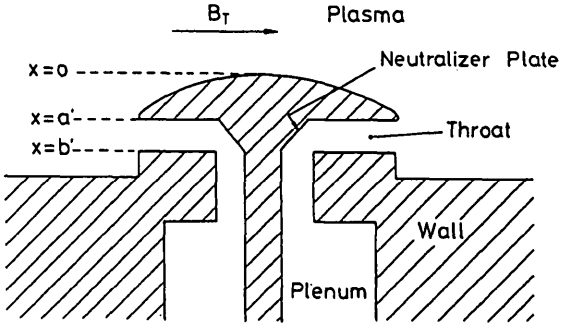

FIG. 84. Schematic diagram of a pumped limiter. Here, $r = a + x$, where a is the minor radius of the plasma. At $r = a$, $x = 0$.

the leading edge is shaped for a glancing angle of field lines to minimize the heat flux, and the surface at normal incidence is removed approximately one or two power e-folding lengths behind the LCFS. This is possible because the flux e-folding length is larger than the power e-folding length and, with such a design, it is still possible to direct 5–10% of the total particle flux into the throat of the pumped limiter. An earlier review of pumped limiters was given by Mioduszewski [568].

To estimate the fraction of the total particle outflux which can be removed by a pumped limiter, we consider exponential radial profiles for density, temperature, power and particle flux in the SOL (see Section 3). Let us assume that the radius where the limiter surface is normal to the field lines is two power e-folding lengths behind the LCFS. (This corresponds to 86% of the total power to the limiter being deposited on the front surface.) From the relationship between power, density, temperature and flux e-folding lengths (λ_P, λ_n, λ_T and λ_Γ, see Section 3) we can calculate the ratio λ_P/λ_Γ if we know λ_T/λ_n. Typically, λ_T/λ_n varies from 1 to 5 and, thus, over this range, λ_P/λ_Γ = 0.67–0.85; let us take λ_P/λ_Γ = 0.75.

The fraction of the total particle flux entering the pumped limiter throat, termed the exhaust fraction F_{ex}, is given by

$$F_{ex} = \frac{\int_{a'}^{b'} w\,\Gamma_0 \exp[-(r-a)/\lambda_\Gamma]\,dr}{\int_0^{\infty} w\,\Gamma_0 \exp[-(r-a)/\lambda_\Gamma]\,dr}$$

$$= \exp\left(-\frac{a'}{\lambda_\Gamma}\right) - \exp\left(-\frac{b'}{\lambda_\Gamma}\right) \qquad (7.1)$$

where w is the poloidal length of the limiter and Γ_0 is the flux density at the LCFS, i.e. where r = a (Fig. 84). From the above discussion we have $a' = 2\,\lambda_P = 1.5\,\lambda_\Gamma$. The value of b′ will be determined by the width of the throat required for optimum trapping efficiency. Choosing $b' = 3\,\lambda_P = 2.25\,\lambda_\Gamma$, we obtain F_{ex} = 12%.

The trapping coefficient ϵ_t is defined as that fraction of the flux incident on the limiter throat which is actually pumped. In the simple case where plasma effects can be neglected, i.e. at low plasma densities, the trapping coefficient is equal to the ratio of the applied pumping speed to the return conductance into the plasma chamber. Under these conditions, $\epsilon_t \approx 0.5$ can be realized [569]. The overall exhaust efficiency η_{ex} of the pumped limiter is $\eta_{ex} = \epsilon_t F_{ex}$. For the examples quoted, F_{ex} = 0.12 and ϵ_t = 0.5, η_{ex} = 0.06. At higher densities, ions which are reflected or thermalized at the neutralizer plate have a finite probability of being re-ionized in the plasma of the limiter throat. These ions are then subject to friction with the arriving plasma ions and the pre-sheath electric fields (see Section 3). The physics involved is complex, and the problem of whether the backstreaming particles escape from the throat or return to the neutralizer plate ('plasma plugging') has not yet been fully resolved [568].

Initial experimental measurements were carried out with small passive 'pumped limiters'; the pressure in the plenum was allowed to rise until the backflow equalled the incident flux. Early experiments on ALCATOR A, Macrotor, ISXB and PDX were reviewed by Mioduszewski [568] and Conn [200]. More recently, pumped limiters were used on T-10 [6], TEXTOR [570], TFR [32], PLT [571] and DITE [17]. Pressure rises in the range 10^{-3} torr to 3×10^{-2} torr were observed, with the pressure rise being proportional to some power of the average density $\bar{n}_e$ between 1 and 2. It was observed that the power dependence was higher with pumped limiters in which there was a longer throat. This was attributed to 'plasma plugging'.

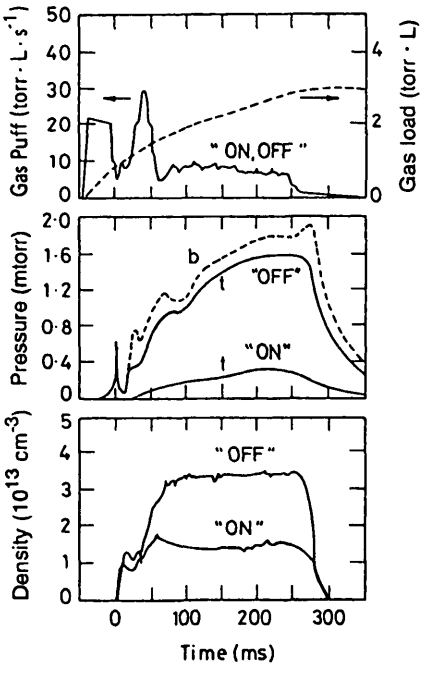

FIG. 85. Graphs of gas puff, pressure in the limiter, and core plasma density as a function of time during a discharge in ISX [568]. 't' and 'b' signify 'top' and 'bottom' limiter locations; 'off' and 'on' indicate whether pumping in the module is off or on.

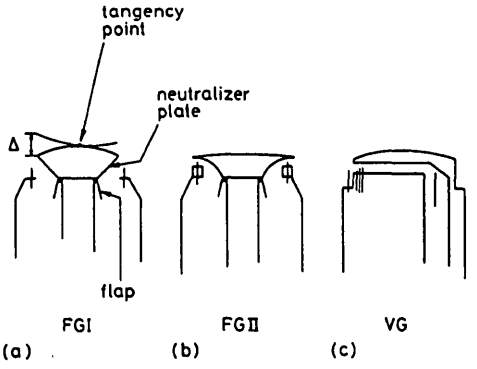

FIG. 86. TEXTOR: Schematic sketch of the different modules of ALT I. The position of the Langmuir probes is indicated.

Later designs have used pumping in the limiter heads to control the density. Two designs on ISXB have demonstrated a reduction in the average plasma density $\bar{n}_e$ for a given gas flow rate when the pumping was turned on. Results with pumping on and off are compared in Fig. 85. With the pumping on, the pressure in the pump plenum falls by a factor of five and the average density is reduced by nearly a factor of three [568]. The ALT-I limiter has also demonstrated significant density control [200, 570]. The density drop in the plenum is similar to that in ISX-B. Using measurements of the pressure and of the incident flux from Langmuir probes, it is deduced that between 6.5 and 13% of the plasma outflux enters the throat of ALT-I. Of this, 60% is pumped, leading to an overall exhaust efficiency of between 3.8% and 7.6% and an exhaust rate of 7×10^{19} ions$\cdot$s^{-1}. Figure 86 gives a comparison of the different pumped limiter geometries in TEXTOR [572]. The particle removal rates vary markedly, with the highest rate of 8 torr$\cdot$L$\cdot$s^{-1} being obtained with the single-sided 'variable geometry' limiter head at high density. The FG I head (Fig. 86) had a typical removal rate of 0.8 torr$\cdot$L$\cdot$s^{-1} and FG II had a removal rate of 2 torr$\cdot$L$\cdot$s^{-1}. Surprisingly, the construction material of the pumped limiter head also affected the removal rate, indicating surface pumping. A change from a double-sided pumped limiter to a single-sided pumped limiter in TFR also resulted in increases of a factor of two in the particle removal rate [32] and a reduction of the recycling coefficient from 0.91 to 0.68 with active pumping. Care has to be taken in the interpretation of the experimental data on exhaust efficiencies, since surface pumping can be significant, particularly for hydrogen isotopes in carbon.

In many of the double-sided pumped limiters, marked asymmetries in the particle removal rate between the two sides were noted [6, 572]. In T-10, these asymmetries were attributed to plasma rotation at low densities and to a poloidal asymmetry in the cross-field transport at high density. Because cross-field diffusion is largest on the low field side midplane of a tokamak [9], the side of the pumped limiter which is most directly connnected to this region by the field line geometry will receive the larger flux. The flux asymmetry reversed when the plasma current was reversed, as expected. These asymmetries are discussed in more detail in Section 10.1.

Most pumped limiter experiments have been carried out with relatively small limiters, typically 10–20% of the poloidal extent of the plasma circumference. However, a complete toroidal limiter, ALT-II [573], has been installed on TEXTOR. Experimental data indicate that, so far, the pumping capability is similar to that of smaller limiters [574]. This is due, at least partly, to the flux e-folding length being rather small when operating with ALT-II. This illustrates a general point, namely that as the limiter area increases, the connection length decreases and hence the particle e-folding length decreases. The available flux increases only slowly with increasing limiter size.

As can be seen from Fig. 51 (Section 4), exhaust efficiencies of 10% or better, i.e. edge recycle refuelling of less than ten times the core fuelling (by pellets or neutral beams), can result in peaked plasma density profiles which are effective in increasing the net fusion energy production and possibly also in improving the confinement (see Section 4.1.3).

Detailed design studies have been carried out for pumped limiters on INTOR [575]. Although pumping appears to be adequate for density control, major difficulties are expected to arise in the control of impurities due to sputtering and with evaporation due to disruptions.

7.2.3. Ergodization of the boundary layer

One of the most promising ways of reducing the effects of plasma-wall interaction is to divert the outermost field lines of the confinement system into another chamber. There are a variety of ways in which this can be done, and these systems are described in Section 7.3. It was pointed out by Karger and Lackner [576] that under some circumstances the use of helical poloidal coils could produce magnetic islands and divert poloidal field lines outside the main confinement region (Fig. 87). They proposed that a resonant helical divertor could be formed using currents which are a small fraction ($\sim 1\%$) of the plasma current. This

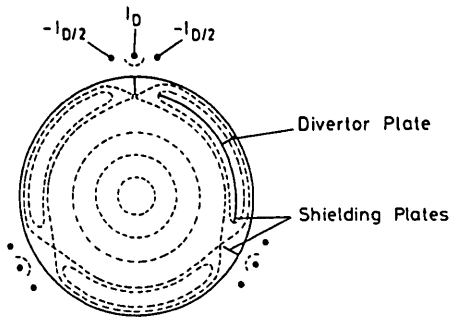

FIG. 87. Cross-section of a helical divertor with triplet helical windings outside the vacuum chamber and shielding plates only in the outer section of the torus (resonance at q = 3) [576].

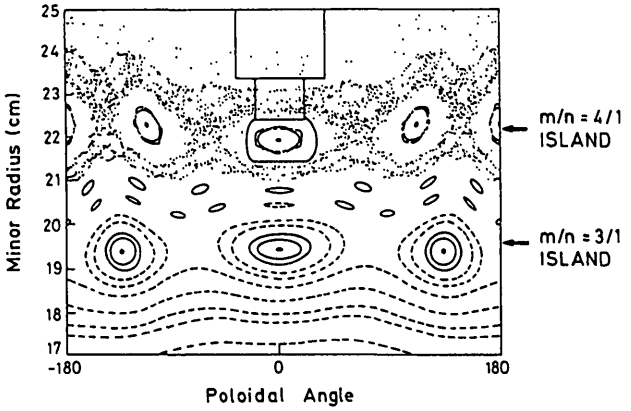

FIG. 88. Magnetic field mapping, showing the formation of the m/n = 3/1 and 4/1 magnetic islands near the plasma edge on JIPP T-IIU [578]. The parameters are B_T = 2.4 T, I_p = 170 kA and I_h = 5 kA.

seemed to be a very attractive way of forming a divertor with a minimum of engineering complications. However, they used an infinite aspect ratio, circular cross-section model in their analysis. Subsequently, it was shown that the symmetric structure as shown in Fig. 87 is destroyed, at least partly, by finite toroidal curvature and non-circular cross-sections [243]. Under these conditions the pitch of the field line becomes non-uniform, the q value at a given radius varies with plasma pressure, and the structure of the helical flux surfaces becomes 'ergodized', i.e. there is a random walk of field lines in the radial direction, crossing the previously unperturbed flux surfaces. This effect tends to destroy the divertor action. However, small magnetic islands of finite size are present, and some evidence of divertor action has been found in experiments using a small scoop limiter in TEXT [577] and in JIPP T-IIU [578] (Fig. 88). It is difficult to increase the size of the magnetic islands, since the current required increases quadratically with the spatial extent of the islands. Thus, it is unlikely that this approach will be able to provide any significant effect other than to deflect the field lines around small limiters.

Use of an ergodic layer, produced by a set of helical coils which are deliberately designed to break up the magnetic surfaces, has been proposed as an alternative approach to controlling the plasma-surface interaction [310, 579]. The ergodization of field lines is caused by overlapping magnetic islands, produced by superposition of the field of a resonant helical winding on the toroidal field. The principles of the design of the helical coil system to produce the ergodic layer have been given by Samain et al. [580].

Engelhardt and Feneberg [310] have used a simple model of impurity transport (see Section 5) to show that by enhancing the cross-field diffusion in the boundary outside the LCFS, a significant reduction in the central impurity concentration would be produced. The proposed helical winding with m = 6, n = 2 was predicted to produce a diffusion coefficient perpendicular to B_T of 9 $m^2 \cdot s^{-1}$ — possibly an order of magnitude higher than the usual anomalous cross-field diffusion. Because the particle confinement time in the layer is short, any impurities which are ionized in the layer flow rapidly back to the wall. Such an arrangement is called an ergodic magnetic limiter. It is important that the plasma density and temperature in the ergodic layer are maintained at sufficiently high levels for ionization of the neutral impurity influx. Theoretical estimates indicate that for the ergodic magnetic limiter these levels should be adequate [310, 579], but there are as yet no good experimental data. A detailed design was presented for a large ergodic limiter on Tore Supra [581, 582]. Experimental studies on the TEXT tokamak demonstrated changes in the heat load pattern on the limiter, reduction in the confinement of the boundary layer and shielding of impurities [583].

Initially, it was also believed that an ergodic layer would lead to more uniform heat loading on the wall. However, so far, there are no full-scale demonstrations of the operation of such an ergodic limiter, and a number of difficulties may arise. Firstly, the mixing of field lines depends on their undergoing many toroidal transits. As soon as a material surface is interposed, magnetic islands are formed and the heat loading on the wall becomes non-uniform. Secondly, the ergodization needs to be large in order to be comparable with anomalous cross-field diffusion. Large amplitude perturbing fields can lead to plasma disruptions [584]. In general, analyses of the effects of the ergodic magnetic

limiter are not self-consistent with respect to impurity production. A constant impurity production rate is assumed in these analyses. However, any screening of impurities will result in less radiation from the plasma and hence more power conducted and convected to the walls, which will probably lead to increased impurity production. This is discussed in more detail in Section 6.

7.2.4. Experiments with a biased limiter

Varying the potential of a limiter, V_L, can vary the plasma potential, V_p, since there is a constant potential difference — the sheath potential drop V_{sf} — between the limiter and the plasma, i.e.

$$V_p = V_{sf} + V_L \qquad (7.2)$$

Thus, if there is only one limiter, varying the limiter potential will only change the electric field in the SOL between the plasma and the wall. However, if a small limiter is biased with respect to a main limiter, then changes in the local plasma potential can be induced. Experiments with biased probes were carried out on Macrotor [585], TEXT [34] and TOSCA [24]. The aim of these experiments was to control the radial electric field in order to improve plasma confinement.

In Macrotor, the use of cold cathodes or hot filaments to inject electrons resulted in significant variations of the radial profile of the potential [585]. By biasing the plasma negative with respect to the edge, the radial transport of both hydrogen and impurity ions could be reduced, leading to a density increase and an accumulation of impurities. Eventually, the increase in impurity concentration resulted in disruptions. Reversing the bias caused strong hydrogen outflux and a reduction of the plasma density.

Similar effects were observed in TEXT [34]. A probe limiter (120 mm diameter) was put 15 mm radially inside the main poloidal limiter and biased positively and negatively. The negative bias resulted in an increased particle confinement time for both plasma ions and impurities. This was attributed to a local reduction in the outward particle flux due to reduced electrostatic turbulence. The impurity confinement in the centre of the plasma (measured using laser ablation injection of impurities) did not change as a result of the biasing.

In contrast to the above two experiments, results from TOSCA [24] showed no measurable effect of the limiter bias on the level or the spectrum of density fluctuations or plasma potential fluctuations. Positive and negative biases were applied between the limiter and the vessel wall or between the electron and the ion drift sides of a split limiter. The biasing did change the mean level of the floating potential at probes both near the limiter and far from it.

7.3. Divertors

7.3.1. Introduction

The use of conventional limiters to define the LCFS encounters two principal deficiencies:

(1) *Impurities.* Much of the plasma-surface interaction occurs at the limiter which is in direct, virtually unshielded contact with the main plasma.
(2) *Pumping.* Auxiliary heating can raise the main plasma density to the density limit, and a means of edge pumping of the hydrogen is therefore required. In the DT phase of operation, the helium ash must also be continuously pumped. Conventional limiters provide only limited opportunities for achieving edge pumping.

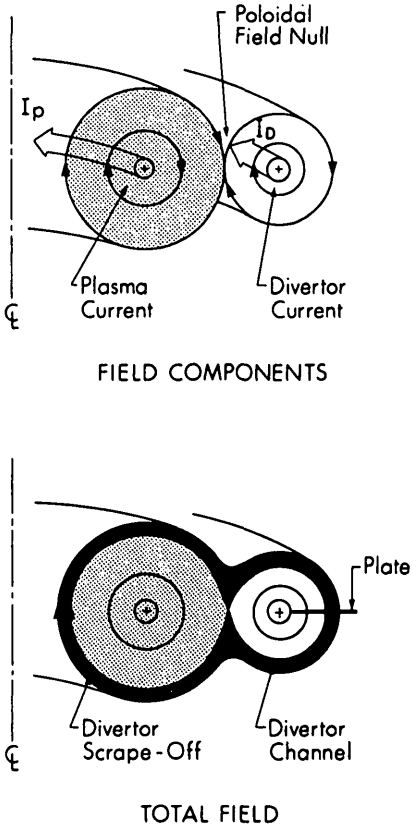

FIG. 89. Schematic diagram of a poloidal divertor. I_p and I_D are the plasma and divertor coil currents.

Use of divertors is a means of dealing with the two intrinsic deficiencies of limiters. Several divertor configurations have been proposed and/or studied [243, 586, 587]. The discussion here is restricted to the poloidal divertor configuration (Fig. 89), which is the preferred one. An external coil carries a current I_d parallel to the plasma current I_p, thus diverting the poloidal magnetic field and creating a magnetic null. A *magnetic separatrix* thus defines the LCFS. Flux surfaces outside the LCFS can be conveyed some distance away from the main plasma — perhaps into a separate divertor chamber — where the plasma-surface interaction occurs at the divertor target plates. In other divertor configurations, external magnetic coils can be used to divert the toroidal magnetic field. However, the poloidal divertor enjoys several advantages: (a) toroidal symmetry, (b) large target area, and (c) the external fields need only be of order B_p, rather than B_T.

Because the location of the principal plasma-surface interaction is now remote from the main plasma, the latter can, in principle, be kept cleaner. By conveying the plasma exhaust stream into a separate chamber, the neutralization at the plates can result in a buildup of the pressure of the neutral gas in the divertor chamber, facilitating efficient pumping.

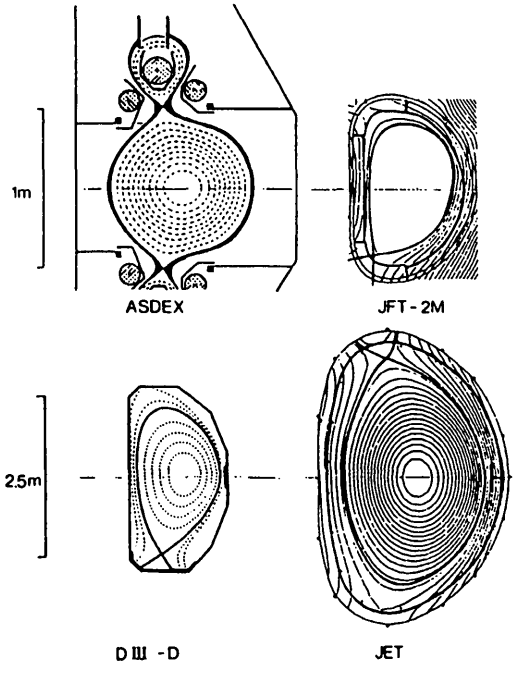

FIG. 90. Open and closed divertor configurations. ASDEX closed; DIII-D, JFT-2M and JET open [606].

The initial poloidal divertor studies on ASDEX and PDX [588, 605] employed such a 'closed' divertor geometry (Fig. 90, ASDEX example). However, on DIII it was demonstrated [589, 590] that an 'open' divertor geometry (Fig. 90, JFT-2M, DIII-D, JET examples) can achieve the same benefits as the closed one. It appears that, provided the 'plasma fan' striking the divertor plate is sufficiently extended and is sufficiently dense, both the hydrogen and the impurities recycling at the plate are trapped locally by the strong ionization in the fan. The divertor plasma fan can be quite voluminous owing to the expansion of the poloidal flux surfaces and the (potentially) large wall/X-point distance (see Fig. 90). Since the open divertor configuration requires less vessel volume, it is favoured for future reactor designs such as ITER [591]. It was also employed on JET [592, 593], which, although not originally designed as a divertor tokamak, required relatively minor modifications to achieve the open, 'X-point', configuration (Fig. 90).

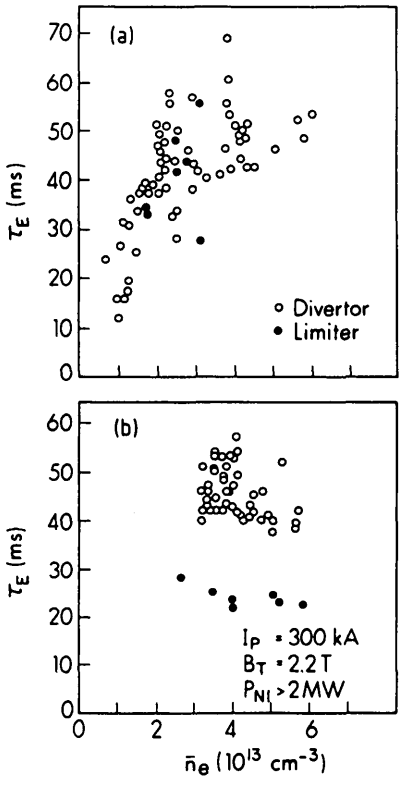

FIG. 91. ASDEX: Density variation of the global energy confinement time of limiter and divertor discharges, with (a) Ohmic heating and (b) beam heating [243]. For limiter operation (without H-mode), beam heating decreases τ_E for a given $\bar{n}_e$. For divertor operation with an H-mode, τ_E is not decreased by beam heating.

A third, unanticipated benefit from divertors was discovered in ASDEX [371, 594], namely achievement of the H-mode. Normally, for limiter discharges, τ_E decreases with additional heating (compare Figs 91(a) and 91(b)). Operating with a divertor, and with sufficiently high beam power, a high τ_E mode was discovered in ASDEX (Fig. 91(b)). This H-mode has since been reproduced on other divertor tokamaks — DIII [595], PDX [596], PBX [597], JET [592], JT-60 [598], JFT-2M [599], DIII-D [600] — and although it was originally thought to be unique to the divertor configuration, it was recently demonstrated in JFT-2M [601] and DIII-D [602] using an inner wall limiter.

Recently, edge modelling studies of the divertor configuration, including comparisons with experimental measurements, have been reviewed by Neuhauser et al. [603].

In the following five sections, we review the experimental evidence with regard to five key features of the edge plasma for divertor operation:

- the achievement of a cold, dense plasma at the divertor plate;
- the achievement of strong gas compression in the divertor region;
- impurity control;
- edge conditions and the H-mode;
- the high recycling divertor.

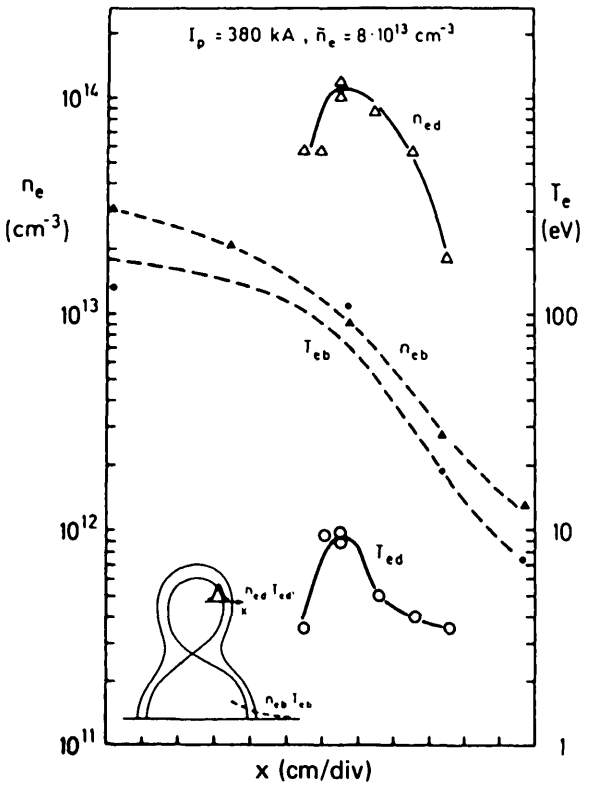

FIG. 92. ASDEX: Radial profiles of electron temperature and density at two characteristic positions along the SOL, namely in the torus midplane (n_{eb}, T_{eb}) and in the divertor chamber (n_{ed}, T_{ed}), for a beam heated discharge (P_{NI} = 2.5 MW). The midplane values are measured by laser scattering, the divertor data are obtained from a Langmuir probe. The inset shows the location for the measurements [243].

7.3.2. *The cold divertor plasma*

Experimentally, a strong temperature gradient has been observed [371, 604] along the divertor SOL, from the zone near the main plasma to the divertor target (Fig. 92). Assuming that the pressure is constant along $\vec{B}$, a strong density gradient would also be anticipated, and was actually found (see Fig. 92). Such an operating regime has the following attractive features (see Ref. [605]):

(a) The temperature of the plasma actually in contact with the surface can be quite low, reducing sputtering.

(b) The temperature of the edge plasma in contact with the main plasma can be relatively high, thus maintaining higher temperatures in the main plasma; it also appears that a high edge temperature is required for the H-mode, perhaps because the shear stabilization near the separatrix is only effective at high temperatures [243, 602, 606].

(c) *Shielding:* The high plasma density in the divertor reduces the probability of neutral (hydrogen and impurity) escape into the main plasma, yielding several benefits: (i) gas compression is improved, aiding pumping; (ii) contamination of the main plasma by plate material is reduced; (iii) charge exchange processes in the main vessel are reduced, reducing wall sputtering by cx neutrals; and (iv) the edge of the main plasma is not cooled by the atomic processes associated with the recycling of hydrogen and impurities.

While experimental evidence for the achievement of these strong gradients is often clear, the reason for their existence is less evident. We need to know if such gradients can be expected for reactor conditions and whether they could also be achieved with limiters. We therefore consider some simple analytic modelling of the divertor. More extended analytic modelling has been presented in the literature [243, 589, 607-609],

together with extensive numerical (code) analyses [229, 587, 610-618, 673]. Here, we consider the most simplified model capable of reproducing the basic features of the divertor, namely the strong gradients along the SOL.

We use three equations for the analysis:

(1) *Pressure balance:*

$$n_d T_d = 0.5\, n_u T_u \tag{7.3}$$

(2) *Sheath heat transfer:*

$$\frac{F_p P_c}{A_{SOL}} = \gamma_s n_d\, kT_d\, c_{sd} \tag{7.4}$$

(3) *Parallel heat conduction in the SOL:*

$$T_u^{7/2} = T_d^{7/2} + \frac{7 P_c L_c}{2 A_{SOL} \kappa_0} \tag{7.5}$$

where the subscript d indicates the conditions at the divertor plate; the subscript u indicates upstream conditions, i.e. for the SOL near the main plasma; F_p is the fraction of the divertor power reaching the plates; P_c is the power entering the SOL from the main plasma; $F_p P_c$ is the power reaching the plates, i.e. $(1 - F_p)P_c$ represents volume energy losses in the divertor plasma; A_{SOL} is the effective area of the SOL for carrying power ($= 4\pi R_m \lambda_p B_p / B_T$), i.e. the SOL area projected perpendicular to $\vec{B}$; L_c is the connection length ($\approx \pi R_m q$); and $\kappa_\parallel = \kappa_0 T_e^{5/2}$ is the parallel heat conductivity, where $\kappa_0 \simeq 2000/Z_{eff}$ (for power density in units of $W \cdot m^{-2}$ and T in eV) (Spitzer [619]).

The pressure balance equation (7.3) assumes that total pressure, $nT(1 + M^2)$, is conserved along $\vec{B}$ (M is the Mach number) and that $M_d = 1$ and $M_u = 0$. The heat conduction equation (7.5) is the solution of

$$\frac{d}{dz} \kappa_\parallel \frac{dT_e}{dz} = 0 \tag{7.6}$$

with one boundary condition being

$$-\kappa_\parallel \left.\frac{dT_e}{dz}\right|_u = \frac{P_c}{A_{SOL}} \tag{7.7}$$

i.e. for simplicity, all of the power is assumed to enter at the upstream end of the flux tube. The second boundary condition is given by Eq. (7.4).

It has been assumed that heat is conducted rather than convected along the SOL. Neglect of convection is justified here because the ionization of the recycled hydrogen is assumed to occur very close to the divertor plate because of the high value of n_d. This causes M to remain very low over most of the length of the SOL, only rising rapidly to unity through the narrow zone of ionization in front of the plate [620]. One reason why it is difficult to achieve strong temperature gradients for the limiter configuration is that it is more difficult to ionize the recycling neutrals entirely within the rather narrow SOL at the limiter (compared with the large divertor plasma fan) and much of the re-ionization occurs inside the LCFS (see Section 5). Thus, M remains relatively high along the length of the limiter SOL and convection tends to reduce the temperature gradients.

By combining Eqs (7.3), (7.4) and (7.5), it can be shown [198, 205, 621] that the existence of a significant temperature gradient, $T_u \gtrsim 2T_d$, requires that the following criterion be satisfied:

$$F_d \equiv \frac{Z_{eff}\, n_u L_c}{F_p T_u^2} \gtrsim 10^{17}\ m^{-2} \cdot eV^{-2} \tag{7.8}$$

Assuming that Z_{eff} and L_c are not likely to vary greatly between machines and that T_u must not be too low (say, $\simeq 100$ eV) in order to maintain a sufficiently hot plasma at the separatrix for the H-mode, then this

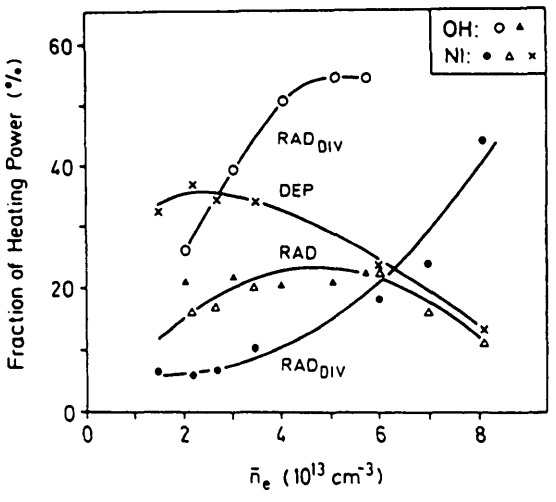

FIG. 93. ASDEX: Fraction of the heating power in the loss channels: main plasma radiation (RAD), divertor radiation (RAD_{DIV}) and deposition onto the target plates (DEP) for ohmically heated (P_{OH} = 0.4–0.5 MW) and beam heated (P_{NI} = 2.1 MW) discharges [243].

criterion indicates that there are essentially only two ways to achieve a strong temperature gradient: sustainment of high edge densities and/or sustainment of high volume energy losses. It appears that machines such as ASDEX and DIII have often exploited small values of F_p, while reactor designs such as INTOR assume high edge densities as a means to achieve the same result.

In ASDEX [622, 623], PDX [624] and DIII [625], strong volumetric power losses have been measured in the divertor region (Fig. 93) with F_p dropping to $\simeq 0.15$ at the highest plasma densities. The nature of these losses is not entirely clear. On ASDEX, impurity and hydrogenic radiation appears to be small, implying that neutral particle (F–C and cx neutral) losses are responsible. In DIII, radiation can account for the loss. Unless the plasma temperature falls to a very low value, $\lesssim 5$ eV, the volume losses associated with hydrogenic recycle cannot re-direct very much of SOL input power away from the plate (see Section 3.6.1). This limitation on the role of volume losses is made clear in an example taken from an INTOR study [229] where essentially all of the ionization of the recycled hydrogen occurred within the divertor; nevertheless, the power flux to the plate still constituted 87% of the power flux into the SOL. This INTOR divertor plasma, however, was still relatively hot (~ 25 eV), while the ASDEX temperatures were much lower (Fig. 92) and were in the range where volume losses are more important [228].

The criterion given by Eq. (7.8) can be illustrated by giving representative values: for ASDEX, $Z_{eff} = 2$, $n_u = 10^{19}$ m^{-3}, $L_c = 10$ m, $F_p = 0.15$, $T_u = 100$ eV, which gives $F_d = 1.5 \times 10^{17}$ m$^{-2}\cdot$eV^{-2}; for INTOR, $F_p = 1$, $n_u = 5 \times 10^{19}$ m^{-3}, $T_u = 100$ eV, $Z_{eff} = 1$, $L = 20$ m, which gives $F_d = 1 \times 10^{17}$ m$^{-2}\cdot$eV^{-2}. Thus, for these two cases, temperature gradients are achieved by two different means. ASDEX [626] has also been operated in regimes with strong temperature gradients, but with little volume energy loss, $F_p \simeq 1$, and only moderately high density, $n_u \simeq 10^{19}$ m^{-3}; in such cases, however, $T_u < 100$ eV, Eq. (7.8). Examples of these cases are given in Figs 94a, 94b, where n_u, T_u, T_d and F_d are plotted as functions of Γ_d[s$^{-1}\cdot$m^{-2}], the neutral flux density in the divertor chamber. F_d was calculated assuming $Z_{eff}L_c/F_p = 20$ m. As can be seen from this figure, significant temperature gradients only occur when $F_d \gtrsim 10^{17}$ m$^{-2}\cdot$eV^{-2}.

With regard to the feasibility of achieving strong gradients in limiter configurations, it can be said that neither mechanism is as readily implemented as with a divertor. Confining volume energy losses to the SOL near the limiter is difficult, as discussed above.

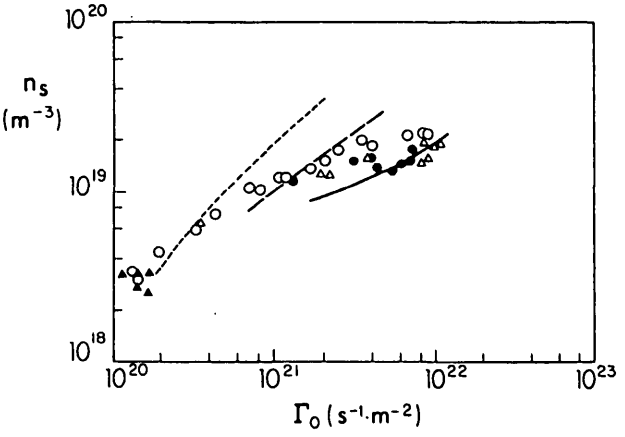

FIG. 94a. ASDEX: Midplane separatrix density n_s as a function of the neutral flux density Γ_0 in the divertor chamber (deuterium, $q_\parallel = 1.2 \times 10^7$ W·m^{-1}). The measured values for Ohmic discharges (symbols) are compared with simulations for fixed power input, but varying atomic and molecular sticking factors (--- 0.5, 0.1; —— 0.3, 0.02; ——— 0.01, 0.02 [626]. Different symbols indicate different discharges.

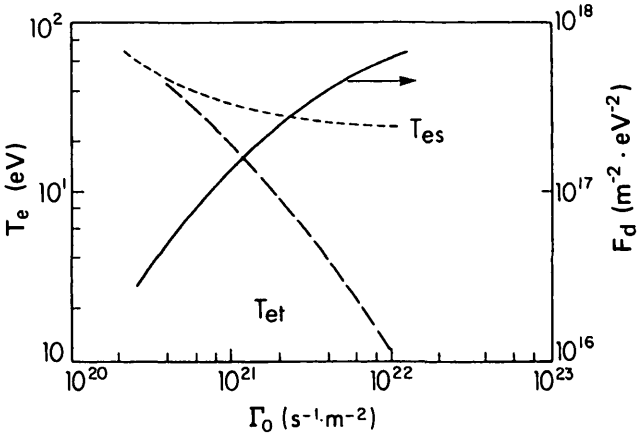

FIG. 94b. ASDEX: Electron temperature values for the same conditions as in Fig. 94a. T_{es} (= T_u) is the average value of the midplane temperature. T_{et} (= T_d) is the average value of the target plasma temperature. F_d is defined in Eq. (7.8).

Operation with a high value of n_u may be possible, say a few 10^{19} m^{-3}; however, if a high T_u/T_d ratio is in fact achieved, the result will be a high ratio of n_d/n_u. In this case, a high n_d plasma would be directly in contact with the main plasma, rather than being remote and not directly coupled with the main plasma as in the divertor configuration. Such a high edge density plasma localized near the limiter would, to some degree, force the main plasma density to rise, possibly to disruptive levels. Therefore, achievement of a high gradient SOL in a limiter configuration would appear to be difficult.

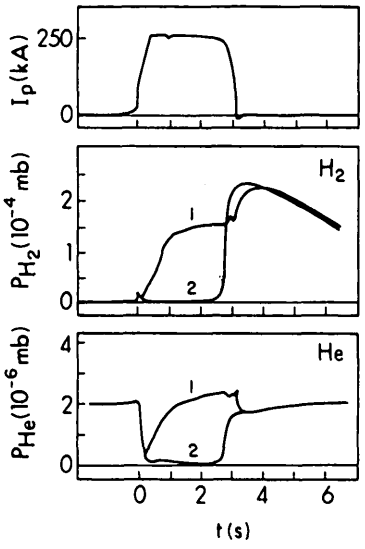

FIG. 95. ASDEX: Hydrogen and helium partial pressures in the main plasma (2) and the divertor chamber (1), during and after a discharge of 250 kA plasma current [243].

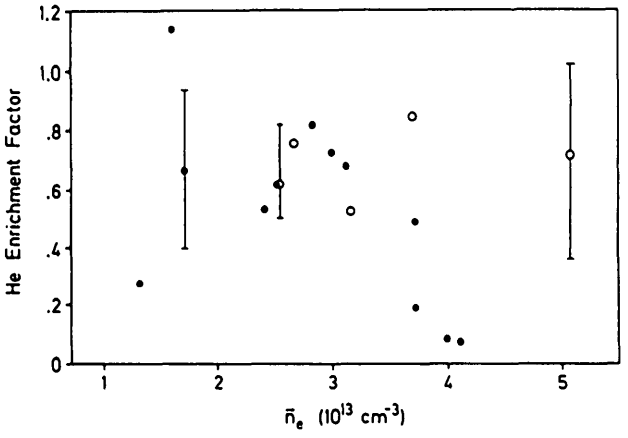

FIG. 96. DIII: Helium enrichment relative to hydrogen for the XB (closed symbols) and the SN (open symbols) configuration. Neither configuration shows helium enrichment; the XB configuration shows helium de-enrichment at higher plasma density [243].

7.3.3. Gas compression in the divertor

Both for reasons of plasma density control and in order to remove the fusion product helium, it is necessary to pump away a significant fraction of the total particle outflow from the plasma [509]. During a discharge the neutral pressure near the walls is generally very low [243, 627], of order 10^{-6} mbar or less, and so the required pumping speed may be prohibitively large unless some plasma-induced compression can be achieved. The divertor configuration has been demonstrated to produce such a compression both for hydrogen and for helium seeded into the gas feed (see Fig. 95) [243]. During the ASDEX discharge shown in Fig. 95, the H_2 compression ratio between the main chamber and the divertor was about 100, while the He ratio was ~20. Such strong compressions have also been demonstrated on an open divertor tokamak, DIII [589, 590] and DIII-D [627], where the large plasma fan appears to be as effective at retaining the gas locally as the closed-off volume of ASDEX. On DIII [590, 628] the question of He enrichment by the divertor has also been examined; the He enrichment factor η_{He} is defined as:

$$\eta_{He} \equiv \frac{n_{He}/n_H \text{ (divertor)}}{n_{He}/n_H \text{ (plasma)}} \tag{7.9}$$

The results in Fig. 96 [243] indicate some de-enrichment; nevertheless, the He compression itself is an order of magnitude or more, for the single-null configuration.

On JT-60 [629, 630], operated with a closed divertor, hydrogen compressions of up to 45 have been achieved in L-mode operation. The divertor chamber is pumped with Zr/Al getters which provide a pumping rate of 6.8 $m^3 \cdot s^{-1}$. In L-mode operation, this provided sufficient particle removal to totally compensate for the large neutral beam fuelling (75 keV, 20 MW H_0) and so density control was readily achieved with a gas puff valve. By contrast, for limiter operation the neutral beam injection caused $\bar{n}_e$ to increase by more than 50%. During H-mode operation the gas compression dropped to ~20, which was insufficient to compensate the beam fuelling.

7.3.4. Impurity control by divertors

The original motivation for the divertor concept was the achievement of lower central impurity levels than could be obtained with a limiter. The existing evidence for reaching this goal can be divided into two categories: (a) direct comparisons of Z_{eff} values for limiter and divertor configurations, and (b) specialized impurity studies employing divertors. With regard to direct comparisons, the evidence for cleaner plasmas is mixed and not entirely convincing. Specialized divertor impurity studies indicate that the expectations of improved impurity control are largely fulfilled. It appears, therefore, that the potential of divertors to achieve cleaner plasmas may exist, but full realization of this potential requires careful optimization. On the other hand, a number of deleterious processes peculiar to impurity behaviour with divertors have been identified in recent years, and it is possible that, when all

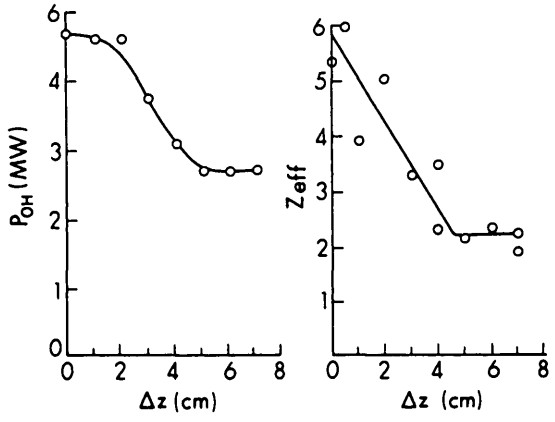

FIG. 97. ASDEX: Variation of the Ohmic power input P_{OH} and of Z_{eff} with the vertical distance Δz between the single-null plasma and the toroidal limiter [243].

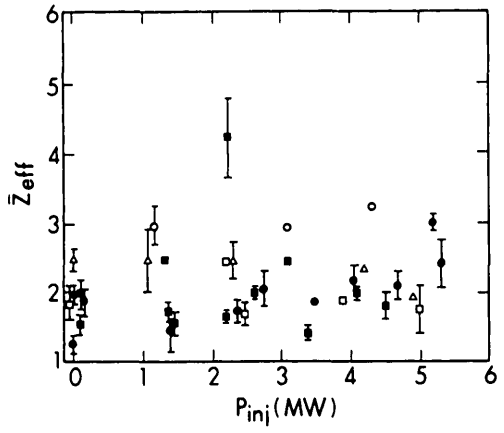

FIG. 98. PDX: Z_{eff} from Thomson scattering data for neutral beam heated plasmas operating with graphite rail limiters, the inner wall bumper limiter or the Dee shaped divertor. Spitzer resistivity is assumed for all cases [635].

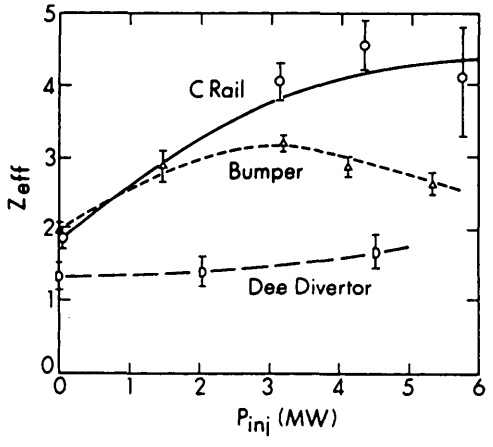

FIG. 99. PDX: Visible bremsstrahlung measurements of Z_{eff} after at least ~200 ms of neutral injection for several configurations [636]: ● — carbon rail (cooled, conditioned), ○ — carbon rail (uncooled, unconditioned); × — scoop; ■ — closed divertor; □ — open divertor.

processes are taken into account, the divertor configuration may not be intrinsically superior to limiters regarding achievement of central plasma purity.

Turning first to direct comparisons of divertors and limiters: The earliest experiments in PDX [588] and ASDEX [605] showed that plate/limiter metals in the central plasma were reduced when a divertor was employed. In PDX [631], with titanium limiters/plates, Z_{eff} was reduced from 3.1 to 1.7, while the central Ti levels dropped by an order of magnitude. In DIII [632], where Inconel was used, a similar drop in the Ni level occurred. In T-12 [633] the radiation loss was decreased by a factor of two to three when the plasma was transferred from the limiters to the divertor. In ASDEX [634], a comparison was made between divertor (Ti plate) operation and toroidal limiter (graphite) operation (Fig. 97). As the distance ΔZ between the single-null plasma and the limiter was reduced, Z_{eff} increased dramatically, from ~2 to ~6. In PDX [635], the carbon rail or bumper limiters showed significantly higher Z_{eff} values than those obtained with a Ti divertor (Fig. 98).

These early comparative studies thus seemed rather convincing. It now appears, however, that the limiters were not optimally operated in these studies. Further studies carried out on PDX [636] with better conditioned and cooled carbon limiters showed little apparent difference between limiter and divertor configurations (Fig. 99); on the strength of this, Fonck et al. [636] noted: "... the impurity control advantage of the divertor is no longer obvious for PDX discharges". (The authors also noted, however, that the PDX limiter discharges tended to be at higher $\bar{n}_e$, and, since Z_{eff} is almost universally observed to decrease with $\bar{n}_e$, the comparison may still be interpreted in favour of divertors.) The very high Z_{eff} value (~6) found in ASDEX using a graphite limiter (Fig. 97) would also appear to be associated with a poorly conditioned limiter.

In JET [219], operating at the same $\bar{n}_e$ (2.2×10^{19} m^{-3}) and with a well conditioned graphite limiter, values of Z_{eff} ~ 2 were found (Fig. 100). In fact, when JET [592] was operated with an open divertor configuration, *higher* values of Z_{eff} than for limiter operation were found (Fig. 100) (although in this case it is probably the *divertor* operation which was not optimized). In JT-60 [598], operated with graphite limiters or divertor plates, little difference in the Z_{eff} values between the two operational modes was found (see Section 5, Fig. 52c) (although also in this case the divertor operation probably was not optimized since the X-point was on the outside of the plasma). Interestingly, when JT-60 was operated with metal walls (TiC + Mo), divertor operation showed

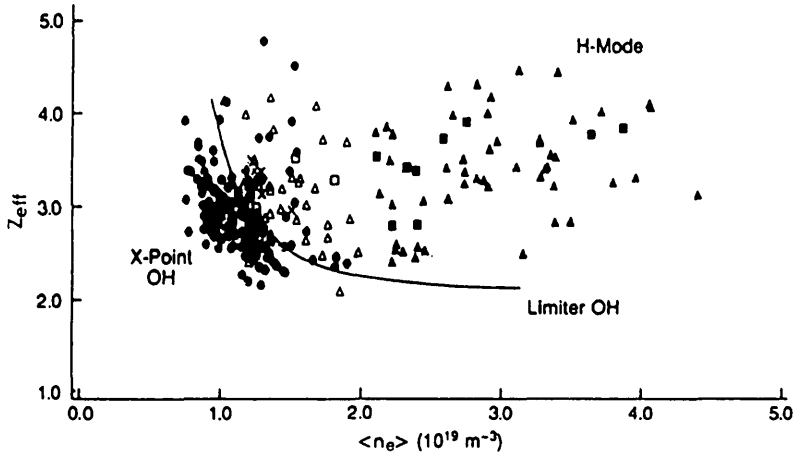

FIG. 100. JET: Z_{eff} versus $\langle n_e \rangle$ for X-point plasmas with Ohmic heating (⊕), NB heating (△) and combined heating (□); (solid symbols denote the H-mode). For comparison, the continuous line shows the typical behaviour of limiter plasmas with Ohmic heating. In the H-mode, Z_{eff} does not decrease with increasing $\bar{n}_e$ in the normal way [219].

a remarkable superiority over limiter operation [598]: the main chamber radiation was reduced from ~50% of the power input to only 5-10%. As in the case of ASDEX and PDX, the effectiveness of the divertor appears clearest for metals.

The following conclusions can be obtained from the direct comparisons of divertors and limiters:

- Overall, the evidence for a difference between the two operating modes is not convincing;
- Such comparisons are, however, very difficult to interpret since it is rarely the case that both configurations are optimized;
- For all-metal devices the evidence for superior divertor performance is good, but for carbon devices there is no obvious difference.

The problems encountered in direct limiter-divertor comparisons can be avoided by carrying out specialized divertor studies aimed at testing certain predicted effects. One important type of divertor impurity study involves puffing of an impurity gas, such as neon or argon, into either the main chamber or the divertor region and measuring the ability of the divertor to retain, confine or concentrate the impurity. This was carried out on ASDEX [637, 638] and on DIII [589, 632], sometimes with quite convincing results (Fig. 101). For the ASDEX tests with Ohmic discharges, the neon level in the main plasma was three times higher without a divertor. In DIII [589], the retention capability of the open divertor was found to increase strongly with increasing $\bar{n}_e$. However, in ASDEX, with NBI,

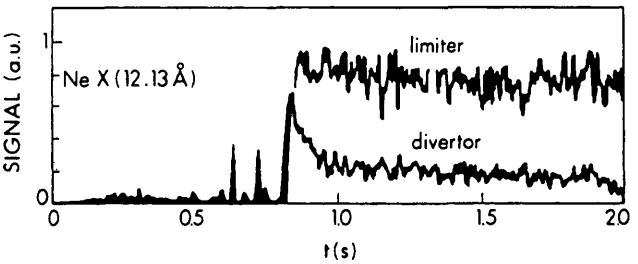

FIG. 101. ASDEX: Comparison of the NeX radiation in limiter and divertor discharges. The neon gas valve opened at 0.8 s for 6 ms [243].

a drastic breakdown of argon retention by the divertor occurred [638]. The reason for this breakdown is not known; it may be associated with temperature gradient forces or with the development of 2-D flow recirculation patterns under high recycling conditions (see Section 7.3.6). The anticipated ability of a divertor to remove impurities from the main plasma and to retain them is thus evidenced, at least under some circumstances.

Closely related tests focus on the ability of the divertor to retain the intrinsic impurities, i.e. those produced at the plates. Despite the strong cooling of the divertor plasma, plate sputtering is still observed to occur (see Section 5, Fig. 55). When titanium plates were used in ASDEX, it was not possible to test for titanium retention since the main vessel walls had already been contaminated. A change to copper in the

ASDEX divertor has now permitted a retention test [639]. The Cu influx measured at the plates is found to decrease with increasing $\bar{n}_e$ (Fig. 102). The central plasma Cu content, however, decreases much more rapidly (Fig. 103). Quantitative analysis indicates that, at the lowest densities, about 15% of the sputtered Cu reaches the core plasma, while, at the highest densities, this percentage is only about 0.3%. Impurity deposition detectors distributed at various locations in ASDEX showed that, integrated over many discharges and various conditions, only about 10% of the eroded plate material was deposited on the main vessel walls [640]. Thus, the expected capability of a divertor to retain its own impurities is confirmed (although whether this retention is effective *enough* in the H-mode is unclear, see below).

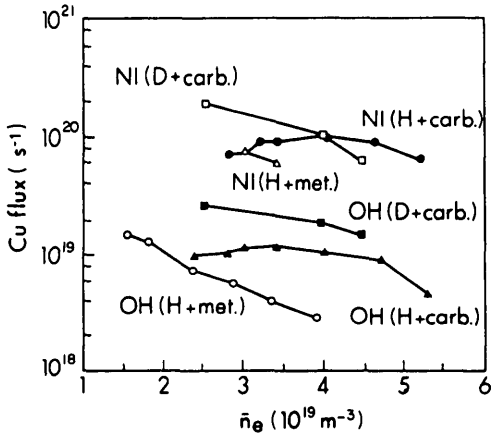

FIG. 102. ASDEX: Total copper flux versus $\bar{n}_e$ in the case of H^+ and D^+ discharges (heated by both OH and NI ($H^0 \rightarrow D^+$)) and under conditions of carbonized and bare metal main chamber walls [639].

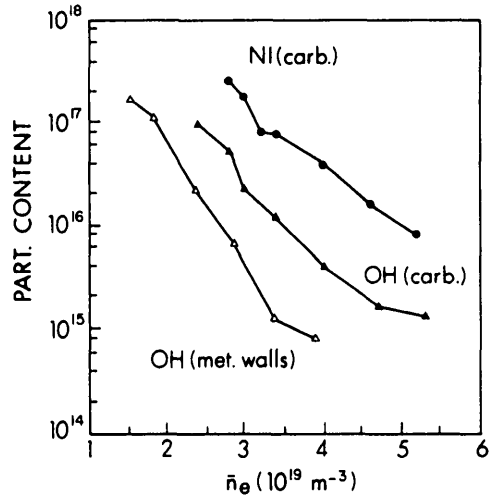

FIG. 103. ASDEX: Total copper particle content in the plasma versus $\bar{n}_e$ for Ohmic discharges (metallic wall, carbonized wall) and NI heated discharges (carbonized wall, $H^0 \rightarrow H^+$) [639].

What prevents a more dramatic and clear-cut demonstration of overall divertor superiority? As already mentioned, the lack of full, optimized comparisons is part of the problem. This is probably not the complete explanation, however, since comparisons of different machines — ones optimized for divertor operation versus others optimized for limiters — still show no clear-cut superiority. The explanation may lie in a number of impurity processes that were originally not anticipated, such as the following ones.

(a) *Wall sputtering by charge exchange neutrals.* As discussed in detail in Section 5, a comprehensive set of studies on ASDEX [361] identified cx sputtering of the walls as the principal source of central impurities in hydrogen discharges (for He discharges, ion sputtering at the divertor entrance shield was also important). Presumably, for a divertor tokamak which was actually operating with complete recycle in the divertor, there would be no cx wall sputtering, and so the implication for reactor operation is not clear.

(b) *Impurity accumulation in the H-mode.* A divertor tokamak can be particularly susceptible to even small impurity sources, since impurity accumulation [372] can characterize the H-mode [641, 642, 643] and can result in radiative collapse of the discharge [371, 373]. In PBX [643], impurity accumulation is also seen in the L-mode. It can therefore be critical to control even relatively small influxes [644], particularly of the highly radiating medium-Z and high-Z impurities, which underlines the importance of the detailed Fe and Cu ASDEX studies. In order for impurity accumulation not to reach disruptive levels, it is estimated [372] that the metal fraction before the beginning of the H-mode must not exceed $\simeq 10^{-4}$, while a level of $\lesssim 2\%$ is tolerable for C and O. The problem of impurity accumulation may, however, not be a problem exclusive to divertors: a variety of high τ_E modes on ASDEX, such as pellet injection, counter-injection of neutral beams and improved Ohmic confinement (IOC), also result in impurity accumulation [372].

There are, however, H-mode conditions where no impurity accumulation takes place. For DIII-D [645] it is found that regular, sporadic expulsion of particles and energy into the edge (edge localized modes, ELMs) tends to purify the plasma. Unfortunately, the peak heat loads on the plates during the ELM bursts can reach extremely high levels, >30 MW·m^{-2}, with the risk of plate melting.

(c) *Counter-stream forces on impurities in the divertor.* In the simplest model, the impurities are entrained in the highly collisional hydrogenic flow to the divertor plate and are thus retained at the plate. Unfortunately, the strong parallel-field temperature gradient results in a force on the impurities which pushes them away from the plate [507, 646]. At the same time, the hydrogenic frictional force is substantially reduced in its effectiveness by operation of the divertor in the high recycling mode. In the 1-D model, this mode causes most of the SOL and the divertor plasma to be nearly stagnant. In the 2-D model, the situation is still more serious since a recirculating pattern becomes possible, with back-streaming of the hydrogenic plasma occurring at some radial locations [610, 647, 648]. Whether these theoretically identified processes can account for the observed divertor retention limitations has not yet been demonstrated. Extrapolation to reactor conditions is therefore still uncertain.

(d) *Suprathermal ions and electrons.* The bulk of the plasma adjacent to the divertor plate may be quite cold, but fast, 'suprathermal' ions and electrons — which are nearly collisionless — can penetrate to the plates from the main plasma SOL where the temperature is high. The resulting sputtering due to the fast ions can exceed that due to the cold plasma ions in the divertor [362], while the fast electrons can melt the plates. It should, however, be possible to avoid such problems by operating at sufficiently high (density) conditions and/or by magnetically sweeping the plasma fan across the plates.

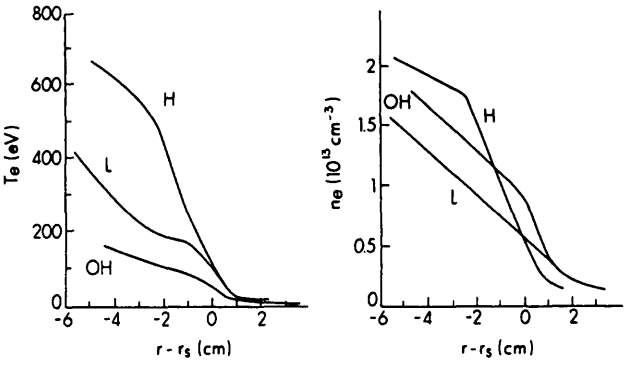

FIG. 104. ASDEX: Radial profiles of electron temperature and electron density at the plasma boundary for the three different confinement regimes, OH, L and H. r_s is the separatrix radius. I_p = 320 kA, $\bar{n}_e = 4 \times 10^{13}$ cm^{-3}, P_{NI} = 2.85 MW [653].

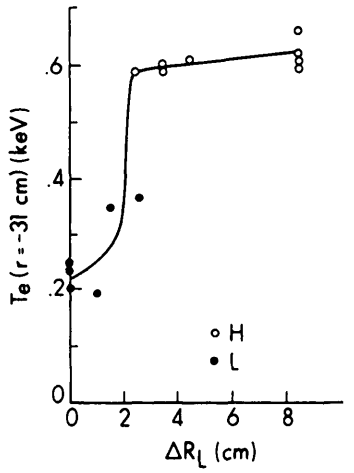

FIG. 105. ASDEX: Variation of the edge electron temperature when the outside poloidal limiter ring is moved to the plasma surface. The data points for $\Delta R_L = 0$ are obtained from limiter discharges without energized divertor coils [653]. P_{NI} = 2.4 MW, I_p = 380 kA.

7.3.5. *Edge conditions and the H-mode*

It was first observed on the ASDEX divertor tokamak [649] that when sufficiently high neutral beam injection power was applied, the energy confinement time τ_E suddenly increased from the low value usually characteristic of auxiliary heated tokamaks (L-mode). One of the clearest signals of the onset of this high τ_E mode, the H-mode, is an abrupt decrease in the edge H_α signals, implying reduced losses to the edge. The threshold power required to achieve an H-mode was found [594, 649–652] to depend on B_T, $\bar{n}_e$, the heating method (Ohmic, NBI, ICRH, ECH), the hydrogen isotope, the direction of the ion $\nabla\vec{B}$ drift, the distance between the X-point and the wall, and I_p.

The H-mode is characterized by steep density and temperature gradients just inside the separatrix [602, 606, 653–655] (Fig. 104). Related to this, the transport coefficients near the edge can decrease dramatically; on DIII-D, for example, transport changed substantially compared with Ohmic conditions [656]; on ASDEX [657], $\chi_\perp$ and $D_\perp$ decrease about a factor of six (H/L comparison); on JET [658] it is found that the decreased transport is only just near the edge. At the same time, edge fluctuation levels suddenly decrease [602, 655]. These n and T 'pedestals' [653, 659] increase the energy content of the plasma, resulting in the higher value of τ_E in the H-mode. Various models [243, 621, 660–663] attempt to explain when an H-mode equilibrium state is possible and how a transition to it is triggered. It is not evident that the H-mode is triggered by changes originating in the edge.

It is clear, however, that certain edge processes are characteristic of the H-mode. The high edge temperature appears to be critical [602, 606]. When the ASDEX separatrix was moved closer to a limiter, the edge temperature was cooled and an abrupt loss of the H-mode resulted (Fig. 105) [653]. By puffing impurities into ASDEX, a similar loss of the H-mode could be produced [653], evidently due to edge cooling. The achievement of the H-mode in the first place requires a certain minimum energy input [660] from auxiliary heating — apparently to overcome the edge heat losses. It has been demonstrated on JFT-2M [664] that the neutral beam power threshold for producing the H-mode can be substantially lowered if the localized electron cyclotron heating of the plasma just inside the separatrix is sufficient to raise the temperature there to 360 ± 40 eV.

The nature of hydrogenic recycling also appears to be critical, possibly because of the cooling associated with the ionization. The general signal of the onset of the H-mode is a sharp drop in the H_α signal at the plates, indicating improved particle confinement time and reduced re-ionization processes. A particularly illuminating study was carried out on PDX [659], showing the importance of the location of recycling. As originally operated, PDX employed a rather 'leaky' divertor chamber and, since the divertor plasma fan was not very large [587], the ability to achieve retainment of hydrogen in the divertor region was not good. The H-mode could not be achieved with this configuration. By blocking the gas passages connecting the divertor and the main chamber, the H-mode was achieved. The quality of the H-mode could then be degraded by gas puffing so as to raise the main chamber pressure artificially (Fig. 106) [659]. On DIII-D [665], the recycling hydrogen was reduced by pre-conditioning the large graphite surfaces using He glow-cleaning discharges so as to release the trapped hydrogen; this raised τ_E in the H-mode by 10–15%. When the graphite coverage was increased to 40%, it was only with such conditioning that an H-mode could be achieved. On JFT-2M, the edge neutral density was reduced by eliminating the gas input from the gas injectors, leading to a limiter H-mode and a low power divertor H-mode [601]. Recently, the ASDEX divertor design was altered to provide a larger gas conductance from the divertor chamber back to the main chamber. As a result, the gas compression effect was greatly reduced and the H-mode was essentially lost [666].

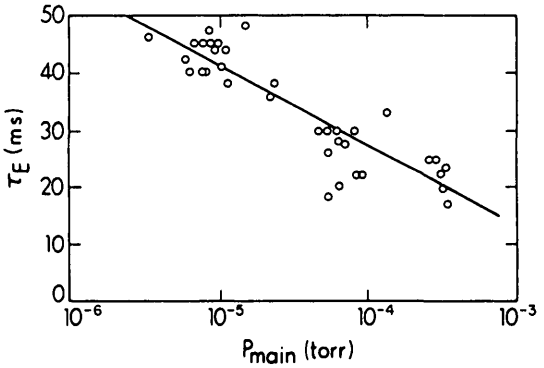

FIG. 106. PDX: Total equilibrium confinement time versus neutral pressure in the main chamber, for I_p = 400 kA, B_T = 1.6 T discharges [659]. H-mode, $D^0 \rightarrow D^+$, equilibrium analysis.

It thus appears to be important to keep the recycling neutrals away from the main plasma, to keep the edge radiation low, and to provide sufficient heating power to overcome these energy losses so that the high edge temperatures that are evidently critical to the H-mode are achieved. Since the L → H transition is abrupt, the effect evidently involves a bifurcation, which becomes possible when a minimum edge temperature is achieved. A possible explanation of such a bifurcation and of the role of edge recycle is given in the work of Hinton [594, 661]. When the cooling effect of recycling is low, the values of T_i near the separatrix can become large enough for the ions to become collisionless and to behave neoclassically. In this case: (i) the ion energy transport across the separatrix has two possible solutions [661] — a low-gradient solution and a high-gradient solution; and (ii) the ion grad-$\vec{B}$ drift can be effective, which should manifest itself in an up-down asymmetry in flows into single-null divertors located at the top or bottom of the torus — an effect which has in fact been observed [594, 650]. Rebut et al. [667] propose a different mechanism of bifurcation in which two solutions for heat transport near the separatrix exist: one with high edge temperatures a few centimetres inside the separatrix (~1 keV), with electron transport dominating, and one with comparatively colder temperatures (~250 eV), with ion transport dominating. The bifurcation, however, can only occur for such high absolute temperatures near the edge, indicating a power threshold; this is in approximate agreement with observation.

The phenomenology of the H-mode, and models to explain it, have recently been reviewed [602, 606, 655].

7.3.6. The high recycling divertor

In the limiter configuration, recycle ionization occurs near the limiter and thus also near, or in, the

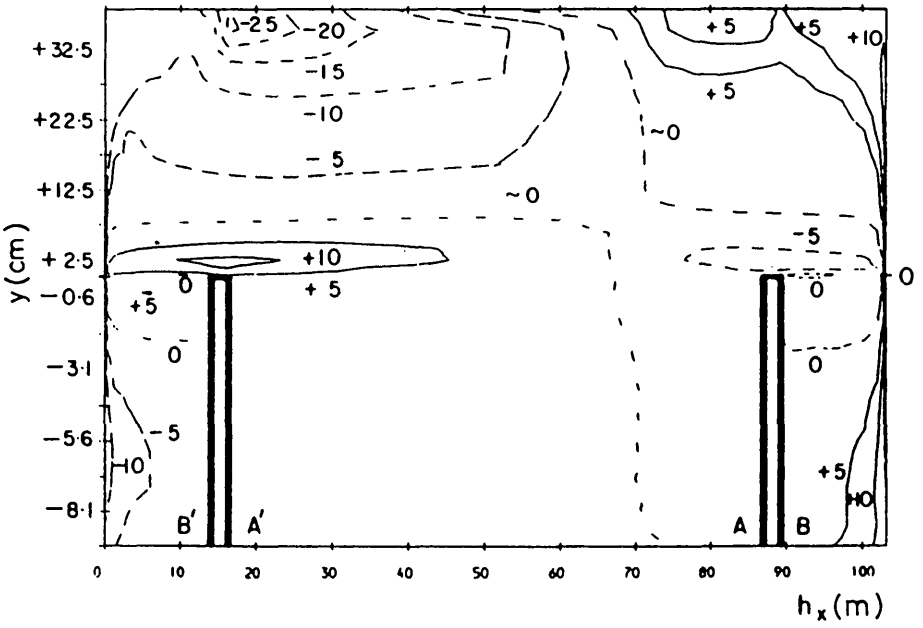

FIG. 107. Contours of parallel plasma flow velocity in the SOL and divertor regions from a 2-D code calculation [670]. The outer target is at the right-hand end, the inner target at the left-hand end; the separatrix is along y = 0; the main plasma is at large positive y; geometrical equivalent to the actual geometry (see Ref. [670] for details). Solid lines: flow towards the outer target, dashed lines: flow towards the inner target; units are 10^3 m·s^{-1}. Note that the flow reverses around the separatrix (y = 0) adjacent to both of the divertor entrances (h_x = 15 and 88 m).

main plasma. In the divertor configuration it is possible, by operating at high density, to arrange for the recycle ionization to occur near the divertor plate, i.e. at a location well removed from the main plasma. Although the evidence is incomplete and contradictory, it appears that the cross-field plasma transport is influenced by the location of ionization. In ASDEX, a new high τ_E divertor regime has been reported, the IOC regime [260]. This is achieved by reducing the gas puff early in the discharge, leading to a change in the particle transport parameters $D_\perp$ and v_{in}, in such a way that more peaked density profiles are obtained. The latter in turn seems to explain the observed higher τ_E values, which are perhaps due to stabilization of ion temperature gradient modes.

Pellet injection has often been observed to increase τ_E (see Ref. [668] and references therein). In recent ASDEX [668] pellet experiments, the improvement in τ_E was found to correlate with the achievement of the high recycling mode in the divertor. By contrast, when the tokamak was operated with strong gas pumping in the divertor, so that the ionization in the main vessel constituted a significant fraction of the total ionization, then lower τ_E values resulted. On the other hand, pellet experiments on DIII [664, 669] were associated with reduced recycling and reduced edge densities.

While the picture is not clear, it appears that it can be advantageous to manipulate the location of recycle ionization, with a view to influencing the energy confinement properties of the plasma. One of the advantages of the divertor, in that case, is that it can be used for such manipulation.

Possibly offsetting such advantages are the complex plasma flow patterns which, on the basis of simple theoretical considerations as well as 2-D plasma code results [610, 648, 670–672], are believed to result when the hydrogen is re-ionized very near the target plates. Figure 107 shows the 2-D flow pattern calculated [670] for the INTOR divertor configuration using the Braams plasma code [648, 671]. Immediately in front of the plates the plasma flow is towards the plates, but, a short distance further out, the flow is calculated to reverse for regions near the separatrix, although it remains towards the plates in regions away from the separatrix. To date, there is, unfortunately, only limited confirmation for the existence of such flow patterns [593]. The implications for impurity retention by the divertor are evident: the flow reversal region

could cause a major impurity leakage to the part of the SOL adjacent to the main plasma. This inherently 2-D effect may be the most important process regarding divertor impurity behaviour, and high priority is indicated for obtaining experimental information on 2-D flow patterns in the edge.

7.3.7. Conclusions

It appears that the divertor configuration has one proven and critically important advantage compared with conventional limiter operation: it is capable of gas compression and thus more efficient pumping of hydrogen and helium. The effectiveness of divertors at achieving significantly cleaner plasma conditions compared with limiter tokamaks remains to be demonstrated. The benefit of improved energy confinement in the H-mode is negated if impurity accumulation cannot be controlled.

Clearly, divertors are, in principle, more flexible instruments of edge plasma control than conventional limiters. The edge plasma conditions of reactors may be significantly different from any conditions encountered in present machines — whether those operated with limiters or with divertors. New possibilities for manipulation of edge behaviour will probably present themselves in these new conditions, provided some relatively active, flexible instrument such as a divertor is available.

8. AUXILIARY HEATING AND THE EDGE

8.1. Introduction

Although there are tokamak concepts which aim at achieving ignition solely on the basis of Ohmic heating, most designs call for significant auxiliary heating using NBI, ICRH, ECRH, etc. In addition, the achievement of steady state plasma currents may require the use of lower hybrid current drive (LHCD).

The application of power to the plasma at constant density must, in general, result in an increase in the power flowing to the edge and hence an increase in the edge temperature. The increased temperature may result in increased particle influx, both of plasma species and impurities, due to desorption, sputtering, etc. The resulting feedback mechanism is discussed in Section 6.2. One must be careful, therefore, to distinguish between changes in the edge due to the addition of power, by any method, and changes due to specific types of heating. ICRH is of particular concern as it appears that, under many conditions, local edge heating and impurity production specific to this heating technique can occur.

This section concentrates on reviewing the basic experimental information on the SOL under auxiliary heating conditions — primarily for the parameters n_{LCFS}, T_{LCFS}, λ_n and λ_T. Thus, it is the equivalent to Section 2.1 for Ohmic heating. More detailed issues, for example edge changes associated with NBI induced H-modes, are dealt with in other sections.

The experimental database for the tokamak edge plasma under auxiliary heating [674] is still less complete than that for Ohmic conditions. General conclusions are not possible, for the most part, and thus the review in the following sections is essentially phenomenological. Because of the evidence of direct interaction of ICRH with the edge, ICRH is the most studied of the auxiliary heating methods, and we give the main emphasis here to these studies. The edge plasma appears to be less directly affected by NBI heating. Little information about the edge exists for the other auxiliary heating methods.

8.2. Ion cyclotron resonance heating

Tokamak plasma-surface interactions during ICRF heating were reviewed by Cohen et al. [675] and Tachon [674] in 1984. The strong interaction between the edge plasma and ICRH arises from the requirement that the antenna be in close proximity to the edge plasma for efficient power coupling. Figure 108 shows the general schematic arrangement of the ICRH antenna in JET. Figure 109 gives the loading resistance of the JET-TFR antenna versus the plasma-antenna distance. (It should be noted, however, that most power deposition calculations predict that virtually all of the coupled power goes to a region near the resonance radius, generally positioned near the centre of the plasma, and not directly into the edge plasma.)

The close proximity of the antenna to the plasma, however, results in enhanced impurity production from the antenna structure and other wall components. The resulting high impurity radiation losses have posed serious problems for ICRH from its inception, although the power levels which can be successfully coupled have risen by two orders of magnitude, from $\gtrsim$0.1 MW (TFR, 1981) [676] to $\gtrsim$20 MW (JET, 1988) [677].

An increase in the SOL decay lengths with the application of ICRF power was almost universally observed, for example in TFR [678, 679], PLT [675], ATC [680], JIPP T-IIU [681], TO-2 [682], TEXTOR

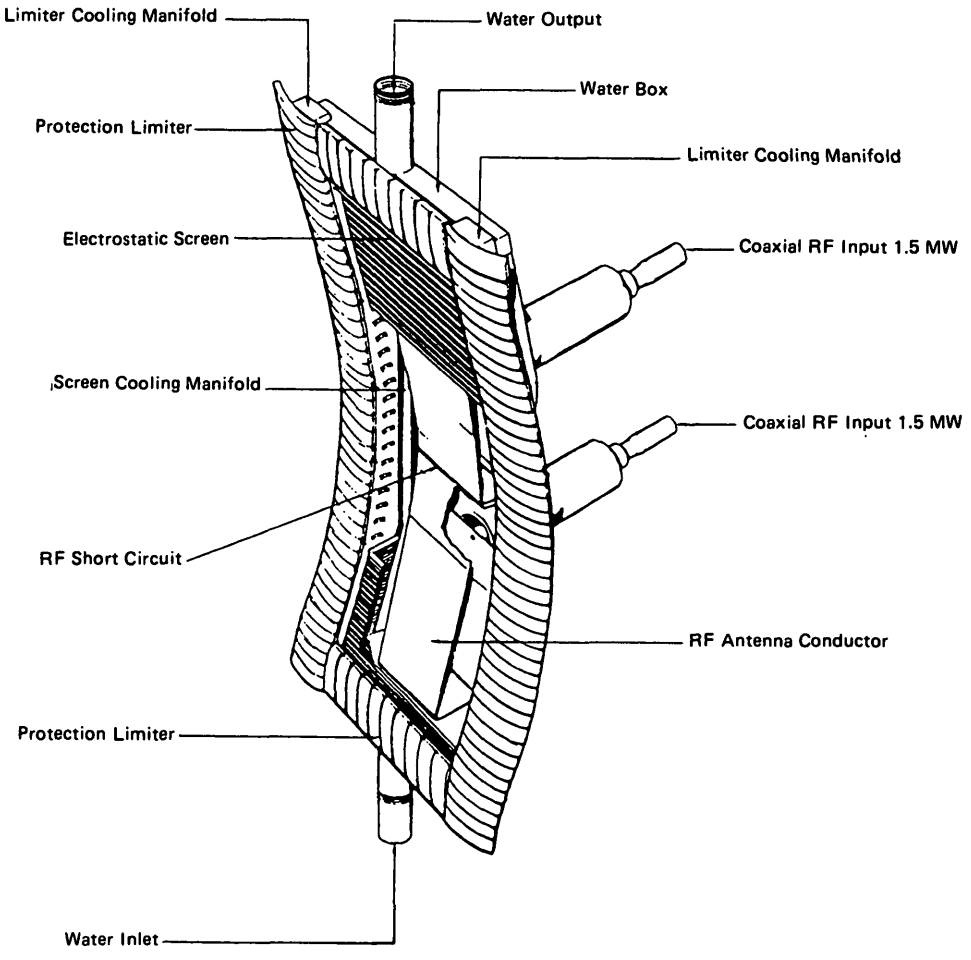

FIG. 108. JET: ICRF heating antenna.

[683, 684], ALCATOR C [685, 686] and JET [87, 677, 687]. In some of these tokamaks, and also in JFT-2M [688] and T-10 [689], the values of n_{LCFS} and/or T_{LFCS} also increase with the application of ICRH. An example of edge profiles (14 MW ICRH), measured by a reciprocating Langmuir probe in JET, is shown in Fig. 110, demonstrating increases in λ_n, λ_T, n_{LCFS} and T_{LCFS} over the Ohmic values. Figure 111 shows the JET results for T_{LCFS} and n_{LCFS} as a function of total power. It is also widely reported that changes occur in the SOL almost immediately upon the application of ICRH power — and not just after one energy confinement time, as would be expected for energy being deposited in the plasma core. TFR [678] reported a delay of less than 200 μs; in JET [87], the rise time of the edge Langmuir probe signal (250 μs) was about the same as the rise time of the RF power itself (see Fig. 112). In addition, in TFR [679] it was demonstrated that when the resonance zone was moved entirely out of the plasma (thereby stopping heating of the main plasma) the changes in the SOL with the application of

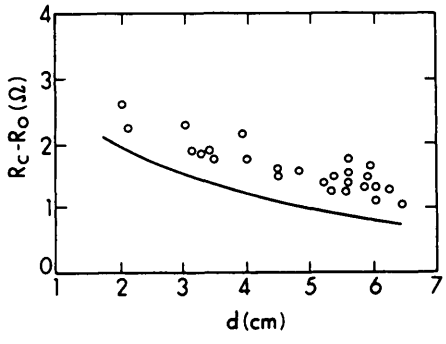

FIG. 109. JET: Loading resistance of the TFR antenna versus the distance between the plasma boundary and the central conductor (full curve, theory; open circles, experiment) [675].

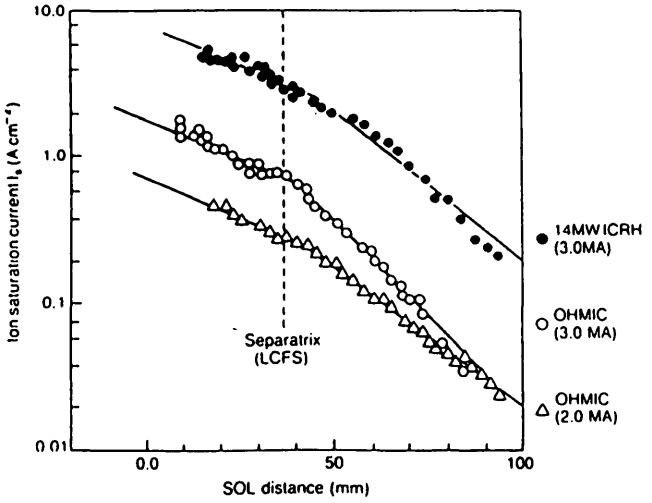

FIG. 110. JET: Effect of ICRH on the flux and temperature profiles for different values of I_p (I_p = 2.0 MA, B_T = 3.47 T; I_p = 3.0 MA, B_T = 3.4 T) and ICRH power (I_p = 3.0 MA, B_T = 3.4 T) [677].

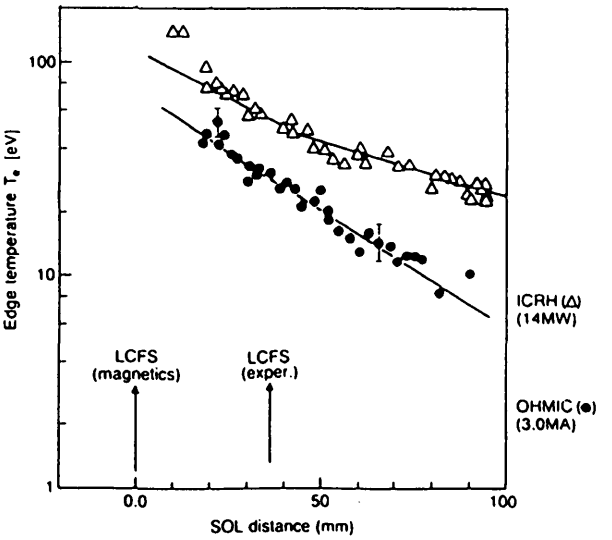

FIG. 111. JET: Effect of ICRH on the edge density and temperature for discrete and belt limiter configurations.

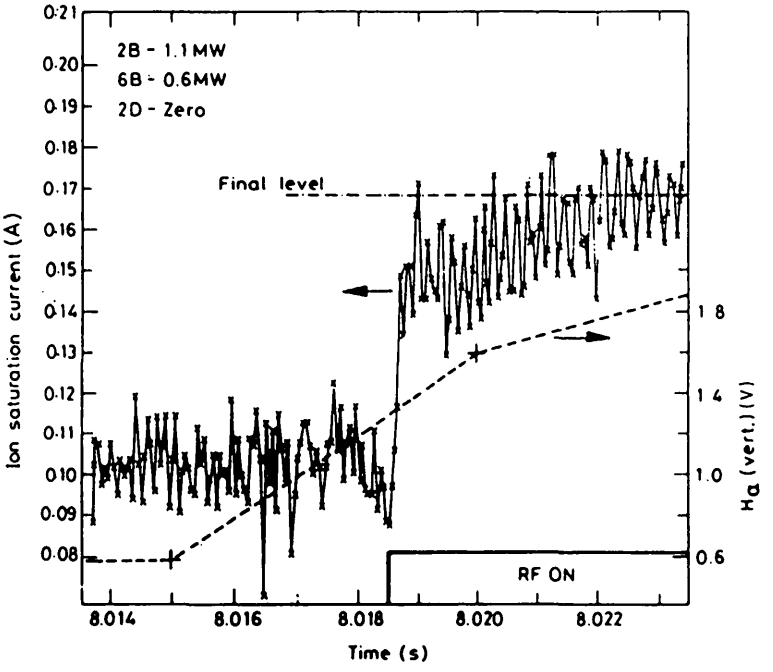

FIG. 112. JET: Raw data from the antenna Langmuir probe, taken at intervals of 50 μs during ICRH switch-on. The dotted curve shows the H_α light signal [87].

ICRH remained the same. It thus appears that, despite original theoretical expectations, some ICRH power is directly deposited in the SOL [676–678, 686, 689, 690].

As a result of the increased power flowing into the SOL, the hydrogenic fluxes to and from the limiters and walls increase strongly with ICRH [691]. An example of this for JET is shown in Fig. 113 [690]. Quite apart from the enhanced impurity production, this increased power influx is in itself undesirable since it causes a rise in $\bar{n}_e$, possibly to the density limit [690]. Compared with NBI of the same power, the influxes associated with ICRF presumably cause a cooler plasma periphery, which may explain the difficulty of achieving the H-mode with ICRF in JET.

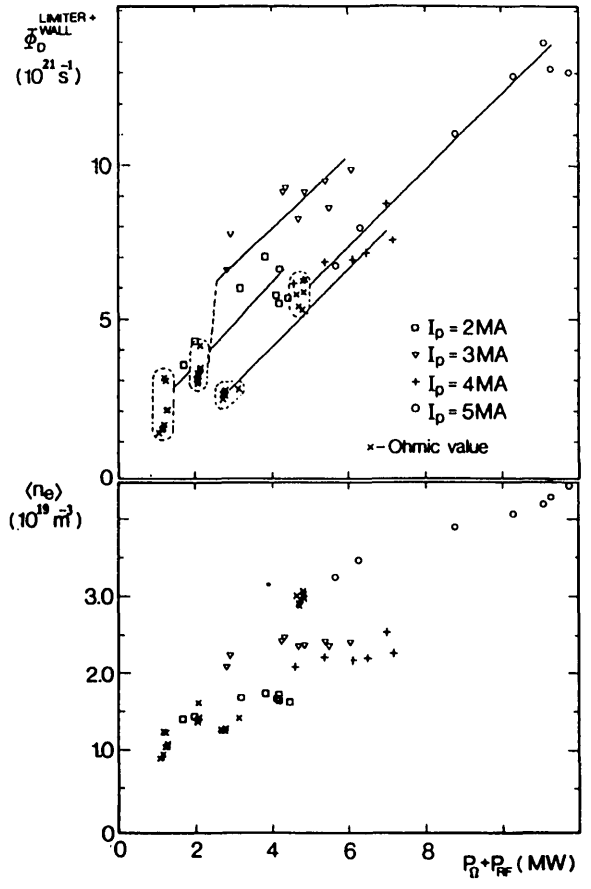

FIG. 113. JET: Power dependence of the total fluxes and the volume averaged density in deuterium discharges with ^{3}He as a minority species, for different plasma currents [690].

In the earliest applications of ICRH, the tokamak walls and all components of the antennas were metallic. Large metal influxes were generally observed to correlate with the application of ICRH power [361, 675, 676, 678, 685, 686]. Replacement of the metal limiters and antenna shields ('protection limiters', Fig. 108) by ones made of graphite, in some cases supplemented by carbonization of the entire interior (TEXTOR [683, 692], ASDEX [361] and JET [693]), was successful in greatly reducing metal influxes. It is difficult, however, to replace the Faraday screens by non-metal screens, and so metal (nickel) influxes remain a problem, for example, in JET at high (≃20 MW) power [694]. In addition, influxes of light impurities, C and O, can increase with ICRH power [681]. The benefits of carbonization disappear rapidly in ASDEX [361], again indicating enhanced plasma-surface interactions during ICRH.

In PLT, fast ions (~100 keV) were directly measured by Manos et al. [695] in the edge during ICRH, using a special probe (Fig. 114). The probe was inserted radially and could be rotated about its axis. The sensors were placed deep in the probe housing and thus only registered ions with large Larmor radii. Fast ions were found at the outside midplane, but not at the top of the torus. The strong carbon erosion observed in PLT was attributed to the fast ions.

There appear to be few reliable generalizations concerning ICRH and the plasma edge. Even the almost universal observation of the SOL thickness increasing with P_{ICRF} is no longer clear in the light of recent high power experiments on JET in well conditioned operation. Figure 115 shows the particle flux e-folding length λ_Γ versus the input power P_T for different edge conditions in JET. Case (a) is for the

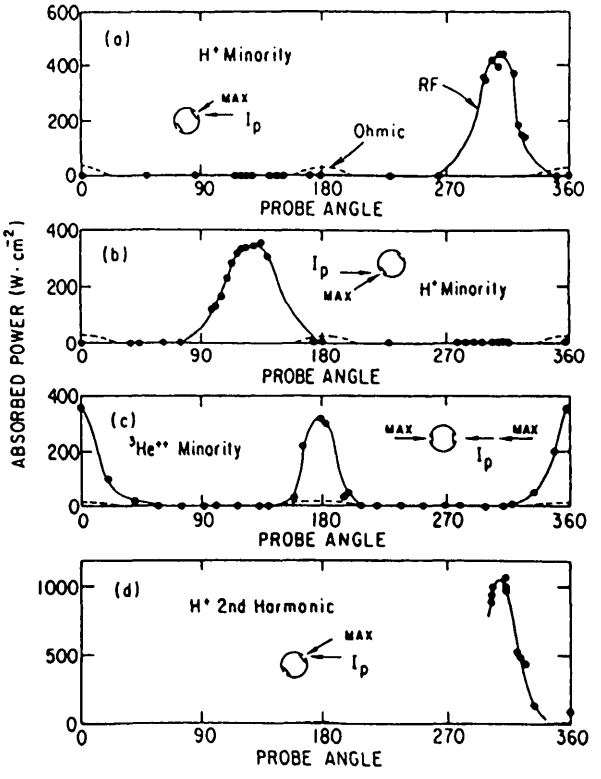

FIG. 114. PLT: (a) Heat flux to the probe as a function of rotation angle relative to plasma current. For D^+ plasma with H^+ minority, heated by 1 MW of RF power at 42 MHz.
(b) Same as in (a), with all fields and with the current reversed.
(c) Same as in (a), with $^3He^{++}$ minority, heated by 1.5 MW of RF power at 30 MHz.
(d) Same as in (a), for pure H^+ plasma, heated by 2 MW of RF power at the 2nd harmonic frequency [695].

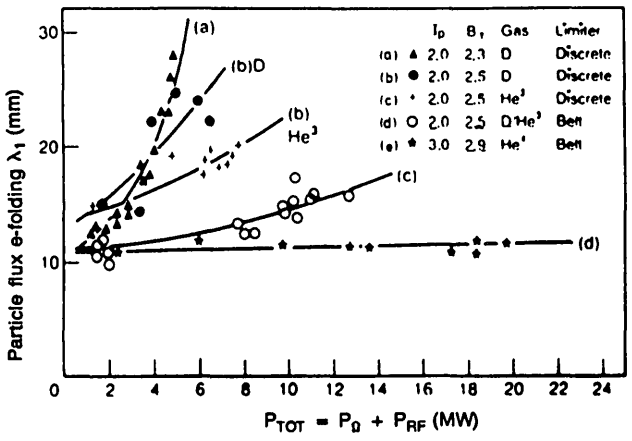

FIG. 115. JET: Effect of machine conditioning on the particle flux e-folding length for a constant plasma current and increasing ICRH power: (a) before carbonization, (b) in D and in ^{3}He after carbonization, (c) 2.0 MA and (d) 3.0 MA in the belt limiter configuration [677].

discrete graphite limiters and an Inconel first wall; the broadening of the scrape-off width with increasing P_T is dramatic. This strong dependence was weakened, however, by heavy carbonization of the vessel (case (b), for D) and by He conditioning discharges (case (b), for He). During 1987, more graphite protection tiles and two large-area graphite toroidal belt limiters were added, giving about 55% carbon wall coverage. These changes resulted in a considerable weakening of the dependence of λ on P_T (case (c)). For higher currents, the flattening of the radial profiles became negligible (case (d)), and no differences were found when the main gas was changed from He to D_2. As further evidence of the impact of the vessel condition on λ, one may consider the JET results shown in Fig. 116; these apply to the same situation as in case (d) of Fig. 115, but in this case there was substantial nickel contamination on the limiters, resulting from a series of high power ($P_T \simeq 22$ MW) ICRH discharges. For the case shown in Fig. 116 there is again a significant increase of λ with power. The JET authors [677] noted further: "Broader density profiles are observed in discharges following a plasma disruption and in the first few discharges in D_2 after several discharges in He. The particle flux and density SOL profiles are also found to be broader when the plasma density does not reach equilibrium during the heating phase [696]. This increase in e-folding lengths in a non-equilibrium state suggests that the modifications of SOL profiles during ICRH are determined by the state of cleanliness of the limiters and wall of the tokamak."

The high power JET studies [677], however, show that in the SOL the width of the electron *temperature* profiles always broadens with ICRH power, again implying direct heating of the SOL.

Although the situation is clearly in a state of evolution and general conclusions are not possible,

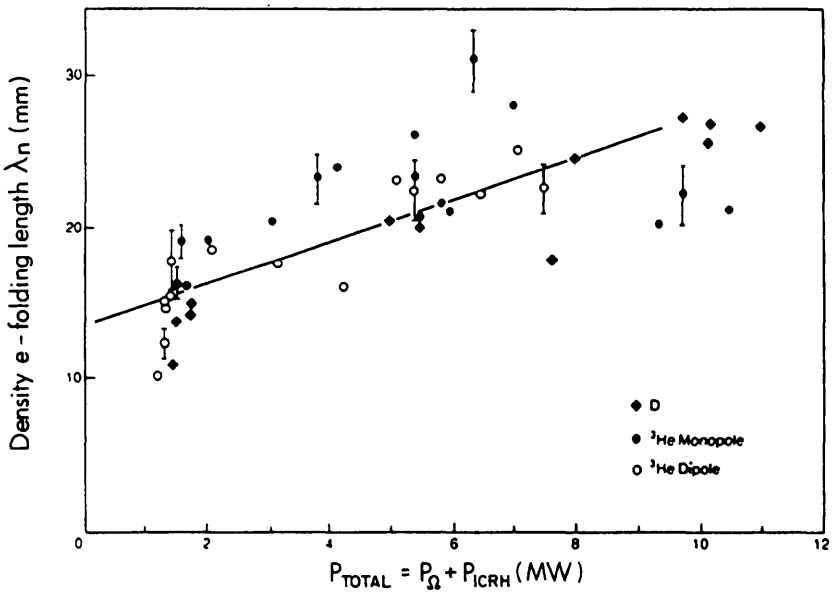

FIG. 116. JET: Effect of antenna phasing and total input power on the density e-folding length. The data are taken for plasma pulses with a limiter highly contaminated by nickel after high power discharges in ICRH ($\approx$22 MW); I_p = 3.0 MA, B_T = 2.9 T [677].

one might consider the following tentative model of ICRH in the edge:

(1) Some fraction of the ICRH power is directly transported into the SOL, heating it and thus increasing λ_T.
(2) Dependent on the state of conditioning of the walls, limiters and antenna components, this extra heat input may induce increased influxes of fuel gas and/or impurities. The increased SOL ionization associated with these influxes, when present, would then broaden λ_n (see Section 3).
(3) This effect is then amplified, since the increase in the values of λ means that bombarding fluxes extend radially further out into the SOL, contacting surfaces normally out of plasma contact and thereby releasing more neutrals.

This situation, in which significant heat and particle sources exist in the SOL itself, make the SOL 'complex' in the sense defined in Section 3. Unfortunately, this means that it is difficult to answer the question which is of critical importance regarding SOL cross-field transport during ICRH, namely whether the values of $D_\perp^{SOL}$ and $\chi_\perp^{SOL}$ increase. Without detailed information on the spatial distribution of sources it is not possible to deduce plasma transport properties [87, 687].

Further questions also remain, such as the following:

(a) What is the mechanism of direct SOL heating by ICRH? Coupling of ICRH to the evanescent slow wave at the edge has been proposed [697].

(b) How can the impurity generation at the Faraday screen [128, 382, 698–700] be explained? This influx does not appear to be simply the result of increasing scrape-off length since it occurs only for the antenna actually being activated [687]. It has been suggested [701] that this influx is the result of sheath effects at the antenna or of reactive $\vec{E}_{RF}$ fields near the antenna [688, 700, 702–704].

(c) Can the impurity generation at the walls and limiters be entirely explained by the increased values of λ_n, λ_T, n_{LCFS} and T_{LCFS} (the latter thus increasing the sheath drop), i.e. by enhanced physical sputtering by the thermal edge plasma [675, 679, 685, 686, 705, 706]? Or do the fast ($\sim$ 100 keV) ions produced by ICRH [695] cause significant erosion [675]? Does impurity (C, O) ion sputtering [361, 675, 706, 707] contribute significantly? What role does neutral sputtering play? In PLT [306, 675], strong increases in the charge exchange neutral flux were recorded during ICRH (Fig. 117) which were found to quantitatively explain the impurity influxes from the wall. Similar increases

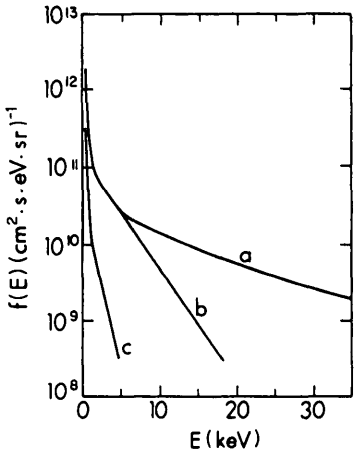

FIG. 117. PLT: Charge exchange flux spectra for ohmically heated and ICRF heated (P_{RF} = 1 MW) plasmas [675]. (a) H^+ spectra, 2nd harmonic heating; (b) D^+ spectra, ^{3}He minority heating; (c) target plasma.

in neutral outfluxes during ICRH were reported from TFR [679] and TEXTOR [708]. In JIPP T-IIU [681] the enhanced oxygen influx from the walls was attributed to fast neutral outfluxes. In ALCATOR-C [685], however, the impurity influx was not found to correlate with the fast outflux. In TFR [674], the impurity production rate did not change with changes in the high energy tail of the proton distribution. Does arcing play a role?

(d) What is the role of the antenna configuration (monopole, dipole, quadrupole) or of the antenna location in the vessel (low-B side, high-B side [678, 688]) or of the wave number spectrum [687, 709]? In JET, earlier indications of significant differences between configurations [687] have now become less pronounced [677].

8.3. NBI heating

The interaction of NBI heating with the SOL appears to be more straightforward than the interaction of the heating process with the SOL in the case of ICRH, although there is less experimental information.

The present generation of large tokamaks, JT-60 [598], TFTR [710-712] and JET [713], have operated with high levels of NBI power, $\sim$20 MW. Unfortunately, only few experimental data are obtained at the LCFS for such power levels. Measurements, made in JET [714] at 15 mm outside the LCFS and extrapolated to the LCFS, are shown in Fig. 118 for NBI power up to 5.3 MW; Fig. 119 shows λ_n for the

same discharges. Measurements made in TFTR [710] at NBI power up to 20 MW are shown in Fig. 120 for a probe located 12.5 cm outside the LCFS; since the TFTR scrape-off lengths are $\lambda_n \simeq 4.5$ cm and $\lambda_T = 5$ cm, extrapolation to the LCFS is somewhat uncertain.

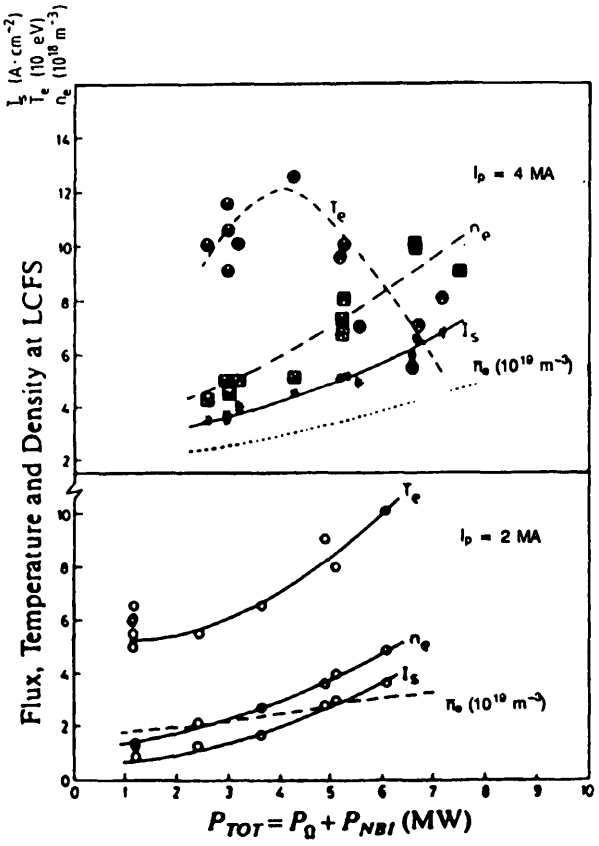

FIG. 118. JET: Effect of total input power on edge parameters at the LCFS. The average plasma density is also shown [714].

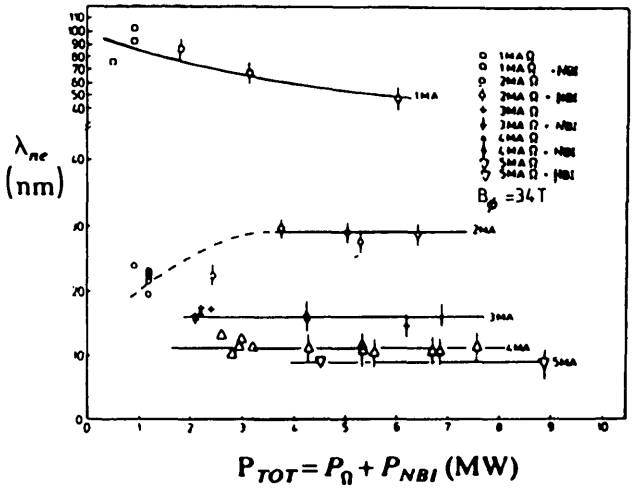

FIG. 119. JET: Effect of the total input power on the density e-folding length for a plasma current of 1.5 MA [714].

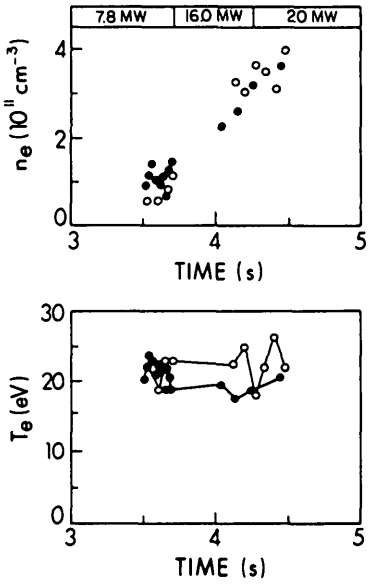

FIG. 120. TFTR: Electron density and temperature measured 12 cm outside the LCFS, 36 cm above the outboard midplane, for high power NBI [710]. Open symbols: flat-top current; closed symbols: ramped current

A complication in the interpretation of the SOL is that the central density continuously rises during NBI. This is shown in Fig. 118 (dotted lines) for the JET cases. For the TFTR case shown in Fig. 120, $\bar{n}_e$ rose from $\sim 10^{19}$ m^{-3} to $\sim 4 \times 10^{19}$ m^{-3}. This strong increase in $\bar{n}_e$ may explain the otherwise surprising result that T_{LCFS} can decrease as P_T increases (Fig. 118).

It appears that NBI does not cause direct heating of the SOL, as does ICRH. In JET [714], the edge conditions were found to change after the initiation of NBI with a time constant of 0.3–0.5 s, i.e. comparable to τ_E.

Of course, fast beam particles can directly reach the edge as 'shine-through' of the beam or via unconfined fast ions which have not thermalized [674]. Prompt heating of the TFR limiter [715] upon initiation of NBI has been taken as evidence of power deposition by high energy unconfined ions. Fast ions on large banana orbits have also been registered on an edge charge detector during NBI on TFR [674]. Asymmetric heat fluxes on limiters in DIII [716] were reported at very high levels, ≈ 3.5 kW·cm^{-2}, for ~ 4.5 MW NBI, and attributed to fast ions. These losses were found to account for 20–30% of the absorbed beam power.

Charge exchange between fast beam neutrals and plasma ions can also be a source of enhanced plasma-surface interaction during NBI. In ASDEX, this can be the principal source of impurity influx (see Section 5).

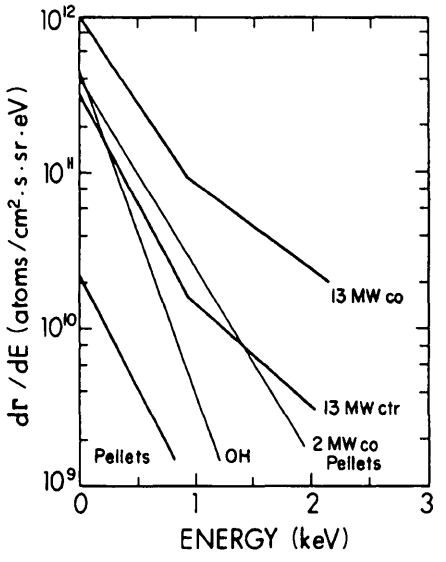

FIG. 121. ASDEX: Atom flux energy distributions for various discharge conditions measured at the walls of the main chamber [644]. Carbon resistance probe.

Figure 121 shows the energy distribution of charge exchange neutrals measured at the edge of ASDEX using a carbon resistance probe [644]; the enhanced neutral fluxes during NBI correspond to the enhanced impurity influxes. This figure also shows a difference between the effect of co-injection and the effect of counter-injection. Such differences have also been found in other tokamaks. For example, in TFTR [710], the plasma conditions at the bottom side of the plasma are radically different for the two injection directions (although less so at the outside midplane). The direction of injection has also been shown in ISX [717], ASDEX [361] and other devices to have a strong influence on impurity transport as well as on influx rates.

These complications associated with NBI prevent simple generalizations. Nevertheless, the experimental evidence suggests that the edge is not changed fundamentally or directly during NBI, as it can be during ICRH. In TFTR [710] and DITE [22] the scrape-off lengths are not significantly changed between Ohmic heating and NBI heating; the JET [714] values of λ_n during NBI (Fig. 119) are also little different from those for Ohmic conditions (see Section 2.1) and show little dependence on power. In JET, the changes of n_{LCFS} and T_{LCFS} with power (Fig. 118) appear to be simply the result of increases in $\bar{n}_e$ and power transferred to the SOL [714]. The more intense edge conditions during NBI result in greater impurity influx, but, since $\bar{n}_e$ is also increased, Z_{eff} is observed to change little during NBI in JET [128].

In the case of divertor discharges, one encounters the complication of n and T gradients along $\vec{B}$ in the SOL (see Sections 3 and 7.3). Measurements made in ASDEX [718] in the main part of the SOL, using a lithium beam, show that λ_n varies for the conditions: Ohmic (Ω) → L-mode (L) → H-mode (H) as: $\lambda_n^{\Omega}/\lambda_n^{H} \simeq 1.2\text{-}1.7$ and $\lambda_n^{L}/\lambda_n^{H} \approx 1.5\text{-}2.3$, with $\lambda_n^{H} \simeq 1\text{-}1.4$ cm; also at the LCFS [719] $n^{L} < n^{\Omega} < n^{H}$. Probe measurements in DIII [720] have been reported for both the main plasma and the divertor plasma, showing the edge density increasing with power and $\bar{n}_e$; the edge temperature dependence on $\bar{n}_e$ or P_T is ambiguous [83, 720]. Other experimental data for divertor operation are reviewed in Section 7.3.

8.4. Other auxiliary heating methods

Electron cyclotron resonance heating has been employed on T-10 [36, 689] at power levels up to 2 MW and on DITE [721] up to 400 kW. In both machines, the edge temperatures change little from Ohmic levels, but the densities increase. In an earlier T-10 study [689] and also in DITE, λ_n varied little from the Ohmic level; in later T-10 studies [36] at higher power, however, λ_n was found to increase. The increased λ_n may be due to SOL ionization at the high levels of n_{LCFS}, $\approx 2 \times 10^{19}$ m^{-3}. While the DITE edge changes occurred almost immediately ($\lesssim 1$ ms), the T-10 [36] edge was found to change more slowly (~ 5 ms), making it unclear whether direct power coupling into the edge is important. In T-10, at 2 MW ECRH, the total particle flux to the edge increased almost an order of magnitude above the Ohmic value. In both tokamaks, good energy balance was found during ECRH, using the probe measurements and measured values of P_R.

Alfvén wave heating up to 200 kW has been studied on TCA [674, 722–724] using different antenna designs. The edge temperatures increased with power, but the density decreased. A strong interaction between the edge plasma and the antenna was observed and attributed to sheath rectification effects. The electron distribution was found to be non-Maxwellian during wave heating. Wave heating was also found [725, 726] to have a strong influence on the correlations of low frequency fluctuations in the SOL.

RF waves near the lower hybrid resonance frequency can be used, at low $\bar{n}_e$, to couple energy to the high energy tail of the electrons, thus producing a net plasma current (LHCD) which can replace or supplement the Ohmic current, potentially leading to the possibility of non-pulsed tokamak operation. At higher

$\bar{n}_e$, lower hybrid heating (LHH) can be achieved. A fraction of the fast electrons produced in LHCD and LHH, however, reach the edge, causing hot spots, melting and sublimation of limiters [674, 675, 727–729]; during LHH, fast ions can be produced which are also able to reach the edge [728, 730], causing sputtering. In FT [731, 732] the application of a lower hybrid pump wave at 2.45 GHz reduced the SOL density by an order of magnitude, but the effect was less dramatic at 8 GHz. The rarefaction is explained quantitatively by ponderomotive effects and edge plasma heating due to the lower hybrid electric field in front of the RF grill. Similar density changes were reported from ASDEX [733] and JIPP T-IIU [734]. In JFT-2 [735], application of relatively low LHH powers ($\lesssim 100$ kW) was found to have little effect on the SOL temperature or density.

Thus, the general result is that $\bar{n}_e$ increases with power and $n_e(a)$ increases with $\bar{n}_e$.

9. FLUCTUATIONS IN THE EDGE PLASMA

Cross-field transport of particles and energy occurs at rates much faster than can be accounted for by collisional effects, and it is widely believed that such anomalous transport is due to fine-scale fluctuations [326, 736–738]. For example, a fluctuating poloidal electric field $\tilde{E}_\theta$ will cause a fluctuating $\tilde{E}_\theta \times B$ radial drift. Provided the plasma density also fluctuates ($\tilde{n}$) and the phase between $\tilde{E}$ and $\tilde{n}$ is appropriate, then a net, time averaged radial particle outflow results:

$$\Gamma_\perp^{ES} = \frac{1}{B} \langle \tilde{n}\, \tilde{E}_\theta \rangle \tag{9.1}$$

where ES indicates electrostatic. A net electromagnetic fluctuation flux can also occur:

$$\Gamma_\perp^{EM} = \left\langle \tilde{n}\, v_\parallel \frac{\tilde{B}_r}{B} \right\rangle \tag{9.2}$$

where $\tilde{B}_r$ is the fluctuating radial component of the magnetic field and $v_\parallel \approx c_s$ in the SOL; in effect, a component of the parallel flux is deflected in the radial direction.

Four fluctuation contributions to the cross-field heat flux density q can also be identified:

$$q_{conv.}^{ES,EM} = \frac{5}{2} kT\, \Gamma_\perp^{ES,EM} \tag{9.3), (9.4}$$

$$q_{cond.}^{ES} = \frac{5}{2} \frac{n_e}{B} \langle k\tilde{T}\, \tilde{E}_\theta \rangle \tag{9.5}$$

$$q_{cond.}^{EM} = -n_e \chi(\tilde{B}_r) \frac{dT}{dr} \tag{9.6}$$

where cond./conv. indicates conduction/convection. $\chi(\tilde{B}_r)$ is model dependent [739]; the Rechester-Rosenbluth [740] model for electrons, for example, gives $\chi_e(\tilde{B}_r) = qRv_{th,e}(\tilde{B}_r/B)^2$. There is disagreement in the literature about whether a factor of 3/2 or a factor of 5/2 is appropriate for Eqs (9.3) to (9.5) [326].

These flux expressions can be used to calculate the associated diffusion coefficients and heat conductivities, e.g., $D_\perp \equiv -\Gamma_\perp/(dn/dr)$. However, this does not imply that $\Gamma_\perp$ necessarily depends on the density gradient nor that $D_\perp$ is even positive.

The experimental evaluation of these fluxes requires measurement of a considerable quantity of information. For example [741],

$$\Gamma_\perp^{ES} = \frac{1}{B} \int n_{rms}(\omega)\, V_{rms}(\omega)\, \bar{k}_\theta(\omega)\, \gamma(\omega)\, \sin(\alpha(\omega)) d\omega \tag{9.7}$$

where V_p is the plasma potential (often designated ϕ in fluctuation papers), n_{rms}, V_{rms} are the amplitudes obtained

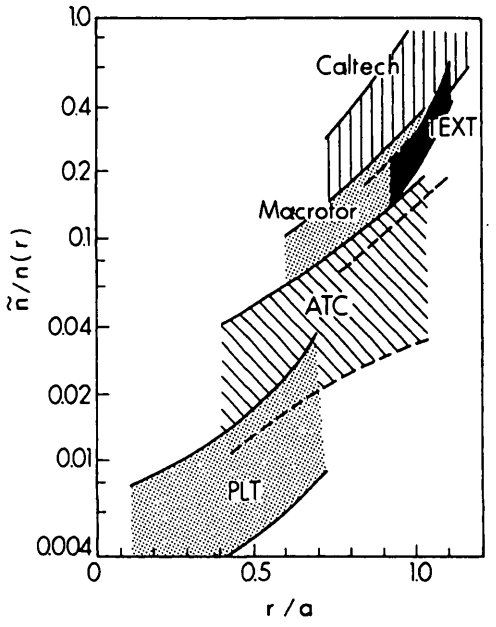

FIG. 122. Relative fluctuation levels ñ(r)/n(r) versus r/a measured in several tokamaks [736].

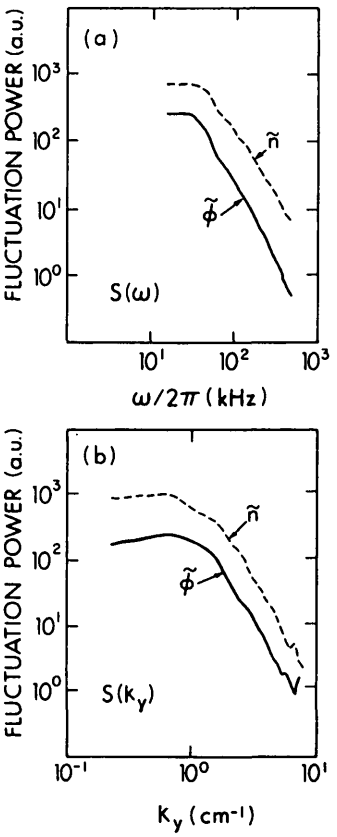

FIG. 123. Pretext: Examples of integrated spectra. Note the power law trend for the asymptotic portion of the spectra [741]. $\phi \equiv V_p$ in this case.

from the auto-power spectra of $\tilde{n}$ and $\tilde{V}_p$, $k_\theta(\omega)$ is the poloidal wave number at frequency ω, ($\tilde{E}_\theta = \tilde{\phi} k_\theta$), $\alpha(\omega)$ is the phase angle between $\tilde{n}$ and $\tilde{V}_p$, and $\gamma(\omega)$ is the degree of mutual coherence between $\tilde{n}$ and $\tilde{V}_p$.

The subject of plasma fluctuations is a very large one and has been the subject of a recent, comprehensive review by Liewer [736]. Here we will briefly review the experimental facts, as dealt with much more extensively by Liewer. Particular emphasis will be on measurements in the edge plasma, and on comparisons of $\Gamma_\perp^{ES}$, etc., with fluxes (and τ_p) measured in other ways.

In the edge plasma, fluctuations are most readily measured using Langmuir probes [736, 742-744]. Scattering of electromagnetic waves [736] has been widely used as a technique to measure fluctuations in the central plasma. This technique, however, unlike the probe techniques, did not provide the auto- and cross-correlation information required (Eq. (9.7)) to evaluate $\Gamma_\perp$ and $q_\perp$ (Eqs (9.1)-(9.6)).

The basic experimental information concerning fluctuations [736] can be summarized as follows:

- The density fluctuation levels vary strongly with minor radius, approaching $\tilde{n}/n \simeq 1$ at the edge (Fig. 122) [736];
- The fluctuations span a wide range of frequencies and poloidal wave numbers k_θ; Fig. 123 gives examples from probe measurements in the Pretext edge plasma [741]. The main power lies in the ranges 10–100 kHz and 0.1–10 cm^{-1}. The power spectrum generally varies as ω^{-n}, with $n \approx 2$–4 [16, 741, 744]. Typically, the wave number along the field, $k_\parallel$, is much less than k_θ [326, 736].
- Magnetic fluctuations [326, 736] are generally in the range $\tilde{B}_r/B \sim 10^{-5}$ to 10^{-4}.

9.1. Experimental techniques

With regard to measurements of the local plasma potential V_p, the simplest procedure is to infer it from measurements of the floating potential V_f and to then

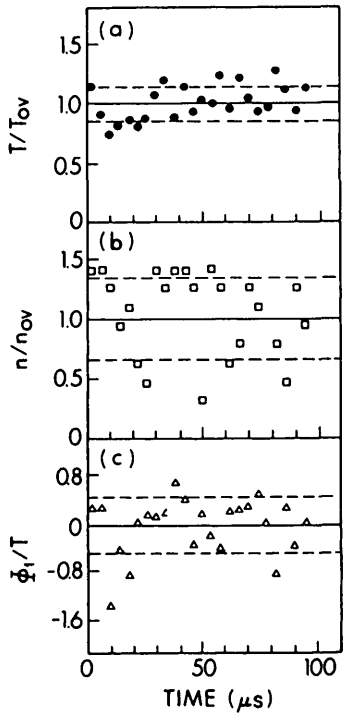

FIG. 124. Caltech Tokamak: Typical variations of T_e versus time, compared with typical variations in n_e (as monitored by the variations in electron saturation current) and ϕ_f (as monitored by a separate probe). The dashed lines are the rms deviations from the mean in each case [747]. $\phi_f \equiv V_f$.

use a theoretical relation to relate V_p and V_f (see Section 3):

$$V_{sf} = V_p - V_f \frac{kT_e}{2e}$$

$$\times \ln\left[\left(2\pi \frac{m_e}{m_i}\right)\left(1 + \frac{T_i}{T_e}\right)(1-\delta)^{-2}\right] \qquad (9.8)$$

The obvious difficulty with inferring $\tilde{V}_p$ by this method is that temperature fluctuations, if present, would introduce a very large error since $V_p - V_f \simeq 3kT_e/e$. In most studies, it is nevertheless simply assumed that $\tilde{T}/T$ is very small and this effect is neglected [33, 267, 739, 741, 744-746]. Liewer et al. [747] directly measured the temperature fluctuations in the Caltech tokamak by using a very fast ($\lesssim$250 kHz) voltage sweep on the Langmuir probe. Results (Fig. 124) confirm that $\tilde{T}/T$ is much smaller than $\tilde{n}/n$ or $\tilde{V}_p/T_e$, namely $\tilde{n}/n$ and $\tilde{V}_p/(kT_e/e)$ are in the range 30–50%, while $\tilde{T}/T \simeq 15\%$. This indicates that the usual assumption that fluctuations in the probe ion saturation current, $\tilde{I}_s^+/I_s^+$, give the levels of $\tilde{n}/n$ is not a bad approximation since $I_s^+ \propto nT^{1/2}$; however, the neglect of temperature fluctuations in inferring $\tilde{V}_p$ is less valid since $V_p - V_f \simeq 3kT_e/e$.

A completely different probe technique was developed by Robinson and Rusbridge [742] and has been used in several studies to measure $\tilde{T}/T$ [16, 742, 748]. The Robinson–Rusbridge technique exploits the non-linear I(V) characteristic of a double probe to simultaneously measure $\tilde{n}/n$, $\tilde{V}_p/kT_e$, the correlation function $\langle \tilde{n}\, \tilde{V}_p \rangle / (n_{rms} V_{rms})$ and $\tilde{T}/T$ under the assumption that

$$\tilde{T}_e/T_e = (\gamma - 1)\, \tilde{n}_e/n_e \qquad (9.9)$$

where γ is the ratio of specific heats (the method, in fact, measures γ). Using this technique in ISX [748], fairly substantial temperature fluctuation levels were found: $\tilde{T}/T \simeq 0.5\, \tilde{n}/n$, whereas on TOSCA [16] quite small levels were found: $\tilde{n}/n \simeq 0.5$, $\tilde{T}/T \simeq 0.01$. In recent TEXT studies [749] using this method, fairly substantial temperature fluctuations were found, with the levels $\tilde{T}/T \simeq 0.4\, \tilde{n}/n$ being typical. It thus appears that temperature fluctuations may or may not be substantial enough to compromise the technique of inferring $\tilde{V}_p$ from $\tilde{V}_f$ and that for reliable measurements either the Robinson–Rusbridge or the fast sweep [747] technique is required.

In the 'usual' probe method, k_θ is obtained by deploying two small probes at a poloidal separation of $\lesssim$1 cm. The probe tips are typically of diameter $\lesssim$1 mm, which means that their collection length (Section 2.1) is $\lesssim$1 cm, i.e. the probes do not measure at a single toroidal location, but measure the average over a toroidal length of $\lesssim$1 cm. Fortunately, $k_\parallel \lesssim 1\ cm^{-1}$, and so spatial resolution is not destroyed, although it may be somewhat compromised.

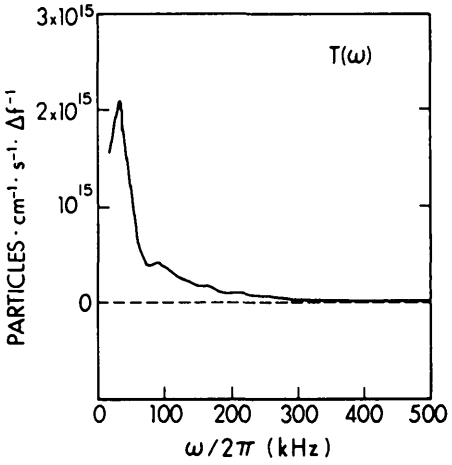

FIG. 125. Pretext: Spectrally resolved particle flux, $\Gamma = \sum_\omega T(\omega) = 2 \times 10^{16}\ cm^2 \cdot s^{-1}$ [741].

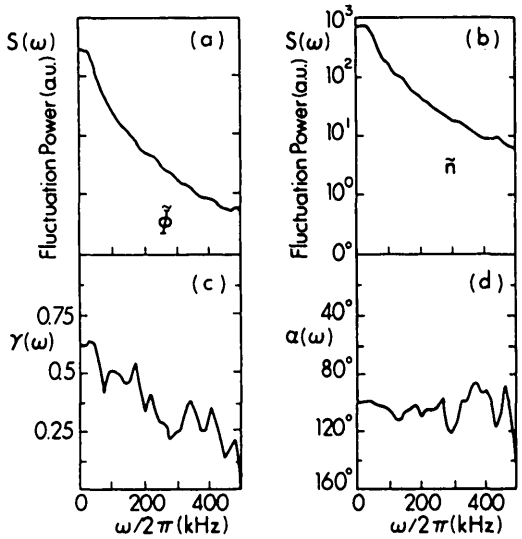

FIG. 126. Pretext: Factors contributing to the particle flux in Fig. 125: (a) S(ω) for potential fluctuation, (b) S(ω) for density fluctuation, (c) mutual coherence γ(ω) between potential and density, and (d) phase angle α(ω) between potential and density [741]. $\phi \equiv V_p$.

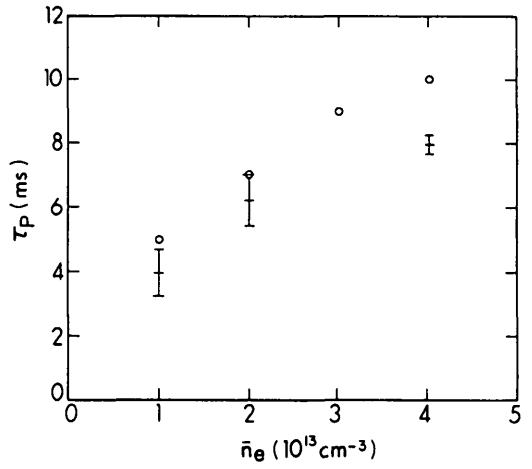

FIG. 127. TEXT: Global particle confinement (+) and particle confinement time predicted from electrostatic fluctuation measurements (o) versus chord averaged electron density. For this scan, B_T = 2.0 T and I_p = 200 kA [267].

9.2. Particle transport due to fluctuations

An example of the inference of the cross-field particle flux $\Gamma_\perp^{ES}$, using Eq. (9.7), made on Pretext [741] is shown in Fig. 125 for a radial position 1 cm inside the limiter. The flux is found to be radially outward at all radii and, as can be seen from this figure, most of the flux is due to frequencies of < 100 kHz. In Fig. 126, the factors contributing to the flux shown in Fig. 125 are given as a function of ω: $\tilde{V}_p$, $\tilde{n}$, $\gamma(\omega)$, $\alpha(\omega)$. A similar value of mutual coherence, $\gamma \sim 0.5$, was found in the TOSCA [16] and Caltech [744] studies. The phase angle of $\sim 90°$ is also approximately the same as that found in the TOSCA [16], Caltech [744] and TEXT [267] studies.

In a recent TEXT study, the particle transport $\Gamma_\perp^{ES}$, inferred from edge probe measurements, has been compared with measurements of particle confinement time, τ_p, from H_α measurements (Section 4). The fluctuation inferred confinement time is $\tau_p = N_e/\Gamma_\perp^{ES}A$, where N_e is the total plasma content inside the LCFS of area A. The results (Fig. 127) show good agreement, which is particularly remarkable considering the assumption of poloidal/toroidal symmetry, the inherent limitations in deducing τ_p from H_α measurements (Section 4) and the uncertainties associated with the neglect of temperature fluctuations. In other studies, the diffusion coefficient inferred from $D_\perp^{ES} = -\Gamma_\perp^{ES}/(dn/dr)$ has been obtained (see Table XI). Since from measurements of the density scrape-off length in the SOL, λ_n, it is also found that in the edge $D_\perp = D_{Bohm}$ (see Section 3), it can be concluded that cross-field

TABLE XI. VALUES OF MEASURED $D_\perp^{ES}$ FROM SEVERAL TOKAMAKS COMPARED WITH $D_\perp^{Bohm}$

Tokamak	Ref.	$D_\perp^{ES}$ ($m^2 \cdot s^{-1}$)	$D_\perp^{Bohm}$ ($m^2 \cdot s^{-1}$)
Pretext	[741]	1	1.3
Caltech	[745]	10	3.4
TOSCA	[16]	2.1	1.8
ISX	[748]	0.5-1	~2

$D_\perp^{ES} = -\Gamma_\perp^{ES}/(dn/dr)$, $D_\perp^{Bohm} \equiv 0.06\ T_e$ [eV]/B [T].

particle transport in the edge of tokamaks can probably be accounted for by electrostatic turbulence. It appears that transport due to electromagnetic turbulence, $\Gamma_\perp^{EM}$ (Eq. (9.2)), is relatively less important in the edge [737, 739] considering the small measured fluctuation levels of $\tilde{B}_r/B = 10^{-5}$ to 10^{-4}, implying fluxes of $\lesssim 1\%$ of the measured values. Nevertheless, correlations between the magnetic fluctuation levels and the confinement time have been reported for some tokamaks such as TCA [750].

9.3. Energy transport

Turning to the matter of cross-field energy transport, there is less published information and the situation is less conclusive than for particle transport:

(a) In TOSCA [16] it was found that $q_{conv.}^{ES}$ was about two orders of magnitude larger than $q_{conv.}^{EM}$ or $q_{cond.}$. The absolute magnitude of $q_{conv.}^{ES}$, however, was too small by a factor of more than ten to account for the observed value of τ_E = 0.2 ms on TOSCA, and it was speculated that radiative losses were dominant in the device.

(b) In the Caltech tokamak [747] it was found that $q_{conv.}^{ES} = q_{cond.}^{ES}$ and that these values were about two orders of magnitude higher than q^{EM}. Moreover, the absolute magnitude of these electrostatic fluctuation losses were found to be of the right order to account for the measured τ_E value of 0.5-1 ms.

(c) In an initial TEXT study [739] it was found that $q_{conv.}^{ES}$ was much larger than q^{EM}, but it was about an order of magnitude too small to explain the measured heat loss rate for low density discharges. It was noted that an unreasonably high level of $\tilde{T}/T \sim 1$ ($\tilde{T}/T$ was not in fact measured) would have to be postulated in

order for $q^{ES}_{cond.}$ to account for the measured power outflow. For higher density discharges, however, there was some indication that $q^{ES}_{conv.}$ might account for the observed heat outflux.

Clearly, the problem of establishing whether or not fluctuation related transport can account for the heat loss is yet more difficult than the problem of establishing this for particle transport. The reasons for this are:

- Radiative and neutral particle energy loss processes are generally important, or even dominant, near the edge.
- Ion heat conduction is probably more important than was originally assumed, and χ_i may be about the same as χ_e rather than being at the lower levels given by neoclassical theory. Thus, one cannot simply relate the measured energy flux to q_e, even when radiation, etc., is unimportant.
- With regard to the actual fluctuation measurements, more information is required than for particle measurements, for example on the correlation between $\tilde{E}_\theta$ and $\tilde{T}$.

9.4. Conclusions

In conclusion, fluctuation studies of edge transport using probes have provided convincing evidence that particle transport may be attributed to electrostatic turbulence. The situation regarding energy transport is less clear at present, but, given the large uncertainties inherent in the studies to date, it is possible that electrostatic turbulence can also explain cross-field plasma heat transport.

Fluctuation transport studies to date have generally been carried out in tokamaks employing poloidal or rail limiters, which can create highly non-symmetrical edge plasmas (see Section 2). Since probe measurements are typically made at only one toroidal and one poloidal location, there are uncertainties in comparing such local measurements of $\Gamma_\perp$ and $q_\perp$ with values inferred from global quantities such as τ_p and τ_E. Fluctuation probe studies carried out on tokamaks with toroidal limiters may help to reduce such uncertainties.

10. ASYMMETRIES IN THE EDGE PLASMA

While the main plasma is expected to be one-dimensional, with only radial spatial variation, it is expected that the edge plasma outside the LCFS will generally be three-dimensional, with radial, poloidal and toroidal variations. The actual experimental information confirming this expectation is quite scarce, however, since edge measurements typically consist of radial scans at single poloidal/toroidal locations. The experimental and theoretical information regarding the strong radial gradients in the SOL has already been dealt with in Section 2; here, attention is focused on the variations in the other two geometrical directions.

Clearly, the limiter configuration must play a major role in edge asymmetries — a point already discussed in Section 2. The simplest limiter configuration would appear to be a single, continuous toroidal limiter located at the inside or the outside midplane. In this case, one would anticipate that the edge properties, n, T, etc., would show, at most, a two-dimensional variation, i.e. in the radial direction and perhaps also in the direction along $\vec{B}$. In the simplest model of the SOL (see Section 3.2), i.e. with high heat conductivity, negligible ionizing radiation, etc., one would expect constant temperature at a given radius, with density only dropping by a factor of ≈ 2 from the symmetry point to the limiter along the SOL. In the absence of neoclassical effects, one would not expect any up–down symmetries. This simple pattern is unlikely to be altered by non-symmetrical outfluxes of particles or energy from the main plasma into the SOL: Given sufficiently rapid parallel field transport, one would anticipate that the SOL density and temperature would only reflect the *average* source value, and any spatial structure of the sources would be smoothed, i.e. integrated out, since, with a single toroidal limiter at the inside/outside midplane, each SOL flux tube samples a complete poloidal circumference.

The majority of tokamaks operated to date have not employed toroidal limiters, but rather poloidal ring limiters and/or discrete, localized limiters. That such configurations might be expected to result in quite non-symmetrical edge plasmas has already been discussed in Section 2 (see, for example Fig. 1). Therefore, the majority of experimental evidence bearing on the matter of edge plasma asymmetries largely pertains to tokamaks where non-symmetries would be expected, if only for geometrical reasons. It is important to distinguish such geometrical effects from more fundamental ones, e.g. neoclassical or edge ballooning effects [661, 663], particularly since, for reasons of the power load, only toroidal limiters may be of reactor relevance.

The edge diagnostic techniques themselves can induce the asymmetries which they then record. The simplest example of this relates to the collection length

of a probe of finite size (Section 2.2.1). When a probe is used to simultaneously measure plasma or impurity fluxes parallel and anti-parallel to $\vec{B}$, non-symmetrical signals will result if the collection length is greater than the connection length in one direction and vice versa in the other direction. The flow of the SOL plasma past a probe, towards a limiter, for example, induces different signals on the upstream and downstream surfaces, and their interpretation to recover the undisturbed signals involves uncertainties.

With regard to the spatial homogeneity of the SOL, one wishes to know the answer to certain specific and practical questions: (i) Are the plasma conditions measured at one poloidal/toroidal location indicative of the SOL as a whole? (ii) Are the particle and heat fluxes to surfaces such as limiters the same in the ion and the electron drift directions? (iii) Are the plasma flows along $\vec{B}$ to the surfaces ambipolar or are net currents carried? If the measured pattern should turn out to be in fact quite inhomogeneous, it is difficult to see how one can proceed further; any quantitative interpretation of edge behaviour in this case appears to be difficult or impossible. If e-side/i-side asymmetries are substantial, then the optimal distribution of heat fluxes over power removing surfaces is compromised, as are particle removing systems such as pumped limiters. If the plasma flows to surfaces are significantly non-ambipolar, then the heat transmission coefficient of the sheath (see Section 3.3) is altered. Circulating currents in the SOL and through edge structures such as limiters could affect the plasma equilibrium and possibly exert damaging $j \times B$ forces.

As discussed in Section 2, there is evidence of substantial poloidal variation in poloidal/rail limiter devices. Such tokamaks have also sometimes shown significant e-side/i-side asymmetrical limiter loadings, and non-ambipolar flows have been measured. A study of this information would shed light on basic edge processes leading to asymmetries. However, in view of the difficulty of separating basic effects from limiter-geometry-induced effects, and because of space limitations, such a study is not attempted here. Instead, we give a brief review of literature concerning asymmetries observed in poloidal/rail limiter tokamaks, and a discussion of the limited data from toroidal limiter tokamaks.

10.1. Asymmetries in poloidal and rail limiter tokamaks

Studies in tokamaks employing poloidal or rail limiters have provided a considerable amount of evidence regarding asymmetries in a number of categories:

- *The edge plasma itself (n, T):* ALCATOR-C [8, 9], T-10 [6, 10, 77, 312], ISX [30], DITE [17, 22, 620], TEXTOR [13, 751], CASTOR [752, 753], PDX [754], T-4 [755];
- *Impurities and deuterium deposited on probes:* TEXTOR [401, 404, 424, 756, 784], T-10 [757, 758], FT [759, 760], TCA [761], PLT [762], CASTOR [753];
- *Erosion/deposition patterns on limiters:* FT [759], ASDEX (poloidal limiter) [415], TFR [417], TFTR (movable limiter) [330], T-10 [254, 763, 764], JIPP T-IIU [425, 785], UNITOR [765];
- *Gas loadings on pumped limiters, etc.:* T-10 [6];
- *Heat load patterns on limiters:* PLT [212], T-10 [213], ISX [192], DITE [22], TEXTOR [38], DIII [766];
- *Non-ambipolar currents to surfaces:* DITE [767], T-10 [768];
- *H_α and impurity radiation patterns on limiters:* TEXT [769], TEXTOR [131].

For purposes of illustration of these types of asymmetry, we consider two examples of particularly well diagnosed SOLs — a poloidal limiter study from ALCATOR-C [9] and a rail limiter study from T-10 [312]. On ALCATOR-C, operated with two poloidal limiters 180° apart, a poloidal array of about 100 probes, called DENSEPAK, was deployed about midway between the limiters. The array of probes almost completely spanned the poloidal circumference and also involved radial staggering of the probes to provide information on radial variation in the SOL. For $I_p = 350$ kA and $B_T = 8$ T, the pitch angle of the field was such that each probe sampled a flux tube which averaged over a 40° poloidal arc. It is to be noted that the presence of the poloidal limiters meant that all flux tubes in the SOL were isolated from each other and thus, if cross-field transport varied poloidally, this should be directly reflected by differences in probe signals in the SOL. The poloidal variations were in fact found to be remarkably strong. Figure 128 shows λ_n and n_{LCFS} as a function of θ (with $\theta \equiv 0$ at the outside midplane, increasing in the clockwise direction). The temperature showed similar, although less dramatic, poloidal variations.

The $\lambda_n(\theta)$ variation appears to imply a very great poloidal variation in $D_\perp$ (Eq. (3.34)), up to a factor of 30. On the other hand, measurements of fluctuations in I_s^+ showed little poloidal variation, although the DENSEPAK probes were too far apart to provide the

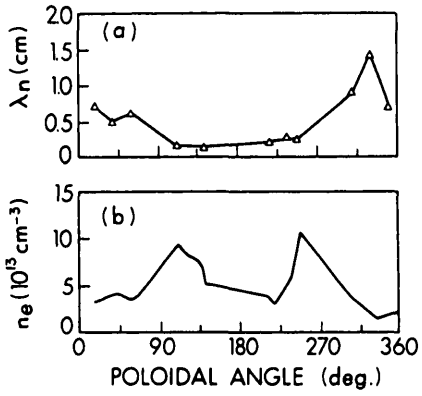

FIG. 128. ALCATOR-C: Poloidal profiles of (a) radial density e-folding length and (b) density extrapolated to the limiter radii at t = 250 ms. The poloidal asymmetry in density is found to persist at the limiter radius and indicates that plasma outside the SOL region ($r \leq a$) also exhibits strong poloidal asymmetries [9].

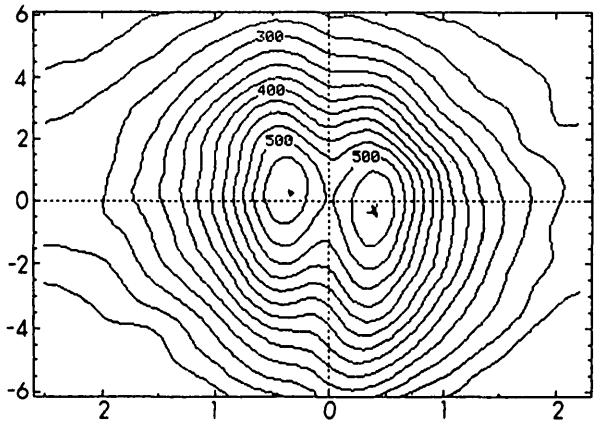

FIG. 129a. T-10: Map of isotherms on the span-roof-like surface of a bottom rail limiter (torus centre upward). The dashed vertical line denotes the limiter ridge, the left-hand side is on the ion drift side. The two axes are in cm, the temperature is given in °C [11, 312, 770].

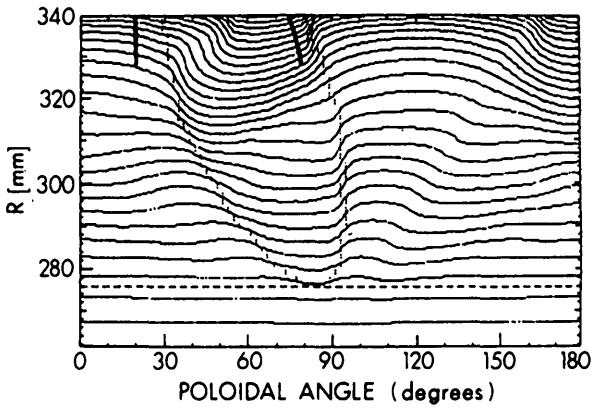

FIG. 129b. T-10: Lines of constant plasma density with logarithmic scaling ($\Delta \ln n_e = 0.5$ from line to line). The dashed line indicates the LCFS; the solid lines indicate two sites probed for Fig. 129d [11].

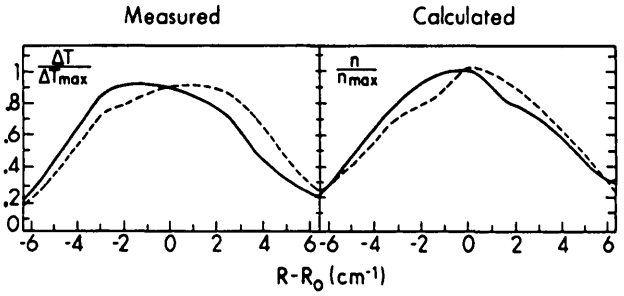

FIG. 129c. T-10: Profiles of the measured limiter surface temperature and the calculated density along lines parallel to the limiter ridge. Dashed line — ion drift side, solid line — electron drift side. The torus centre is to the right.

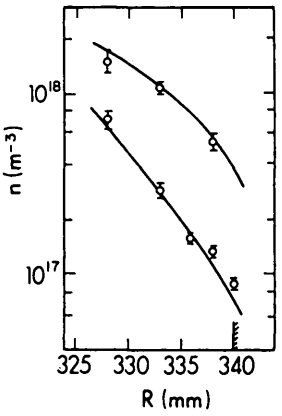

FIG. 129d. T-10: Radial profiles measured at two locations of Fig. 129b. The solid lines are from the contours of Fig. 129b, assuming $D_\perp = 0.2\ m^2 \cdot s^{-1}$ and $T_e = 8.5$ eV (measured) [11].

measurements of fluctuation correlations required to calculate $\Gamma_\perp^{ES}$ (Eq. (9.7)). Radial $\vec{E} \times \vec{B}$ drifts were inferred from the probe measurements of floating potential, but were found to be an order of magnitude too small to explain the poloidal variations in λ_n.

The very large poloidal variations observed on ALCATOR do not appear to be solely a feature of high-$\vec{B}$, high-$\bar{n}_e$ tokamaks, since similarly strong variations were observed behind the T-10 *poloidal* limiter (see Section 2, Fig. 1) (the T-10 *rail* limiter is considered below). The fact that plasma outflow from the core is poloidally varying, with the maximum being on the outside, has been commented on earlier, particularly in the context of divertor machines where the fluxes to the outside and inside plates can be compared. Further light on this matter was shed by studies of ELMs on the DIII-D divertor tokamak [650, 769]. By timing the arrival of the pulses at the plates,

it was established that the expulsion occurred near the outside midplane. It was proposed that the outside plasma surfaces are unstable to ballooning modes which are triggered when the radial pressure gradient is sufficiently high. It may be noted from Fig. 128 that, in ALCATOR, λ_n is largest on the outside midplane, implying that the highest cross-field transport occurs there. The same observation was made for the SOL behind the poloidal limiter on T-10 [10] (Fig. 1), with λ_n on the outboard side being four to five times greater than on the inboard side. The T-10 studies also show the asymmetries to be dependent on $\bar{n}_e$.

In T-10 [11, 312, 770, 771] a rail limiter with a 'span roof' shape has been employed, where each side of the roof receives fluxes from one side only. The measured heat flux pattern on the limiter is given in Fig. 129a; this pattern exhibits a skewness that cannot be explained by the pitch angle of $\vec{B}$, which is a comparatively small effect and would influence the pattern in the opposite direction. This pattern has been quantitatively explained by tracing the individual flux tubes extending from one point of contact with the limiter, around the torus for a sufficient number of transits until the tubes strike the other side of the limiter. The surface of the limiter may thus be mapped into different zones, with each zone being characterized by a different connection length. The effect of the varying connection length, together with an assumed value of $D_\perp$ (taken as constant, however), is then used to compute $n(r, \theta)$ in the SOL (Fig. 129b). From this plot, the density along the limiter is calculated and compared with the surface temperature (Fig. 129c). Although the comparison is not of strictly equivalent quantities, it evidently explains the observed heat fluxes on the limiter (Fig. 129a). The 2-D SOL modelling was further tested by measuring $n_e(r)$ in the SOL using a Langmuir probe at different poloidal locations (Fig. 129d). The agreement between theory and experiment is excellent, assuming a value of $D_\perp = 0.2\ m^2 \cdot s^{-1}$, close to the Bohm value for the measured $T_e = 8.5$ eV. The authors also successfully applied their model to explain the 2-D variation of $n_e(r, \theta)$ measured on TEXTOR [692, 772] for a rail limiter.

Further insight concerning the nature of edge asymmetries was provided by Li pellet injection experiments on T-10, with the Li outflux being measured by deposition probes [257, 773]. For discharges with injection, or ones immediately following injection, the Li deposition patterns were found to be rather simple and explicable with little electron–ion side asymmetry, and the Li impurity scrape-off length was consistent with λ_n for the background plasma. For intrinsic (Fe) impurities, or for Li in discharges well separated in time from injected discharges, the impurity deposition patterns were complex, asymmetrical and difficult to interpret. The explanation provided by the authors is that when the flux to the probe is dominated by outflux from the core — which is presumably relatively symmetrical — then simple deposition patterns can be anticipated. Normally, however, complex recycling patterns exist and the relative location of the probe to the strongest recycling locations (unknown) becomes important. Similar poloidal variations have also been observed in the non-axisymmetric bundle divertor in DITE. Tangential views of the SOL using a camera show clear patterns due to depletion of the density by the flux tube connected to the divertor [774].

10.2. Asymmetries in toroidal limiter tokamaks

PDX, JET and TFTR have been operated by pushing the plasma against the inner column, which then constitutes a toroidal limiter. Unfortunately, this configuration is a difficult one for edge probe diagnosis, since the probe is generally inserted from the outside, top or bottom of the torus, making identification of the LCFS at the probe uncertain. Slight motion of the plasma column centre can cause large changes in the edge signals and can also pose heat-load risks to the probe, which is therefore often deployed only at some considerable distance outside of the LCFS, resulting in uncertainty about the validity of extrapolation. Clearly, an outside toroidal limiter is preferable. JET is currently operated with two complete belt limiters, located at approximately 1 m above and below the outside midplane. This configuration, unfortunately, separates the SOL into inner and outer zones; in addition, unless the loading of the two limiters is balanced, further asymmetry results. Generally, there is disagreement between the inference of a balanced state based on magnetic equilibrium calculations and that based on limiter viewing measurements, such as H_α signals. The interpretation of the JET double belt configuration is therefore not straightforward. Before 1987, JET had a set of eight rail limiters, each 1 m high and 40 cm wide (toroidally), symmetrically deployed toroidally around the outside midplane. For sufficiently large q-values, each magnetic flux tube in the SOL therefore struck a limiter on each pass through the outside midplane — making the assembly of limiters, in effect, a continuous toroidal limiter. Even for values of q too small for this to occur, it appears that the array still acted in effect as a toroidal limiter, possibly owing to poloidal transport

[209]. The collection of edge data obtained in this configuration appears to be the most extensive one obtained on an (effectively) toroidal limiter tokamak (see Section 2.1) and we will consider below the data for this device which bears on the question of SOL asymmetry.

Recently, TEXTOR has operated with a toroidal pumped limiter [574] located at the large radius side. The configuration is not symmetrical, however, since the limiter poloidal location is 45° below the midplane. The TEXTOR data are reviewed later.

Evidence from JET is restricted here to Ohmic heating conditions (to avoid potential auxiliary heating asymmetries) and is considered under several categories:

— *Langmuir probe measurements.* A movable Langmuir probe was located at the top of the torus, providing a detailed radial scan of the SOL. At the outside midplane, two fixed Langmuir probes provided data for two radial locations. Figure 130 gives an example, comparing measurements of I_s^+ at these two poloidal locations made in the same discharge [209]. The agreement is perhaps fortuitously good considering the uncertainties in identifying the location of the LCFS at the top probe. The radial information at the midplane is also limited; nevertheless, to within experimental uncertainty, the SOL plasma is not different at the poloidal and the toroidal locations.

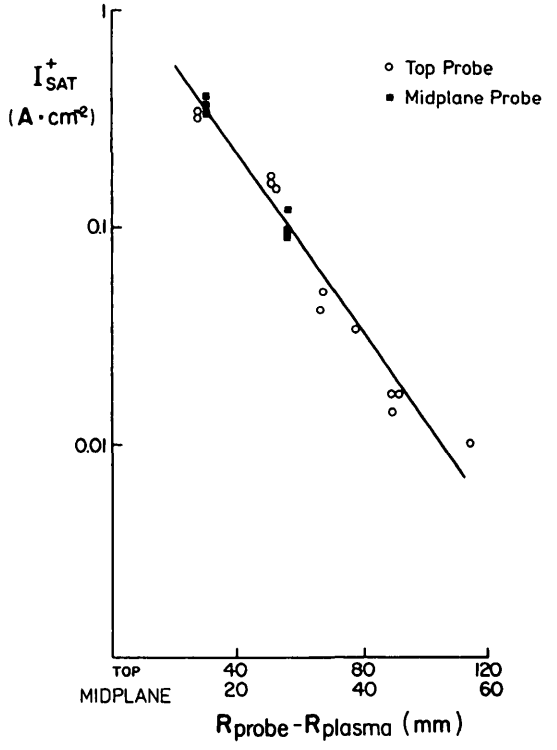

FIG. 130. JET: Edge profiles at the top and the midplane [209].

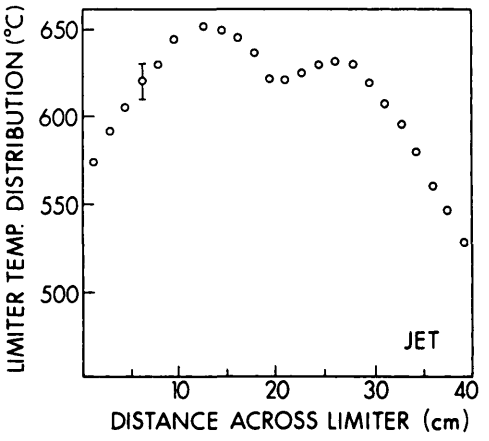

FIG. 131. JET: Temperature distribution in the toroidal direction across the graphite limiter, showing the typical temperature difference between the ion side and the electron side. The ion side is hotter [775].

— *H_α and infrared radiation 'footprints' on the limiters.* The limiters were straight vertically, with a curvature toroidally. The e-side and i-side 'footprints' of plasma contact were thus clearly separated (see Fig. 131) [775]. The asymmetry between the two sides was generally rather small, typically $<30\%$ [776], the i-side being favoured.

— *Deuterium and metals deposited on the limiters.* Post-mortem analysis of the limiters indicated nearly symmetrical patterns of metal [418] and deuterium [777] deposition.

— *Carbon erosion/re-deposition.* The graphite tiles were measured for net erosion/re-deposition after one year's exposure (1986). Results [778] are also nearly symmetrical (Section 5, Fig. 71a).

— *Up-down asymmetries.* Bolometric measurements on JET [779] sometimes show up-down asymmetries ($\lesssim 30\%$) in emissivity, apparently indicating differences in impurity densities of this order.

— *Reversal of $\vec{B}_T$ and $\vec{I}_p$.* For a set of JET discharges, both the toroidal magnetic field and the plasma current directions were reversed. The two fixed probes at the midplane were thus changed from facing the i-drift to facing the e-drift. As a result, for a given $|I_p|$, the I_s^+ values decreased slightly ($\sim 25\%$).

It thus appears that for the case of JET Ohmic discharges operated with an (effective) outside midplane toroidal limiter, e/i asymmetries are not large

($\lesssim$25%), with the i-side being favoured. Plasma variations along $\vec{B}$ in the SOL are also not large, although the evidence for the latter is weaker.

We turn next to the results from the TEXTOR toroidal pumped limiter [39, 40, 574, 780]. Fixed Langmuir probes were located at the e-side entrance (usually facing the large R side) and at the i-side entrance (facing the bottom and the small R side) to the pumped limiter (Fig. 132). The SOL conditions were monitored further away, using Li beams [40], one at the top and one at the bottom of the torus, and by a movable Langmuir probe [39] at the outside midplane. In addition, the heat fluxes to the limiter were monitored by thermography [780, 781]. The following observations relating to asymmetries were reported:

- The movable Langmuir probe at the midplane and the Li beam at the top gave essentially the same $n_e(r)$ and $T_e(r)$ profiles in the SOL (see Section 2, Fig. 13) [40], indicating little variation along the SOL over this 90° poloidal path.
- The fixed Langmuir probe at the e-side of the pumped limiter measured the same SOL plasma conditions as the movable probe [39], thus indicating that there was in fact little poloidal variation between +90° and -45°.
- The density scrape-off length λ_n measured with the Li beam at -90° was, however, somewhat shorter than that measured with the movable probe (Fig. 133) [40], λ_n = 0.9 cm compared with λ_n = 1.35 cm. The ratio (1.5) was nearly the same as that (1.7) measured by probes in the limiter facing the e/i side.

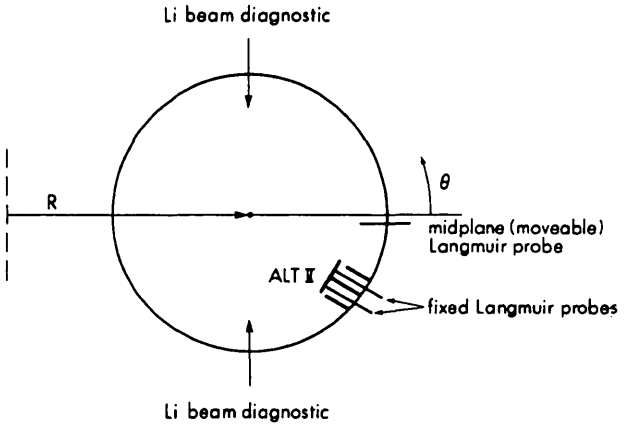

FIG. 132. Schematic of TEXTOR, with the ALT II toroidal pumped limiter at the poloidal location, 45°.

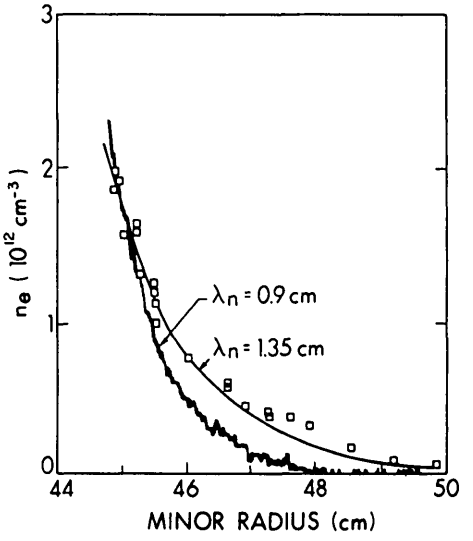

FIG. 133. TEXTOR: Density results of the movable probe (□) and of the bottom Li beam (thick line) [40].

- The flux *density* [780] on the i-side, however, exceeded that on the e-side. The results for the *total* fluxes on the two sides — when the different values of λ_n were allowed for — were thus approximately equal. This asymmetry of the flux densities decreased with increasing $\bar{n}_e$. In a similar case, the asymmetry of the heat flux densities decreased with $\bar{n}_e$ [781].
- The scrape-off lengths at the top were always longer than those at the bottom, independent of ion and electron drift directions [684].

In summary, the TEXTOR results appear to indicate the following points:

- The SOL has two regions: region A starts somewhere on the inside of the machine and extends to the top of the limiter, and region B starts near the inside and extends to the bottom side of the limiter (Fig. 132);
- Within each of these SOL regions there appears to be little variation along $\vec{B}$;
- $\lambda_n^A > \lambda_n^B$;
- $F_{LCFS}^A < F_{LCFS}^B$ (F is heat/particle flux density).

A possible explanation of the TEXTOR results may be suggested: (i) $\lambda_n^A > \lambda_n^B$ may be the result of two effects. First, the tendency for transport from the core to favour the large-R side [5, 6] — the 'ballooning transport effect' — means, in effect, that $\bar{D}_\perp^A > \bar{D}_\perp^B$. Second, the cross-sectional area of a SOL flux tube varies as 1/R, causing a constriction at the inside midplane and hence some impediment to parallel transport;

thus, $L_c^A > L_c^B$ (L is the SOL length along $\vec{B}$ ($L_c^A + L_c^B = \pi Rq$)). Both these effects imply $\lambda_n^A > \lambda_n^B$ since $\lambda_n \propto (LD_\perp)^{1/2}$. (ii) $F_{LCFS}^A < F_{LCFS}^B$ may be an edge neoclassical transport effect [7, 148-151, 782, 783]. As with the JET results, the i-side appears to be favoured, at least at low densities (corresponding to low collisionality).

In conclusion, the evidence for the presence of large non-symmetries in the SOL is quite substantial. Most of these effects, however, may be the result of using symmetry breaking limiters, i.e. poloidal rail limiters and non-symmetrically located toroidal limiters. The experimental data for toroidally symmetrical devices are not extensive; these data are, however, consistent with a rather simple picture of the SOL, characterized by little poloidal or toroidal variation. Further experimental evidence is of critical importance for answering the important practical questions related to edge asymmetry.

11. CONCLUSION

Over the last decade, the field of plasma-surface interactions has become increasingly recognized as one of the critical elements in the pursuit of a viable fusion energy source based on the tokamak concept. The field has been characterized by relative growth within the overall fusion effort — a situation which can be expected to persist in the next decade. Progress during the past ten years has been reviewed; it is evident that the experimental database regarding edge properties has increased markedly. Understanding of the basic properties of the edge, including impurity behaviour, has improved substantially during this period, and the relation between the edge plasma and the confined plasma is now understood, at least in the simplest circumstances. The field is rapidly evolving and the present review is one of work in progress, rather than a summary of a completed opus. For the next years, a significantly expanded commitment of diagnostic and modelling effort to the plasma boundary is required. Successful operation of the next generation of tokamak devices is likely to depend as much on such effort as on any other single aspect of tokamak studies.

ACKNOWLEDGEMENTS

The authors wish to thank the following persons for helpful discussions: R. Behrisch, S.A. Cohen, J.W. Davis, A.A. Haasz, I.H. Hutchinson, H. Lingertat, J. Neuhauser, V. Philipps, C.S. Pitcher, R.A. Pitts, S. Sengoku, P.E. Stott and V.A. Vershkov.

Support by the Canadian Fusion Fuels Technology Project is acknowledged.

REFERENCES

[1] McCRACKEN, G.M., STOTT, P.E., Nucl. Fusion **19** (1979) 889.

[2] LANGLEY, R.A., BOHDANSKY, J., ECKSTEIN, W., et al., Data Compendium for Plasma-Surface Interactions, Special Issue, Nucl. Fusion (1984).

[3] POST, D.E., BEHRISCH, R. (Eds), Physics of Plasma-Wall Interactions in Controlled Fusion, Plenum Press, New York (1986).

[4] Proceedings of the International Conferences on Plasma-Surface Interactions in Controlled Fusion Devices, published by the Journal of Nuclear Materials:
Proc. 1st Conf. Argonne National Laboratory, Chicago, IL, 1974 (KAMINSKY, M., Ed.), J. Nucl. Mater. **53** (1974).
Proc. 2nd Conf. San Francisco, CA, 1976 (BAUER, W., FINFGELD, C.R., KAMINSKY, M., Eds), J. Nucl. Mater. **63** (1976).
Proc. 3rd Conf. Culham, Oxfordshire, 1978 (McCRACKEN, G.M., STOTT, P.E., THOMPSON, M.W., Eds), J. Nucl. Mater. **76&77** (1978).
Proc. 4th Conf. Garmisch-Partenkirchen, 1980 (VERNICKEL, H., BEHRISCH, R., SCHERZER, B.M.V., WAGNER, F., Eds), J. Nucl. Mater. **93&94** (1980).
Proc. 5th Conf. Gatlinburg, TN, 1982 (LANGLEY, R.A., ISLER, R.C., ROBERTO, J.B., Eds), J. Nucl. Mater. **111&112** (1982).
Proc. 6th Conf. Nagoya, 1984 (MIYAHARA, A., TAWARA, H., ITOH, N., KAMADA, K., McCRACKEN, G.M., Eds), J. Nucl. Mater. **128&129** (1984).
Proc. 7th Conf. Princeton, NJ, 1986 (COHEN, S.A., CECCHI, J.L., DYLLA, H.F., Eds), J. Nucl. Mater. **145-147** (1987).
Proc. 8th Conf. Jülich, 1988 (WINTER, J., PHILIPPS, V., SAMM, U., SCHWEER, B., Eds), J. Nucl. Mater. **162-164** (1989).
Proceedings of the Symposium on Energy Removal and Particle Control in Fusion Devices, Princeton, NJ, 1983 (CECCHI, J.L., COHEN, S.A., DYLLA, H.F., POST, D.E., Eds), J. Nucl. Mater. **121** (1984).

[5] KEILHACKER, M., DAYBELGE, U., Nucl. Fusion **21** (1981) 1505.

[6] VERSHKOV, V.A., GRASHIN, S.A., CHANKIN, A.V., J. Nucl. Mater. **145-147** (1987) 611.

[7] DAYBELGE, U., Nucl. Fusion **21** (1981) 1589.

[8] WAN, A.S., LaBOMBARD, B., LIPSCHULTZ, B., et al., J. Nucl. Mater. **145-147** (1987) 191.

[9] LaBOMBARD, B., LIPSCHULTZ, B., Nucl. Fusion **27** (1987) 81.

[10] VERSHKOV, V.A., J. Nucl. Mater. **162-164** (1989) 195.

[11] LINGERTAT, J., GUENTHER, K., DIETRICH, L., Plasma Phys. Controll. Fusion **29** (1987) 1365.

[12] ERENTS, S.K., TAGLE, J.A., McCRACKEN, G.M., et al., Nucl. Fusion **28** (1988) 1209.
[13] GOEBEL, D.M., CAMPBELL, G.A., CONN, R.W., et al., Langmuir Probe Measurements in the TEXTOR Tokamak during ALT-I Pump Limiter Experiments, Rep. UCLA-PPG-945, California Univ., Los Angeles (1986).
[14] PERICOLI-RIDOLFINI, V., Plasma Phys. Controll. Fusion **27** (1985) 493.
[15] MATTHEWS, G.F., FIELDING, S.J., McCRACKEN, G.M., et al., Nucl. Fusion **28** (1988) 2209.
[16] HOWLING, A.A., PhD Thesis, Oxford Univ. (1985).
[17] JOHNSON, P.C., FIELDING, S.J., MATTHEWS, G.F., et al., J. Nucl. Mater. **162–164** (1989) 686.
[18] PROUDFOOT, G., HARBOUR, P.J., J. Nucl. Mater. **111&112** (1982) 44.
[19] KAHN, C., BURRELL, K.H., FAIRBANKS, E., et al., J. Nucl. Mater. **128&129** (1984) 172.
[20] BEREZOVKIJ, E.L., VASIN, M.L., VERSHKOV, V.A., et al., in Controlled Fusion and Plasma Heating (Proc. 15th Eur. Conf. Dubrovnik, 1988), Vol. 12B, Part I, European Physical Society (1988) 679.
[21] ALEXANDER, K.F., GUENTHER, K., HINTZE, W., et al., Nucl. Fusion **26** (1986) 1575.
[22] McCRACKEN, G.M., ERENTS, S.K., GOODALL, D.H.J., et al., J. Nucl. Mater. **128&129** (1984) 150.
[23] SIMONINI, R., SPENCE, J., STANGEBY, P.C., Contrib. Plasma Phys. **28** (1988) 459.
[24] HOWLING, A., COTE, A., DOYLE, E.J., et al., in Controlled Fusion and Plasma Physics (Proc. 12th Eur. Conf. Budapest, 1985), Vol. 9F, Part I, European Physical Society (1985) 311;
HOWLING, A. (Culham Laboratory), personal communication, 1984.
[25] BOBROVSKIJ, G.A., KONDRAT'EV, A.A., Fiz. Plazmy **3** (1977) 209.
[26] GIMZESKI, J.K., HOFMAN, F., HOLLENSTEIN, Ch., et al., Scrape-Off Measurements during Alfvén Wave Heating in the TCA Tokamak, Rep. LRP 226/83, Lab. de Recherches en Physique des Plasmas, Lausanne (1983).
[27] GOMAY, Y., FUJISAWA, N., MAENO, M., et al., Nucl. Fusion **18** (1978) 849.
[28] OGAWA, H., ODAJIMA, K., OHTSUKA, H., et al., J. Nucl. Mater. **128&129** (1984) 298.
[29] MIODUSZEWSKI, P., J. Nucl. Mater. **111&112** (1982) 253.
[30] WATKINS, J.G., YOKOYAMA, K.E., WOOTTON, A.J., J. Nucl. Mater. **145–147** (1987) 255.
[31] GROSSMAN, A. (CEN Cadarache), personal communication, 1984.
[32] TFR Group, J. Nucl. Mater. **145–147** (1987) 819.
[33] RITZ, C.P., BENGSTON, R.D., LEVINSON, S.J., et al., Phys. Fluids **27** (1984) 2956.
[34] PHILLIPS, P.E., WOOTTON, A.J., ROWAN, W.L., et al., J. Nucl. Mater. **145–147** (1987) 807.
[35] BUDNY, R., J. Vac. Sci. Technol. **20** (1982) 1238.
[36] VASIN, N.L., VERSHKOV, V.A., GRASHIN, S.A., et al., J. Nucl. Mater. **162–164** (1989) 300.
[37] KEILHACKER, M., LACKNER, K., BEHRINGER, K., et al., Phys. Scr. **T2/2** (1982) 443.
[38] BOGEN, P., HARTWIG, H., HINTZ, E., et al., J. Nucl. Mater. **128&129** (1984) 157.
[39] CORBETT, W.J., GOEBEL, D.M., CONN, R.W., J. Nucl. Mater. **162–164** (1989) 221.
[40] POSPIESZCZYK, A., AUMAYR, F., BAY, H.L., et al., J. Nucl. Mater. **162–164** (1989) 574.
[41] KILPATRICK, S.J. (Princeton Plasma Physics Laboratory), personal communication, 1984.
[42] MANOS, D., KILPATRICK, S., BELL, M.G., et al., J. Nucl. Mater. **162–164** (1989) 251.
[43] ERENTS, S.K., TAGLE, J.A., McCRACKEN, G.M., et al., J. Nucl. Mater. **162–164** (1989) 226.
[44] SCATURRO, L.S., KUSSE, B., Nucl. Fusion **18** (1978) 1717.
[45] HAYZEN, A.J., Probe Measurements in the Boundary Plasma in ALCATOR C, Rep. PFC/JA-81-19, Massachusetts Institute of Technology, Cambridge (1981).
[46] TAGLE, J.A., ERENTS, S.K., McCRACKEN, G.M., et al., in Controlled Fusion and Plasma Physics (Proc. 14th Eur. Conf. Madrid, 1987), Vol. 11D, Part II, European Physical Society (1987) 662.
[47] TONKS, L., LANGMUIR, I., Phys. Rev. **34** (1929) 876.
[48] BOHM, D., in The Characteristics of Electrical Discharges in Magnetic Fields (GUTHRIE, A., WAKERLING, R.K., Eds), McGraw-Hill, New York (1949) Ch. 3.
[49] HARRISON, E.R., THOMPSON, W.B., Proc. Phys. Soc. **72** (1959) 2145.
[50] ALLEN, J.E., J. Phys., D **9** (1976) 2331.
[51] STANGEBY, P.C., in Physics of Plasma-Wall Interactions in Controlled Fusion (POST, D.E., BEHRISCH, R., Eds), Plenum Press, New York (1986) 41.
[52] STANGEBY, P.C., Phys. Fluids **27** (1984) 682.
[53] STAIB, P., J. Nucl. Mater. **111&112** (1982) 109.
[54] MATTHEWS, G.F., McCRACKEN, G.M., SEWELL, P., et al., J. Nucl. Mater. **145–147** (1987) 225.
[55] PITTS, R.A., McCRACKEN, G.M., MATTHEWS, G.F., J. Nucl. Mater. **162–164** (1989) 568.
[56] CHEN, F.F., Plasma Diagnostic Techniques (HUDDLETONE, R.H., LEONARD, S.L., Eds), Academic Press, London (1965).
[57] SWIFT, J.D., SCHWAR, M.J., Electric Probes for Plasma Diagnostics, American Elsevier, London (1969).
[58] MANOS, D., McCRACKEN, G.M., in Physics of Plasma-Wall Interactions in Controlled Fusion (POST, D.E., BEHRISCH, R., Eds), Plenum Press, New York (1986) 135.
[59] STANGEBY, P.C., in Plasma Diagnostics, Vol. 1 (AUCIELLO, O., FLAMM, D., Eds), Academic Press, Boston (1988) 157.
[60] CHUNG, P.M., TALBOT, L., TOURYAN, K.J., Electric Probes in Stationary and Flowing Plasmas, Springer-Verlag, Berlin (1975).
[61] SMY, R.R., Adv. Phys. **25** (1976) 517.
[62] CLEMENTS, R.M., J. Vac. Sci. Technol. **15** (1978) 193.
[63] MANOS, D.M., J. Vac Sci. Technol. A **3** (1985) 1059.
[64] LIPSCHULTZ, B., HUTCHINSON, I., LaBOMBARD, B., et al., J. Vac. Sci. Technol. A **4** (1986) 1810.
[65] HUTCHINSON, I.H., Principles of Plasma Diagnostics, Cambridge University Press (1988).
[66] HERSHKOWITZ, N., in Plasma Diagnostics (AUCIELLO, O., FLAMM, D., Eds), Academic Press, Boston (1988) 113.
[67] COHEN, S.A., J. Nucl. Mater. **76&77** (1978) 68.

[68] BROWN, I.G., COMPHER, A.B., KUNKEL, W.B., Phys. Fluids **14** (1971) 1377.
[69] KILPATRICK, S.J., MANOS, D.M., BUDNY, R.V., et al., J. Vac. Sci. Technol. A **4** (1986) 1817.
[70] ERENTS, S.K., TAGLE, J.A., McCRACKEN, G.M., et al., Nucl. Fusion **26** (1986) 1591.
[71] STANGEBY, P.C., J. Phys. D **15** (1982) 1007.
[72] STANGEBY, P.C., J. Phys. D **18** (1985) 1547.
[73] MATTHEWS, G.F., STANGEBY, P.C., J. Phys. D **22** (1989) 644.
[74] STANGEBY, P.C., Phys. Fluids **28** (1985) 644.
[75] STANGEBY, P.C., J. Nucl. Mater. **121** (1984) 36.
[76] ERENTS, S.K., Fusion Technol. **6** (1984) 453.
[77] LAUX, M., GROTE, H., GUENTHER, K., et al., J. Nucl. Mater. **162–164** (1989) 200.
[78] CHODURA, R., in Physics of Plasma-Wall Interactions in Controlled Fusion (POST, D.E., BEHRISCH, R., Eds), Plenum Press, New York (1986) 99.
[79] CHODURA, R., Phys. Fluids **25** (1982) 1628.
[80] CHODURA, R., J. Nucl. Mater. **111&112** (1982) 420.
[81] CHODURA, R., in Controlled Fusion and Plasma Physics (Proc. 11th Eur. Conf. Aachen, 1983), Vol. 7D, Part II, European Physical Society (1983) 979.
[82] STANGEBY, P.C., McCRACKEN, G.M., ERENTS, S.K., et al., J. Vac. Sci. Technol. A **2** (1984) 702.
[83] SHIMADA, M., WASHIZU, M., SENGOKU, S., et al., J. Nucl. Mater. **128&129** (1984) 340.
[84] KOBAYASHI, T., SHIMADA, M., SENGOKU, S., et al., J. Nucl Mater. **121** (1984) 17.
[85] SENGOKU, S., SHIMADA, M., MIYA, N., et al., Nucl. Fusion **24** (1984) 415.
[86] PITCHER, C.S., McCRACKEN, G.M., STANGEBY, P.C., et al., J. Nucl. Mater. **145–147** (1987) 539.
[87] ERENTS, S.K., TAGLE, J.A., McCRACKEN, G.M., et al., J. Nucl. Mater. **145–147** (1987) 231.
[88] ALLEN, S.L., RENSINK, M.E., HILL, D.N., J.Nucl. Mater. **162–164** (1989) 80.
[89] DAYBELGE, V., BEIN, B., Phys. Fluids **24** (1981) 1190.
[90] THEILHABER, K., BIRDSALL, C.K., Phys. Fluids B **1** (1989) 2260.
[91] RUZIC, D., MOORE, R., MANOS, D., et al., J. Vac. Sci. Technol. **20** (1982) 1313.
[92] WOODS, M.E., HOPKINS, B.J., McCRACKEN, G.M., Surf. Sci. **162** (1985) 928.
[93] BUDNY, R., MANOS, D., J. Nucl. Mater. **121** (1984) 41.
[94] TAGLE, J.A., STANGEBY, P.C., ERENTS, S.K., Plasma Phys. Controll. Fusion **29** (1987) 297.
[95] BUTLER, H.S., KINO, G.S., Phys. Fluids **6** (1963) 1346.
[96] BOSCHI, A., MAGISTRELLI, F., Nuovo Cim. **29** (1963) 487.
[97] GARSCADDEN, A., EMELEUS, K.G., Proc. Phys. Soc. **79** (1962) 535.
[98] CRAWFORD, F.W., J. Appl. Phys. D **34** (1963) 1897.
[99] STAMPA, A., WOLF, H.O., J. Phys. D **11** (1978) 1119.
[100] STANGEBY, P.C., J. Nucl. Mater. **128&129** (1984) 969.
[101] PROUDFOOT, G., Culham Laboratory, personal communication, 1987.
[102] DITTE, U., GRAVE, T., Probe and Thermographic Measurements in the ASDEX Divertor, Rep. III/102, Max-Planck-Institut für Plasmaphysik, Garching (1985).
[103] BOGEN, P., HINTZ, E., in Physics of Plasma-Wall Interactions in Controlled Fusion (Proc. NATO Advanced Study Institute Val-Morin, Quebec, 1984), NATO ASI Series, Vol. 131, Plenum Press, New York (1986) 211.
[104] POSPIESZCZYK, A., ROSS, G.G., Rev. Sci. Instrum. **59** (1988) 605.
[105] POSPIESZCZYK, A., ROSS, G.G., in Controlled Fusion and Plasma Physics (Proc. 14th Eur. Conf. Madrid, 1987), Vol. 11D, Part III, European Physical Society (1987) 1281.
[106] McCORMICK, K., and ASDEX Team, Rev. Sci. Instrum. **56** (1985) 1063.
[107] McCORMICK, K., MURMANN, H., SHAER, M.E.R., et al., J. Nucl. Mater. **121** (1984) 48.
[108] KADOTA, K., TSUCHIDA, T., KAWASUMI, Y., et al., Plasma Phys. **20** (1978) 1011.
[109] GUENTHER, K., HAYESS, E., KREBS, K.H., et al., J. Nucl. Mater. **162–164** (1989) 562.
[110] WEST, W.P., Rev. Sci. Instrum. **57** (1986) 2006.
[111] YAMADA, H., KADOTA, K., OKUNA, K., et al., Jpn J. Appl. Phys. **26** (1987) 468.
[112] POSPIESZCZYK, A., ROSS, G.G., Rev. Sci. Instrum. **59** (1988) 1491.
[113] SALZMANN, H., in Basic and Advanced Diagnostic Techniques for Fusion Plasmas (Proc. Course and Workshop Int. School of Plasma Physics, Varenna, 1986), Vol. 2, Monotypia Franchi, Perugia (1988) 477.
[114] SHEFFIELD, J., Plasma Scattering of Electromagnetic Radiation, Academic Press, New York (1975).
[115] MURMANN, H., HUANG, M., Thomson Scattering Diagnostics in the Boundary Layer of ASDEX, Rep. III/95, Max-Planck-Institut für Plasmaphysik, Garching (1983).
[116] SOLTWISCH, H., in Basic and Advanced Diagnostic Techniques for Fusion Plasmas (Proc. Course and Workshop Int. School of Plasma Physics, Varenna, 1986), Vol. 1, Monotypia Franchi, Perugia (1988) 273.
[117] COSTLEY, A.E., ibid., Vol. 2, p. 379.
[118] PRENTICE, R., COSTLEY, A.E., ibid., Vol. 2, p. 451.
[119] COSTLEY, A.E., ibid., Vol. 1, p. 119.
[120] SALMON, N.A., BARTLETT, D.V., COSTLEY, A.E., ibid., Vol. 1, p. 273.
[121] SALMON, N.A., BARTLETT, D.V., COSTLEY, A.E., et al., in Controlled Fusion and Plasma Physics (Proc. 14th Eur. Conf. Madrid, 1987), Vol. 11D, Part III, European Physical Society (1987) 1248.
[122] PITCHER, C.S., McCRACKEN, G.M., STANGEBY, P.C., et al., J. Nucl. Mater. **145–147** (1987) 539.
[123] GOODALL, D.H.J., FIELDING, S.J., PITCHER, C.S., et al., J. Nucl. Mater. **145–147** (1987) 596.
[124] PITCHER, C.S., MATTHEWS, G.F., GOODALL, D.H.J., et al., Contrib. Plasma Phys. **28** (1988) 489.
[125] PITCHER, C.S., STANGEBY, P.C., GOODALL, D.H.J., et al., J. Nucl. Mater. **162–164** (1989) 337.
[126] JOHNSON, L.G., HINNOV, E., J. Quant. Spectrosc. Radiat. Transfer **13** (1973) 333.
[127] McNEILL, D.H., J. Vac. Sci. Technol. A **2** (1984) 689.
[128] BEHRINGER, K.J., J. Nucl. Mater. **145–147** (1987) 145.
[129] FIELDING, S.J., JOHNSON, P.C., FORREST, M.J., J. Nucl. Mater. **162–164** (1989) 482.
[130] SAMM, U., BOGEN, P., HARTWIG, E., et al., J. Nucl. Mater. **162–164** (1989) 24.

[131] BAY, H.L., SCHWEER, B., J. Nucl. Mater. **128&129** (1984) 257.
[132] BOGEN, P., RUSBUELDT, D., SAMM, U., J. Nucl. Mater. **162-164** (1989) 545.
[133] BOGEN, P., DOBELE, H.F., MERTENS, P., J. Nucl. Mater. **145-147** (1987) 435.
[134] KISLYAKOV, A.I., in Basic and Advanced Diagnostic Techniques for Fusion Plasmas (Proc. Course and Workshop Int. School of Plasma Physics, Varenna, 1986), Vol. 2, Monotypia Franchi, Perugia (1987) 623.
[135] VERBEEK, H., ASDEX Team, J. Nucl. Mater. **145-147** (1987) 523.
[136] VOSS, D.E., COHEN, S.A., J. Nucl. Mater. **93&94** (1982) 405.
[137] RUZIC, D.N., HEIFETZ, D.B., COHEN, S.A., J. Nucl. Mater. **145-147** (1987) 527.
[138] MATTHEWS, G.F., McCRACKEN, G.M., SEWELL, P., et al., J. Nucl. Mater. **145-147** (1987) 225.
[139] PITTS, R.A., McCRACKEN, G.M., MATTHEWS, G.F., in Controlled Fusion and Plasma Physics (Proc. 16th Eur. Conf. Venice, 1989), Vol. 13B, Part III, European Physical Society (1989) 955.
[140] MATTHEWS, G.F., in Controlled Fusion and Plasma Physics (Proc. 12th Eur. Conf. Budapest, 1985), Vol. 9F, Part II, European Physical Society (1985) 591.
[141] WAN, A.S., LIPSCHULTZ, B., McDERMOTT, F.S., et al., J. Nucl. Mater. **162-164** (1989) 292.
[142] MATTHEWS, G.F., J. Nucl. Mater. **162-164** (1989) 38.
[143] ULRICKSON, M., PEARSON, G.G., J. Nucl. Mater. **111&112** (1982) 91.
[144] GOODALL, D.H.J., AUSTIN, G.E., WEAVER, J.M., Fusion Technol. **6** (1984) 393.
[145] TFR Group, J. Nucl. Mater. **105** (1982) 62.
[146] CARSLAW, H.S., JAEGER, J.C., Conduction of Heat in Solids, 2nd edn, Oxford Univ. Press, Oxford (1959) 401.
[147] POST, D.E., LACKNER K., in Physics of Plasma-Wall Interactions in Controlled Fusion (Proc. NATO Advanced Study Institute Val-Morin, Quebec, 1984), NATO ASI Series, Vol. 131, Plenum Press, New York (1986) 627.
[148] SINGER, C.E., ibid., p. 607.
[149] PETROV, V.G., Nucl. Fusion **24** (1984) 259.
[150] NEDOSPASOV, A.V., PETROV, V.G., FIDELMAN, G.N., Nucl. Fusion **25** (1985) 21.
[151] NEDOSPASOV, A.V., PETROV, V.G., Nucl. Fusion **26** (1986) 1529.
[152] FENEBERG, W., ZANINO, R., in Controlled Fusion and Plasma Physics (Proc. 14th Eur. Conf. Madrid, 1987), Vol. 11D, Part II, European Physical Society (1987) 748.
[153] REBUT, P.-H., DIETZ, K.J., LALLIA, P.P., J. Nucl. Mater. **162-164** (1989) 172.
[154] SELF, S.A., EWALD, H.N., Phys. Fluids **6** (1963) 1762.
[155] WOODS, L.C., J. Fluid. Mech. **23** (1965) 315.
[156] SELF, S.A., EWALD, H.N., Phys. Fluids **9** (1966) 2486.
[157] KINO, G.S., SHAW, W.K., Phys. Fluids **9** (1966) 587.
[158] PROUDFOOT, G., HARBOUR, P.J., ALLEN, J., et al., J. Nucl. Mater. **128&129** (1984) 180.
[159] EMMERT, G.A., WIELAND, R.M., MENSE, A.T., et al., Phys. Fluids **23** (1980) 803.
[160] BISSELL, R.C., JOHNSON, P.C., Phys. Fluids **30** (1987) 779.
[161] ZAWAIDEH, E., NAJMABADI, F., CONN, R.W., Phys. Fluids **29** (1986) 463.
[162] BISSELL, R.C., PhD Thesis, Oxford Univ. (1986).
[163] BISSELL, R.C., JOHNSON P.C., STANGEBY, P.C., Phys. Fluids B **1** (1989) 1133.
[164] SCHEUER, J.T., EMMERT, G.A., Phys. Fluids B **2** (1990) 445.
[165] CHUNG, K.-S., HUTCHINSON, I.H., Phys. Rev. A **38** (1988) 4721.
[166] SCHEUER, J.T., EMMERT, G.A., Phys. Fluids **31** (1988) 1748.
[167] GIERSZEWSKI, P., McKENTY, P., McCULLEN, J., et al., Phys. Rev. Lett. **49** (1982) 650.
[168] ALLEN, J.E., THONEMANN, P.C., Proc. Phys. Soc. B **67** (1954) 768.
[169] BOOZER, A.H., The Bohm Stability Criterion and the MHD Theory of Plasma Flow to an Absorbing Wall, Rep. MATT-1148, Princeton Plasma Physics Laboratory (1975).
[170] BISSELL, R.C. (Culham Laboratory, Abingdon, Oxfordshire), personal communication, 1988.
[171] HOBBS, G.D., WESSON, J.A., Plasma Phys. **9** (1967) 85.
[172] HARBOUR, P.J., HARRISON, M.F.A., J. Nucl. Mater. **76&77** (1978) 513.
[173] HARBOUR, P.J., The Effect of Secondary Electron Emission on a Plasma Sheath, Rep. CLM-P-535, Culham Laboratory, Abingdon, Oxfordshire (1978).
[174] FUCHS, G., NICOLAI, A., J. Nucl. Mater. **76&77** (1978) 573.
[175] HARBOUR, P.J., HARRISON, M.F.A., Nucl. Fusion **19** (1979) 695.
[176] KIMURA, H., MAEDA, H., UEDA, N., et al., Nucl. Fusion **18** (1978) 1195.
[177] NEDOSPASOV, A.V., PETROV, V.G., J. Nucl. Mater. **76&77** (1978) 490.
[178] KISELEVSKIJ, L.I., SIZONENKO, V.L., SHERGIN, G.G., Sov. J. Plasma Phys. **9** (1983) 639.
[179] DeWALD, A.B., BAILEY, A.W., BROOKS, J.N., Phys. Fluids **30** (1987) 267.
[180] ROTH, J., in Physics of Plasma-Wall Interactions in Controlled Fusion (Proc. NATO Advanced Study Institute Val-Morin, Quebec, 1984), NATO ASI Series, Vol. 131, Plenum Press, New York (1986) 351.
[181] HAASZ, A.A., DAVIS, J. W., WU, C.H., J. Nucl. Mater. **162-164** (1989) 915.
[182] RUZIC, D.N., CHIN, H.K., J. Nucl. Mater. **162-164** (1989) 904.
[183] STANGEBY, P.C., MANOS, D., Princeton Plasma Physics Laboratory, unpublished results, 1984.
[184] MATTHEWS, G.F., FIELDING, S.J., McCRACKEN, G.M., et al., Investigation of the fluxes to a surface at grazing angles of incidence in the tokamak boundary, submitted to Plasma Phys. Controll. Fusion.
[185] ZWEBEN, S.J., TAYLOR, R.J., Nucl. Fusion **23** (1983) 513.
[186] TFR Group, J. Nucl. Mater. **93&94** (1980) 272.
[187] SENGOKU, S., OHTSUKA, H., et al., J. Nucl. Mater. **93&94** (1980) 75.
[188] STANGEBY, P.C., McCRACKEN, G.M., VINCE, J., J. Nucl. Mater. **111&112** (1982) 81.
[189] STANGEBY, P.C., McCRACKEN, G.M., ERENTS, S.K., et al., J. Vac. Sci. Technol. A **1** (1983) 1302.

[190] ERENTS, S.K., McCRACKEN, G.M., PARTRIDGE, J.W., et al., J. Nucl. Mater. **128&129** (1984) 383.
[191] COOK, T.B., KING, P.W., ROBERTO, J.B., et al., J. Nucl. Mater. **128&129** (1984) 253.
[192] MIODUSZEWSKI, P.K., EDMONDS, P.H., EMERSON, L.C., et al., J. Nucl. Mater. **145&147** (1987) 210.
[193] ERTL, K., J. Nucl. Mater. **128&129** (1984) 163.
[194] LACKNER, K., DITTE, U., FUSSMANN, G., et al., in Plasma Physics and Controlled Nuclear Fusion Research 1984 (Proc. 10th Int. Conf. London, 1984), Vol. 1, IAEA, Vienna (1985) 319.
[195] UEHARA K., GOMAY, Y., YAMAMOTO, T., et al., Plasma Phys. **21** (1979) 89.
[196] STAUDENMAIER, G., STAIB, P., VENUS, G., et al., J. Nucl. Mater. **76&77** (1978) 445.
[197] MENSE, A.T., EMMERT, G.A., CALLEN, J.D., Nucl. Fusion **15** (1975) 703.
[198] STANGEBY, P.C., J. Nucl. Mater. **145–147** (1987) 105.
[199] LIPSCHULTZ, B., BECKER, H., BONDI, P., et al., J. Nucl. Mater. **162–164** (1989) 793.
[200] CONN, R.W., J. Nucl. Mater. **128&129** (1984) 407.
[201] VOLKOV, T.F., KIRILLOV, V.D., Sov. J. Plasma Phys. **9** (1983) 521.
[202] CHEETHAM, A., CHRISTIANSEN, J.P., CORTI, S., et al., in Controlled Fusion and Plasma Heating (Proc. 13th Eur. Conf. Schliersee, 1986), Vol. 10C, Part I, European Physical Society (1986) 240.
[203] BARTLETT, D.V., BICKERTON, R.J., BRUSATI, M., et al., Nucl. Fusion **28** (1988) 73.
[204] GERHAUSER, H., CLAASSEN, H.A., Calculation of Poloidal Rotation in the Edge Plasma of Limiter Tokamaks, Rep. Jülich-2125, KFA, Jülich (1987).
[205] McCRACKEN, G.M., STANGEBY, P.C., Plasma Phys. Controll. Fusion **27** (1985) 1411.
[206] HUGILL, J. S., Nucl. Fusion **23** (1983) 331.
[207] BECKER, G., ASDEX Team, Neutral Injection Team, Nucl. Fusion **28** (1988) 139.
[208] BRACCO, G., BRUSATI, M., CORTI, S., et al., in Controlled Fusion and Plasma Physics (Proc. 14th Eur. Conf. Madrid, 1987), Vol. 11D, Part II, European Physical Society (1987) 670.
[209] STANGEBY, P.C., TAGLE, J.A., ERENTS, S.K., et al., Plasma Phys. Controll. Fusion **30** (1988) 1787.
[210] De KOCK, L., BEHRISCH, R., BERGSÅKER, H., et al., J. Nucl. Mater. **145–147** (1987) 26.
[211] HEIFETZ, D.B. (Princeton Plasma Physics Laboratory), personal communication, 1987.
[212] RITTER R.S., BUDNY, R.V., COHEN, S.A., J. Nucl. Mater. **145–147** (1987) 793.
[213] CHANKIN, A.V., CHICHEROV, V.M., EFSTIGNEEV, S.A., et al., J. Nucl. Mater. **145–147** (1987) 789.
[214] COHEN, S.A., in Physics of Plasma-Wall Interactions in Controlled Fusion (Proc. NATO Advanced Study Institute Val-Morin, Quebec, 1984), NATO ASI Series, Vol. 131, Plenum Press, New York (1986) 773.
[215] GOLDSTON, R., Plasma Phys. Controll. Fusion **29** (1984) 87.
[216] COHEN, S.A., EHRENBERG, J., JONES, T.T.C., et al., Plasma Phys. Controll. Fusion **29** (1987) 1205.
[217] OGDEN, J.M., SINGER, C.E., POST, D.E., et al., IEEE Trans. Plasma Sci. **PS-9** (1981) 274.
[218] SHIMAMURA, Y., MAEDA, H., J. Nucl. Mater. **76&77** (1978) 45.
[219] BICKERTON, R.J., ALLADIO, F., BARTLETT, D.V., et al., Plasma Phys. Controll. Fusion **28** (1986) 55.
[220] HEIFETZ, D.B., in Physics of Plasma-Wall Interactions in Controlled Fusion (Proc. NATO Advanced Study Institute Val-Morin, Quebec, 1984), NATO ASI Series, Vol. 131, Plenum Press, New York (1986) 695.
[221] CUPINI, E., DeMATTEIS, A., SIMONINI, R., NIMBUS — Monte Carlo Simulation of Neutral Particle Transport in Fusion Devices, Rep. EUR.XII 324/9, CEC, Brussels (1983).
[222] MADDISON, G.P., ALLEN, J., FIELDING, S.J., et al., J. Nucl. Mater. **145–147** (1987) 534; Culham Laboratory, personal communication, 1987.
[223] MADDISON, G.P., MATTHEWS, G., Culham Laboratory, personal communication, 1987.
[224] STANGEBY, P.C., J. Nucl. Mater. **121** (1984) 55.
[225] ULRICKSON, M., POST, D.E., J. Vac. Sci. Technol. A **1** (1983) 907.
[226] BUGARYA, V.I., GRASHIN, S.A., CHANKIN, A.V., Sov. J. Plasma Phys. **10** (1984) 761.
[227] CHANKIN, A.V., Sov. J. Plasma Phys. **11** (1985) 589.
[228] JANEV, R.K., POST, D.E., LANGER, W.D., et al., J. Nucl. Mater. **121** (1984) 10.
[229] HARRISON, M.F.A., HARBOUR, P.J., HOTSTON, E.S., et al., Nucl. Fusion Technol. **3** (1983) 432.
[230] CAROLAN, P.G., PIOTROWICZ, V.A., Plasma. Phys. **25** (1983) 1065.
[231] POST, D.E., JENSON, R.V., TARTAR, C.B., et al., At. Data Nucl. Data Tables **20** (1977) 397.
[232] ABRAMOV, V.A., KROTOVA, G.I., Sov. J. Plasma Phys. **13** (1987) 133.
[233] STANGEBY, P.C., J. Phys. D **20** (1987) 1472.
[234] CHODURA, R., Contrib. Plasma Phys. **28** (1988) 303, 325.
[235] IGITKHANOV, Yu.L., RUNOV, A.M., Contrib. Plasma Phys. **28** (1988) 333.
[236] IGITKHANOV, Yu.L., YUSHMANOV, P.N., Contrib. Plasma Phys. **28** (1988) 341.
[237] KRASHENINNIKOV, S.I., Sov. Phys. — JETP **67** (1988) 2483.
[238] PIGAROV, A., VERSHKOV, V., Kurchatov Institute, Moscow, personal communication, 1988.
[239] JONES, E.M., Atomic Collision Processes in Plasma Experiments: Analytic Expressions for Selected Cross-Sections and Maxwellian Coefficients. II, Rep. CLM-R 175, Culham Laboratory, Abingdon, Oxfordshire (1977).
[240] BICKERTON, R.J., Plasma Phys. Controll. Fusion **29** (1987) 1219.
[241] FONCK, R.J., BEIERSDORFER, P., BELL, M., et al., in Heating in Toroidal Plasmas (Proc. 4th Int. Symp. Rome, 1984), Vol. 1, ENEA, Rome (1984) 37.
[242] KEILHACKER M., GIERKE, G. von, MÜLLER, E.R., et al., Plasma Phys. Controll. Fusion **28** (1986) 29.
[243] WAGNER, F., LACKNER, K., in Physics of Plasma-Wall Interactions in Controlled Fusion (Proc. NATO Advanced Study Institute Val-Morin, Quebec, 1984), NATO ASI Series, Vol. 131, Plenum Press, New York (1986) 931.
[244] STRACHAN, J.D., BITTER, M., RAMSEY, A.T., et al., Phys. Rev. Lett. **58** (1987) 1004.

[245] DYLLA, H.F., LaMARCHE, P.H., ULRICKSON, M., et al., Nucl. Fusion **27** (1987) 1221.
[246] GREENWALD, M., GWINN, D., MILORA, S., et al., Phys. Rev. Lett. **53** (1984) 352.
[247] FIELDING, S., HUGILL, J., McCRACKEN, G.M., et al., Nucl. Fusion **17** (1977) 1382.
[248] MURAKAMI, M., CALLEN, J.D., BERRY, L.A., Nucl. Fusion **16** (1976) 347.
[249] GIBSON, A., Nucl. Fusion **16** (1976) 546.
[250] REBUT, P.-H., GREEN, B., in Plasma Physics and Controlled Nuclear Fusion Research 1976 (Proc. 6th Int. Conf. Berchtesgaden, 1976), Vol. 2, IAEA, Vienna (1977) 3.
[251] WESSON, J., GOWERS, C., HAN, W., et al., in Controlled Fusion and Plasma Physics (Proc. 12th Eur. Conf. Budapest, 1985), Vol. 9F, Part I, European Physical Society (1985) 147.
[252] TENDLER, M., J. Nucl. Mater. **128&129** (1984) 100.
[253] SENGOKU, S., JFT-2M Team, J. Nucl. Mater. **145–147** (1987) 556.
[254] CHICHEROV, V.M., J. Nucl. Mater. **145–147** (1987) 117.
[255] ALEXANDER, K.F., HINTZE, W., Ann. Physik **43** (1986) 138.
[256] BAKER, D.R., SNIDER, R.T., NAGAMI, M., Nucl. Fusion **22** (1982) 807.
[257] WOLFF, H., Contrib. Plasma Phys. **28** (1988) 131.
[258] KLÜBER, O., ENGELHARDT, W., CANNICI, B., et al., Nucl. Fusion **15** (1975) 1194.
[259] GAUDREAU, M., GONDHALEKAR, A., HUGHES, M.H., et al., Phys. Rev. Lett. **39** (1977) 1266.
[260] SÖLDNER, F.X., MÜLLER, E.R., WAGNER, F., et al., Phys. Rev. Lett. **61** (1988) 1105.
[261] VASIN, N.L., VERSHKOV, V.A., KARZHAVIN, Yu. Yu., et al., in Controlled Fusion and Plasma Heating (Proc. 15th Eur. Conf. Dubrovnik, 1988), Vol. 12B, Part I, European Physical Society (1988) 59.
[262] MORGAN, P.D., CORTI, S., EHRENBERG, J., et al., in Controlled Fusion and Plasma Physics (Proc. 12th Eur. Conf. Budapest, 1985), Vol. 9F, Part II, European Physical Society (1985) 535.
[263] EHRENBERG, J., COAD, P., De KOCK, L., et al., J. Nucl. Mater. **162–164** (1989) 63.
[264] SHIMADA, M., RAMSEY, A.T., OWENS, D.K., et al., J. Nucl. Mater. **145–147** (1987) 544.
[265] FUJIMOTO, T., MIYACHI, S., SAWADA, K., Nucl. Fusion **28** (1988) 1255.
[266] McNEILL, D.H., J. Nucl. Mater. **162–164** (1989) 476.
[267] ROWAN, W.L., KLEPPER, C.C., RITZ, C.P., et al., Nucl. Fusion **27** (1987) 1105.
[268] HARRISON, M.F.A., in Physics of Plasma-Wall Interactions in Controlled Fusion (Proc. NATO Advanced Study Institute Val-Morin, Quebec, 1984), NATO ASI Series, Vol. 131, Plenum Press, New York (1986) 281.
[269] BEHRISCH, R., ECKSTEIN, W., ibid., p. 413.
[270] ECKSTEIN, W., VERBEEK, M., in Data Compendium for Plasma-Surface Interactions, Special Issue, Nucl. Fusion (1984) 12.
[271] JANEV, R.K., LANGER, W.D., EVANS, K., Jr., et al., Elementary Processes in Hydrogen-Helium Plasmas, Springer-Verlag, Berlin (1987).
[272] HEIFETZ, D.B., EHRHARDT, A.B., RAMSEY, A.T., et al., J. Vac. Sci. Technol. A **6** (1988) 2564.
[273] POST, D.E., SINGER, C.E., J. Numer. Methods **128&129** (1984) 78.
[274] BIERSACK, J.P., HAGGMARK, L.G., Nucl. Instrum. Methods **174** (1980) 257.
[275] ROBINSON, M., Phys. Rev. B **9** (1974) 5008.
[276] ECKSTEIN, W., HEIFETZ, D.B., J. Nucl. Mater. **145–147** (1987) 332.
[277] BASKES, M.I., FOILES, S.M., MELIUS, C.F., J. Nucl. Mater. **145–147** (1987) 339.
[278] TENDLER, M., HEIFETZ, D., Fusion Technol. **11** (1987) 289.
[279] LANGER, W.D., Nucl. Fusion **22** (1982) 751.
[280] LANGER, W.D., EHRHARDT, A.B., J. Nucl. Mater. **162–164** (1989) 329.
[281] HUGHES, M.H., POST, D.E., J. Comput. Phys. **28** (1978) 43.
[282] MURASE, K., Jpn J. Appl. Phys. **21** (1982) 109.
[283] REITER, D., NICOLAI, A., J. Nucl. Mater. **128&129** (1984) 458.
[284] MARABLE, J.H., OBLOW, E.M., Nucl. Sci. Eng. **61** (1987) 90.
[285] REITER, D., Randschicht-Konfiguration von Tokamaks, Entwicklung und Anwendung Stochastischer Modelle zur Beschreibung des Neutralgastransports, Rep. JÜL-1947, Kernforschungsanlage Jülich (1984).
[286] HOGAN, J.T., J. Nucl. Mater. **111&112** (1982) 413.
[287] HOGAN, J.T., KLEPPER, C.C., HILLIS, D.L., et al., J. Nucl. Mater. **162–164** (1989) 469.
[288] REITER, D., NICOLAI, A., J. Nucl. Mater. **111&112** (1982) 434.
[289] GIERSZEWSKI, P.J., Plasma/Neutral Gas Transport in Divertors and Limiters, Rep. PFC/RR-83-28, Massachusetts Institute of Technology, Cambridge (1983).
[290] HASAN, M.Z., CONN, R.W., Fusion Technol. **12** (1987) 416.
[291] HASAN, M.Z., CONN, R.W., Comput. Phys. **71** (1987) 371.
[292] PRINJA, A.K., Phys. Fluids **30** (1987) 840.
[293] IGITKHANOV, Yu.L., STAKHANOV, I.P., Nucl. Fusion **19** (1979) 1534.
[294] TENDLER, M.B., AGREN, O., Phys. Fluids **25** (1982) 1037.
[295] TENDLER, M., CHABRA, R.S., Phys. Fluids **25** (1982) 2101.
[296] AUDENAERDE, K., EMMERT, G.A., GORDINIER, M., J. Comput. Phys. **34** (1980) 268.
[297] BURRELL, K.H., J. Comput. Phys. **27** (1978) 88.
[298] DÜCHS, D.F., POST, D.E., RUTHERFORD, P.H., Nucl. Fusion **17** (1977) 565.
[299] GARCIA, R.D., POMRANING, G.C., SIEWERT, C.E., et al., Plasma Phys. **24** (1982) 903.
[300] MARUSCHENKO, N.B., PYATOV, V.N., TURKIN, Yu.A., Sov. J. Plasma Phys. **9** (1983) 717.
[301] LEPE, L.I., NAUMENKOV, S.P., STAKHANOV, I.P., Sov. J. Plasma Phys. **13** (1987) 653.
[302] BRUSATI, M., Diagnostics for Fusion Experiments (Proc. Course Varenna, 1978), Pergamon Press, New York (1979) 35.
[303] EUBANK, H.P., ibid., p. 7.
[304] WESSON, J., Tokamaks, Clarendon Press, Oxford (1987) 250.

[305] ORLINSKIJ, D.V., MAGYAR, G., Nucl. Fusion **28** (1988) 611.
[306] COHEN, S.A., RUZIC, D., VOSS, D.E., et al., Nucl. Fusion **24** (1984) 1490.
[307] VOSS, D.E., COHEN, S.A., Rev. Sci. Instrum. **53** (1982) 1696.
[308] VERBEEK, H., J. Phys. E **19** (1986) 964.
[309] VERBEEK, H., DOSE, V., FU, K., J. Nucl. Mater. **162-164** (1989) 557.
[310] ENGELHARDT, W., FENEBERG, W., J. Nucl. Mater. **76&77** (1978) 518.
[311] ENGELHARDT, W., BECKER, G., BEHRINGER, K., et al., J. Nucl. Mater. **111&112** (1982) 337.
[312] ALEXANDER, K.F., DIETRICH, L., GRÖTE, H., et al., in Plasma Physics and Controlled Nuclear Fusion Research 1986 (Proc. 11th Int. Conf. Kyoto, 1986), Vol. 1, IAEA, Vienna (1987) 237.
[313] PODESTA, G., ENGELMANN, F., in Toroidal Plasma Confinement (Proc. 3rd Int. Symp. Garching, 1973), Max-Planck-Institut für Plasmaphysik, Garching (1973) C3.
[314] TENDLER, M.B., AGREN, O., Phys. Fluids **25** (1982) 1037.
[315] LEHNERT, B., Nucl. Fusion **23** (1983) 1327.
[316] LEHNERT, B., Plasma Phys. Controll. Fusion **26** (1984) 1237.
[317] GONDHALEKAR, A., CAMPBELL, D., CHEETHAM, A.D., et al., in Controlled Fusion and Plasma Heating (Proc. 15th Eur. Conf. Dubrovnik, 1988), Vol. 12B, Part I, European Physical Society (1988) 151.
[318] YAMADA, K., TSUJI, S., SHIMIZU, K., et al., Nucl. Fusion **27** (1987) 1203.
[319] GENTLE, K.W., RICHARDS, B., WAELBROECK, F., Plasma Phys. Controll. Fusion **29** (1987) 1077.
[320] WOOTTON, A.J., AUSTIN, M., BENGSTON, R.D., et al., in Plasma Physics and Controlled Nuclear Fusion Research 1988 (Proc. 12th Int. Conf. Nice, 1988), Vol. 1, IAEA, Vienna (1989) 293.
[321] WAGNER, F., Nucl. Fusion **25** (1985) 525.
[322] GEHRE, O., GENTLE, K.W., RICHARDS, B., et al., in Controlled Fusion and Plasma Heating (Proc. 15th Eur. Conf. Dubrovnik, 1988), Vol. 12B, Part I, European Physical Society (1988) 7.
[323] EFTHIMION, P.C., BITTER, M., FREDRICKSON, E.D., et al., in Plasma Physics and Controlled Fusion Research 1988 (Proc. 12th Int. Conf. Nice, 1988), Vol. 1, IAEA, Vienna (1989) 307.
[324] LARIONOV, M.M., LEVIN, L.S., PETROV, Yu.V., et al., Plasma Phys. Controll. Fusion **30** (1988) 1637.
[325] UEHARA, K., FUJISAWA, N., YAMAMOTO, T., et al., J. Phys. Soc. Jpn **48** (1980) 1333.
[326] WOOTTON, A.J., AUSTIN, M.E., BENGSTON, R.D., et al., Plasma Phys. Controll. Fusion **30** (1988) 1479.
[327] DYLLA, H.F., ULRICKSON, M., BELL, M.G., J. Nucl. Mater. **162-164** (1989) 128.
[328] WAMPLER, W., MAGEE, C.W., J. Nucl. Mater. **103&104** (1980) 509.
[329] MÖLLER, W., ROTH J., in Physics of Plasma-Wall Interactions in Controlled Fusion (Proc. NATO Advanced Study Institute Val-Morin, Quebec, 1984), NATO ASI Series, Vol. 131, Plenum Press, New York (1986) 439.
[330] DYLLA, H.F., TFTR Team, J. Nucl. Mater. **145-147** (1987) 48.
[331] YOSHIKAWA, M., JT-60 Team, Plasma Phys. Controll. Fusion **28** (1986) 165.
[332] JONES, T.T.C., CUTHBERTSON, J.W., EHRENBERG, J., J. Nucl. Mater. **162-164** (1989) 503.
[333] MÖLLER, W., J. Nucl. Mater. **162-164** (1989) 138.
[334] CAUSEY, R., J. Nucl. Mater. **162-164** (1989) 151.
[335] ROTH, J., J. Nucl. Mater. **145-147** (1987) 87.
[336] BOHDANSKY, J., in Nucl. Fusion, Special Issue, Data Compendium for Plasma-Surface Interactions (1984) 61.
[337] ROTH, J., BOHDANSKY, J., OTTENBERGER, W., J. Nucl. Mater. **165** (1989).
[338] ROTH, J., ECKSTEIN, W., BOHDANSKY, J., J. Nucl. Mater. **165** (1989) 199.
[339] PITCHER, C.S., McCRACKEN, G.M., STANGEBY, P.C., et al., in Controlled Fusion and Plasma Physics (Proc. 16th Eur. Conf. Venice, 1989), Vol. 13B, Part III, European Physical Society (1989) 879.
[340] STAMP, M.F., FORREST, M.J., MORGAN, P.D., ibid., Part IV, p. 1513.
[341] JENSEN, R.V., POST, D.E., GRASBERGER, W.H., et al., Nucl. Fusion **17** (1977) 1187.
[342] JENSEN, R.V., POST, D.E., JASSBY, D.L., Nucl. Sci. Eng. **65** (1978) 282.
[343] REBUT, P.-H., BRUSATI, M., Plasma Phys. Controll. Fusion **28** (1986) 113.
[344] ROBERTS, D.E., Nucl. Fusion **23** (1983) 311.
[345] HIRAYAMA, T., SHIRAI, H., SHIMIZU, K., et al., J. Nucl. Mater. **145-147** (1987) 854.
[346] LIPSCHULTZ, B., LaBOMBARD, B., MARMAR, E., Nucl. Fusion **24** (1984) 977.
[347] NEUHAUSER, J., SCHNEIDER, W., WÜNDERLICH, R., Nucl. Fusion **26** (1986) 1679.
[348] STRINGER, T.E., in Controlled Fusion and Plasma Physics (Proc. 12th Eur. Conf. Budapest, 1985), Vol. 9F, Part I, European Physical Society (1985) 86.
[349] DRAKE, J.F., Phys. Fluids **30** (1987) 2429.
[350] POSPIESZCZYK, A., BAY, H.L., BOGEN, P., J. Nucl. Mater. **145-147** (1987) 574.
[351] McCRACKEN, G.M., ALLEN, J., AXON, K., et al., J. Nucl. Mater. **145-147** (1987) 181.
[352] STRACHAN, J.D., BOODY, F.P., BUSH, C.E., et al., J. Nucl. Mater. **145-147** (1987) 186.
[353] TROYON, F., GRUBER, R., SAURENMANN, H., et al., Plasma Phys. Controll. Fusion **26** (1984) 209.
[354] BEHRINGER, K., BOILEAU, A., BOMBARDA, F., in Plasma Physics and Controlled Nuclear Fusion Research 1986 (Proc. 11th Int. Conf. Kyoto, 1986), Vol. 1, IAEA, Vienna (1987) 197.
[355] JT-60 Team, presented by KISHIMOTO, H., in Plasma Physics and Controlled Nuclear Fusion Research 1988 (Proc. 12th Int. Conf. Nice, 1988), Vol. 1, IAEA, Vienna (1989) 67.
[356] CAMPBELL, D.J., DUPERREX, P.A., EDWARDS, A.W., et al., in Plasma Physics and Controlled Nuclear Fusion Research 1986 (Proc. 11th Int. Conf. Kyoto, 1986), Vol. 1, IAEA, Vienna (1987) 433.
[357] ENGELMANN, F., CHAZALON, M., HARRISON, M.F.A., et al., J. Nucl. Mater. **145-147** (1987) 154.

[358] POSPIESZCZYK, A., BOGEN, P., SAMM, U., in Controlled Fusion and Plasma Physics (Proc. 11th Eur. Conf. Aachen, 1983), Vol. 7D, Part I, European Physical Society (1983) 417.
[359] SCHWEER, B., BOGEN, P., HINTZ, E., et al., J. Nucl. Mater. **111&112** (1982) 71.
[360] BEHRINGER, K., FUSSMANN, G., POSCHENRIEDER, W., et al., in Controlled Fusion and Plasma Physics (Proc. 11th Eur. Conf. Aachen, 1983), Vol. 7D, Part II, European Physical Society (1983) 467.
[361] FUSSMANN, G., J. Nucl. Mater. **145-147** (1987) 96.
[362] FUSSMANN, G., DITTE, U., ECKSTEIN, W., et al., J. Nucl. Mater. **128&129** (1984) 350.
[363] ISLER, R.C., BEHRINGER, K., KÄLLNE, E., et al., Nucl. Fusion **25** (1985) 1635.
[364] ISLER, R.C., Nucl. Fusion **24** (1984) 1599.
[365] PITCHER, C.S., McCRACKEN, G.M., GOODALL, D.H.J., et al., Nucl. Fusion **26** (1986) 1641.
[366] PITCHER, C.S., STANGEBY, P.C., GOODALL, D.H.J., et al., J. Nucl. Mater. **162-164** (1989) 337.
[367] STAMP, M.F., BEHRINGER, K., FORREST, M.J., et al., J. Nucl. Mater. **145-147** (1987) 236.
[368] STAMP, M.F., BEHRINGER, K.H., FORREST, M.J., et al., J. Nucl. Mater. **162-164** (1989) 404.
[369] COHEN, S.A., J. Nucl. Mater. **63** (1976) 65.
[370] ENGELHARDT, W., in Diagnostics for Fusion Reactor Conditions, Rep. EUR-8351-1, Vol. 1, CEC, Brussels (1982) 11.
[371] KEILHACKER, M., FUSSMANN, G., von GIERKE, G., in Plasma Physics and Controlled Nuclear Fusion Research 1984 (Proc. 10th Int. Conf. London, 1984), Vol. 1, IAEA, Vienna (1985) 71.
[372] FUSSMANN, G., HOFFMAN, J., JANESCHITZ, G., et al., J. Nucl. Mater. **162-164** (1989) 14.
[373] MÜLLER, E.R., JANESCHITZ, G., SMEULDERS, P., et al., Nucl. Fusion **27** (1987) 1817.
[374] STAUDENMAIER, G., WAMPLER, W., J. Nucl. Mater. **145-147** (1987) 569.
[375] BEHRINGER, K., SUMMERS, H.P., DENNE, B., Plasma Phys. Controll. Fusion **31** (1989) 2059.
[376] POSPIESZCZYK, A. (KFA Jülich), personal communication, 1989.
[377] ZUHR, R.A., ROBERTO, J.B., APPLETON, B.R., Nucl. Sci. Appl. **1** (1984) 617.
[378] HILDEBRANDT, D., HINTZE, W., JUTTNER, B., et al., J. Nucl. Mater. **93&94** (1980) 310.
[379] EHRENBERG, J., BEHRISCH, R., MARTINELLI, P., et al., in Controlled Fusion and Plasma Physics (Proc. 12th Eur. Conf. Budapest, 1985), Vol. 9F, Part II, European Physical Society (1985) 575.
[380] PAVLOV, Yu.D., PETROV, D.P., SOLNTSEV, A.M., et al., Sov. J. Plasma Phys. **12** (1986) 739.
[381] BEHRISCH, R., BLEWER, R.S., KUKRAL, H., et al., J. Nucl. Mater. **76&77** (1978) 437.
[382] BEHRISCH, R., WESNER, F., WIELUNSKI, M., et al., in Controlled Fusion and Plasma Physics (Proc. 14th Eur. Conf. Madrid, 1987), Vol. 11D, Part II, European Physical Society (1987) 778.
[383] COHEN, S.A., DYLLA, H.F., ROSSNAGEL, S.M., et al., J. Nucl. Mater. **76&77** (1978) 459.
[384] STAIB, P., KUKRAL, H., GLOCK, E., et al., J. Nucl. Mater. **111&112** (1982) 173.
[385] WAMPLER, W., PICRAUX, S.T., COHEN, S.A., et al., J. Nucl. Mater. **93&94** (1980) 139.
[386] ROBERTO, J.B., ZUHR, R.A., WITHROW, S.P., J. Nucl. Mater. **93&94** (1980) 146.
[387] HORI, Y., SAGARA, A., KABEYA, Z., et al., J. Nucl. Mater. **111&112** (1982) 137.
[388] MOHRI, M., SATAKE, T., HASHIBA, M., et al., J. Nucl. Mater. **111&112** (1982) 147.
[389] ZHU, Y.K., FENG, G.Z., YAN, D.H., et al., J. Nucl. Mater. **162-164** (1989) 448.
[390] BERGSÅKER, H., NAGATA, S., EMMOTH, B., et al., in Controlled Fusion and Plasma Physics (Proc. 14th Eur. Conf. Madrid, 1987), Vol. 11D, Part II, European Physical Society (1987) 728.
[391] COAD, J.P., BEHRISCH, R., ROTH, J., ibid., p. 744.
[392] EMERSON, L.C., CLAUSING, R.E., HEATHERLY, L., J. Nucl. Mater. **76&77** (1978) 472.
[393] ZUHR, R.A., WITHROW, S.P., ROBERTO, J.B., J. Nucl. Mater. **93&94** (1980) 127.
[394] COHEN, S.A., DYLLA, H.F., J. Nucl. Mater. **76&77** (1978) 425.
[395] McCRACKEN, G.M., DEARNALEY, G., GILL, R.D., et al., J. Nucl. Mater. **76&77** (1978) 431.
[396] CHICHEROV, V., HILDEBRANDT, D., LAUX, M., et al., J. Nucl. Mater. **93&94** (1980) 133.
[397] STAIB, P., DYLLA, H.F., ROSSNAGEL, S.M., J. Nucl. Mater. **93&94** (1980) 166.
[398] TAGLAUER, E., SCHERZER, B.M.U., VARGA, P., et al., J. Nucl. Mater. **111&112** (1982) 142.
[399] EMMOTH, B., BRAUN, M., SÄTHERBLOM, H.E., et al., J. Nucl. Mater. **128&129** (1984) 195.
[400] WIENHOLD, P., WINTER, J., ESSER, H.G., et al., J. Nucl. Mater. **145-147** (1987) 631.
[401] EMMOTH, B., NAGATA, S., BERGSÅKER, H., et al., J. Nucl. Mater. **145-147** (1987) 637.
[402] BEHRISCH, R., COAD, J.P., EHRENBERG, J., et al., J. Nucl. Mater. **162-164** (1989) 598.
[403] BERGSÅKER, H., RUBEL, M., EMMOTH, B., J. Nucl. Mater. **162-164** (1989) 595.
[404] EMMOTH, B., RUBEL, M., BERGSÅKER, H., J. Nucl. Mater. **162-164** (1989) 409.
[405] TAGLAUER, E., MARTINELLI, A.P., JANESCHITZ, G., J. Nucl. Mater. **162-164** (1989) 419.
[406] KILPATRICK, S.J., DYLLA, H.F., WAMPLER, W.R., J. Nucl. Mater. **162-164** (1989) 757.
[407] BERGSÅKER, H., COAD, J.P., DeKOCK, L., et al., in Controlled Fusion and Plasma Physics (Proc. 14th Eur. Conf. Madrid, 1987), Vol. 11D, Part II, European Physical Society (1987) 732.
[408] TAGLAUER, E., J. Nucl. Mater. **128&129** (1984) 141.
[409] STAUDENMAIER, G., J. Vac. Sci. Technol. A **3** (1985) 1091.
[410] STANGEBY, P.C., Phys. Fluids **30** (1987) 3262.
[411] HILDEBRANDT, D., GRÖTE, H., HERMANN, A., et al., Nucl. Fusion **25** (1985) 1745.
[412] HILDEBRANDT, D., Contrib. Plasma Phys. **26** (1986) 231.
[413] BAKOS, J.S., HILDEBRANDT, D., PASZTI, F., et al., J. Nucl. Mater. **162-164** (1989) 376.

[414] BAKOS, J.S., BURGER, G., IGNACZ, P.N., et al., J. Nucl. Mater. **162-164** (1989) 381.
[415] BEHRISCH, R., BØRGESON, P., EHRENBERG, J., et al., J. Nucl. Mater. **128&129** (1984) 470.
[416] MARTINELLI, A.P., BEHRISCH, R., ENGLERT, W., in Controlled Fusion and Plasma Physics (Proc. 12th Eur. Conf. Budapest, 1985), Vol. 9F, Part II, European Physical Society (1985) 623.
[417] TFR Group, J. Nucl. Mater. **145-147** (1987) 681.
[418] BEHRISCH, R., EHRENBERG, J., BERGSÅKER, H., et al., J. Nucl. Mater. **145-147** (1987) 731.
[419] EHRENBERG, J., McCRACKEN, G.M., BEHRISCH, R., et al., in Controlled Fusion and Plasma Heating (Proc. 13th Eur. Conf. Schliersee, 1986), Vol. 10C, Part I, European Physical Society (1986) 391.
[420] WAMPLER, W.R., DOYLE, B.L., LEE, S.R., et al., J. Vac. Sci. Technol. A **6** (1988) 2111.
[421] McGRATH, R.T., BROOKS, J.N., J. Nucl. Mater. **162-164** (1989) 350.
[422] DYLLA, H.F., ULRICKSON, M.A., LaMARCHE, P.H., et al., J. Vac. Sci. Technol. A **3** (1985) 1105.
[423] PONTAU, A.E., CAUSEY, R.A., BOHDANSKY, J., J. Nucl. Mater. **145-147** (1987) 775.
[424] McGRATH, R.T., DOYLE, B.L., BROOKS, J.N., et al., J. Nucl. Mater. **145-147** (1987) 660.
[425] AMEMIYA, S., KANEUCHI, A., KATOH, T., et al., J. Nucl. Mater. **145-147** (1987) 713.
[426] DOYLE, B.L., WAMPLER, W.R., DYLLA, H.F., et al., J. Nucl. Mater. **128&129** (1984) 955.
[427] MILLS, B.E., BUCHENAUER, D.A., PONTAU, A.E., et al., J. Nucl. Mater. **162-164** (1989) 343.
[428] STANGEBY, P.C., FARRELL, C., Contrib. Plasma Phys. **28** (1988) 495.
[429] REINHOLD, G., HACKMANN, J., UHLENBUSCH, J., J. Nucl. Mater. **128&129** (1984) 240.
[430] MERTENS, Ph., BOGEN, P., J. Nucl. Mater. **128&129** (1984) 551.
[431] BESSENRODT-WEBERPALS, M., HACKMANN, J., UHLENBUSCH, J., J. Nucl. Mater. **145-147** (1987) 849.
[432] FONCK, R.J., FINKENTHAL, M., GOLDSTON, R.J., et al., Phys. Rev. Lett. **49** (1982) 737.
[433] McCRACKEN, G.M., FIELDING, S.J., MATTHEWS, G.F., et al., J. Nucl. Mater. **162-164** (1989) 392.
[434] STOTT, P.E., Nucl. Fusion **28** (1988) 1469.
[435] BEHRINGER, K., DENNE, B., MORGAN, P.D., et al., J. Nucl. Mater. **162-164** (1989) 398.
[436] LEBEDEV, S.V., MOSHKALEV, S.A., RAZDOBARIN, G.T., et al., Nucl. Fusion **25** (1985) 931.
[437] LIPSCHULTZ, B., LaBOMBARD, B., MARMAR, E.S., et al., J. Nucl. Mater. **128&129** (1984) 555.
[438] HINTZ, E., BOGEN, P., J. Nucl. Mater. **128&129** (1984) 229.
[439] MULLER, C.H., EAMES, D.R., BURRELL, K.H., et al., J. Nucl. Mater. **111&112** (1982) 56.
[440] DAVIS, J.W., HAASZ, A.A., STANGEBY, P.C., J. Nucl. Mater. **145-147** (1987) 417.
[441] VIETZKE, E., FLASKAMP, K., HENNES, M., et al., Nucl. Instrum. Methods B **2** (1984) 617.
[442] YAMADA, R., J. Nucl. Mater. **145-147** (1987) 359.
[443] HAASZ, A.A., DAVIS, J.W., AUCIELLO, O., et al., J. Nucl. Mater. **145-147** (1987) 412.
[444] VIETZKE, E., TANABE, T., PHILLIPS, V., et al., J. Nucl. Mater. **145-147** (1987) 425.
[445] VIETZKE, E., PHILLIPS, V., FLASKAMP, K., J. Nucl. Mater. **162-164** (1989) 898.
[446] VIETZKE, E., PHILLIPS, V., Fusion Technol. **15** (1988) 108.
[447] HAASZ, A.A., DAVIS, J.W., J. Nucl. Mater. **151** (1987) 77.
[448] GOEBEL, D.M., HIROOKA, Y., CONN, R.W., et al., J. Nucl. Mater. **145-147** (1987) 61.
[449] GOEBEL, D.M., BOHDANSKY, J., CONN, R.W., et al., Nucl. Fusion **28** (1988) 1041.
[450] ROTH, J., BOHDANSKY, J., ROBERTO, J.B., J. Nucl. Mater. **128&129** (1984) 534.
[451] PONTAU, A.E., WILSON, K.L., J. Vac. Sci. Technol. **20** (1982) 1322.
[452] ROTH, J., FUSSMANN, G., JANESCHITZ, G., et al., in Controlled Fusion and Plasma Physics (Proc. 12th Eur. Conf. Budapest, 1985), Vol. 9F, Part II, European Physical Society (1985) 543.
[453] PHILLIPS, V., VIETZKE, E., ERDWEG, M., J. Nucl. Mater. **162-164** (1989) 550.
[454] PHILLIPS, V., VIETZKE, E., ERDWEG, M., et al., Plasma Phys. Controll. Fusion **31** (1989) 1685.
[455] SAMM, U., BOGEN, P., HARTWIG, H., et al., J. Nucl. Mater. **162-164** (1989) 24.
[456] DYLLA, H.F., BLANCHARD, W.R., J. Vac. Sci. Technol. A **1** (1983) 1297.
[457] RAMSEY, A.T., STRATTON, B.C., BOODY, F.P., et al., J. Nucl. Mater. **145-147** (1987) 592.
[458] ROTH, J., in Physics of Plasma-Wall Interactions in Controlled Fusion (Proc. NATO Advanced Study Institute Val-Morin, Quebec, 1984), NATO ASI Series, Vol. 131, Plenum Press, New York (1986) 351.
[459] NISHINO, N., KUBO, H., SAKASAKI, A., et al., J. Nucl. Mater. **162-164** (1989) 386.
[460] VERTIPOROKH, A.N., EVSTIGNEEV, S.A., IVANOV, I.V., in Controlled Fusion and Plasma Physics (Proc. 12th Eur. Conf. Budapest, 1985), Vol. 9F, Part II, European Physical Society (1985) 563.
[461] DREMIN, M.M., PAVLOV, Yu.D., PETROV, D.P., et al., Sov. J. Plasma Phys. **13** (1987) 149.
[462] BARATOV, D.G., VASILYEV, A.A., DEMYANENKO, V.N., et al., J. Nucl. Mater. **145-147** (1987) 601.
[463] WAELBROECK, W., WINTER, J., ALI-KHAN, I., et al., Cleaning and Conditioning of the Walls of Plasma Devices by Glow Discharges in Hydrogen, Rep. 1692, KFA, Jülich (1980).
[464] WAELBROECK, W., ESSER, H.G., WINTER, J., et al., J. Nucl. Mater. **145-147** (1987) 665.
[465] ULRICKSON, M., BELL, M.G., BUDNY, R., et al., in Plasma Physics and Controlled Nuclear Fusion Research 1988 (Proc. 12th Int. Conf. Nice, 1988), Vol. 3, IAEA, Vienna (1989) 419.
[466] BOHDANSKY, J., ROTH, J., in Fusion Technology (Proc. 15th Symp. Utrecht, 1988), Elsevier, Amsterdam (1989) 889.
[467] HUGON, M., LALLIA, P., REBUT, P.-H., A Comparison between Beryllium and Graphite as Materials for JET Limiters and Wall Surfaces, Rep. JET-R(89)14, JET Joint Undertaking, Abingdon, Oxfordshire (1989).

[468] THOMPSON, M.W., Philos. Mag. **18** (1968) 377.
[469] GENTLE, K.W., BENGSTON, R.D., BRAVENEC, R., et al., Plasma Phys. Controll. Fusion **26** (1984) 1407.
[470] FUSSMANN, G., Nucl. Fusion **26** (1986) 983.
[471] CASTRACANE, J., DEMERS, Y., MAI, H.H., et al., Plasma Phys. Controll. Fusion **29** (1987) 759.
[472] STRATTON, B.C., RAMSEY, A.T., BOODY, F.P., et al., Nucl. Fusion **27** (1987) 1147.
[473] MARMAR, E.S., RICE, J.E., TERRY, J.L., et al., Nucl. Fusion **22** (1982) 1567.
[474] TFR Group, Phys. Rev. Lett. **36** (1976) 1306.
[475] BURRELL, K.H., WONG, S.K., MULLER, C.H., et al., Nucl. Fusion **21** (1981) 1009.
[476] BEHRINGER, K., ENGELHARDT, W., FUSSMANN, G., in Divertors and Impurity Control (Proc. IAEA Tech. Comm. Mtg Garching, 1981), Max-Planck-Institut für Plasmaphysik, Garching (1981) IC6.
[477] COPPI, B., SHARKY, N., in Physics of Plasmas Close to Thermonuclear Conditions (Proc. Course Varenna, 1978), Rep. EUR-FU-BRU/XI/476/80, CEC, Brussels (1980).
[478] TFR Group, in Plasma Physics and Controlled Nuclear Fusion Research 1982 (Proc. 9th Int. Conf. Baltimore, 1982), Vol. 3, IAEA, Vienna (1983) 219.
[479] HIRSHMAN, S.P., SIGMAR, D.J., Nucl. Fusion **21** (1981) 1079.
[480] STANGEBY, P.C., FARRELL, C., HOSKINS, S., et al., Nucl. Fusion **28** (1988) 1945.
[481] NAGAMI, M., MAEDA, H., KASAI, S., et al., J. Nucl. Mater. **76&77** (1978) 521.
[482] SENGOKU, S., AZUMI, M., MATSUMOTO, Y., et al., Nucl. Fusion **19** (1979) 1327.
[483] PITCHER, C.S., STANGEBY, P.C., Plasma Phys. Controll. Fusion **31** (1989) 1305.
[484] STANGEBY, P.C., FARRELL, C., WOOD, L., Contrib. Plasma Phys. **28** (1988) 501.
[485] STANGEBY, P.C., Contrib. Plasma Phys. **28** (1988) 507.
[486] CLAASSEN, H.A., REPP, H., Nucl. Fusion **21** (1981) 589.
[487] CLAASSEN, H.A., REPP, H., Nucl. Fusion **23** (1983) 597.
[488] CLAASSEN, H.A., GERHAUSER, H., in Controlled Fusion and Plasma Physics (Proc. 12th Eur. Conf. Budapest, 1985), Vol. 9F, Part II, European Physical Society (1985) 460.
[489] CLAASSEN, H.A., GERHAUSER, H., in Controlled Fusion and Plasma Physics (Proc. 14th Eur. Conf. Madrid, 1987), Vol. 11D, Part II, European Physical Society (1987) 752.
[490] KASTELWICZ, M., Contrib. Plasma Phys. **28** (1988) 483.
[491] McCRACKEN, G.M., EHRENBERG, J., STOTT, P.E., et al., J. Nucl. Mater. **145–147** (1987) 621.
[492] TOKAR', M.Z., Nucl. Fusion **25** (1985) 713.
[493] HARBOUR, P.J., MORGAN, J.G., in Controlled Fusion and Plasma Physics (Proc. 11th Eur. Conf. Aachen, 1983), Vol. 7D, Part II, European Physical Society (1983) 427.
[494] BROOKS, J.N., Nucl. Technol./Fusion **4** (1983) 33.
[495] BROOKS, J.N., J. Nucl. Mater. **145–147** (1987) 837.
[496] BROOKS, J.N., PETRAVIC, M., KUO-PETRAVIC, G., Contrib. Plasma Phys. **28** (1988) 465.
[497] DeWALD, A.B., BROOKS, J.N., KRAUSS, A.R., et al., J. Nucl. Mater. **145–147** (1987) 373.
[498] BROOKS, J.N., MATTAS, R.F., HASSENEIN, A.M., et al., J. Nucl. Mater. **128&129** (1984) 400.
[499] McGRATH, R.T., BROOKS, J.N., J. Nucl. Mater. **162–164** (1989) 350.
[500] BROOKS, J.N., BRICE, D.K., DeWALD, A.B., et al., J. Nucl. Mater. **162–164** (1989) 363.
[501] KAWAMURA, T., ONO, T., MASUDA, Y., et al., Contrib. Plasma Phys. **28** (1988) 427.
[502] BRAAMS, B., PhD Thesis, Univ. of Utrecht (1986).
[503] GALKOWSKI, A., ZOGORSKI, R., Contrib. Plasma Phys. **28** (1988) 471.
[504] IGITKHANOV, V., Contrib. Plasma Phys. **28** (1988) 477.
[505] KRASHENINNIKOV, S.I., Contrib. Plasma Phys. **28** (1988) 433.
[506] KRASHENINNIKOV, S.I., KUKUSHKIN, A.S., Contrib. Plasma Phys. **28** (1988) 439.
[507] NEUHAUSER, J., SCHNEIDER, W., WÜNDERLICH, R., et al., Nucl. Fusion **24** (1984) 39.
[508] KRECH, M., NEUHAUSER, J., SCHNEIDER, W., et al., Contrib. Plasma Phys. **28** (1988) 373.
[509] KAUFMANN, M., LACKNER, K., NEUHAUSER, J., et al., Nucl. Fusion **25** (1985) 89.
[510] UEDA, N., ITOH, K., ITOH, S.I., et al., J. Nucl. Mater. **162–164** (1989) 607.
[511] STANGEBY, P.C., FARRELL, C., Plasma Phys. Controll. Fusion, in press.
[512] McCRACKEN, G.M., STANGEBY, P.C., PITCHER, C.S., Contrib. Plasma Phys. **28** (1988) 447.
[513] McCRACKEN, G.M., STANGEBY, P.C., GOODALL, D.H.J., Fusion Eng. Des. **11** (1989) 370.
[514] HACKMANN, J., UHLENBUSCH, J., J. Nucl. Mater. **128&129** (1984) 418.
[515] EDMONDS, P.H., DIETZ, K.J., MIODUSZEWSKI, P.K., et al., J. Vac. Sci. Technol. A **3** (1985) 1100.
[516] THOMAS, P.R., JET Team, "Results of JET operation with beryllium", presented at Int. Conf. on Plasma-Surface Interactions, Bournemouth, 1990; to be published in J. Nucl. Mater.
[517] HWANG, A., STAMP, M.F., SUMMERS, D.D.R., et al., "The impurity, spatial distributions, sputtering yields and power deposition at beryllium and carbon belt limiters in JET", presented at 9th Int. Conf. on Plasma-Surface Interactions, Bournemouth, 1990; to be published in J. Nucl. Mater.
[518] LOWRY, C.G., CAMPBELL, D., GOTTARDI, N., et al., "Density limits in JET with beryllium", presented at 17th Eur. Conf. on Controlled Fusion and Plasma Physics, Amsterdam, 1990, to be published by European Physical Society.
[519] BUREŠ, M., JACQUINOT, J., STAMP, M., et al., ICRF Heating/Plasma Edge Interaction in JET with Be Gettering, Rep. JET-P(89)72, JET Joint Undertaking, Abingdon, Oxfordshire (1989), to be published in Fusion Eng. Des.
[520] EHRENBERG, J., PHILLIPS, V., De KOCK, L., et al., "Analysis of deuterium recycling in JET under beryllium first wall conditions", presented at 9th Int. Conf. on Plasma-Surface Interactions, Bournemouth, 1990; to be published in J. Nucl. Mater.
[521] GONDHALEKAR, A., CHEETHAM, A., ERENTS, S.K., et al., "Impurity control in JET using fueling", presented at 9th Int. Conf. on Plasma-Surface Interactions, Bournemouth, 1990; to be published in J. Nucl. Mater.

[522] SARTORI, R., SAIBENE, G., GOODALL, D.H.J., et al., "Deuterium release measurements in the Be phase of JET and determination of tritium content in the exhaust gas", presented at 9th Int. Conf. on Plasma-Surface Interactions, Bournemouth, 1990; to be published in J. Nucl. Mater.
[523] JONES, P.M.S., GIBSON, R., Hydrogen in Beryllium, AWRE Rep. O-2/67, Atomic Weapons Research Establishment, Aldermaston (1967).
[524] CLEMENT, S., ERENTS, S.K., SAIBENE, G., et al., "Edge fuelling scenarios and scrape-off layer parameters in JET with beryllium limiters", presented at 9th Int. Conf. on Plasma-Surface Interactions, Bournemouth, 1990; to be published in J. Nucl. Mater.
[525] KEILHACKER, M., JET Team, Phys. Fluids (1990), in press.
[526] HUGILL, J., FIELDING, S.J., GILL, R.D., in Controlled Fusion and Plasma Physics (Proc. 8th Eur. Conf. Prague, 1977), Vol. 1, Czechoslovak Academy of Sciences, Prague (1977) 39.
[527] BICKERTON, R.J., Plasma Phys. Controll. Fusion **26** (1984) 1355.
[528] GIBSON, A., WATKINS, M.L., in Controlled Fusion and Plasma Physics (Proc. 8th Eur. Conf. Prague, 1977), Vol. 1, Czechoslovak Academy of Sciences, Prague (1977) 31.
[529] McCRACKEN, G.M., Plasma Phys. Controll. Fusion **29** (1987) 1273.
[530] SMITH, D.L., BROOKS, J.N., POST, D.E., et al., in Engineering Problems in Fusion Research (Proc. 9th Symp. Chicago, 1982), Inst. of Electrical and Electronics Engineers, New York (1982) 719.
[531] ASHBY, D.E.T.F., HUGHES, M.H., Nucl. Fusion **21** (1981) 911.
[532] O'ROURKE, J., CAMPBELL, D., DENNE, B., et al., in Controlled Fusion and Plasma Physics (Proc. 12th Eur. Conf. Budapest, 1985), Vol. 9F, Part I, European Physical Society (1985) 155.
[533] POSPIESZCZYK, A., BAY, H.L., BOGEN, P., et al., J. Nucl. Mater. **145-147** (1987) 574;
SAMM, U., BAY, H., BOGEN, P., et al., Properties of "Detached" Plasmas, Rep. Jül-2123, KFA, Jülich (1987).
[534] STRACHAN, J.D., in Controlled Fusion and Plasma Physics (Proc. 14th Eur. Conf. Madrid, 1987), Vol. 11D, Part I, European Physical Society (1987) 152.
[535] STRACHAN, J.D., BOODY, F.P., BUSH, C., et al., in Controlled Fusion and Plasma Physics (Proc. 12th Eur. Conf. Budapest, 1985), Vol. 9F, Part I, European Physical Society (1985) 339.
[536] BUSH, C.E., STRACHAN, J.D., SCHIVELL, J., et al., Neutral Beam Heating in Detached Plasmas, Rep. PPPL-2616, Princeton Plasma Physics Laboratory, Princeton University, NJ (1989).
[537] LIPSCHULTZ, B., J. Nucl. Mater. **145-147** (1987) 15.
[538] CECCHI, J.L., KNIZE, R.J., DYLLA, H.F., et al., J. Nucl. Mater. **111&112** (1982) 305.
[539] DYLLA, H.F., J. Nucl. Mater. **93&94** (1980) 61.
[540] OREN, L., TAYLOR, R.J., Nucl. Fusion **17** (1977) 1143.
[541] MATSUZUKI, Y., OGAWA, H., MIURA, Y., J. Nucl. Mater. **145-147** (1987) 704.
[542] WINTER, J., WAELBROECK, F., BRANDT, B., et al., J. Nucl. Mater. **93&94** (1980) 812.
[543] WAELBROECK, F., WINTER, J., ALI KHAN, I., et al., Cleaning and Conditioning of the Walls of Plasma Devices by Glow Discharges in Hydrogen, Rep. Jül-1692, KFA, Jülich (1980).
[544] WINTER, J., J. Nucl. Mater. **145-147** (1987) 131;
WINTER, J., Wandkonditionierung von Fusionsanlagen durch reaktive Plasmen, Rep. Jül-2207, KFA, Jülich (1988).
[545] ORCHARD, J. (JET Joint Undertaking, Oxfordshire), personal communication, 1988.
[546] WAMPLER, W.R., DOYLE, B.L., J. Nucl. Mater. **163-165** (1989) 1025.
[547] LANGLEY, R.A., J. Nucl. Mater. **162-164** (1989) 1030.
[548] WAELBROECK, F., WINTER, J., WIENHOLD, P., et al., in Proc. 9th Int. Vacuum Congress and 5th Int. Conf. on Solid Surfaces, Madrid (1983) 693.
[549] ANGUS, J.C., KOIDL, P., DOMITZ, S., in Plasma Deposited Thin Films, CRC Press, Boca Raton, FL (1986) Ch. 4.
[550] STORK, D., JET Joint Undertaking, Abingdon, Oxfordshire, personal communication, 1988.
[551] BARNES, M., JET Joint Undertaking, Abingdon, Oxfordshire, personal communication, 1987.
[552] VEPREK, S., HAGUE, M.R., OSWALD, H.R., J. Nucl. Mater. **63** (1976) 405.
[553] WINTER, J., ESSER, H.G., KONEN, L., et al., J. Nucl. Mater. **162-164,** (1989) 713.
[554] REDHEAD, P., HOBSON, J.P., KORNELSEN, E.V., The Physical Basis of Ultra High Vacuum, Chapman and Hall (1968).
[555] MIODUSZEWSKI, P., J. Nucl. Mater. **128&129** (1984) 884.
[556] DYLLA, H.F., LaMARCHE, P.H., BLANCHARD, W.R., et al., J. Vac. Sci. Technol. A **4** (1986) 1753.
[557] REBUT, P.-H., HUGON, M., BOOTH, S.J., et al., Low Z Material for Limiters and Wall Surfaces in JET: Beryllium and Carbon, Rep. R(85)03, JET Joint Undertaking, Abingdon, Oxfordshire (1985).
[558] MIODUSZEWSKI, P., Nucl. Fusion **26** (1986) 1171.
[559] BOL, K., ARUNASALAM, V., BITTER, M., et al., in Plasma Physics and Controlled Nuclear Fusion Research 1987 (Proc. 7th Int. Conf. Innsbruck, 1978), Vol. 1, IAEA, Vienna (1979) 11.
[560] PFEIFFER, W.W., WALTZ, R.E., Empirical Scaling Laws for Energy Confinement in Ohmically Heated Tokamaks, Rep. GA-A-14727, General Atomic Co., San Diego, CA (1978).
[561] ICHIMURA, K., INOUE, N., ASHIDA, K., et al., J. Nucl. Mater. **128&129** (1984) 876.
[562] LOWRY, C.G., BOYD, D.A., CHALLIS, C.D., in Controlled Fusion and Plasma Physics (Proc. 16th Eur. Conf. Venice, 1989), Vol. 13B, Part I, European Physical Society (1989) 87.
[563] JACQUINOT, J., BHATNAGAR, V., BRUSATI, M., et al., Bull. Am. Phys. Soc. **33** (1988) 2031.
[564] BIEGER, W., DIPPEL, K.H., FÜCHS, G., et al., in Plasma-Wall Interactions (Proc. Int. Symp. Jülich, 1986), Pergamon Press, Oxford (1977) 609.
[565] SCHIVELL, J.G., Method of Plasma Impurity Control without Magnetic Divertor, Rep. PPPL-1342, Princeton Plasma Physics Laboratory, Princeton, NJ (1977).

[566] MATTHEWS, G.F., McCRACKEN, G.M., STANGEBY, P.C., et al., Plasma Phys. Controll. Fusion **29** (1987) 189.
[567] CONN, R.W., SVIATOSLAVSKY, I.N., SZE, D.K., in Engineering Problems of Fusion Research (Proc. 8th Int. Symp. San Francisco, CA, 1979), Vol. 1, IEEE, New York (1979) 568.
[568] MIODUSZEWSKI, P., in Physics of Plasma-Wall Interactions in Controlled Fusion (Proc. NATO Advanced Study Institute Val-Morin, Quebec, 1984), NATO ASI Series, Vol. 131, Plenum Press, New York (1986) 891.
[569] EVANS, K., HEIFETZ, D., POST, D., et al., J. Nucl. Mater. **128&129** (1984) 452.
[570] PONTAU, A.E., GUTHRIE, S.E., MALINOWSKI, M.E., et al., J. Nucl. Mater. **128&129** (1984) 434.
[571] COHEN, S.A., BUDNY, R.V., CORSO, V., et al., J. Nucl. Mater. **128&129** (1984) 430.
[572] FINKEN, K.H., DIPPEL, K.H., REITER, D., et al., J. Nucl. Mater. **145–147** (1987) 825.
[573] CONN, R.W., GOEBEL, D.M., GROTZ, S.P., et al., J. Nucl. Mater. **121** (1984) 350.
[574] GOEBEL, D., CONN, R.W., CORBETT, W.J., et al., J. Nucl. Mater. **162–164** (1989) 115.
[575] INTOR GROUP, International Tokamak Reactor, Phase Two A, Part I (Rep. Int. Workshop Vienna, 1981–1983), IAEA, Vienna (1983) (US Contribution to the Impurity Control Physics, Session IV of the Workshop).
[576] KARGER, F., LACKNER, K., Phys. Lett. A **61** (1977) 385.
[577] DeGRASSIE, J.S., EVANS, T.E., JACKSON, G.L., et al., in Plasma Physics and Controlled Nuclear Fusion Research 1988 (Proc. 12th Int. Conf. Nice, 1988), Vol. 1, IAEA, Vienna (1989) 341.
[578] EVANS, T.E., ADATI, K., ANDO, A., et al., ibid., p. 347.
[579] FENEBERG, W., WOLF, G., Nucl. Fusion **21** (1981) 669.
[580] SAMAIN, A., GROSSMAN, A., FENEBERG, W., J. Nucl. Mater. **111&112** (1982) 408.
[581] DESCHAMPS, P., GROSSMAN, A., LIPA, M., et al., J. Nucl. Mater. **128&129** (1984) 38.
[582] SAMAIN, A., GROSSMAN, A., BLENSKI, T., et al., J. Nucl. Mater. **128&129** (1984) 395.
[583] EVANS, T.E., DeGRASSIE, J.S., JACKSON, G.L., et al., J. Nucl. Mater. **145–147** (1986) 812.
[584] KARGER, F., LACKNER, K., FUSSMANN, G., et al., in Plasma Physics and Controlled Nuclear Fusion Research 1976 (Proc. 6th Int. Conf. Berchtesgaden, 1976), Vol. 1, IAEA, Vienna (1977) 267.
[585] OREN, L., KELLER, L., SCHWIRZKE, F., et al., J. Nucl. Mater. **111&112** (1982) 34.
[586] SENGOKU, S., MATSUDA, T., MATSUMOTO, H., et al., J. Nucl. Mater. **93&94** (1980) 178.
[587] LACKNER, K., KEILHACKER, M., J. Nucl. Mater. **128&129** (1984) 368.
[588] MEADE, D., ARUNASALAM, V., BARNES, C., et al., in Plasma Physics and Controlled Nuclear Fusion Research 1980 (Proc. 8th Int. Conf. Brussels, 1980), Vol. 1, IAEA, Vienna (1981) 665.
[589] MAHDAVI, Ali M., DeBOO, J.C., HSIEH, C.L., et al., Phys. Rev. Lett. **47** (1981) 1602.
[590] SHIMADA, M., NAGAMI, M., IOKI, K., et al., Phys. Rev. Lett. **47** (1981) 796.
[591] POST, D.E., in Plasma Physics and Controlled Nuclear Fusion Research 1988 (Proc. 12th Int. Conf. Nice, 1988), Vol. 3, IAEA, Vienna (1989) 233.
[592] TANGA, A., BEHRINGER, K.H., COSTLEY, A.E., et al., Nucl. Fusion **27** (1987) 1877.
[593] HARBOUR, P.J., SUMMERS, D.D.R., CLEMENT, S., et al., J. Nucl. Mater. **162–164** (1989) 236.
[594] WAGNER, F., Confinement Studies on ASDEX, Rep. IPP-III/131, Max-Planck-Institut für Plasmaphysik, Garching (1988).
[595] BURRELL, K., in Controlled Fusion and Plasma Physics (Proc. 11th Eur. Conf. Aachen, 1983), Vol. 7D, Part I, European Physical Society (1983) 11.
[596] KAYE, S., BELL, M., BOL, K., et al., ibid., p. 19.
[597] OKABAYASHI, M., BEIERSDORFER, P., BOL, K., et al., in Plasma Physics and Controlled Nuclear Fusion Research 1984 (Proc. 10th Int. Conf. London, 1984), Vol. 1, IAEA, Vienna (1985) 229.
[598] HOSOGANE, H., JT-60 Team, J. Nucl. Mater. **162–164** (1989) 93.
[599] SENGOKU, S., JFT-2M Team, J. Nucl. Mater. **145–147** (1987) 556.
[600] BURRELL, K.H., EJIMA, S., SCHISSEL, D.P., et al., Phys. Rev. Lett. **59** (1987) 1432.
[601] SENGOKU, S., FUNAHASHI, A., HASEGAWA, M., et al., Phys. Rev. Lett. **59** (1987) 450.
[602] BURRELL, K.H., ALLEN, S.L., BRAMSON, G., Plasma Phys. Controll. Fusion **31** (1989) 1649.
[603] NEUHAUSER, J., BESSENRODT-WEBERPALS, M., BRAAMS, B.J., et al., Plasma Phys. Controll. Fusion **31** (1989) 1551.
[604] SENGOKU, S., SHIMADA, M., MIYA, N., et al., Nucl. Fusion **24** (1984) 415.
[605] KEILHACKER, M., ALBERT, D.B., BEHRINGER, K., et al., in Plasma Physics and Controlled Nuclear Fusion Research 1980 (Proc. 8th Int. Conf. Brussels, 1980), Vol. 2, IAEA, Vienna (1981) 351.
[606] KEILHACKER, M., Plasma Phys. Controll. Fusion **29** (1987) 1401.
[607] HARBOUR, P.J., Nucl. Fusion **24** (1984) 1211.
[608] INTOR GROUP, International Tokamak Reactor, Phase Two A, Part III (Rep. Int. Workshop Vienna, 1985–1987), Vol. 1, IAEA, Vienna (1988).
[609] HARRISON, M.F.A., HOTSTON, E.S., Critical Issues in European Contributions to the INTOR Phase Two A Workshop, Vol. 2, Appendix 4.3, Advances in Modelling of the Divertor of the Reference Option of NET-DN, Rep. EUR-FU-BRU/XII-139/88/EDVI, CEC, Brussels (1988) III, 131.
[610] NEUHAUSER, J., WÜNDERLICH, R., J. Nucl. Mater. **145–147** (1987) 877.
[611] PETRAVIC, M., HEIFETZ, D.B., KUO-PETRAVIC, G., et al., J. Nucl. Mater. **145–147** (1987) 841.
[612] OHYABU, N., DeGRASSIE, J.S., EVANS, T.E., J. Nucl. Mater. **145–147** (1987) 844.
[613] PARBHAKER, K.J., POST, D.E., J. Nucl. Mater. **145–147** (1987) 864.
[614] UEDA, N., ITOH, K., ITOH, S.I., et al., J. Nucl. Mater. **162–164** (1989) 607.
[615] CHODURA, R., Contrib. Plasma Phys. **28** (1988) 303.
[616] UEDA, N., KASAI, M., TANAKA, M., et al., Nucl. Fusion **28** (1988) 1183.

[617] POST, D.E., HEIFETZ, D.B., PETRAVIC, M., J. Nucl. Mater. **111&112** (1982) 383.
[618] HARBOUR, P.J., MORGAN, J.G., Models and Codes for the Plasma Edge Region, Rep. CLM-R234, UKAEA, Culham Lab., Abingdon, Oxfordshire (1982).
[619] SPITZER, L., Physics of Fully Ionized Gases, Wiley, New York (1962).
[620] PROUDFOOT, G., HARBOUR, P.J., ALLEN, J., et al., J. Nucl. Mater. **128&129** (1984) 180.
[621] ITOH, S.I., ITOH, K., Model of H/L Transition in Tokamak, Res. Rep. HIFT-141, Hiroshima Univ. (1987).
[622] MÜLLER, E.R., BEHRINGER, K., NIEDERMEYER, H., Nucl. Fusion **22** (1982) 1651.
[623] MÜLLER, E.R., KEILHACKER, M., STEINMETZ, K., et al., J. Nucl. Mater. **121** (1984) 138.
[624] BELL, M.G., FONCK, R.J., GREK, B., et al., J. Nucl. Mater. **121** (1984) 132.
[625] SHIMADA, M., NAGAMI, M., IOKI, K., et al., Nucl. Fusion **22** (1982) 643.
[626] SCHNEIDER, W., NEUHAUSER, J., HAAS, G., Contrib. Plasma Phys. **28** (1988) 387.
[627] ALLEN, S.L., RENSINK, M.E., HILL, D.N., J. Nucl. Mater. **162-164** (1989) 80.
[628] DeBOO, J.C., BROOKS, N.H., DeGRASSIE, J.S., et al., Nucl. Fusion **22** (1982) 572.
[629] MIYA, M., NAKAMURA, H., TSUJI, S., et al., J. Nucl. Mater. **162-164** (1989) 618.
[630] HOSHINO, K., YAMAMOTO, T., SUZUKI, N., et al., Nucl. Fusion **28** (1988) 301.
[631] OWENS, D.K., ARUNASALAM, V., BARNES, C., et al., J. Nucl. Mater. **93&94** (1980) 213.
[632] NAGAMI, M., FUJISAWA, N., IOKI, K., et al., in Plasma Physics and Controlled Nuclear Fusion Research 1980 (Proc. 8th Int. Conf. Brussels, 1980), Vol. 2, IAEA, Vienna (1981) 367.
[633] BREVNOV, N.N., VERTIPOROKH, A.N., DYABILIN, K.S., et al., Sov. J. Plasma Phys. **8** (1982) 36.
[634] VERNICKEL, H., BEHRINGER, K., CAMPBELL, D., et al., J. Nucl. Mater. **111&112** (1982) 317.
[635] FONCK, R.J., BELL, M., BOL, K., et al., J. Nucl. Mater. **111&112** (1982) 343.
[636] FONCK, R.J., BELL, M., BOL, K., et al., J. Nucl. Mater. **128&129** (1984) 330.
[637] FUSSMANN, G., POSCHENRIEDER, W., BERNHARDI, K., et al., J. Nucl. Mater. **121** (1984) 164.
[638] JANESCHITZ, G., FUSSMANN, G., KOTZÉ, P.B., et al., Nucl. Fusion **26** (1986) 1725.
[639] JANESCHITZ, G., FUSSMANN, G., HOFMANN, J., et al., J. Nucl. Mater. **162-164** (1989) 624.
[640] WANG, Wen-Min, ROTH, J., BEHRISCH, R., et al., J. Nucl. Mater. **162-164** (1989) 422.
[641] WAGNER, F., BECKER, G., BEHRINGER, K., et al., in Plasma Physics and Controlled Nuclear Fusion Research 1982 (Proc. 9th Int. Conf. Baltimore, 1982), Vol. 1, IAEA, Vienna (1983) 43.
[642] DENNE, B., BEHRINGER, K., EDWARDS, A. (JET Joint Undertaking, Abingdon, Oxfordshire), personal communication, 1988.
[643] SESNIC, S.S., FONCK, R.J., IDA, K., et al., J. Nucl. Mater. **145-147** (1987) 580.
[644] STAUDENMAIER, G., WAMPLER, W.R., J. Nucl. Mater. **162-164** (1989) 414.
[645] JACKSON, G.L., TAYLOR, T.S., ALLEN, S.L., et al., J. Nucl. Mater. **162-164** (1989) 489.
[646] BRAGINSKII, S.I., in Reviews of Plasma Physics, Vol. 1 (LEONTOVICH, M., Ed.), Consultants Bureau, New York (1965) 205.
[647] PETRAVIC, M., HEIFETZ, D., HEIFETZ, S., et al., J. Nucl. Mater. **128&129** (1984) 91.
[648] BRAAMS, B.J., Modelling of a Transport Problem in Plasma Physics, Rep. CLM-P725, UKAEA, Culham Laboratory, Abingdon, Oxfordshire (1984).
[649] WAGNER, F.W., BECKER, G., BEHRINGER, K., et al., Phys. Rev. Lett. **49** (1982) 1408.
[650] BURRELL, K.H., ALLEN, S.L., BRAMSON, G., in Plasma Physics and Controlled Nuclear Fusion Research 1988 (Proc. 12th Int. Conf. Nice, 1988), Vol. 1, IAEA, Vienna (1989) 193.
[651] SUZUKI, N., MIURA, Y., HASEGAWA, M., in Controlled Fusion and Plasma Physics (Proc. 14th Eur. Conf. Madrid, 1987), Vol. 11D, Part I, European Physical Society (1987) 217.
[652] TANGA, A., BARTLETT, D., BURES, M., et al., in Controlled Fusion and Plasma Heating (Proc. 15th Eur. Conf. Dubrovnik, 1988), Vol. 12B, Part I, European Physical Society (1988) 235.
[653] WAGNER, F., KEILHACKER, M., J. Nucl. Mater. **121** (1984) 103.
[654] OHYABU, N., BURRELL, K.H., CARLSTROM, T.N., et al., in Controlled Fusion and Plasma Heating (Proc. 15th Eur. Conf. Dubrovnik, 1988), Vol. 12B, Part I, European Physical Society (1988) 227.
[655] LACKNER, K., Plasma Phys. Controll. Fusion **31** (1989) 1629.
[656] MAHDAVI, Ali M. (General Atomics, San Diego, CA), personal communication, 1988.
[657] BECKER, G., in Controlled Fusion and Plasma Heating (Proc. 15th Eur. Conf. Dubrovnik, 1988), Vol. 12B, Part I, European Physical Society (1988) 211.
[658] KEILHACKER, M., BALET, B., CORDEY, J., et al., ibid., p. 231.
[659] KAYE, S.M., BELL, M.G., BOL, K., et al., J. Nucl. Mater. **121** (1984) 115.
[660] OHKAWA, T., CHU, M.S., HINTON, F.L., Phys. Rev. Lett. **51** (1983) 2101.
[661] HINTON, F.L., Nucl. Fusion **25** (1985) 1457.
[662] OHYABU, N., LEE, J.K., DeGRASSIE, J.S., Nucl. Fusion **26** (1986) 593.
[663] BISHOP, C.M., Nucl. Fusion **26** (1986) 1063.
[664] SENGOKU, S., ABE, M., HOSHINO, K., et al., in Plasma Physics and Controlled Nuclear Fusion Research 1984 (Proc. 10th Int. Conf. London, 1984), Vol. 1, IAEA, Vienna (1985) 405.
[665] JACKSON, G.L., TAYLOR, T.S., ALLEN, S.L., et al., J. Nucl. Mater. **162-164** (1989) 489.
[666] HAAS, G., POSCHENRIEDER, W., NEUHAUSER, J., et al., J. Nucl. Mater. **162-164** (1989) 509.
[667] REBUT, P.-H., WATKINS, M.L., LALLIA, P.P., in Controlled Fusion and Plasma Heating (Proc. 15th Eur. Conf. Dubrovnik, 1988), Vol. 12B, Part I, European Physical Society (1988) 247.

[668] KAUFMANN, M., BUCHL, K., FUSSMANN, G., et al., Nucl. Fusion **28** (1988) 827.
[669] SCHISSEL, D.P., BAUR, J., BRAMSON, G., Nucl. Fusion **27** (1987) 1063.
[670] HARRISON, M.F.A., HOTSTON, E.S., DeMATTEIS, A., Plasma Edge Physics for NET/INTOR, Rep. EUR-FU/XII-361/86/50, CEC, Brussels (1986).
[671] BRAAMS, B.J., HARBOUR, P.J., HARRISON, M.F.A., et al., J. Nucl. Mater. **121** (1984) 75.
[672] COOKE, P.I.H., PRINJA, A.K., Nucl. Fusion **27** (1987) 1165.
[673] GIERSZEWSKI, P.J., Plasma/Neutral Gas Transport in Divertors and Limiters, Rep. PFC/RR-83-28, Massachusetts Institute of Technology, Cambridge (1983).
[674] TACHON, J., in Physics of Plasma-Wall Interactions in Controlled Fusion (Proc. NATO Advanced Study Institute Val-Morin, Quebec, 1984), NATO ASI Series, Vol. 131, Plenum Press, New York (1986) 1005.
[675] COHEN, S.A., BERNABEI, S., BUDNY, R., et al., J. Nucl. Mater. **128&129** (1984) 280.
[676] TFR Group, Plasma Phys. Controll. Fusion **25** (1984) 165.
[677] TAGLE, J.A., ERENTS, S.K., BUREŠ, M., J. Nucl. Mater. **162–164** (1989) 282.
[678] TFR Group, Plasma Phys. Controll. Fusion **26** (1984) 1141.
[679] TFR Group, J. Nucl. Mater. **128&129** (1984) 292.
[680] HSUAN, H., HAWRYLUK, R.J., SUCKEWER, S., et al., in Radiofrequency Plasma Heating (Proc. 3rd Top. Conf. Pasadena, CA, 1978), UCLA Press, Pasadena (1978) C8.
[681] NODA, N., J. Nucl. Mater. **128&129** (1984) 304.
[682] ARTEMENKOV, L.I., VUKOLOV, K.Yu., GOTT, Yu.V., et al., in Controlled Fusion and Plasma Heating (Proc. 15th Eur. Conf. Dubrovnik, 1988), Vol. 12B, Part II, European Physical Society (1988) 702.
[683] MESSIAEN, A.M., BHATNAGAR, V.P., DELVIGNE, T., et al., Plasma Phys. Controll. Fusion **28** (1986) 71.
[684] GOEBEL, D.M., CORBETT, W.J., CONN, R.W., in Controlled Fusion and Plasma Heating (Proc. 15th Eur. Conf. Dubrovnik, 1988), Vol. 12B, Part II, European Physical Society (1988) 667.
[685] MANNING, H.L., TERRY, J.L., LIPSCHULTZ, B., et al., Nucl. Fusion **26** (1986) 1665.
[686] WAN, A.S., LIPSCHULTZ, B., McDERMOTT, F.S., et al., J. Nucl. Mater. **162–164** (1989) 292.
[687] BURES, M., BRINKSCHULTE, H., JACQUINOT, J., et al., Plasma Phys. Controll. Fusion **30** (1988) 149.
[688] OGAWA, H., ODAJIMA, K., OHTSUKA, H., et al., J. Nucl. Mater. **128&129** (1984) 298.
[689] HILDEBRANDT, D., GRÖTE, H., HERRMANN, A., in Controlled Fusion and Plasma Physics (Proc. 12th Eur. Conf. Budapest, 1985), Vol. 9F, Part II, European Physical Society (1985) 615.
[690] BURES, M., BHATNAGAR, V.P., JACQUINOT, J., et al., Density Behaviour and Particle Influxes During ICRF Heating of Limiter Discharges in JET, Rep. JET-P(88)03, JET Joint Undertaking, Abingdon, Oxfordshire (1988).
[691] TFR Group, TERREAULT, B., Rep. EUR-CEA-FC-120, CEC, Brussels (1984).
[692] SAMM, U., BAY, H.L., BOGEN, P., et al., Plasma Phys. Controll. Fusion **29** (1987) 132.
[693] START, D.F.H., BHATNAGAR, V., BUREŠ, M., et al., in Controlled Fusion and Plasma Heating (Proc. 15th Eur. Conf. Dubrovnik, 1988), Vol. 12B, Part I, European Physical Society (1988) 354.
[694] JET Team, STOTT, P.E., J. Nucl. Mater. **162–164** (1989) 3.
[695] MANOS, D.M., STANGEBY, P.C., BUDNY, R.V., et al., J. Nucl. Mater. **128&129** (1984) 319.
[696] BRINKSCHULTE, H., CLEMENT, S., COAD, J.P., et al., in Controlled Fusion and Plasma Heating (Proc. 15th Eur. Conf. Dubrovnik, 1988), Vol. 12B, Part I, European Physical Society (1988) 659.
[697] KIMURA, H., MATSUMOTO, H., ODAJIMA, K., et al., in Plasma Physics and Controlled Nuclear Fusion Research 1982 (Proc. 9th Int. Conf. Baltimore, 1982), Vol. 2, IAEA, Vienna (1983) 113.
[698] NOTERDAEME, J.M., JANESCHITZ, G., McCORMICK, K., et al., in Controlled Fusion and Plasma Physics (Proc. 14th Eur. Conf. Madrid, 1987), Vol. 11D, Part II, European Physical Society (1987) 678.
[699] STRATTON, B., Nucl. Fusion **24** (1984) 767.
[700] CAUGHMANN, J.B.O., RUZIC, D.N., HOFFMAN, D.J., J. Vac. Sci. Technol. A **5** (1987) 2301.
[701] VAN NIEUWENHOVE, R., VAN OOST, G., J. Nucl. Mater. **162–164** (1989) 288.
[702] TAYLOR, R.J., EVANS, J., KELLER, L., et al., in Plasma Physics and Controlled Nuclear Fusion Research 1984 (Proc. 10th Int. Conf. London, 1984), Vol. 1, IAEA, Vienna (1985) 581.
[703] GRIGOR'EVA, L.I., PASHCHENKO, A.V., SMERDOV, B.I., et al., J. Nucl. Mater. **128&129** (1984) 317.
[704] ITOH, S.I., FUKUYAMA, A., GOTO, A., et al., in Heating in Toroidal Plasmas (Proc. 4th Int. Symp. Rome, 1984), Vol. 1, International School of Plasma Physics, Varenna (1984) 407.
[705] TFR Group, ibid., Vol. 1, p. 277.
[706] ODAJIMA, K., MATSUMOTO, H., KIMURA, H., et al., ibid., p. 243.
[707] TFR Group, in Controlled Fusion and Plasma Physics (Proc. 11th Eur. Conf. Aachen, 1983), Vol. 7D, Part I, European Physical Society (1983) 165.
[708] SHMAYDA, W.T., WINTER, J., WAELBROECK, F., et al., J. Nucl. Mater. **145–147** (1987) 201.
[709] TFR Group, SAND, F., Nucl. Fusion **25** (1985) 1719.
[710] MANOS, D.M., KILPATRICK, S.J., BELL, M.G., J. Nucl. Mater. **162–164** (1989) 251.
[711] KILPATRICK, S.J., MANOS, D.M., BUDNY, R.V., et al., J. Vac. Sci. Technol. A **4** (1986) 1817.
[712] BUDNY, R.V., HEIFETZ, D.B., KILPATRICK, S.J., et al., J. Nucl. Mater. **145–147** (1987) 245.
[713] JET TEAM, in Plasma Physics and Controlled Nuclear Fusion Research 1988 (Proc. 12th Int. Conf. Nice, 1988), Vol. 1, IAEA, Vienna (1989) 247.
[714] ERENTS, S.K., TAGLE, J.A., McCRACKEN, G.M., in Controlled Fusion and Plasma Physics (Proc. 14th Eur. Conf. Madrid, 1987), Vol. 11D, Part II, European Physical Society (1987) 740.
[715] TFR Group, J. Nucl. Mater. **105** (1982) 62.
[716] PETRIE, T.W., ARMENTROUT, C., BURRELL, K.H., et al., J. Nucl. Mater. **128&129** (1984) 487.

[717] BUSH, C.E., BATES, S.C., DUNLOP, J.L., et al., Nucl. Fusion **23** (1983) 67.
[718] McCORMICK, G.K., PIETRZYK, Z.A., ASDEX Team, J. Nucl. Mater. **162–164** (1989) 264.
[719] McCORMICK, G.K., PIETRZYK, Z.A., MURMANN, H., et al., in Controlled Fusion and Plasma Physics (Proc. 14th Eur. Conf. Madrid, 1987), Vol. 11D, Part II, European Physical Society (1987) 666.
[720] KAHN, C., BURRELL, K.H., FAIRBANKS, E., et al., J. Nucl. Mater. **128&129** (1984) 172.
[721] PITTS, R.A., MATTHEWS, G.F., McCRACKEN, G.M., J. Nucl. Mater. **162–164** (1989) 276.
[722] De CHAMBRIER, A., COLLINS, G.A., DUPERREX, P.-A., et al., J. Nucl. Mater. **128&129** (1984) 310.
[723] MARTIN, Y., HOLLENSTEIN, Ch., in Controlled Fusion and Plasma Heating (Proc. 15th Eur. Conf. Dubrovnik, 1988), Vol. 12B, Part II, European Physical Society (1988) 687.
[724] HOFMANN, F., HOLLENSTEIN, Ch., JOYE, B., et al., J. Nucl. Mater. **121** (1984) 22.
[725] HOLLENSTEIN, Ch., MARTIN, Y., SIMM, W., J. Nucl. Mater. **145–147** (1987) 260.
[726] MARTIN, Y., HOLLENSTEIN, Ch., J. Nucl. Mater. **162–164** (1989) 270.
[727] MARMAR, E., FOORD, M., LaBOMBARD, B., et al., J. Nucl. Mater. **121** (1984) 69.
[728] CLEMENT, M., ICHTCHENKO, G., HESS, W., and Petula Group, in Heating in Toroidal Plasmas (Proc. 4th Int. Symp. Rome, 1984), Vol. 1, International School of Plasma Physics, Varenna (1984) 634.
[729] MARMAR, E., FOORD, M., LaBOMBARD, B., et al., J. Nucl. Mater. **121** (1984) 69.
[730] MANOS, D.M., BUDNY, R.V., KILPATRICK, S., et al., Rev. Sci. Instrum. **57** (1986) 2107.
[731] PERICOLI RIDOLFINI, V., Plasma Phys. Controll. Fusion **27** (1985) 709.
[732] CESARIO, R., McWILLIAMS, R., PERICOLI RIDOLFINI, V., in Controlled Fusion and Plasma Heating (Proc. 15th Eur. Conf. Dubrovnik, 1988), Vol. 12B, Part III, European Physical Society (1988) 896.
[733] LENOCI, M., HAAS, G., BECKER, G., et al., in Controlled Fusion and Plasma Heating (Proc. 13th Eur. Conf. Schliersee, 1986), Vol. 10C, Part II, European Physical Society (1986) 397.
[734] MATSUMOTO, K., OHKUBO, K., ibid., p. 429.
[735] UEHARA, K., FUJISAWA, N., YAMAMOTO, T., et al., J. Phys. Soc. Jpn **48** (1980) 1333.
[736] LIEWER, P.C., Nucl. Fusion **25** (1985) 543.
[737] ROBINSON, D.C., in Turbulence and Anomalous Transport in Magnetized Plasmas, Editions de Physique, Les Ulis (1986) 21.
[738] SURKO, C.M., in Turbulence and Anomalous Transport in Magnetized Plasmas, Editions de Physique, Les Ulis (1986) 93.
[739] RITZ, C.P., BRAVENEC, R.V., BENGSTON, R.D., et al., J. Nucl. Mater. **145–147** (1987) 241.
[740] RECHESTER, A.B., ROSENBLUTH, M.N., Phys. Rev. Lett. **40** (1978) 38.
[741] LEVINSON, S.J., BEALL, J.M., POWERS, E.J., et al., Nucl. Fusion **24** (1984) 527.
[742] ROBINSON, D.C., RUSBRIDGE, M.G., Plasma Phys. **11** (1969) 73.
[743] ZWEBEN, S.J., MENYUK, C.R., TAYLOR, R.J., Phys. Rev. Lett. **42** (1979) 1270.
[744] ZWEBEN, S.J., LIEWER, P.C., GOULD, R.W., et al., J. Nucl. Mater. **111&112** (1982) 39.
[745] ZWEBEN, S.J., GOULD, R.W., Nucl. Fusion **25** (1985) 171.
[746] RITZ, C.P., BROWER, D.L., RHODES, T.L., et al., Nucl. Fusion **27** (1987) 1125.
[747] LIEWER, P.C., McCHESNEY, J.M., ZWEBEN, S.J., et al., Phys. Fluids **29** (1986) 309.
[748] WOOTTON, A.J., HOWE, H., EDMONDS, P.H., et al., Electrostatic Fluctuations and Transport in the Edge of the ISX-B Tokamak, Rep. ORNL/TM-9305, Oak Ridge National Laboratory, TN (1986).
[749] BENGSTON, R.D. (Univ. of Texas, Austin), personal communication, 1988.
[750] DUPERREX, P.A., HOLLENSTEIN, Ch., JOYE, B., et al., Phys. Lett. A **106** (1984) 133.
[751] SAMM, U., BOGEN, P., CLAASSEN, H.A., et al., J. Nucl. Mater. **145–147** (1987) 206.
[752] GÜNTHER, K., HAYESS, E., KREBS, K.H., et al., J. Nucl. Mater. **162–164** (1989) 562.
[753] HILDEBRANDT, D., JUTTNER, B., JAKUBKA, K., et al., Contrib. Plasma Phys. **27** (1987) 455.
[754] BUDNY, R., BELL, M.G., BOL, K., et al., J. Nucl. Mater. **121** (1984) 294.
[755] MIRNOV, S.V., Sov. J. Plasma Phys. **7** (1981) 376.
[756] WIENHOLD, P., WAELBROECK, F., BERGSÅKER, H., et al., J. Nucl. Mater. **162–164** (1989) 369.
[757] HILDEBRANDT, D., J. Nucl. Mater. **145–147** (1987) 606.
[758] GROTE, H., WASA Team, J. Nucl. Mater. **162–164** (1989) 51.
[759] MADDALUNO, G., MARTINELLI, A.P., J. Nucl. Mater. **162–164** (1989) 430.
[760] FRANCONI, E., BROSSA, F., J. Nucl. Mater. **145–147** (1987) 691.
[761] HOLLENSTEIN, Ch., VEPREK, S., RAMBERT, S., J. Nucl. Mater. **145–147** (1987) 717.
[762] CHANG, J., TOBIN, A., MANOS, D., J. Nucl. Mater. **111&112** (1982) 168.
[763] WOLFF, H., GROTE, H., HERRMANN, A., et al., J. Nucl. Mater. **145–147** (1987) 671.
[764] WOLFF, H., GROTE, H., HILDEBRANDT, D., et al., J. Nucl. Mater. **128&129** (1984) 219.
[765] MARTINELLI, A.P., BEHRISCH, R., HAMMER, H., et al., J. Nucl. Mater. **145–147** (1987) 755.
[766] TAYLOR, T., BROOKS, N., IOKI, K., J. Nucl. Mater. **111&112** (1982) 569.
[767] PITCHER, C.S., GOODALL, D.H.J., MATTHEWS, G.F., et al., in Controlled Fusion and Plasma Physics (Proc. 14th Eur. Conf. Madrid, 1987), Vol. 11D, Part II, European Physical Society (1987) 736.
[768] CHANKIN, A.V., VERSHKOV, V.A., J. Nucl. Mater. **162–164** (1989) 208.
[769] ROWAN, W.L., KLEPPER, C.C., PATTERSON, D.M., et al., J. Nucl. Mater. **145–147** (1987) 562.
HILL, D.N., PETRIE, T., ALI MAHDAVI, M., et al., Nucl. Fusion 28 (1988) 902.

[770] GÜNTHER, K., GRUNOW, C., LINGERTAT, J., in Controlled Fusion and Plasma Physics (Proc. 12th Eur. Conf. Budapest, 1985), Vol. 9F, Part II, European Physical Society (1985) 567.
[771] VLASOV, V.P., GRUNOV, C., GÜNTHER, K., et al., Sov. J. Plasma Phys. **13** (1987) 369.
[772] BOGEN, P., HARTWIG, H., HINTZ, E., in Controlled Fusion and Plasma Physics (Proc. 12th Eur. Conf. Budapest, 1985), Vol. 9F, Part II, European Physical Society (1985) 527.
[773] HILDEBRANDT, D., GROTE, H., HERMANN, A., et al., Contrib. Plasma Phys. **28** (1988) 85.
[774] GOODALL, D.H.J., J. Nucl. Mater. **111&112** (1982) 11.
[775] PICK, M.A., SUMMERS, D.D.R., J. Nucl. Mater. **128&129** (1984) 440.
[776] LOWRY, C.G. (JET Joint Undertaking, Abingdon, Oxfordshire), personal communication, 1986.
[777] BERGSÅKER, H., BEHRISCH, R., COAD, J.P., et al., J. Nucl. Mater. **145–147** (1987) 727.
[778] McCRACKEN, G.M., GOODALL, D.H.J., STANGEBY, P.C., J. Nucl. Mater. **162–164** (1989) 356.
[779] GOTTARDI, N., KRAUSE, H., MAST, K.F., in Controlled Fusion and Plasma Physics (Proc. 12th Eur. Conf. Budapest, 1985), Vol. 9F, Part I, European Physical Society (1985) 30.
[780] FINKEN, K.H., WATKINS, J.G., McGRATH, R.T., et al., J. Nucl. Mater. **162–164** (1989) 655.
[781] FINKEN, K.H., WATKINS, J.G., CORBETT, W.J., in Controlled Fusion and Plasma Heating (Proc. 15th Eur. Conf. Dubrovnik, 1988), Vol. 12B, Part II, European Physical Society (1988) 663.
[782] FENEBERG, W., ZANINO, R., in Controlled Fusion and Plasma Physics (Proc. 14th Eur. Conf. Madrid, 1987), Vol. 11D, Part II, European Physical Society (1987) 748.
[783] BURRELL, K.H., WONG, S.K., Nucl. Fusion **19** (1979) 1571.
[784] PHILIPPS, V., ERDWEG, M., VIETZKE, E., J. Nucl. Mater. **128&129** (1984) 199.
[785] SATAKE, T., MOHRI, M., YAMASHINA, T., et al., J. Nucl. Mater. **128&129** (1984) 190.
[786] SOBELMAN, I., VAINSHTEIN, L.A., YUKOV, E.A., Excitation of Atoms and Broadening of Spectral Lines, Springer-Verlag, Berlin (1981).
[787] POSPIESZCZYK, A. (KFA, Jülich), personal communication, 1989.
[788] BELL, K.L., GILBODY, H.B., HUGHES, J.G., et al., Atomic and Molecular Data for Fusion, Part I. Recommended Cross-Sections and Rates for Electron Ionization of Light Atoms and Ions, Rep. CLM R216, UKAEA, Culham Laboratory, Abingdon, Oxfordshire (1982).
[789] ARATARI, R., ECKSTEIN, W., Nucl. Instrum. Methods, Phys. Res., B **42** (1989) 11.
[790] ARATARI, R., ECKSTEIN, W., J. Nucl. Mater. **162–164** (1989) 910.
[791] ANDERSEN, H.H., BAY, H.L., in Sputtering by Particle Bombardment, Vol. 1, Springer-Verlag, Berlin (1981).
[792] PROUDFOOT, G., HARBOUR, P.J., J. Nucl. Mater. **111&112** (1982) 87.

LIST OF SYMBOLS*

Symbol	Section**	Definition
a	2.1	minor radius (horizontal) of tokamak plasma
b	5.1	minor radius (vertical) of tokamak plasma
b_r	2.2.5	branching ratio (atomic levels)
c	2.2.4	velocity of light
$\bar{c}_e$	2.2.1	thermal electron velocity, $(8kT_e/\pi m_e)^{1/2}$
$\bar{c}_i$	2.2.1	thermal ion velocity, $(8kT_i/\pi m_i)^{1/2}$
c_s	2.2.1	ion acoustic velocity, $\approx (k(T_e + T_i)/m_i)^{1/2}$
c_{so}	3.4	ion acoustic velocity at the LCFS
d	2.2.1	characteristic size of the probe
e	2.2.1	unit electrical charge
f	4.6	$\bar{n}_i/n_{pi}$
f_g	4.1	τ_E/τ_{EL}
f_n	4.1	$\hat{n}/\bar{n}$
f_T	4.1	$\hat{T}/\bar{T}$

* Symbols which appear only once or twice in a local context and some obvious, well known symbols are not included in this list.
** Section where the symbol appears first.

Symbol	Section	Definition
$\ell_{e,i}$	2.2.1	electron, ion Larmor radius
$m_{e,i}$	2.2.1	electron, ion mass
m_{imp}	5.2	impurity ion mass
$\hat{n}$	4.1	central plasma density (peak)
n_a	2.2.2	atom density
n_c	2.2.4	cut-off density for wave propagation
n_d	7.3.2	plasma density at divertor plate
n_e	1	electron density
$\bar{n}_e$	2.1	average electron density for complete plasma
n_{ec}	6.2	upper (disruption) limit to the plasma density
n_{em}	6.5	plasma density for Marfe formation
$n_{e\infty}$	2.2.1	electron density far from the surface of the probe
n_{H^0}	2	neutral hydrogen density
n_i	2.2.1	ion density
n_{imp}	2	impurity density
n_{LCFS}	2.1	plasma density at the LCFS (far from the limiter)
n_n	3.2	neutral density
n_0	3.2	plasma density far from the solid surface
n_{pi}	4.6	ion plateau density (central density if $v_{in} = 0$)
n_{se}	3.2	plasma density at the sheath edge
n_u	7.3.2	plasma density upstream from the divertor
p_i	2.2.1	ion pressure
q	3.1	safety factor of the tokamak
q_{cyl}	5.1	cylindrical safety factor
$q^{ES,EM}_{cond,conv}$	9	electrostatic/electromagnetic cross-field flux density conducted/convected owing to fluctuations
q^i	3.2	ion heat conduction flux density
r	2.1	minor radial co-ordinate
r'	2.2.1	reduction factor for electron collection of the probe
r_w	3.4	radial location of the wall
s	2.2.6	saturation parameter
s_h	2.2.8	specific heat
v	3.2	plasma fluid velocity along $\vec{B}$
v_a	2.2.2	atom velocity
v_D	3.6.1	deuterium neutral velocity
$v_{e,i}$	2.2.1	specific electron, ion velocity
v_{in}	4.1	inward drift (pinch) velocity of the plasma
v_{se}	3.2	plasma flow velocity at the sheath edge
v_0	4.6	effective neutral velocity for edge refuelling
w	4.2	wetted length of limiter
x	3.2	co-ordinate along $\vec{B}$
A_{cp}	5.1	cross-sectional area of the tokamak plasma, πab
A_{eff}	2.2.1	effective collection area of the probe
A_{LP}	3.5	limiter area for heat flux
$A_{L\Gamma}$	3.5	limiter area for particle flux
A_p	4.6	plasma surface area of the tokamak, $2\pi R_m\, 2\pi a$
A_{pr}	2.2.1	nominal collection area of the probe
A_{SOL}	7.3.2	cross-sectional area of the SOL perpendicular to $\vec{B}$
$A_\perp$	2.2.1	projected area of the probe
B	2	magnetic field

Symbol	Section	Definition
B_p	4	poloidal magnetic field
B_T	2.1	toroidal magnetic field
$\tilde{B}_r$	9	fluctuating radial magnetic field
$D_\perp$	2.2.1	cross-field particle diffusion coefficient
$D_\perp^{amb}$	2.2.1	ambipolar value of $D_\perp$
$D_\perp^{Bohm}$	2.2.1	Bohm value of $D_\perp$
$D_\perp^e$	2.2.1	electron value of $D_\perp$
$D_{\perp 0}$	3.4	value of $D_\perp$ at the LCFS
$D_\parallel^e$	2.2.1	parallel electron diffusion coefficient
E	3.2	electric field
E_f	4.3	atom energy from molecular dissociation
E_{max}	5.4	maximum energy of sputtered particle
E_0	4.3	ion impact energy on the surface
E_T	6.2	threshold impact energy for sputtering
$\tilde{E}_\theta$	9	fluctuating poloidal electric field
F	4.7	fuelling ratio, N_e^p/N_e^{in}
F_d	7.3.2	divertor factor indicating temperature gradient
F_{ex}	7.2.2	fraction of the particle flux entering the pumped limiter
F_p	7.3.2	fraction of the divertor power reaching the plate
F_{rad}	6.2	fraction of the input power radiated away, P_R/P_T
F_R	3.6.1	ionization recycle factor
I	2.2.1	current (probe)
I_d	7.3.1	divertor coil current
I_p	2.1	plasma current
$I^{+,-}$	2.2.1	ion, electron current (probe)
$I_s^{+,-}$	2.1	ion, electron saturation current (probe)
I_{ph}	2.2.2	intensity of photon emission
L_c	2.1	connection length in the SOL
L_{cp}	2.2.1	connection length of the probe
L_p	2.2.1	collection length (ambipolar) of the probe
L_p^e	2.2.1	electron collection length of the probe
$L_z(T_e)$	3.6.2	radiative cooling rate of impurity
LCFS	1	last closed flux surface
M	3.2	Mach number of plasma fluid, v/c_s
Mur	5.1	Murakami parameter
N	4.1	total number of particles in the plasma
N_e^{in}	4.7	total electron input into the tokamak
N_e^p	4.7	total number of electrons in the plasma
P_c	6.2	power conducted/convected to the edge
$P_c^{e,i}$	3.3	energy flux density of heat removal from the plasma electrons, ions by the sheath
P_F	5.1	fusion power output
P_ℓ	4.1	total power input into the tokamak per unit toroidal length
P_{pen}	5.5.4	penetration probability for impurities
P_R	2	power radiated from the tokamak
$P_{se}^{e,i}$	3.3	electron, ion heat flux density at the sheath edge
P_T	3.5	total power input into the tokamak
Q	6.3	power conducted from the centre
R	2	major radial co-ordinate
$\bar{R}$	4.2	global recycling coefficient of the tokamak

Symbol	Section	Definition
R_E	4.3	energy reflection coefficient
R_N	4.3	ion reflection coefficient
R_m	2.1	major radius of the magnetic axis of the tokamak
R_Ω	6.4	plasma resistance per unit length
Rf	5.5.4	impurity reduction factor of the SOL
S	4.6	plasma inward drift parameter
$S_{C,E}$	4.7	total core, edge fuelling rate
S_p	3.2	particle source strength density
SOL	1	Scrape-off layer
Sol	4.7	hydrogen solubility in the solid
T_d	7.3.2	plasma temperature at the divertor plate
T_e	1	electron temperature
$T_{es,is}$	3.3	electron, ion temperature at the sheath edge
T_i	1	ion temperature
T_{LCFS}	2.1	temperature at the LCFS
T_m	3.6.3	temperature midway between surfaces
T_0	3.2	plasma temperature far from the solid surface
T_s	3.2	(ion) source temperature
T_{sh}	3.6.3	temperature at the sheath
$T_\parallel^i$	3.2	ion parallel temperature
$T_\perp^i$	3.2	ion perpendicular temperature
T_u	7.3.2	plasma temperature upstream from the divertor plate
$\hat{T}$	4.1	central (peak) temperature
U_0	5.4	surface binding energy
V	2.2.1	electrostatic potential
V_c	2.2.1	probe voltage cut-off for T_e measurement
V_f	2.2.1	floating potential of the probe or object
V_L	7.2.4	limiter potential
V_p	2.2.1	plasma potential
V_{se}	3.2	plasma potential at the sheath edge
V_{sf}	2.2.1	sheath (floating) potential drop
Y	3.6.2	sputtering yield
Y_C	5.3.2	carbon self-sputtering yield
Y_D	5.3.2	deuteron sputtering yield
Y_H	5.3.1	hydrogen sputtering yield
Y_s	5.3.1	self-sputtering yield
Z	2.2.1	ion charge
Z_{eff}	3.4	effective ion charge in the plasma
Z_{imp}	5.2	impurity ion charge
α	4.3	angle of incidence of ions on the surface
β	5.1	ratio of plasma pressure to magnetic pressure
γ_s	3.3	total heat transmission coefficient at the sheath
$\gamma_s^{e,i}$	3.3	electron, ion heat transmission coefficient at the sheath
δ	2.2.1	secondary electron emission coefficient
ϵ	2.2.4	dielectric constant
ϵ_p	6.4	average plasma energy density
ϵ_s	2.2.8	surface emissivity
ϵ_t	7.2.2	trapping coefficient, pumped limiter
η_{ex}	7.2.2	overall exhaust efficiency, pumped limiter
η_{He}	7.3.3	helium enrichment factor for the divertor

Symbol	Section	Definition
η_{np}	2.2.1	normalized plasma potential
η_{sc}	5.5.4	screening efficiency of the SOL for impurities
η_w	3.3	normalized (floating) wall potential
$\eta_\perp$	3.2	cross-field viscosity
θ	2.2.1	angle of $\vec{B}$ to the surface
κ	3.5	b/a plasma elongation
$\kappa_0 T^{5/2}$	3.6.3	electron heat conduction coefficient along $\vec{B}$
κ_i	2.2.8	thermal conductivity
$\kappa_\perp$	6.1	cross-field heat conductivity
λ	2.2.3	wavelength
λ_{dep}	5.6	decay length of impurity deposition on limiters
λ_D	3.2	Debye length
λ_{ei}	2.2.1	electron–ion collisional mean free path
$\lambda_{i,e}$	3.4	ion, electron temperature scrape-off length
λ_n	2.1	density scrape-off length in the SOL
$\bar{\lambda}_n$	4.6	poloidally averaged value of λ_n
λ_{iz}^0	4.1	ionization depth into the plasma
λ_P	3.4	power scrape-off length
λ_{pen}	4.6	approximation to neutral penetration length
λ_s	3.1	thickness of the SOL
λ_{SOL}	5.5.1	decay length of impurities in the SOL
λ_T	3	temperature scrape-off length in the SOL
λ_Γ	3.4	particle flux scrape-off length
$\lambda_{1/2}$	4.6	depth into the plasma at which half of the ionization contributing to the plasma density has occurred
μ	2.2.4	refractive index
ν_{ei}	3.4	electron–ion equipartition collision frequency
ρ	5.3.2	fraction of impurity ions returning to the hot spot on the surface
$\overline{\sigma v}_{cx}$	4.6	charge exchange rate coefficient
$\overline{\sigma v}_i$	2.2.2	ionization rate coefficient
$\overline{\sigma v}_{\ell m}$	2.2.2	excitation rate coefficient (from ℓ to m)
τ_E	2.1	energy confinement time
τ_{EH}	4.1	energy confinement time (H-mode)
τ_{EL}	4.1	energy confinement time (L-mode)
τ_p	2.1	particle confinement (replacement) time
τ_p^*	4	decay time of the plasma density
τ_{SOL}	5.5.1	dwell time of impurities in the SOL
τ_w	4.7	wall retention time of particles
$\tau_\parallel$	3.1	plasma particle dwell time in the SOL
ϕ_{ph}	2.2.2	phase delay of the wave
Φ	3.6.2	total particle flux
Φ_{in}	4.2	total particle flux inward
Φ_{in}^0	5.5.1	total neutral impurity influx
Φ_{out}^+	5.5.4	total ion outflux
Φ_L^0	4.5	total neutral flux to limiters
Φ_L^+	4.5	total ion flux to limiters
Φ_{out}	4.2	total particle outflux
Φ_w^0	4.5	total neutral flux to walls
Φ_w^+	4.5	total ion flux to walls
$\chi_\perp$	3	cross-field heat diffusivity

Symbol	Section	Definition
$\chi_{\perp 0}$	3.4	cross-field heat diffusivity at the LCFS
ω	2.2.4	angular frequency of the wave
ω_p	2.2.4	plasma frequency
Γ	3.3	particle flux density
Γ_0	7.2.2	particle flux density at the LCFS
Γ_d	7.3.2	neutral particle flux density in the divertor chamber
$\Gamma_{se}^{e,i}$	3.3	electron, ion flux density at the sheath edge
Γ_n	3.6.1	neutral particle flux density
$\Gamma_\parallel$	2.2.1	charged particle flux density along $\vec{B}$
$\Gamma_\perp$	2.2.1	charged particle flux density normal to $\vec{B}$
$\Gamma_\perp^{ES,EM}$	9	electrostatic, electromagnetic cross-field particle flux density due to fluctuations
Σ	4.6	a combined ionization/charge-exchange cross-section for hydrogen